Characterization and scaling of the tokamak edge transport barrier

Philip Adrian Schneider

München 2012

Characterization and scaling of the tokamak edge transport barrier

Philip Adrian Schneider

Dissertation

der Fakultät für Physik
der Ludwig–Maximilians–Universität
München

durchgeführt am
Max–Planck–Institut für Plasmaphysik

vorgelegt von
Philip Adrian Schneider
aus München

München, den 24.04.2012

Erstgutachter: Prof. Dr. Hartmut Zohm
Zweitgutachter: Prof. Dr. Harald Lesch
Tag der mündlichen Prüfung: 19.07.2012

Zusammenfassung

Das Regime mit hohem Einschluss (H-Mode) in einem Tokamak Plasma zeichnet sich durch eine besondere Randregion aus. Auf einem kleinen räumlichen Bereich von 1-2 cm ändern sich die Eigenschaften des Plasmas signifikant. In dieser Region, auch Pedestal genannt, variieren einige Parameter um 1-2 Größenordnungen. Bisher sind die Entstehung dieses Pedestals und seine Stabilität nur unvollständig verstanden. Daher ist es ein Ziel dieser Dissertation, zu dem Verständnis des Pedestals beizutragen und Skalierungen für größere Maschinen, wie ITER oder DEMO, zu entwickeln.

Mit Messungen von verschiedenen Tokamaks - ASDEX Upgrade, DIII-D, JET - wurde eine Pedestal-Datenbank aufgebaut. Das Pedestal wurde für alle Maschinen mit derselben Methode charakterisiert. Dadurch erhält man den maximalen Wert im Pedestal, seine Breite und seine Steigung, jeweils für die Elektronendichte n_e, Elektronentemperatur T_e und Ionentemperatur T_i. Diese Größen und Ableitungen davon, wie Druck oder Einschlusszeit, wurden analysiert. Für diesen Zweck wurden zwei verschiedene Sets von Parametern verwendet: normierte Größen (Druck β, Zeit $\nu_\star$, Länge $\rho_\star$, Form f_q) und technische Größen (Ausdehnung a, magnetisches Feld B_t, Plasma Strom I_p, Heizleistung P).
Alle Ergebnisse werden durch die Wahl des Koordinatensystems beeinflusst: normierter poloidaler Fluss Ψ_N oder Ortsraum r/a. Bei beiden Parametersets wurde beobachtet, dass die Pedestalbreiten in Elektronentemperatur und Elektronendichte unterschiedlich skalieren. Für ITER oder DEMO würde diese Skalierung bedeuten, dass das Temperaturpedestal deutlich breiter ist als das Dichtepedestal.
Der Druck am Pedestal zeigt verschiedene Abhängigkeiten für Elektronen und Ionen. Die Extrapolationen zu ITER und DEMO geben ein $T_\mathrm{e,ped}$ von 4 keV bzw. 10 keV, allerdings ergeben sich deutlich niedrigere Werte für die Ionentemperatur. Eine zwei-Phasen Analyse der Energieeinschlusszeit τ_E wurde angewandt, um den Beitrag des Pedestals zur gesamten Einschlusszeit abzuschätzen. Die Abhängigkeiten, die sich aus der Skalierung für $\tau_\mathrm{E,ped}$ ergeben, sind nahezu identisch mit denen der IPB98 Skalierung. Dies ist ein deutlicher Hinweis darauf, dass durch das Pedestal ein signifikanter Beitrag zum gesamten Einschluss geleistet wird. Die Extrapolationen zu ITER zeigen eine Einschlusszeit von 3 s, was sich am unteren Rand der IPB98 Skalierung befindet.
Die Pedestalgradienten im Ortsraum zeigen eine deutliche Korrelation mit den Werten am oberen Rand des Pedestals. Besonders ausgeprägt ist diese Abhängigkeit für die Elektronentemperatur, hier wurde zudem keine Abhängigkeit mit einem anderen Parameter beobachtet. Die Gradienten in Ψ_N zeigen keine vergleichbare Korrelation. Der normierte Druckgradient α, der für die Stabilität des Pedestals wichtig ist, ist korreliert mit dem normierten Druck und der Plasmaform. Auch andere Beobachtungen lassen auf eine wichtige Rolle der Plasmaform schließen, was einen starken Einfluss auf Extrapolationen haben kann.

Die vorliegende Studie bestätigt, dass die Randtransport Barriere nicht durch eine einzelne

Theorie beschrieben werden kann. Die Höhe des Pedestals in der Elektronen- und Ionentemperatur sowie der Dichte kann separat durch entsprechenden Transport limitiert sein, während sie zusammen durch eine Stabilitätsgrenze limitiert sind. Gleichzeitig skaliert die radiale Ausdehnung der Temperatur und der Dichte verschieden.

Abstract

The high confinement regime (H-mode) in a tokamak plasma displays a remarkable edge region. On a small spatial scale of 1-2 cm the properties of the plasma change significantly. Certain parameters vary 1-2 orders of magnitude in this region, called the pedestal. Currently, there is no complete understanding of how the pedestal forms or how it is sustained. The goal of this thesis is to contribute to the theoretical understanding of the pedestal and provide scalings towards larger machines, like ITER and DEMO.

A pedestal database was built with data from different tokamaks: ASDEX Upgrade, DIII-D and JET. The pedestal was characterized with the same method for all three machines. This gives the maximum value, gradient and width of the pedestal in n_e, T_e and T_i. These quantities were analysed along with quantities derived from them, such as the pressure or the confinement time. For this purpose two parameter sets were used: normalized parameters (pressure β, time $\nu_\star$, length $\rho_\star$, shape f_q) and machine parameters (size a, magnetic field B_t, plasma current I_p, heating P).
All results are dependent on the choice of the coordinate system: normalized poloidal flux Ψ_N and real space r/a. The most significant result, which was obtained with both parameter sets, shows a different scaling of the pedestal width for the electron temperature and the electron density. The presented scalings predict that in ITER and DEMO the temperature pedestal will be appreciably wider than the density pedestal.
The pedestal top scaling for the pressure reveals differences between the electron and the ion pressure. In extrapolations this results in values for $T_\mathrm{e,ped}$ of 4 keV (ITER) and 10 keV (DEMO), but significantly lower values for the ion temperature. A two-term method was applied to use the pedestal pressure to determine the pedestal contribution to the global confinement time τ_E. The dependencies in the scaling for $\tau_\mathrm{E,ped}$ are nearly identical to the IPB98 global confinement scaling. This strongly suggests a significant pedestal contribution to the global confinement. The extrapolations result in a global confinement time of 3 s for ITER which is at the lower end of the IPB98 scaling.
The pedestal real space gradients show a very strong correlation with the pedestal top values. The trend is particularly pronounced for T_e and shows no deviation due to other parameters. The gradients in Ψ_N coordinates shows no such correlation. The normalized pressure gradient α, which is important for the pedestal stability, has a strong correlation with the normalized pressure and with the plasma shape. The plasma shape plays an important role for the pedestal which can have significant impact on the extrapolations.

The presented study confirms that the pedestal cannot be described by a unifying theory. The different observations favour various mechanisms. The pedestal top values of electron and ion temperature and density can be individually transport limited, but together they can still reach the peeling-ballooning stability limit. At the same time the pedestal widths of temperature and density scale individually.

Acknowledgements

This thesis is the culmination of over three years of research which would not be possible without the support and expertise of a lot of people.

I am especially grateful for the excellent supervision of Elisabeth Wolfrum. She invested a lot of time for long discussions, supported new ideas and showed a never subsiding enthusiasm. Without this catching enthusiasm it would not have been so interesting to keep digging in the database.
I want to thank Hartmut Zohm for a lot of good discussions, that he believed in my work and gave me the opportunity to visit DIII-D and extend my research to other fusion experiments besides AUG. Without this faith my thesis would lack a very important part. I also have to thank him for giving the best lectures I attended during my time at the university and bringing me to plasma physics in the first place.

A special thanks goes to Mike Dunne who provided the kinetic equilibrium reconstructions and who carefully read my manuscripts. He helped a lot to degermanise my English, but could not succeed completely. I want to thank my host in San Diego Rich Groebner who welcomed me warmly at GA and was a great help in achieving all and more goals I planned for this visit. Rich Groebner, Marc Beurskens and Tom Osborne deserve special recognition for generously contributing data from DIII-D and JET to the pedestal database. They also helped significantly to improve the pedestal width chapter with helpful comments and fruitful discussion. I also want to thank Bernd Kurzan who introduced me to the Thomson scattering diagnostic and made sure that I did not have to spend three years in front of my computer terminal. The people who helped me a lot with my questions about the theoretical background are Sibylle Günter, Karl Lackner and Phil Snyder and I am grateful for their efforts to elucidate the plasma physics for me, although one will feel a little dissy after two hours of discussion.
I am grateful for a lot of helpful discussions with Ben Geiger, his remarks to the draft of this thesis and that he was key to the great spirit in our office. I want to thank Ivo Classen who was a great help in learning the concepts of data analysis and is always around to answer any kind of questions. For contributions to this work and fruitful discussion in day-to-day business or at conferences I also want to thank Jurrian Boom, Andreas Burckhart, Thomas Eich, John Ferron, Rainer Fischer, Jörg Hobirk, Jerry Hughes, Otto Kardaun, Paddy McCarthy, Rudi Neu, Thomas Pütterich, Silvia Rathgeber, Francois Ryter, Pierre Sauter, Bill Stacy, Daniel Told, Jose Vicente, Eleonora Viezzer, Ronni Wenninger, Bernd Wieland and Matthias Willensdorfer.
The whole ASDEX Upgrade team has my regard for running the machine on every shotday and to keep her in good nick all the remaining time, without you no experiments would be possible. The same is true for the people who run DIII-D and JET, unfortunately I never had the chance to know them.

I am grateful for all the people who made the time at IPP to not-only-work, especially the PhD office crew and all the daily visitors Leena Aho-Mantila, Matthias Bernert, Diarmuid Curran, Hauke Doerk, Sina Fietz, Tim Happel, Fabian Honecker, Pascal de Marne, Rachael McDermott, Steffen Potzel, Fabian Sommer and Christian Vorpahl. A special reckoning is due for Ben Geiger for supplying our office with beverages and organising the fridge, nobody wants to miss this during a hot summer days.

Finally, I want to express my gratitude to my family. I thank my siblings Sascha, Tilman, Elisa and Johanna for their continuous moral support and especially my parents Hartmut and Ursula Schneider for their unconditional support, for as long as I can remember, but in particular in the last few months when the work piled up and no end was yet in sight.

the pedestal widz is not a joke

Contents

Chapter 1

Introduction

Nuclear fusion is the energy source of our sun and other stars. This means that nuclear fusion is indirectly responsible for most sources of energy which can be utilized on earth. The aim of a fusion power plant is to access this energy source directly.
Much can be said about energy needs [1] and how to address these in the future. This thesis will not attempt to motivate different scenarios for the future energy production, but will start with the assumptions that the present situation is not capable ot satisfing future demands on energy and that a fusion power plant is a worthwhile endeavor which is capable of playing a significant role in the future energy mix.

The most promising reaction for nuclear fusion in a power plant is between the hydrogen isotopes deuterium D and tritium T

$$ {}^{2}_{1}\mathrm{D} + {}^{3}_{1}\mathrm{T} \rightarrow {}^{4}_{2}\mathrm{He} + {}^{1}\mathrm{n} + 17.6\mathrm{MeV}. \tag{1.1} $$

This reaction has a high energy output which is distributed between the kinetic energy of the α-particle ${}^{4}_{2}\mathrm{He}$ (3.5 MeV) and the neutron n (14.1 MeV). It also has a favourable reaction cross section compared to other fusion reactions.
In order to achieve a self sustained cycle of fusion reactions, known as ignition, the ions need to remain in the reacting region for a sufficient time. The α-particle must transfer its energy to the deuterium and tritium ions which must keep their energy long enough to fuse with each other. The approximate limit for ignition is expressed by the triple product [2]

$$ nT\tau_{\mathrm{E}} > 5 \cdot 10^{21} \frac{\mathrm{keVs}}{\mathrm{m}^3}. \tag{1.2} $$

The temperature T defines the reaction cross section and together with the density n the reaction rate. τ_{E} is the energy confinement time. For example, it is possible to surpass this limit with a density of $10^{20}\mathrm{m}^{-3}$ a temperature of 20 keV and a confinement time of a few seconds. A temperature of 20 keV corresponds to over 200 million Kelvin. At such high temperatures, the gas is fully ionized and is called plasma. Due to the high temperatures a solid confinement structure cannot be used. Fortunately, a plasma may be confined with a magnetic field. Charged particles cannot move freely in the presence of a magnetic field. Because of the Lorentz force the charged particles gyrate around the magnetic field lines with a known frequency and radius, while the gyro center can move freely along the field line. The gyro frequency depends on the particle charge q and mass m as well as the applied

magnetic field B [2]

$$\omega_c = \frac{qB}{m}. \tag{1.3}$$

The gyro radius ρ depends on the cyclotron frequency ω_c and the perpendicular velocity of the particle $v_\perp$

$$\rho = \frac{v_\perp}{\omega_c}. \tag{1.4}$$

One of the challenges in a fusion plasma is to have a temperature of over hundred million degree in the plasma center and only a few hundred degrees at the walls enclosing the plasma. This is a difference of 4-5 orders of magnitude. Even with a strong magnetic field, energy transport along this gradient which is perpendicular to the field, cannot be suppressed completely. The typical heat transport is so high that the temperatures for ignition cannot be achieved in moderately sized experiments. Therefore, it is not possible to build a small prototype of a fusion reactor. Instead the physics are explored in smaller experiments with several goals: find the optimal operation parameters, identify and ultimately solve the challenges which might arise in fusion relevant plasmas. The largest experiment presently in operation is still a factor of 2 smaller than a possible prototype.
The approach to understand a fusion plasma can be compared to a wind tunnel experiment,

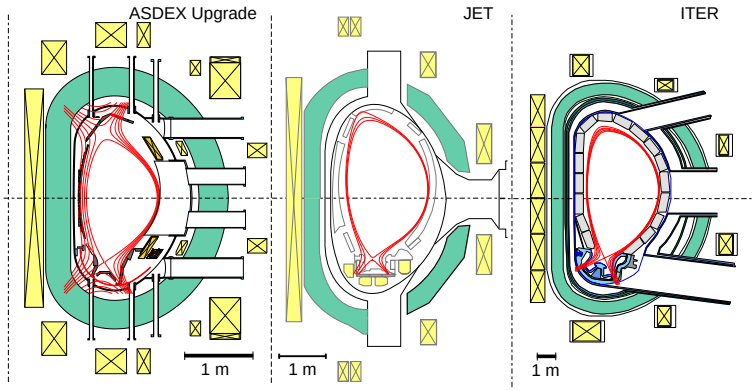

Figure 1.1: Principle of the step ladder approach. Comparison of machines with different size but otherwise similar configuration. (Image: IPP)

only the validation with the original is still missing. This is also described as step ladder approach: to determine the way to the next rung of the ladder, previous steps are carefully analysed. In Figure 1.1 a step ladder is illustrated for three machines with a similar layout for the cross section but with a different size. Experiments on the two smaller machines are used to predict the properties of the larger machine. The parameters accessible with a single experiment are generally limited because of engineering constraints. The parameter range can be extended by comparing different experiments. Several steps have been taken and a lot of research was performed to validate the physical understanding of the plasma processes and to gain confidence about the next step. It would be beyond the scope of this introduction to give an adequate overview of the research done in the last two decades. The review acts which do so are the *ITER Physics Basis* [3] and the *Progress in the ITER Physics Basis* [4]. A summary of this research would have to admit that of many phenomena only some aspects are understood and can be predicted. Also the interaction between different physical mechanisms is often not well understood and only extreme cases, where a single mechanism is dominating, are analysed.

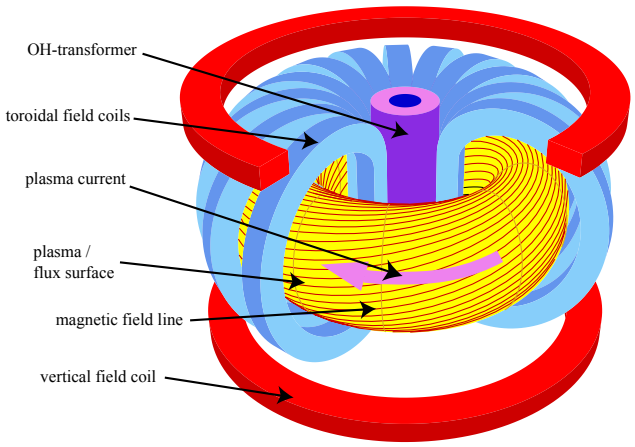

Figure 1.2: Tokamak principle of magnetic confinement. (Image: [5])

This thesis focuses on one particular region in a tokamak. The tokamak is one method to achieve magnetic confinement and will be described in Section 1.1. The outline of this thesis is described in Section 1.2

1.1 Tokamak

One established principle of magnetic confinement is the tokamak. In Figure 1.2 the tokamak principle is illustrated. Toroidal magnetic field coils generate a tube of nested magnetic field surfaces, which is bent to close on itself and form a torus. With a central transformer, a current is driven in this plasma tube. The current generates an additional poloidal magnetic field which is perpendicular to the toroidal field and results in helically twisted magnetic field lines. The different magnetic field components are illustrated in Figure 1.3. The twisting of the field lines increases the stability of the whole magnetic configuration. The winding number of magnetic field lines is called safety factor q. The safety factor is defined as the ratio of the numbers of toroidal and poloidal turns, a field line needs to close on itself

$$q = \frac{\text{number of toroidal transits}}{\text{number poloidal transits}}. \tag{1.5}$$

The vertical field coils, in Figure 1.2, are used for position control and shaping of the plasma. In Figure 1.3 also the coordinate system used throughout this thesis is illustrated. In fact, it consists of a combination of a cylindrical and a polar coordinate system. The cylindrical coordinate system consists of the radial coordinate R, the vertical z and the toroidal angle ϕ. The polar coordinate has its origin at the plasma center R_0, z_0, where R_0 is the major radius of the plasma and $z_0 = 0$, and has the radial coordinate r and the poloidal angle θ. The minor radius a is roughly the distance between plasma center and the last closed flux surface. The detailed definition for a is given in Section 6.3 along with a description of the plasma shape. This coordinate system is in general not used for comparison of different measurements. One can exploit the symmetry of the plasma and the properties of the magnetic flux surface to define a 1D normalized flux coordinate ρ_p. This coordinate ranges from 0 in the plasma center to 1 at the last closed flux surface. A detailed description of this coordinate transformation is given in Section 5.1.

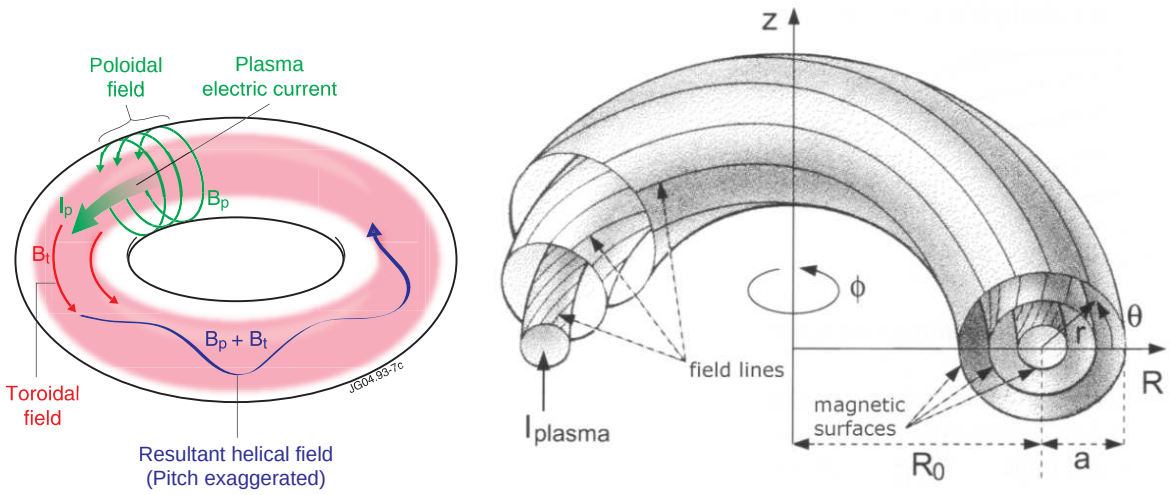

Figure 1.3: Illustration of the different magnetic field components (left) and the coordinate system (right). (Images: EFDA JET and [5])

		AUG	DIII-D	JET
R_0	[m]	1.65	1.67	2.96
a	[m]	0.50	0.67	1.20
B_t	[T]	3.9	2.2	3.4
I_p	[MA]	1.6	3.5	6.0
P_{heat}	[MW]	30	26	32
First Wall		W	C	C

Table 1.1: The main design values of the three tokamaks AUG, DIII-D and JET

The main design values of the three tokamaks AUG, DIII-D and JET which are included in the analysis for this thesis are given in Table 1.1. In fact, the standard operation of the machines is done well below the design values. More realistic parameters for machine operation are given in Chapter 6.

1.2 Thesis Goals and Outline

The region investigated in this thesis is an intermediate region between the hot plasma core, where the main plasma ions (here: deuterium) and most impurity ions (C, N, O, ...) are fully ionized, and the cold unconfined region, where the temperatures are low enough for ions to have bound electrons. Most aspects of the core region are fairly well understood which can be ascribed to the extreme nature of the plasma core. However, in the intermediate region the dominating physical process, or whether there is a single dominant process, is not obvious. For example, a treatment of this region as fully a ionized gas will not describe the physics correctly when in reality ionization processes also play an important role.
In this intermediate region, a pedestal in temperature and density can form under certain conditions. The pedestal causes all fusion relevant parameters ($nT\tau_E$) to increase significantly. Such a plasma has improved confinement and is called high confinement mode, H-mode, and will be described in Chapter 2. The H-mode is one of the favoured plasma

scenarios to achieve ignition. A better understanding of the physics behind the H-mode pedestal would be beneficial on the way to a fusion power plant. It would help to predict and solve challenges which might arise at the higher temperatures and it could be used to improve the plasma performance.
The pedestal is characterized by steep gradients over a few cm and an increase of temperature and density by 1-2 orders of magnitude. This causes typical lengths and times to change significantly on a small radial scale. The pedestal is also characterized by a cyclic instability, the edge localized mode (ELM), which causes the pedestal to collapse with a frequency of up to 200 Hz and is described in Section 2.1. In consequence, it is difficult to describe this region numerically with present day computational power. The scales which must be covered by a simulation increase even more when electrons and ions are treated together. Approximations are applied to describe the plasma numerically. One typical example for a simplification is the fluid approach, where a magnetised plasma is treated as a single fluid which can carry an electric current. In a single fluid, electrons and ions are not treated separately. The resulting simplified picture might not catch all phenomena which are observed. This is one reason why no theory for the pedestal is broadly accepted. A selection of theories describing aspects of the pedestal are introduced in Chapter 3.
The small spatial scales of the pedestal and the cyclic instability require edge diagnostics which have a high temporal and spatial resolution. In the last few years the diagnostics of the three tokamaks ASDEX Upgrade (AUG), DIII-D and JET have been continuously improved and now all three machines are equipped with high resolution edge diagnostics which are described in Chapter 4. This allows us to resolve the pedestal in a way which could not be achieved in the past. In particular, fast edge measurements of the ion temperature have been sorely lacking which allow the resolution of an ELM cycle, and thus compare the pedestal of ions and electrons. The spatial resolution of the edge diagnostics of the JET tokamak were improved in a way which makes it is possible to resolve the pedestal correctly for the first time.
The edge profiles of all three machines are characterized with the same method, which is discussed in Chapter 5. In the same section a comparison of different equilibrium codes is performed, which is crucial for the multi-machine comparison. The characterization of the pedestal results in three quantities: the spatial extent of the pedestal region, the gradient in the pedestal and the value at the transition to the plasma core. These three quantities are analysed for electron temperature, electron density, electron pressure and ion temperature. The pedestal characteristics from AUG, DIII-D and JET are stored together with other plasma properties in a database, which is described in Chapter 6. The results of the analysis of this multi-machine database are presented and discussed in Chapter 7. Instead of a direct validation of various theories, this thesis follows a different approach: the aim is to identify the major influences on the pedestal. These trends are then compared with the theory. In Chapter 8 it is discussed how the results correlate with the next steps on the ladder towards a fusion power plant and what consequences can be drawn for theories and future research.

Chapter 2

H-Mode

The high confinement regime H-mode is one of the most promising scenarios for high energy plasma operation. This chapter describes the general characteristics of the H-mode and why the edge region of the plasma is of special interest for the H-mode. An important instability of the plasma edge will be introduced and at the end the database is described which is used throughout this work.

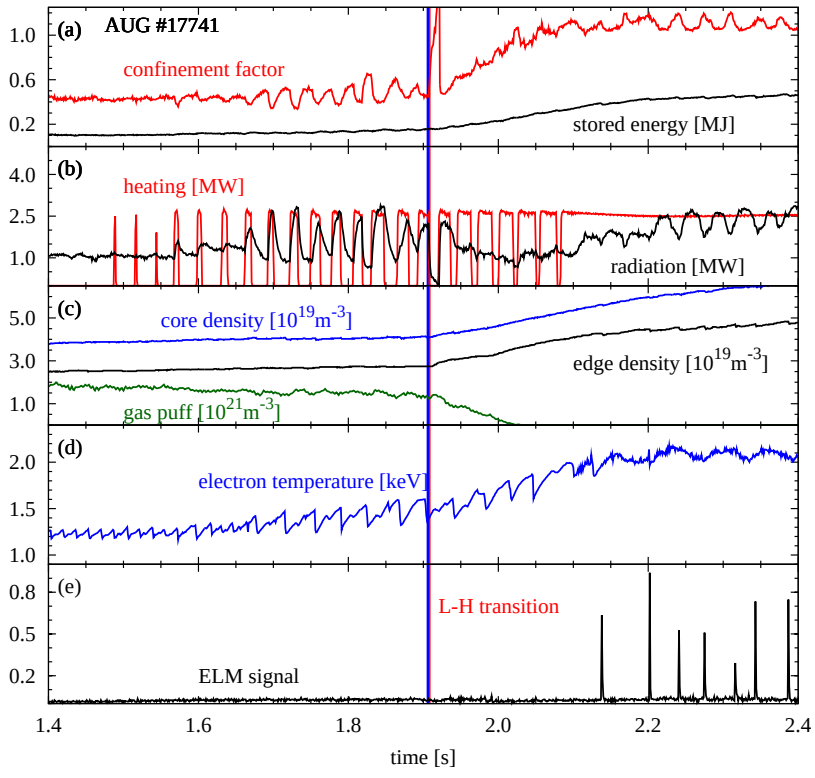

Figure 2.1: Time traces of key plasma parameters during an LH-transition at around 1.9 s.

The H-mode is a regime of increased energy and particle confinement. It was first observed in the ASDEX tokamak in 1980 [6]. Since then all auxiliary heated divertor tokamaks could reproduce the H-mode. The difference between the H-mode and an auxiliary heated low

confinement mode L-mode is best illustrated at the transition between both regimes called the L-H transition. In Figure 2.1 several traces of key plasma parameters are shown across an L-H transition at 1.9 s. The plasma current I_p and toroidal magnetic field B_t are constant in the selected time interval, $I_\mathrm{p} = 1.0$ MA and $B_\mathrm{t} = 2.0$ T. The change applied to the plasma is the auxiliary heating which is ramped from 0 to 2.5 MW (b) (red). During this power ramp the mean of the radiated power (black) stays constant. At a certain heating power the particle confinement increases significantly. Both edge (black) and core (blue) density (c) increase, although, the gas puff (green) is switched off by the feedback control. Further particle fuelling is provided by the neutral heating beams and recycling from the walls. Along with the density, temperature (d) (blue) and stored energy of the plasma (a) (black) increase. In the H-mode also an cyclic burst like edge localised instability (edge localised mode) appears (e). This instability is described with several examples in Section 2.1. The larger stored energy is not only due to the increased heating power but a larger energy confinement time

$$\tau_\mathrm{E} = \frac{W}{P_\mathrm{net}} \tag{2.1}$$

where P_net is the heating power arriving in the plasma, W is the stored energy in the plasma which is

$$W = \frac{3}{2}\int p\mathrm{d}V \tag{2.2}$$

with the total plasma pressure p. For better comparison of the quality of confinement τ_E, normalized to a multi machine scaling of the confinement time, is called H-factor. In the example the H-factor increases from 0.4 in L-mode to 1.1 in H-mode (a) (red). With an H-factor around 1.0 a discharge is called normal H-mode for factors larger than 1.2 improved H-mode. The most common H-mode confinement scaling is the ITER physics basis IPB98(y,2) scaling [3]

$$\tau_\mathrm{E,IPB(y,2)} = 0.0562 \cdot I_\mathrm{p}^{0.93} B_\mathrm{t}^{0.15} n_e^{0.41} P^{-0.69} R^{1.97} \kappa^{0.78} \epsilon^{0.58} M^{0.19}, \tag{2.3}$$

with plasma current I_p, the toroidal magnetic field B_t, the line averaged electron density n_e, loss power P, elongation κ, inverse aspect ratio ϵ and average ion mass M. The H-factor becomes

$$H_\mathrm{IPB(y,2)} = \frac{\tau_\mathrm{E}}{\tau_\mathrm{E,IPB(y,2)}}. \tag{2.4}$$

In Eq. (2.3) the most important influences on the energy confinement time become visible. While larger plasma current and the machine size increase the confinement time it degrades with increasing heating power. Although the H-mode confinement time scales with global plasma parameters, the improvement in confinement originates from a small layer at the plasma edge. In Figure 2.2 this is illustrated for three plasma parameters. The electron temperature (a) strongly increases at the plasma edge in the H-mode case and then continues to increase towards the plasma center with roughly the same gradient length as in the low confinement case. The electron density (b) has a steep gradient, at the edge, already in the L-mode. In the H-mode the density increases by about 25% together with a steepening of the gradient at the edge. The density increase towards the plasma center is not so large as it was for the temperature. The pressure profile (c) essentially shows the same trend as the electron temperature.

The plasma edge region in an H-mode is called pedestal or edge transport barrier because the transport is strongly reduced in this region. Therefore, larger gradients can be sustained and a characteristic pedestal structure forms at the edge. Figure 2.3 shows a pedestal in

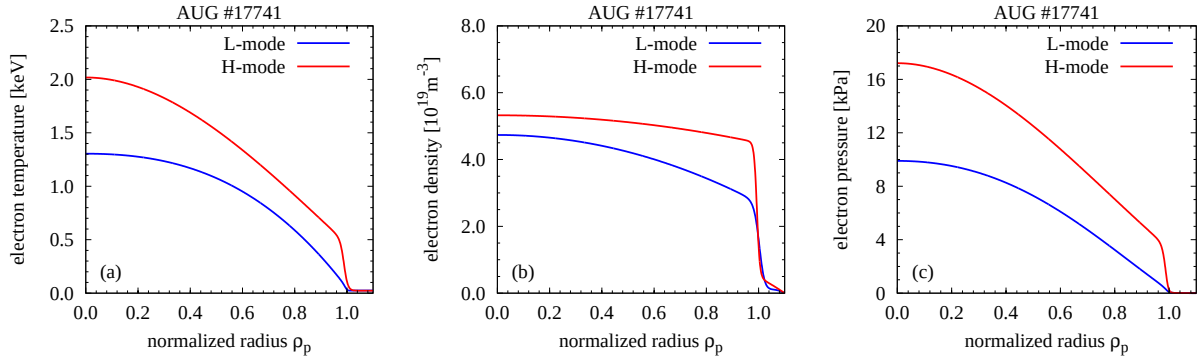

Figure 2.2: Profiles in low confinement (blue) at $t = 1.6$ s and high confinement (red) at $t = 2.1$ s. The improvement is visible in the last few percent of the plasma for the three parameters temperature (a), density (b) and pressure (c).

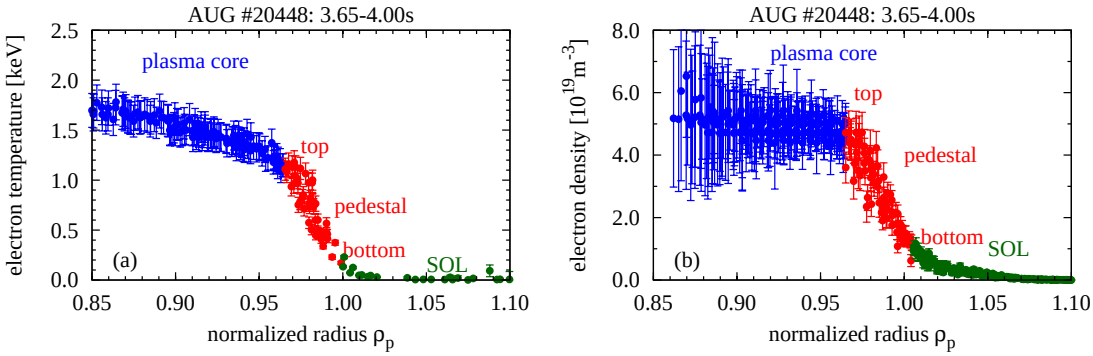

Figure 2.3: ELM synchronised measurements of the plasma edge electron temperature (a) and density (b). Three regions with different gradients are characterised as plasma core (blue), pedestal (red) and scrape off layer SOL (green).

electron temperature (a) and electron density (b). The plasma is classified into separated regions: the plasma core (blue), the pedestal (red) and the scrape off layer SOL (green). The criteria for this classification are discussed in Chapter 5. Measurements of the pedestal in H-mode compared to L-mode show a strong reduction in the radial correlation length of density fluctuations [7]. This is associated with a reduction of turbulent transport. The radial electric field E_r strongly increases in the H-mode pedestal [8, 9]. Two typical profiles of the radial electric field in H-mode (red) and L-mode (blue) have a minimum near the separatrix, the minimum in the H-mode is one order of magnitude deeper than in L-mode (Figure 2.4). The strong shear in the radial electric field is the starting point for various theories for pedestal formation and pedestal characteristics, selected theories will be introduced in Chapter 3.

The main differences found in H-mode are located at the plasma edge. Some effects in the plasma center can be explained with the changes at the edge. In Figure 2.5 several core temperature profiles with different edge temperatures are shown, all profiles have the same gradient length. This suggests the core transport is more or less unaffected by the changes in the edge and the edge is solely responsible for the higher core temperature. This effect is referred to as profile stiffness of the electron temperature [11]. Motivated by the concept of profile stiffness the core and pedestal physics are studied separately. For the plasma

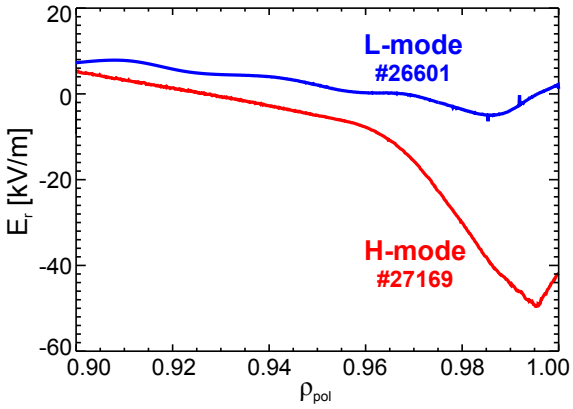

Figure 2.4: Two typical profiles of the radial electric field E_r in L-mode (blue) and H-mode (red). (Reprinted from [10])

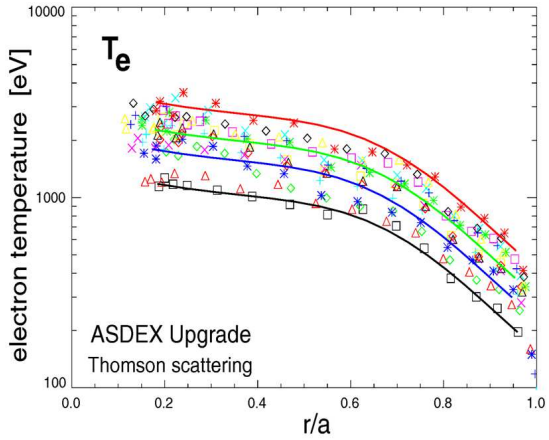

Figure 2.5: Core electron temperature profiles for different pedestal parameter. The core gradient length are the same for all cases. (Reprinted from [11])

stored energy and confinement time this separation is known as two-term model [12, 13]. It is assumed that the contributions to the plasma pressure are a constant offset from the pedestal (red) and the transport dependent core contribution (blue) as illustrated in Figure 2.6. Eq. (2.2) can be rewritten as

$$W = \frac{3}{2} p_\mathrm{ped} \int \mathrm{d}V + \frac{3}{2} \int p - p_\mathrm{ped} \mathrm{d}V = W_\mathrm{ped} + W_\mathrm{core}, \tag{2.5}$$

where p_ped is the pressure at the pedestal top. Also the confinement time can be separated into two contributions

$$\tau_\mathrm{E} = \tau_\mathrm{E,ped} + \tau_\mathrm{E,core} \tag{2.6}$$

The pedestal is responsible for 30-50% of the total stored energy [13] and therefore important for the overall plasma performance. The importance of the pedestal arises from its characteristics in partical and heat transport. Many transport processes are linked to gradient lengths of temperature and density, examples are found in [14, 15, 16, 17]. The electron temperature gradient length is

$$L_{T\mathrm{e}}^{-1} = \frac{\nabla T_\mathrm{e}}{T_\mathrm{e}} = \nabla(\ln T_\mathrm{e}) \tag{2.7}$$

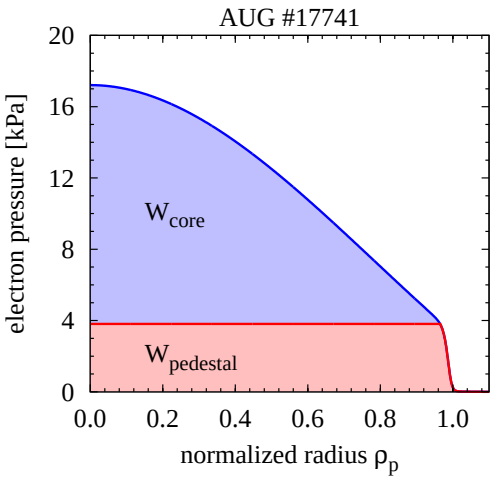

Figure 2.6: Electron pressure profile of an H-mode discharge and indications of the different contributions to the plasma stored energy Eq. (2.2), the pedestal contribution in red and the core contribution in blue.

and the density gradient length is defined analogous. The ratio of gradient lengths becomes

$$\eta_\mathrm{e} = \frac{L_{ne}}{L_{Te}} = \frac{\partial \ln T_\mathrm{e}}{\partial \ln n_\mathrm{e}}, \tag{2.8}$$

therefore its value is the gradient of the curve $\ln T_\mathrm{e}$ versus $\ln n_\mathrm{e}$. The gradient length ratio is expected to be relevant for temperature gradient driven turbulence [**?**]. In Figure 2.7 (a) the different regions of the plasma are numbered using a DIII-D H-mode discharge. The SOL (I) is characterised by very low temperature and density and no distinct correlation of the gradient length ratio. In the pedestal region (II) η_e is constant and larger than in the SOL (here $\eta_\mathrm{e} = 2.4$). In the plasma core (III) the density becomes flat resulting in a larger gradient length which leads to an increase of $\eta_\mathrm{e} \sim 5$, in the very plasma center η_e drops for this example because of a peaked density profile. In Figure 2.7 (b) the fits to the temperature and density measurements in Figure 2.2 are plotted against each other and show the different behaviour in L- and H-mode. The H-mode exhibits a sharp increase of η_e near the pedestal top, with the smaller η_e in the pedestal. The L-mode has a larger $\eta_\mathrm{e} \sim 4$ in the whole confined region. Although a little smaller, the L-mode η_e is comparable to the H-mode core η_e. This is a further sign for the similarity of L-mode and H-mode core profiles.

In summary, the H-mode regime is characterised by improved confinement and larger energy content compared to an L-mode plasma. The improved plasma performance is localized at the plasma edge, where a pedestal forms. Different observations suggest that plasma core and pedestal can be treated separately. In particular does the core transport not change for different pedestal parameters. Due to its importance for the plasma performance formation and characteristics of the H-mode edge transport barrier are an active field of research, which includes the presented work.

2.1 Edge Localised Modes

The Edge Localised Mode (ELM) is a cyclic instability which is localised on the outer 20% of the plasma radius. The mode causes the transport barrier to collapse and expell particles

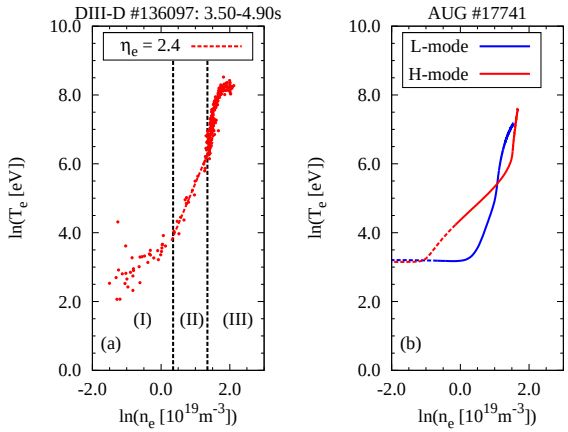

Figure 2.7: Illustration of the gradient length ratio of temperature and density η_e, which equals the gradient of the curve in the log-log plot of T_e and n_e. In (a) different regions are identified: the SOL (I), the pedestal (II) and the plasma core (III). In (b) L- and H-mode are compared - the dashed line indicates a region where the curve is dominated by the boundary conditions of the fit and not the data.

and energy. It is regularly observed in the H-Mode phase of tokamak and stellarator plasmas. The ELM is linked with large gradients which occur in the transport barrier. The trigger mechanism of an ELM and the ELM related dynamics of the transport barrier are active areas of research. In Figure 2.8 the collapse of the edge gradients caused by an ELM is documented. The gradients become smaller in a burst like event and gradually return to their former values. This is observed for the electron temperature (a), density (b) and pressure (c). Figure 2.8 also shows the localised nature of the ELM, for the inner 80% of the plasma radius no effect on the profiles is observed. The ELMs are not only observed

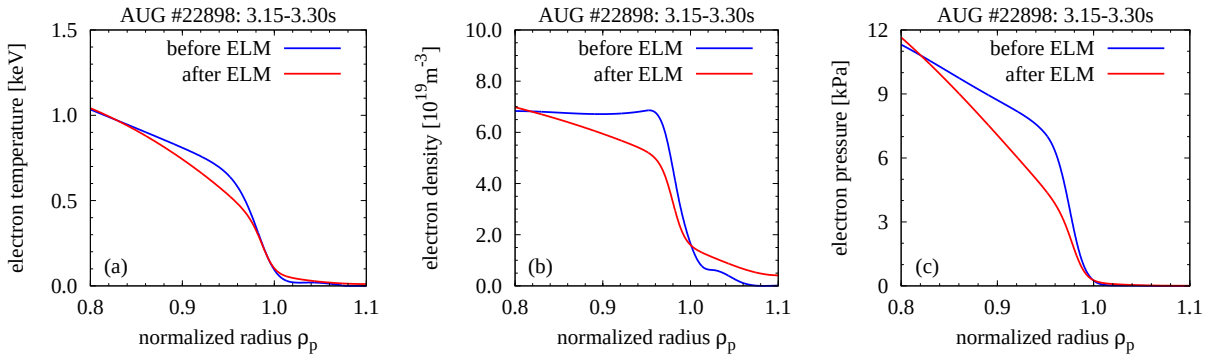

Figure 2.8: Profile evolution during an ELM cycle. In red the start of the cycle immediately after the crash and in blue the end of the cycle before the ELM crash. The profiles are of (a) electron temperature, (b) electron density and (c) electron pressure. The profiles are averaged ELM synchronized over 150 ms. This procedure is explained in detail in Section 5.2.

due to their impact on the profiles. Typical signatures of ELMs in different diagnostics are shown in Figure 2.9. In Figure 2.9 (a) a sudden increase in the currents flowing onto the divertor is observed. This is caused by particles which are expelled from the confined region and flow onto the divertor and are measured by shunts [18]. The ELMs also disturb the magnetic equilibrium in the plasma edge which can be measured with magnetic pick-up coils

around the torus. A time trace showing these burst like perturbations is shown in Figure 2.9 (b). In the soft x-ray radiation from the plasma edge (c) also the gradual recovery between two ELM crashes is measured. The large amount of additional particles in the SOL cause an increase in D_α radiation (d) which is historically the most common indicator for ELMs. Another important measurement of ELMs is their heat signature on the divertor tiles [19]. The heat loads flowing on the walls will define an operational limit for larger machines.

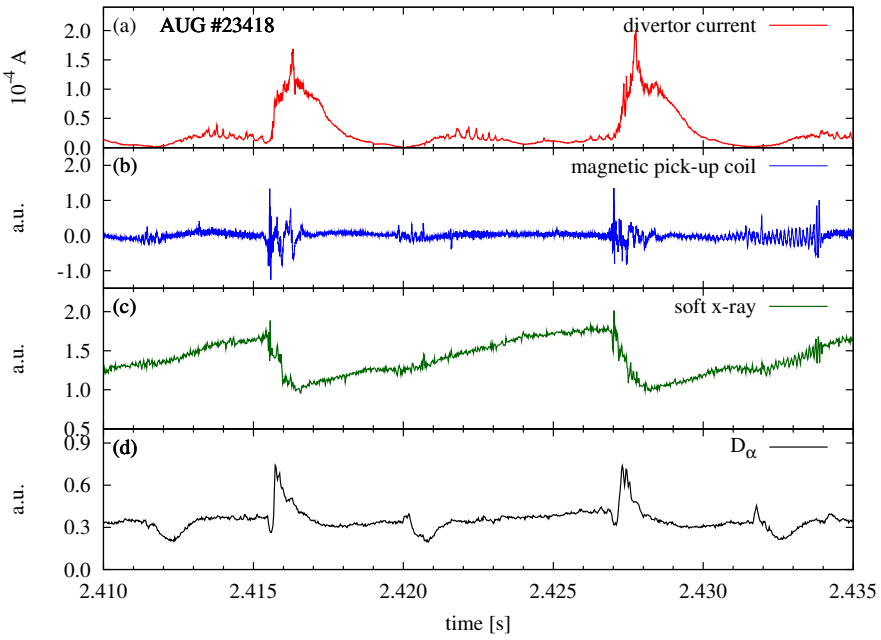

Figure 2.9: The signature of type-I ELMs in different diagnostics. The burst like event is visible in (a) the divertor current, (b) the magnetic pick-up coils, (c) the edge soft x-ray radiation and (d) the D_α radiation. The gradual recovery between ELMs can be observed in the edge soft x-ray signal.

In ideal MHD the ballooning mode could explain aspects of ELMs. At the plasma edge the edge pressure gradient causes a force counteracting the magnetic field line tension. The ballooning instability can occur, when the field line curvature is "bad" and the centre of the curvature is in the same direction as the pressure gradient, and cause the collapse of the edge transport barrier. The bad curvature region is at the low field side of the plasma. At the high field side the good magnetic magnetic curvature stabilises the ballooning mode. It is convenient to define a normalized pressure gradient α which arises from energy balance between the destabilising energy available pressure gradient and the energy required for field line bending [20]

$$\alpha = -\frac{2\mu_0 R_0 q^2}{B_\mathrm{t}^2}\frac{\mathrm{d}p}{\mathrm{d}r}. \tag{2.9}$$

In fact Eq. (2.9) is an approximation for cylindrical plasmas. A more appropriate definition was given in [21]

$$\alpha \equiv -\frac{1}{2\pi^2}\frac{\partial V}{\partial \Psi}\left(\frac{V}{2\pi^2 R_0}\right)^{1/2}\mu_0\frac{\partial p}{\partial \Psi}. \tag{2.10}$$

The main difference between Eq. (2.9) and (2.10) lies in the choice of the derivatives ∂_r and ∂_Ψ. The consequences of these different representations are discussed in Section 5.1.2. In

general tokamak geometry the critical value of α when the ideal ballooning mode becomes unstable is a complicated function of magnetic shear $s = r/q\mathrm{d}q/\mathrm{d}r$ and plasma shape. The ideal ballooning mode can provide a physics picture how pressure gradient driven instabilities form in the plasma. It was associated early on with the ELM instability [22]. However, later more detailed measurements showed that the ELM trigger cannot be explained with ballooning modes because the pressure gradient stays constant several ms before each ELM [23]. Therefore, the theory was extended with a current driven kink instability, the peeling mode. The combined occurrence is referred to as peeling-ballooning mode [24]. A sketch of the ELM cycle in peeling-ballooning theory is illustrated in Figure 2.10. The colored points correspond to the profiles in Figure 2.8. After the ELM crash the edge pressure gradient is low and increases gradually until it hits the ballooning limit for α. The pressure gradient stays constant while the edge current density builds up until the peeling-ballooning mode triggers the collapse of the edge transport barrier. The pressure gradient in the plasma is correlated with the current density due to the bootstrap current which is responsible for a significant part of the edge current density. The bootstrap current is dependent on the density and temperature gradients and therefore, is linked with the pressure gradient [25]. The last phase before the ELM crash is subject of ongoing research. The timescales observed

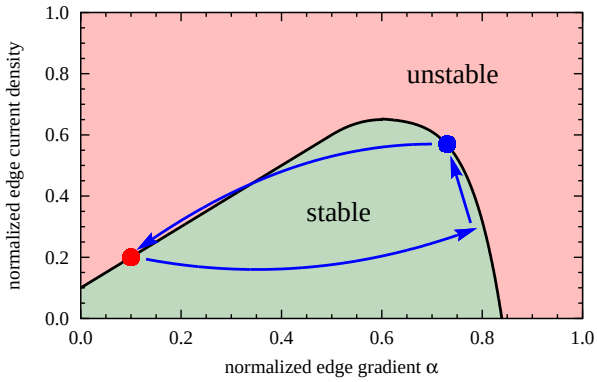

Figure 2.10: A sketch of an ELM cycle in the peeling-ballooning theory adapted from [24]. At high pressure gradient and large current density (blue point) the ELM is triggered and causes the profiles to relax (red point). From there the profile recovers until the next ELM crash occurs.

in the experiment are not in agreement with the peeling-ballooning theory [26]. While the ELM triggering process remains an active field of research, the limit in the pressure gradient due to the peeling-ballooning is widely accepted for plasmas in the type-I ELMy regime. This pressure gradient was tested and validated in different experiments [27, 28, 29, 30, 31]. In a type-I ELMy H-mode the same edge instability occurs. Independently of the progress in the theoretical understanding it can be assumed that a single physical mechanism determines this instability. Therefore, type-I ELMs define a reproducible, standardized regime. The restriction to a single regime suggests with high probability that different physical mechanisms were not mixed. Therefore, only plasma discharges with type-I ELMs are included in the database.

In the next two subsections the characteristics of two different ELM regimes are discussed, the standard case of type-I ELMs and the change of ELMs with addition of nitrogen in the plasma. Other H-mode regimes like type-II ELMs, type-III ELMs, ELM free, ELM suppressed or ELM mitigated are beyond the scope of this work and will not be discussed.

2.1.1 Type-I ELMs

The classification of ELMs into different types was motivated historically. The type-I or giant ELMs are named this way because they were the first type of ELMs observed in the DIII-D tokamak [32]. Their characteristics are increasing frequency f_{elm} with heating power and they are triggered when the gradient hits the critical limit $\alpha = \alpha_{\mathrm{crit}}$ in the peeling-ballooning theory. The latter criterion is to same parts an assumption as it is a definition. One cycle of a type-I ELM can be divided into three phases. At AUG the first phase is the crash which lasts generally 1-2 ms depending on the observed plasma parameter. After the crash there is a profile recovery phase of 4-7 ms. The recovery phase is different for density and temperature and can be divided into further sub-phases [26] which do not influence the analysis in the present work. After the profile recovery phase the maximal pedestal pressure gradient is constant until the next ELM crash. This third phase does not have a fixed timescale, the crash might occur immediately after the recovery or several ms later. Therefore, the frequency of the ELM cycle can vary from several Hz up to 300 Hz. In Figure 2.11 the ELM frequency is plotted against gas puffing at constant heating

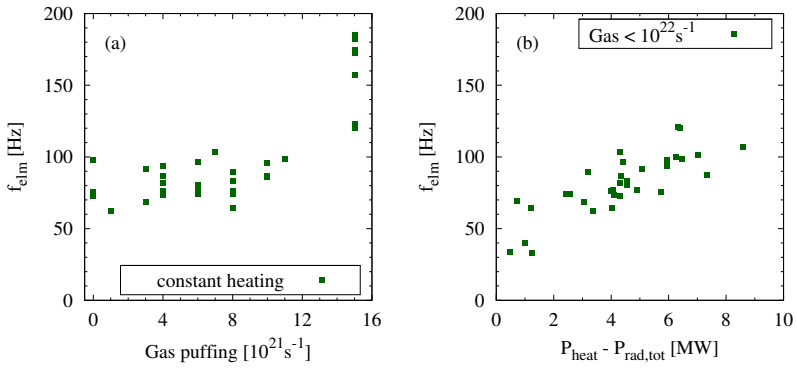

Figure 2.11: Two possibilities to influence the frequency of type-I ELMs. (a) at constant heating power the ELM frequency f_{elm} increases above a gas fuelling level of 10^{22} s^{-1}. (b) at low gas fuelling level $< 10^{22}$ s^{-1} the ELM frequency increases linearly with $P_{\mathrm{heat}} - P_{\mathrm{rad}}$. The plasma current and magnetic field is constant for both cases.

power (a) and against heating power at low gas puffing (b). In the present data set the ELM frequency is not influenced by the gas puffing below a threshold value of 10^{22} s^{-1} and increases by a factor of two for larger gas puffing. The ELM frequency increases linearly with $P_{\mathrm{heat}} - P_{\mathrm{rad}}$ as expected for type-I ELMs. P_{heat} is the auxiliary plus ohmic heating and P_{rad} the total measured radiation which includes radiation outside the confined region. Therefore, $P_{\mathrm{heat}} - P_{\mathrm{rad}}$ is a crude estimate of the power flow over the separatrix. One should note that in both cases the scatter of the ELM frequency is about 50 Hz. This suggests that other plasma properties influence the ELM frequency. While it might be possible to identify these properties in dedicated experiments they are not visible in the available database. This is because some parameters can not be determined accurately enough. One source of uncertainty is the impurity content in the plasma which will be discussed in the next section. The plasma shape was also found to influence the ELM frequency. At JET stronger shaping of the plasma decreased the ELM frequency [33]. Different quantification for the plasma shape are discussed in Section 6.3. In particular this means, increasing the gas puff or the heating power are recipes to increase the ELM frequency. However, at constant gas puff it

is possible to observe the same ELM frequency even with twice the heating power when the experiments were not carefully designed as similarity discharges. The power loss due to a single ELM decreases with ELM frequency, however, the averaged ELM power loss remains constant [34].

2.1.2 ELMs with Nitrogen Seeding

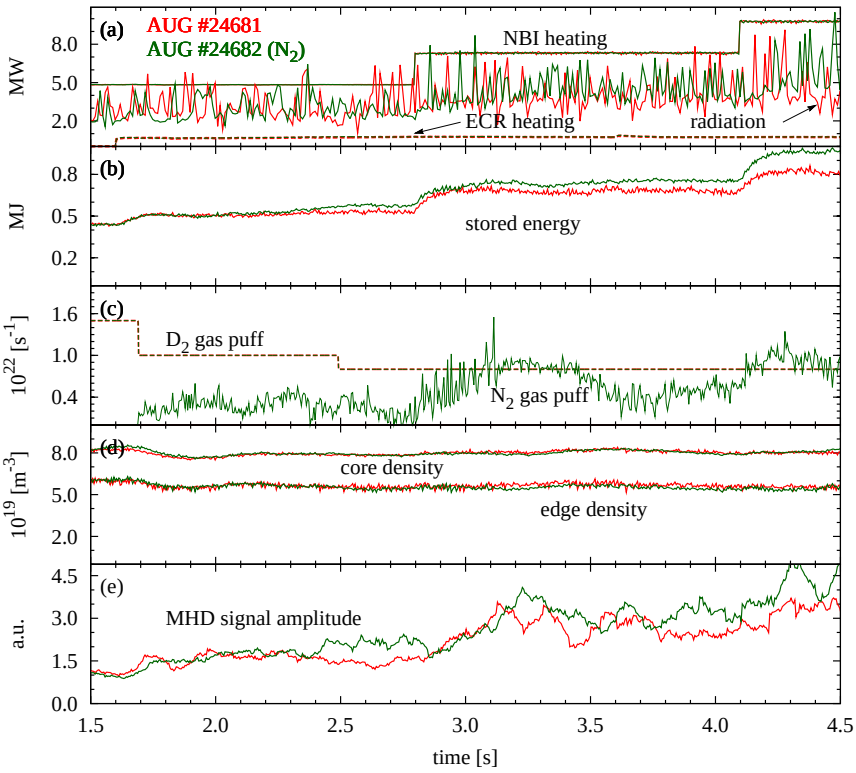

Figure 2.12: Time traces for two comparison discharges one without nitrogen seeding (red) and one with nitrogen seeding (green). Several signals show the similarity of these discharges: heating and radiation (a), stored energy (b), gas puff of deuterium and nitrogen (c), line averaged density (d), MHD activity amplitude (e).

The impurity content in the plasma is one mechanism to influence the characteristics of ELMs. In this section the influence of impurities is discussed using the example of nitrogen seeded discharges. The original reason to apply nitrogen seeding in the divertor was to protect the divertor in high power discharges. With increased impurity content more energy can be radiated and is not completely deposited in a small area where the field lines hit the divertor tiles. Besides its protective nature, nitrogen seeding was observed to improve the global energy confinement in AUG [35, 36, 37]. First an overview is given of the changes caused by nitrogen seeding. A special focus is put on the kinetic edge profiles which are expected to play a major role for ELMs as discussed in the introduction to this section. Then it is documented how the characteristics of an ELM changes in the two different scenarios with and without nitrogen seeding.
This section is of introductory nature to show an example, how plasma properties can be

substantially changed by a small variation in the discharge setup. To illustrate this, already a detailed analysis is presented. However, this section will not influence the results of later chapters, because no discharges with impurity seeding will be included in those analyses.

To document the plasma response to nitrogen seeding a comparison experiment was performed. Two discharges were run with exactly the same parameters directly one after the other - $I_p = 1.0$ MA, $B_t = 2.5$ T, $P_{NBI} = 7.3$ MW, $P_{ECRH} = 0.7$ MW and $\delta = 0.25$. The only difference was a nitrogen gas puff in the divertor of 10^{22} s^{-1} in the second discharge (without nitrogen #24681, with nitrogen #24682). The nitrogen gas puff was additional to a deuterium gas puff of the same magnitude. Several time traces of these quantities are compared for both discharges in Figure 2.12. Figure 2.12(e) shows the envelope of a Mirnov coil measurement which doubles when the NBI heating is increased from 4.9 MW to 7.3 MW. Due to this increase in core MHD activity, the magnetic signature of ELMs is obscured in the phase with high heating power. In the discharge with nitrogen puff the effective charge

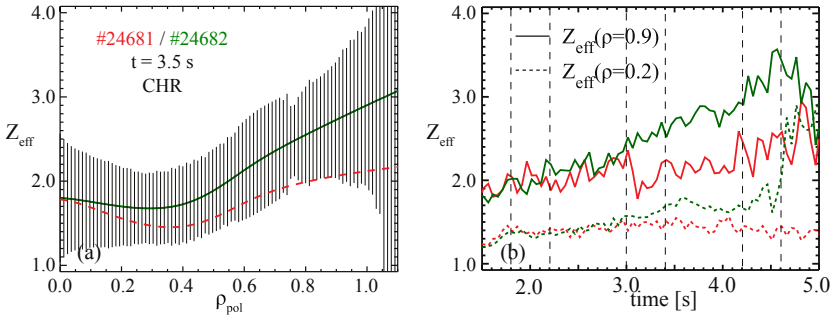

Figure 2.13: Profiles of Z_{eff} at 3.5 s (a) and time traces of Z_{eff} for $\rho_p = 0.2$ and $\rho_p = 0.9$ (b). (Reprinted with permission from [36])

number Z_{eff} increased by about 40% at the plasma edge while it remained unchanged in the center [36] as shown in Figure 2.13. The confinement improvement in this phase of the discharge was about 10%. The ELM frequency increases significantly with the addition of nitrogen. In the case discussed here the increase was nearly a factor of two from 76 to 150 Hz. In other cases the ELM frequency was found to increase by 20-50% [38]. The components of the individual ELMs were investigated with a filament probe in the SOL, a reduction in the number of filaments was found in the case with nitrogen puff [38]. The profiles in the pedestal just before an ELM crash are illustrated in Figure 2.14 where the case with nitrogen is marked with green circles while the reference case is shown with red squares. In Chapters 4 and 5 it is described in detail how these profiles were obtained. The electron density was obtained with a combination of Li-Beam and and reflectometry measurements, because reflectometry data was available for both discharges. Figure 2.14 (b) shows a decrease in electron density and (a) an increase of the electron temperature inside the pedestal top, while the steep gradient region is unaffected. The ion temperature (c) shows a slight increase around $\rho_p = 0.9$. The toroidal rotation profile (d) is unchanged in both cases. Applying the filter technique (Section 5.3.3) allows to quantify these trends. Figure 2.15 illustrates that although the electron temperature (blue, solid) and density (black, dashed) do change from the reference case without nitrogen (a) to the case with nitrogen (b), the electron pressure (c) remains unaffected in the pedestal region. The ion pressure cannot be measured directly. However, it can be estimated with knowledge of Z_{eff} and the constraint of quasineutrality in the plasma. Generally, the measurements of the effective charge number have very large uncertainties in the plasma edge - up to a factor of 2. This prevents an

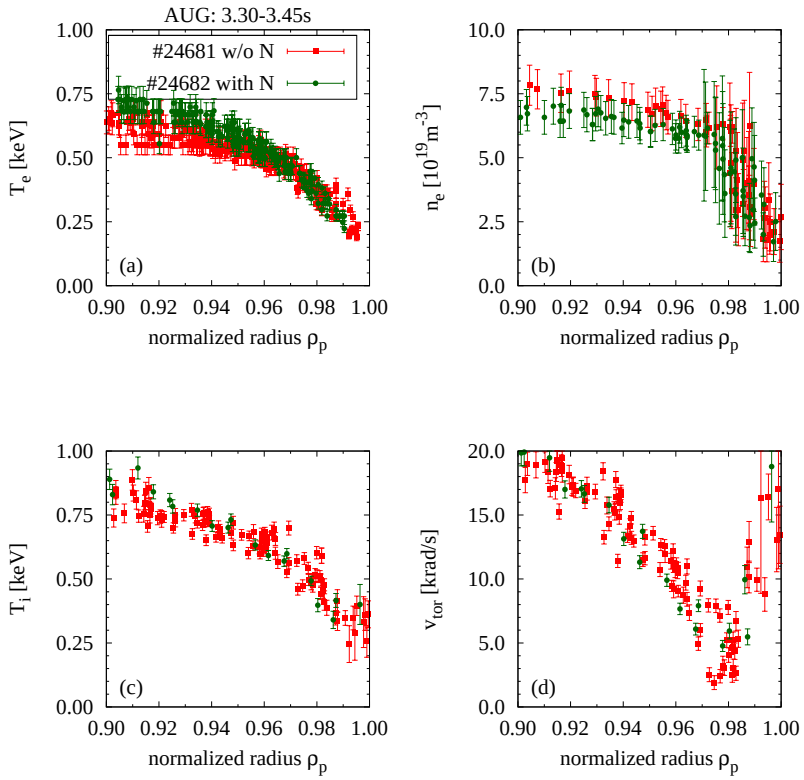

Figure 2.14: Pedestal parameters electron temperature (a), electron density (b), ion temperature (c) and toroidal rotation (d) for two discharges. Both discharges are identical except of the nitrogen puff. The case with nitrogen is indicated with green circles, the case without nitrogen with red squares.

absolute comparison in most cases. In this particular shot to shot comparison the relative trends of Z_{eff} are more important and were thoroughly determined in [36] and found to be around 2.0 without nitrogen and 2.5 with nitrogen - at $\rho_{\mathrm{p}} \sim 0.9$ and 3.3 s. For the estimate of the ion density Z_{eff} profiles are used. The average charge for the dominant ion is assumed to be 7. In the reference case this is the average of fully stripped Oxygen and Carbon. In the case with nitrogen puff it is fully stripped Nitrogen. Due to dilution of the ion density with increasing Z_{eff} n_{i} decreases further with addition of nitrogen (Figure 2.16 (a),(b)). This also results in a reduced ion pressure for the nitrogen case with higher Z_{eff} in Figure 2.16 (c). A possible explanation for the improvement of global confinement by 10% could be the stiffness of the temperature profile [11]. Although the total pressure is slightly decreased at the plasma edge this is not true in the plasma core. While the electron temperature remains larger by 10% also in the core, the electron density is again the same in both cases (see also Figure 2.19). The same should be true for the main ion density since the values for Z_{eff} are similar in the plasma core [36]. Therefore, the total core pressure can increase even if the edge pressure is slightly decreased. The mechanism which decreases the electron density in the edge was not identified. To complete the overview over main pedestal parameters Figure 2.17 shows the collisionality in the plasma edge (a) and the classical Spitzer resistivity (b). Here the collisionality $\nu_{\mathrm{e}\star}$ is calculated using the Eq. (6.14) which includes an approximation for a plasma with finite impurity content. The collisionality increases for the nitrogen case due to higher Z_{eff} in the whole pedestal region ($\rho_{\mathrm{p}} > 0.97$) and is unchanged further within the plasma ($\rho_{\mathrm{p}} < 0.96$). The resistivity (b) is not changed in the steep gradient region but

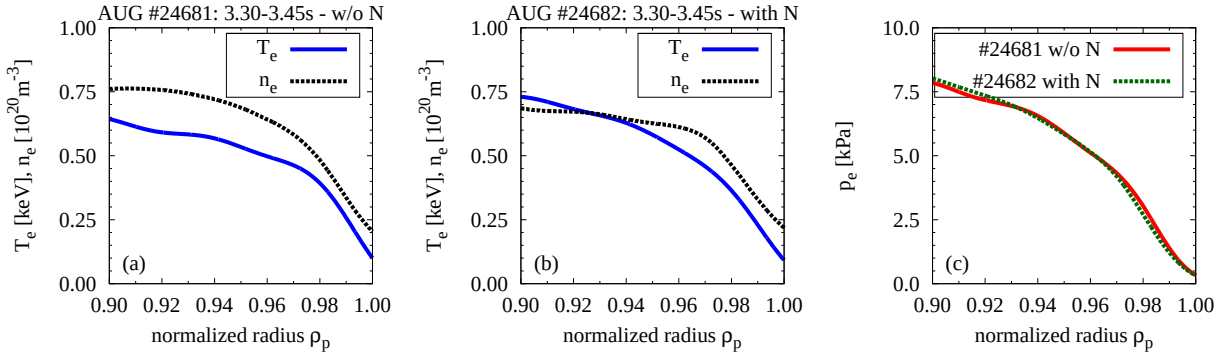

Figure 2.15: Fits to electron temperature (blue, solid) and electron density (black, dashed) from Figure 2.14, for the reference case without nitrogen (a) and the case with nitrogen (b). The electron pressure (c) does not change for the case with nitrogen (red, solid) and without (green, dashed).

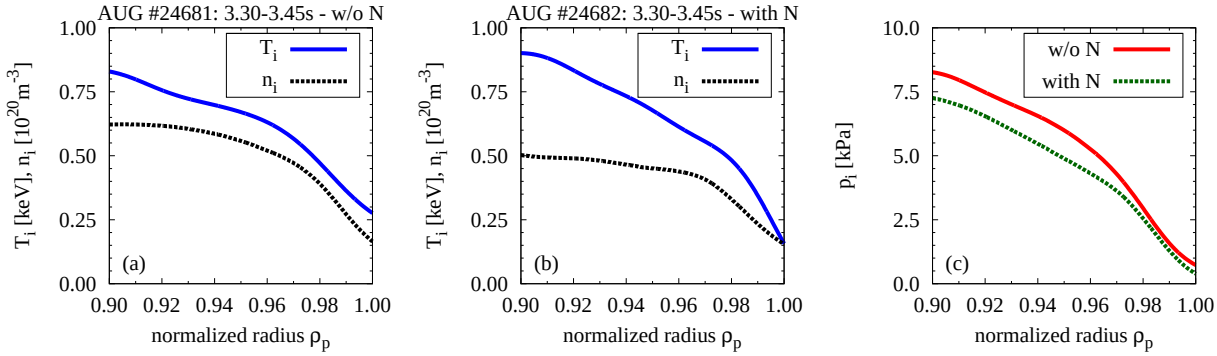

Figure 2.16: Fit to ion temperature (blue, solid) and estimate for the main ion density (black, dashed), for the reference case without nitrogen (a) and the case with nitrogen (b). The calculated ion pressure (c) does change for the case with nitrogen (red, solid) and without (green, dashed).

drops significantly ($\sim 40\%$) inside of the pedestal. The effect of the profiles on the current distribution is illustrated with the flux surface averaged neoclassical bootstrap current (c) which is fairly similar for both cases. In the nitrogen case $\langle \mathbf{j}_{\mathrm{boot}}^{\mathrm{neo}} \cdot \mathbf{B} \rangle$ has a 10% smaller maximum and is 10% broader but this is within the uncertainties. In the other parameters T_e, n_e, p_e, T_i and p_i the steep gradient region remained unaffected by the addition of nitrogen. In temperature, density and ion pressure the region inside of the pedestal top $\rho_\mathrm{p} < 0.97$ changed. The electron pressure remained unaffected in both regions.
In the comparison discharges also a remarkable change in the edge dynamics could be observed. In the case with nitrogen puff the ELMs appear faster and do have less impact on the plasma edge than the ELMs in the reference case. Until now the ELM was only characterized by a collapse of the pedestal and a recovery phase. In Figure 2.18 it becomes clear that more than this distinction is necessary to describe the differences between nitrogen ELMs and regular type-I ELMs. All traces show an exemplary ELM around 2.4 s in the discharges. Note that this is not the same phase as of the profile analysis. Because the core MHD activity strongly influences the measurement of the pick-up coils and prevents a direct comparison of the two cases in the phase with 3 heating beams of 7.3 MW. In the phase with lower heating power, around 2.4 s, the amplitude of the core MHD activity is reduced

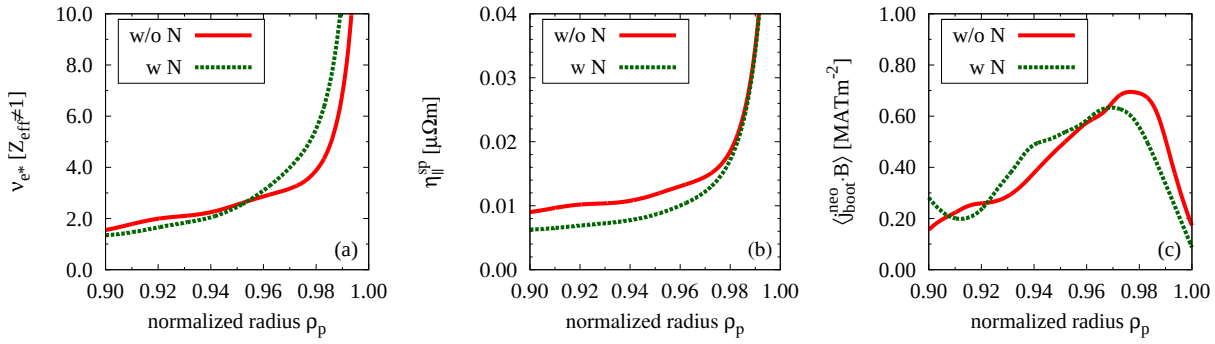

Figure 2.17: An estimate for the electron collisionality (a) in the plasma edge with nitrogen puff (green, dashed) and without (red, solid). Different Z_{eff} result in a larger collisionality for the case with nitrogen puff in the whole pedestal region ($\rho_{\text{p}} > 0.97$). The Spitzer resistivity (b) modified with Z_{eff} after [39] is reduced by 40% inside of the pedestal top. The bootstrap current (c) calculated after [40] does not change significantly.

by a factor of 2. Because, the ELM characteristics are the same for both heating powers the earlier case is used for the illustration. Figure 2.18 (a)-(c) shows the time traces of pick-up coils, the divertor currents and edge soft x-ray measurements for the reference case without nitrogen gas puff. (d)-(f) show the same diagnostics in the case with nitrogen gas puff. With these traces three different phases are identified in the ELM cycle.

(1) the ELM crash: energy and particles are lost from the plasma edge. This is best visible in the soft x-ray edge channel (c),(f) where the radiation drops during the whole phase (1). During the same time magnetic perturbations are measured by the pick-up coils (a),(d). The particles are measured few hundred μs later in the divertor (b),(e).

(2) intermediate phase: the magnetic perturbation of the plasma edge has stopped (a),(d) and the soft x-ray radiation stays constant (c),(f). Thermo-currents produce a decreasing signal as the divertor plasma cools down from the impact of the ELM for about 1 ms (b),(e).

(3) recovery phase: the pedestal recovers and the soft x-ray radiation (c),(f) increases until the next ELM crash. The pick-up coils and divertor shunts only measure a background signal.

In this classification both cases behave identically. The difference originates from the crash phase where the type-I ELM can be divided into two distinct events (1a) and (1b) while the nitrogen ELM has only one (1a). The first crash phase (1a) exhibits the same characteristics on identical time scales in both cases. It starts with a fast ($\sim$ 0.5 ms) drop in the soft x-ray radiation (c),(f) followed by a short (0.3-0.4 ms) saturation phase. During the same time a high frequency oscillation is visible in the magnetic signal (a),(d). This oscillation is only visible in the phase (1a). For the nitrogen ELM phase (1a) is immediately followed by the intermediate phase (2). In the case of type-I ELMs a second crash phase (1b) follows which causes a further drop in the soft x-ray radiation (c) and appears as several spikes on the magnetic signal (a). The phenomena (1b) also cause a steady flow of particles onto the divertor which lasts 1-2 ms (b). Profiles of temperature and density prior and after the

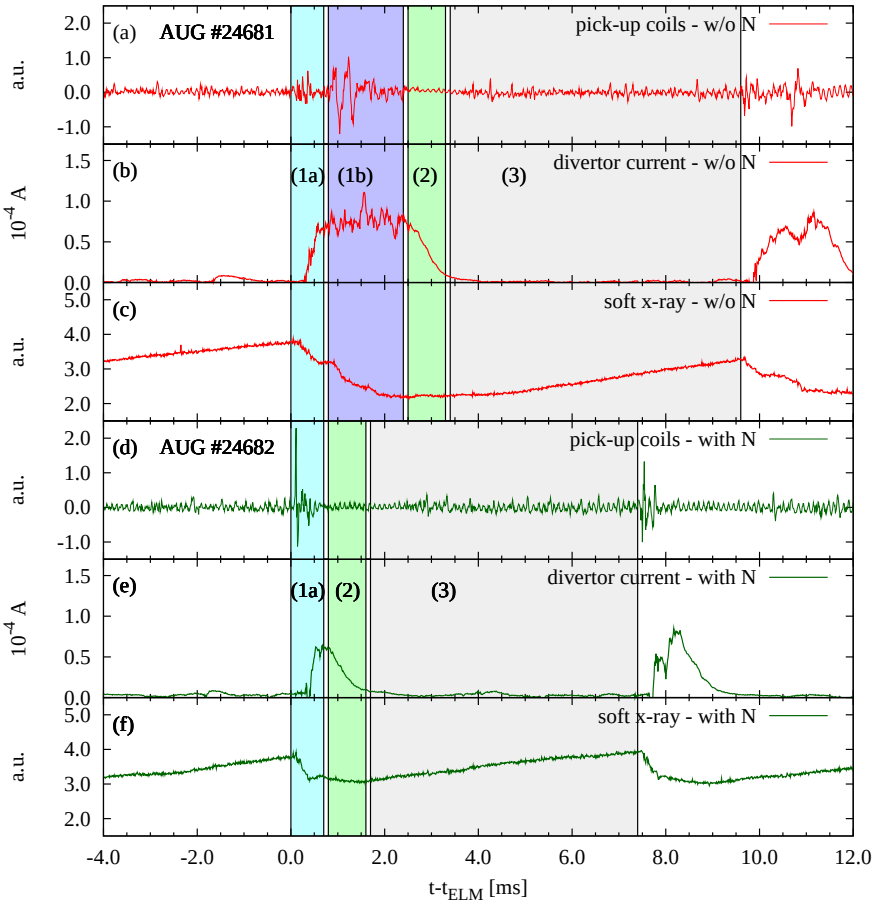

Figure 2.18: The time traces of pick-up coils (a), the divertor current (b) and edge soft x-ray radiation (c) are shown for the reference case without nitrogen gas puff. (d)-(f) show the same diagnostics in the presence of a nitrogen gas puff. Different phases in the ELM cycle are highlighted - cyan and blue for the ELM crash, green for the intermediate phase and grey for the recovery phase.

crash suggest that the first crash phase (1a) is located on top of the pedestal and does not influence the steep gradient region. The second crash phase (1b) is affecting the profiles on different radii which include the steep gradient region. In Figure 2.19 this is documented in detail. The profiles for temperature (a),(b) and density (d),(e) are shown directly before the ELM crash (blue, solid) and immediately after the crash (black, dashed). The intervals used for synchronisation are each 0.5 ms long. They start half a ms before the ELM and after the ELM the start of the interval is timed with the crash in the electron temperature. The T_e-crash-time can be shifted with respect to the ELM-onset-time for the different ELM types. The ELM-onset-time is determined at AUG generally with the divertor current measurement. In the case with nitrogen (Figure 2.19 (b)) the ELM triggers only a quite small drop in the electron temperature from $0.80 < \rho_p < 0.96$ while the steep gradient is preserved until after the ELM. In the reference case Figure 2.19 (a) it is visible that the whole transport barrier collapses. This is observed similarly for the electron density in Figure 2.19 (d),(e). While the transport barrier collapses in the reference case (d) it remains unaffected for the case with nitrogen (e). Furthermore, the density increases in the SOL for the reference case

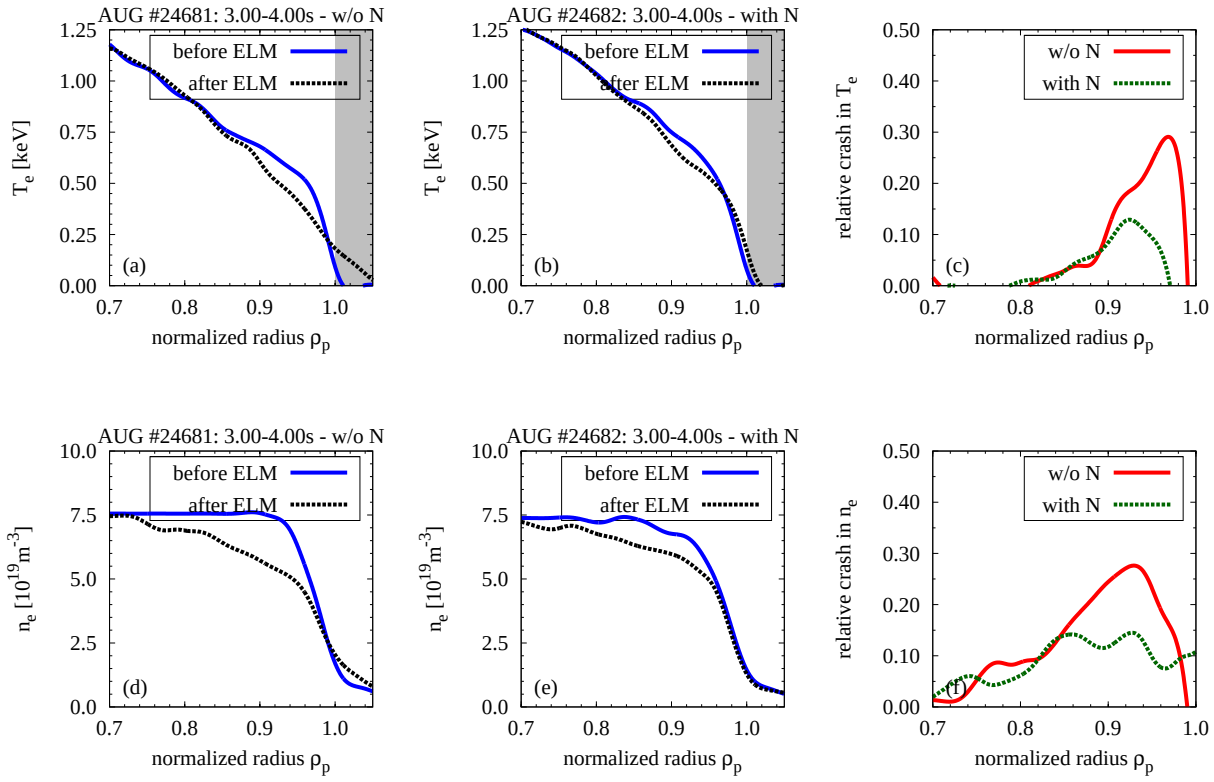

Figure 2.19: Averaged profiles of electron temperature (a)-(d) and electron density (e)-(f) during an ELM crash. Two settings were chosen for the ELM synchronisation, just before the crash (blue, solid) and just after the crash (black, dashed). The relative impact of the crash is compared for the case with N seeding (green, dashed) and the reference case (red, solid). The radii $\rho_\mathrm{p} > 1.0$ are shaded for the temperature measurement because no reliable data was available in this region.

while it stays the same with nitrogen. The difference between density and temperature is that the crash in n_e extends further into the plasma up to $\rho_\mathrm{p} \sim 0.75$. The relative change of T_e (c) and n_e (f) the crash gives an indication of the ELM affected area. Within a certain radius both cases (with and w/o nitrogen) show the same crash characteristics. This is observed for temperature and density. The only difference is visible outside $\rho_\mathrm{p} = 0.85 - 0.90$ and especially in the steep gradient region. Here T_e and n_e drop by roughly 30% for the reference case with the addition of nitrogen a maximal drop of $\sim$ 15% is observed. The neoclassical bootstrap current [40] calculated with profiles of temperature, density and Z_eff has similar values before the ELM crash with and without nitrogen seeding. However, the change of $\langle \mathbf{j}^\mathrm{neo}_\mathrm{boot} \cdot \mathbf{B} \rangle$ during an ELM crash is different in both cases. In the case without nitrogen seeding the $\langle \mathbf{j}^\mathrm{neo}_\mathrm{boot} \cdot \mathbf{B} \rangle$ flattens due to the ELM Figure 2.20 (a). With nitrogen seeding (b) the bootstrap current does not flatten but remains peaked during the ELM crash. Without seeding $\langle \mathbf{j}^\mathrm{neo}_\mathrm{boot} \cdot \mathbf{B} \rangle$ drops by $\sim$ 60% and with seeding only by $\sim$ 30%. This relative crash is illustrated in Figure 2.20 (c). However, the radial profile of the relative changes is not as robust as it was for the temperature and density profiles. Immediatly after an ELM the separatrix position might not be correct which would cause a fictional radial shift of the temperature profiles before and after the ELM crash. A shift of the current profile of 3 mm results in a significantly different profile (green, dotted) than the original one (green, dashed). Therefore, no conclusion can be drawn for the ELM effected area in the current

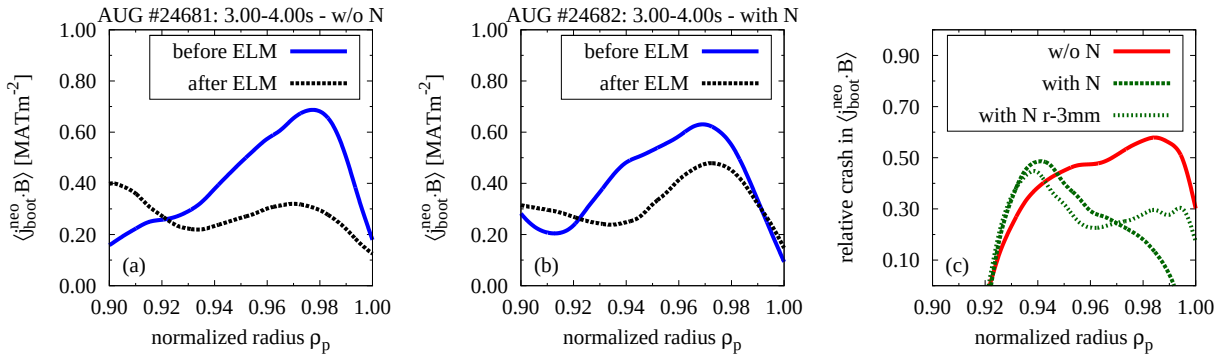

Figure 2.20: Flux surface averaged bootstrap current profile before (blue, solid) and after (black, dashed) the ELM crash for the case without N seeding (a) and with N seeding (b). The relative impact of the crash (c) is compared for the case with N seeding (green, dashed) and the reference case (red, solid). Note the different radial range compared to Figure 2.19.

profile. However, the relative current deceases at the maximum of $\langle \mathbf{j}^{neo}_{boot} \cdot \mathbf{B} \rangle$ stays the same for both radial positions and therefore the relative drop of the maximum is a more robust quantity.

The observations in the different time traces suggest two different mechanisms for the loss of energy and particles in the pedestal. Considering the observations of strongly reduced filament activity in the presence of nitrogen [38] it is likely that the second crash (1b) is related to filamentary losses in the pedestal. The radial extent of ELM losses in electron temperature and density during the different ELM types supports this picture. The radial separation of the two instabilities is illustrated in the sketch Figure 2.21 (a). Also the edge bootstrap current behaves differently for both instabilities a possible scenario is sketched in Figure 2.21 (b). Only in the reference case which showed typical type-I ELMs both instabil-

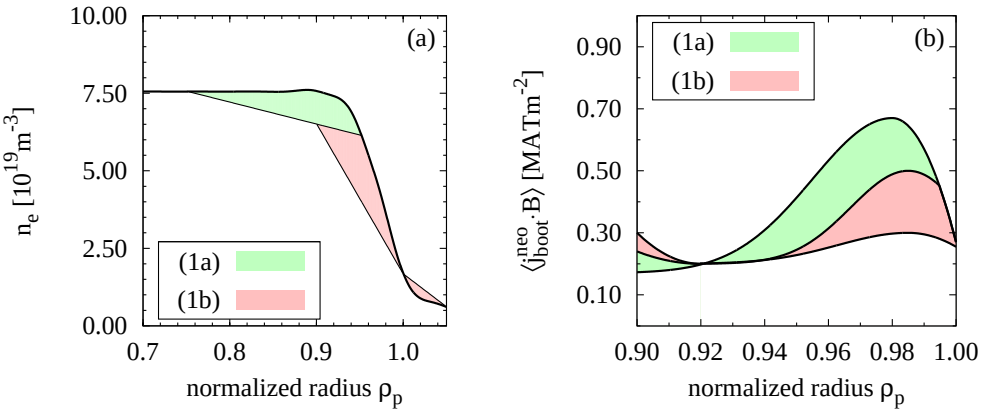

Figure 2.21: A sketch of the observations made with two different discharges for the density (a) and the bootstrap current (b). The discharge with nitrogen seeding showed an instability which affected the green area (1a), in the reference discharge without impurity seeding both instabilities where observed (1a) and (1b) (red).

ities (1a) and (1b) were observed and caused the transport barrier to collapse. The addition

of nitrogen to the plasma stabilised the edge pedestal against the (1b) instability. This consequently leads to an increase of the ELM frequency because the time for the second crash is omitted and the recovery can be faster. The key quantity for the stabilisation of (1b) could not be identified in the available discharge set. The largest differences where observed for quantities dependent on the ratio of T_e/n_e or the impurity content Z_{eff} while quantities with the product $T_e n_e$ varied less. The electron pressure was essentially unchanged in both cases and the total pressure dropped less than 10% due to the increase in Z_{eff}. The collisionality only increased for $\rho_p > 0.96$ for smaller radii the contribution of the changes in Z_{eff} and n_e/T_e^2 cancel each other. The flux surface averaged bootstrap current was the same within 10% for both cases. The resistivity of the plasma was found to drop by 40% over the whole area of the (1b) instability. Reduced resistivity would increase current diffusion and decrease the internal drive of tearing modes. In simulations with the non-linear MHD code JOREK peeling-tearing mode like structures were observed which might act as trigger mechanism for ballooning modes [41]. For a more detailed understanding of these processes simulations with non-linear codes like JOREK are necessary.

Chapter 3

Theory Overview

The edge pedestal in H-mode plasmas is important for the plasma performance as discussed in Chapter 2. Comprehension of the physical processes would allow to predict the pedestal parameters and ultimately alter them to reach an improved plasma performance. Unfortunately most theories are not able to provide precise predictions, because in general significant approximations are applied in order to simplify the equations to solve them. However, numerical models which use fewer approximations are normally computationally intensive, therefore these models are generally only tested against selected discharges. Often the results also depend on boundary conditions which can not be measured but have to be assumed. An example of such a boundary condition is the gas fuelling which cannot be determined precisely due to recycling from the walls. However, the gas fuelling can have a large impact on the results of the modelling. In the pedestal different mechanisms can overlap their area of influence which adds another level of complexity to the problem.

In this chapter the focus is put on theories which explicitly predict certain dependencies for pedestal parameters. Because of the different approximations a precise match with the experimental data is not expected, but the general trends should show similar dependencies. The three pedestal properties top value, gradient and width are not expected to be described by a single mechanism. The gradient in the pedestal is generally assumed to be limited by MHD stability which can be described with the widely accepted peeling-ballooning theory [24]. The instability caused by the peeling-ballooning mode is called ELM and was described in Section 2.1. For the pedestal width different theories have been proposed which predict the extension of the steep gradient region. Several of these theories are still under discussion and will be introduced in the next section. With a fixed gradient and width the pedestal top value is also well defined. The connection between pedestal top value, gradient and width is done with the normalized pressure gradient α introduced in Eq. (2.9) for a circular plasma

$$\begin{aligned}\alpha = -\frac{2\mu_0 R_0 q^2}{B_\mathrm{t}^2}\frac{\mathrm{d}p}{\mathrm{d}r} &= -4\pi^2\frac{(2\mu_0)^2 a^2}{\langle B_\mathrm{p}\rangle^2 R}\frac{\mathrm{d}p}{\mathrm{d}r} \\ &\sim 4\pi^2\frac{(2\mu_0)^2 a^2}{\langle B_\mathrm{p}\rangle^2 R}\frac{p_\mathrm{ped}}{\Delta_\mathrm{m}} \\ &= 4\pi^2\beta_\mathrm{p,ped}\left(\frac{\Delta_\mathrm{m}}{a}\right)^{-1}\epsilon\end{aligned}$$

were $\epsilon = a/R$ is the inverse aspect ratio and $\beta_\mathrm{p,ped} = p_\mathrm{ped}(\langle B_\mathrm{p}\rangle/(2\mu_0))^{-2}$ the normalized

poloidal pedestal top pressure. Consequently the pedestal top pressure would become

$$\beta_{\mathrm{p,ped}} = \frac{\alpha}{4\pi^2\epsilon}\frac{\Delta_{\mathrm{m}}}{a}, \tag{3.1}$$

which is valid only for circular plasmas and therefore does not include any effects of plasma shape.

A different approach to understand the pedestal top was proposed by Cordey et al. [13] which puts the focus on the energy balance in the plasma. The loss power P in the plasma has to balance with thermal conduction and ELM losses or result in a change in the stored energy

$$\dot{W} = P - \frac{W_{\mathrm{ped}}}{\tau_{\mathrm{E,ped}}} - g(\beta, \rho_\star, \nu_\star, \ldots)P. \tag{3.2}$$

One can look at two extreme cases: one with thermal conduction as dominating mechanism. This would suggest a dependence of the pedestal top with engineering parameters, in particular, with the heating power. The other extreme is a pedestal which is only set by the MHD stability limit of the ELM. Then the pedestal top values do not depend directly on engineering parameters but it should be possible to describe them with a typical energy β, a typical length $\rho_\star$ and a typical time $\nu_\star$.

3.1 Pedestal Width

Most theories which predict the extension of the transport barrier namely the pedestal width can be classified in few categories: turbulence suppression, atomic physics and MHD effects. This section only introduces the theories which are relevant for the discussion of the experimental results.

3.1.1 Turbulence Suppression

A possible explanation of the pedestal width is a region where turbulent transport is suppressed. The width is estimated by comparison of turbulence growth rate and turbulence suppression rate. This gives different explanations for the pedestal width. The results depend on the kind of turbulence that is dominating the plasma edge and the mechanism of the suppression. Even for one type of turbulence and one mechanism of suppression like $\mathbf{E}_\mathrm{r} \times \mathbf{B}$ flow shearing with a shearing rate [42]

$$\gamma_{\mathbf{E}\mathrm{r}\times\mathbf{B}} = \frac{(RB_\mathrm{p})^2}{B}\frac{\mathrm{d}}{\mathrm{d}\Psi}\frac{E_\mathrm{r}}{RB_\mathrm{p}} = \frac{1}{B}\frac{\mathrm{d}E_\mathrm{r}}{\mathrm{d}r} \tag{3.3}$$

the source of $\mathbf{E}_\mathrm{r}$ can still be different and lead to diverse predictions of the pedestal width. Two examples for sources of a radial electric field $\mathbf{E}_\mathrm{r}$ are ion orbit losses or differences in the radial force balance due to the pressure gradient. This leaves a large number of different theories and many of them were summarized in review articles [43, 44]. This section only introduces the ones which are relevant for the discussion of the experimental results.

Ion orbit losses become relevant when the ion obits cross the separatrix and allow particles to leave the magnetically confined region. This is the case when particles are less than one

orbit width Δ_{orbit} away from the separatrix. Since $\Delta_{\text{orbit,i}} \gg \Delta_{\text{orbit,e}}$ more ions are lost than electrons and an inwards directed radial electrical field forms. Due to this radial electric field the turbulence can be suppressed via $\mathbf{E}_\text{r} \times \mathbf{B}$ shearing. Therefore, the pedestal width should be related to the radial dimensions of the $\mathbf{E}_\text{r}$ well (see e.g. Figure 2.4) and therefore to the ion orbit width

$$\Delta_{\text{ped,m}} \sim \Delta_{\text{orbit,i}}. \tag{3.4}$$

In 0th order the ion orbits width can be described by the banana width of trapped particles (see e.g. [45])

$$\Delta_{\text{banana,m}} = \frac{\rho_{\text{L,i}} q}{\epsilon^{1/2}} \propto \frac{\sqrt{T_\text{i}}}{B_\text{p}} \tag{3.5}$$

where q is the safety factor and the ion lamor radius $\rho_{\text{L,i}}$ as defined in Section 6. A correlation of pedestal width and banana width could be easily tested. However, the ion orbits are also influenced by the strong radial electric field shear in the plasma edge [46]. This causes a squeezing of the ion orbits by $\sqrt{S_{\text{orbit}}}$ where

$$S_{\text{orbit}} = \left| 1 - \frac{c}{B_\text{p}\Omega_\text{p}} \frac{\mathrm{d}E_\text{r}}{\mathrm{d}r} \right|, \tag{3.6}$$

c is the speed of light and $\Omega_\text{p} = q_\text{i} B_\text{p}/m_\text{i}$ the poloidal gyrofrequency with the ion charge q_i. The orbit squeezing factor S_{orbit} can be significantly larger than 1 [47]. Therefore, it is important to include S_{orbit} in the calculation of the ion orbit width, which becomes

$$\Delta_{\text{orbit,i}} = \frac{\Delta_{\text{banana,m}}}{\sqrt{S_{\text{orbit}}}}. \tag{3.7}$$

This leads to a pedestal width prediction by ion orbit losses which is not easily tested without measurements of the radial electric field. In this thesis an approximation will be applied to estimate the orbit squeezing, for details see Section 7.2

In a different approach the radial electric field is not dominated by ion orbit losses but by the pressure gradient term in the ion momentum equation [48]. Neglecting the contributions of poloidal and toroidal rotation leaves only the diamagnetic term

$$E_\text{r} \sim \frac{1}{q_\text{i} n_\text{i}} \frac{\mathrm{d}p}{\mathrm{d}r}, \tag{3.8}$$

where n_i is the ion density and p the pedestal pressure. With this approximation for the radial electric field the $\mathbf{E}_\text{r} \times \mathbf{B}$ shearing rate Eq. (3.3) becomes

$$\gamma_{\mathbf{E}\text{r}\times\mathbf{B}} = \frac{1}{B}\frac{\mathrm{d}E_\text{r}}{\mathrm{d}r} \sim \frac{1}{B}\frac{\mathrm{d}}{\mathrm{d}r}\left(\frac{1}{q_\text{i} n_\text{i}}\frac{\mathrm{d}p}{\mathrm{d}r}\right) \sim \frac{1}{B}\frac{1}{\Delta_{\text{ped,m}}}\frac{1}{q_\text{i} n_\text{i}}\frac{n_\text{i} T_\text{i}}{\Delta_{\text{ped,m}}} \propto \frac{\rho_\text{i} c_\text{s}}{\Delta^2_{\text{ped,m}}}, \tag{3.9}$$

where $c_\text{s} \propto \sqrt{T_\text{i}}$ is the ion sound speed. Then the criterion for the pedestal width $\Delta_{\text{ped,m}}$ is

$$\gamma_{\mathbf{E}\text{r}\times\mathbf{B}} \gg \gamma_{\text{max,turb}}, \tag{3.10}$$

namely that the $\mathbf{E}_\text{r}\times\mathbf{B}$ shearing rate is larger than the maximal growth rate of any turbulence in the pedestal. This criterion can be tested against different mechanisms for turbulence.

One example for turbulence is based on the drift wave instability (see e.g. [49]) which "is formally a small, linearised perturbation which involves an interaction between the perpendicular $E \times B$ and diamagnetic drifts of the plasma fluid elements and their parallel dynamics" [50]. A growth rate for drift wave turbulence can be approximated when assuming gyro-Bohm type transport and a stabilising effect of the magnetic shear s: $\gamma \sim c_\mathrm{s}/(\Delta_\mathrm{ped,m} s^2)$ [51] with Eq. (3.9) this gives an pedestal width of

$$\left.\frac{\Delta_\mathrm{ped,m}}{a}\right|_\mathrm{DWT} \propto \frac{\rho_\mathrm{i} s^2}{a} \propto \rho_{\mathrm{i}\star} s^2. \tag{3.11}$$

For long wavelength drift waves, where the wavelength is larger then the perpendicular width of the mode, the growth rate can be approximated with a frequency of how often the mode sees the bad magnetic field curvature at the low field side. With the connection length between the bad and the good curvature region qR and the sound speed c_s the growth rate becomes $\gamma \sim c_\mathrm{s}/(qR)$ [44] with Eq. (3.9) this gives an pedestal width of

$$\left.\frac{\Delta_\mathrm{ped,m}}{a}\right|_\mathrm{LWM} \propto \frac{\sqrt{\rho_\mathrm{i} R q}}{a} \propto \rho_{\mathrm{i}\star}^{1/2} \sqrt{\frac{q}{\epsilon}}. \tag{3.12}$$

3.1.2 Neutral Penetration

Atomic processes, such as ionization processes, are often assumed to play a negligible role. This is certainly true for the hot plasma core where all particles are ionized, however, in the plasma edge this can be different. The model of neutral penetration [52, 53] is based on ionization of neutrals to describe the density pedestal width.
The neutral penetration length is given by the characteristic neutral velocity v_n, the velocity averaged ionization cross section $\langle \sigma v \rangle$ and the plasma density n:

$$\lambda_\mathrm{ion} = \frac{v_\mathrm{n}}{\langle \sigma v \rangle n}. \tag{3.13}$$

The neutrals can penetrate into the confined region up to λ_ion where they are ionized and create a particle source. Assuming pure diffusion in the plasma, a density pedestal will form with its top at the particle source. Therefore, the pedestal width Δ_n should equal λ_ion. The neutral penetration length can be approximated as inverse proportional to the density $\Delta_{ne} \propto n_\mathrm{e,ped}^{-1}$) [53] this gives $\nabla n_\mathrm{e} \propto n_\mathrm{e,ped}^2$. This is approximation assumes that the neutrals have roughly the thermal velocity at the separatrix, and are therefore constant, and an ionisation cross section which is constant over the region of interest.
The approximations, allowing to assume $v_\mathrm{n}/\langle \sigma v \rangle$ being constant, might be violated when the SOL plasma changes significantly, for example when gas puffing is applied differently to the plasma. A more detailed discussion of neutral penetration processes can be found in [54, 55].

3.1.3 Kinetic Ballooning Modes

The turbulence driven by kinetic ballooning modes (KBM) is independent of $\mathbf{E}_\mathrm{r} \times \mathbf{B}$ flow shearing and therefore is proposed as limiting mechanism for pedestal gradients even in the

presence of large radial electric fields [56]. The following argumentation is a summary of [56]. The linear threshold for KBM turbulence is

$$\alpha_{\mathrm{KBM}} \sim \alpha \tag{3.14}$$

and was found to be proportional to a function of the local shear $s_{\mathrm{l}} = r/q \cdot \mathrm{d}q/\mathrm{d}r$ which again is inverse proportional to the current density j and therefore

$$\alpha \sim \alpha_{\mathrm{KBM}} \propto \frac{1}{s^{1/2}} \propto \langle j \rangle^{1/2}, \tag{3.15}$$

if the parallel current density j is dominated by the bootstrap current in this region $\langle j \rangle \sim \beta_{\mathrm{p,ped}}$ and combining Eq. (3.1) with Eq. (3.15) gives

$$\frac{\Delta_{\mathrm{m}}}{a} \propto \frac{\beta_{\mathrm{p,ped}}}{\alpha} \propto \beta_{\mathrm{p,ped}}^{1/2}. \tag{3.16}$$

This is different to the approximation given in [56] where $\Delta_{\Psi\mathrm{N}} \propto \beta_{\mathrm{p,ped}}^{1/2}$, as discussed in Section 5.1 $\Delta_{\mathrm{m}}/a \neq \Delta_{\Psi\mathrm{N}}$. However, the deviation from a circular plasma was neglected in both cases, therefore, one would expect a different form of Eq. (3.17) which is

$$\Delta_{\Psi\mathrm{N}} = \beta_{\mathrm{p,ped}}^{1/2} f(f_{\mathrm{q}}, \kappa, \delta, \epsilon, \nu_{\star}, \ldots), \tag{3.17}$$

where f is a function of all neglected parameters, the known approximations are the plasma shape and the collisionality which plays an important role for the bootstrap current besides $\beta_{\mathrm{p,ped}}$. In [57] a density scan (4-8·10^{19} m^{-3}) at constant temperature was simulated with the EPED1.6 code and only a weak $\sim 15\%$ variation in f was observed.
Like the other theories for the pedestal width also the KBM theory is in fact a gradient limit. In combination with a second gradient limit the pedestal width and the pedestal top is determined. In the EPED1.6 code the second gradient limit is derived from the peeling-ballooning mode.

Chapter 4

Diagnostics

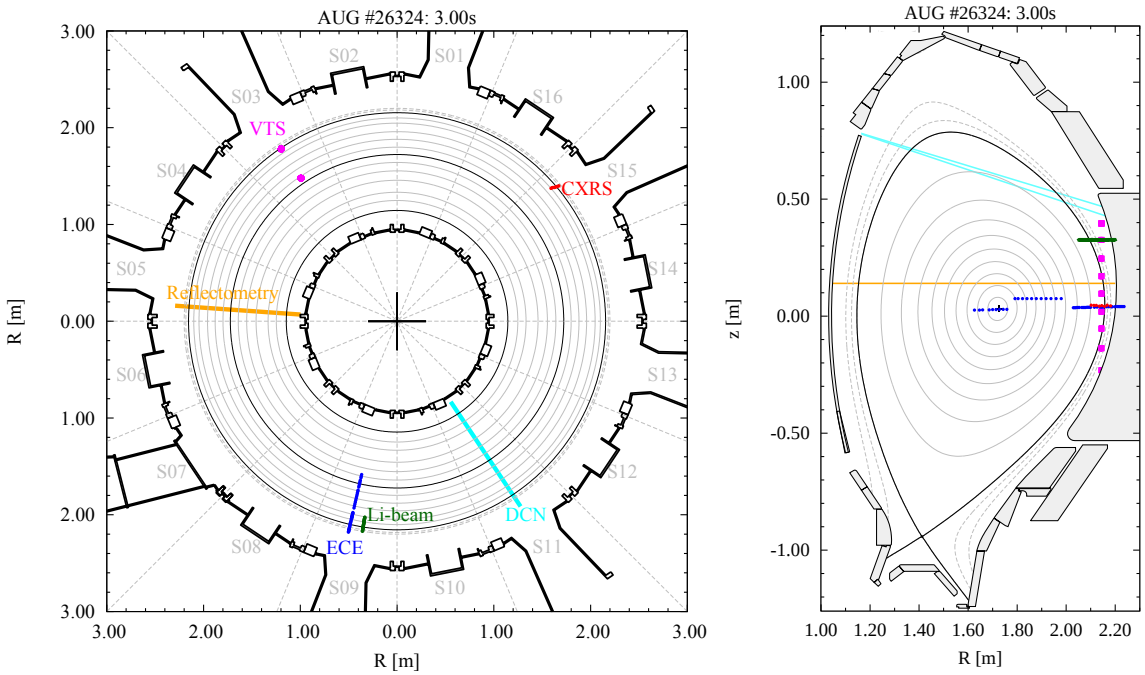

Figure 4.1: Overview with the main edge diagnostics used throughout this work. On the left the toroidal overview is shown with the different locations of the diagnostics in the torus, different sections in the torus are labeled with their sector number in grey. On the right all are mapped onto a single poloidal cross section.

An important aspect in high temperature plasma physics is the challenge to diagnose the plasma without disturbing it. At the plasma edge also the temporal and spatial resolution have to be sufficiently high. To resolve the steep gradient region with an extension of less than 2 cm the spatial resolution of the diagnostics should to be better than 1 cm. The existence of ELMs (Section 2.1) with repetition rates of up to a few 100 Hz sets boundaries to the temporal resolution. The exposure or integration time of a single measurement should be of the order of 1 ms or less. A high sampling rate >1 kHz is beneficial but with appropriate synchronisation a slower sampling rate can be compensated as described in Section 5.2. In this section several techniques to measure temperatures and densities of a fusion plasma are introduced. A basic introduction into the physics behind the measurement is given along with important specifications of the diagnostic setup. An overview of the presented edge

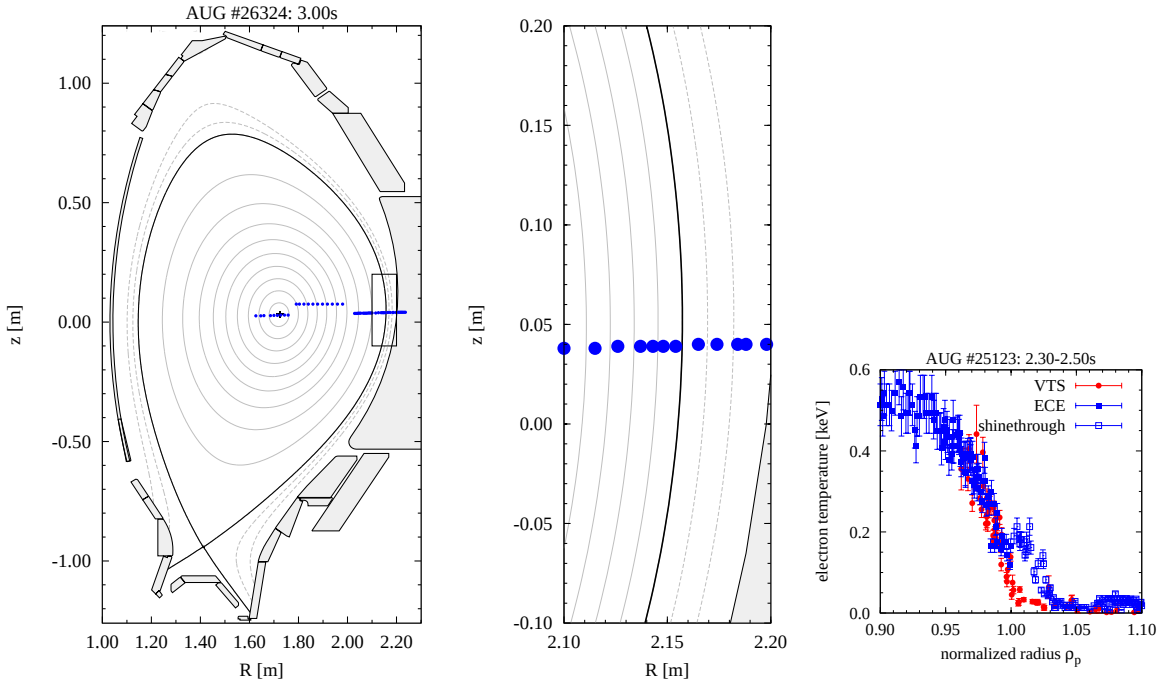

Figure 4.2: Poloidal view of the electron cyclotron emission channels in sector 9. The distance of the field lines is $\Delta\rho_\mathrm{p} = 0.1$ for the full view and $\Delta\rho_\mathrm{p} = 0.02$ for the edge zoom. On the right an exemplary edge ECE measurement (blue) is shown with data from the edge Thomson scattering (red), the ECE shine through region is marked with open symbols.

diagnostics is illustrated in Figure 4.1 where the toroidal and poloidal cross section of the AUG tokamak is illustrated. The electron cyclotron emission (ECE) in blue, the vertical Thomson scattering (VTS) in pink and the charge exchange recombination spectroscopy (CXRS) in red are diagnostics to measure electron or ion temperature. The VTS, the Li-beam in green, the interferometry (DCN) in cyan and the reflectometry in orange are able to measure the electron density. The toroidal and poloidal views illustrate the different locations of diagnostics in the torus. Before the measurements can be compared appropriate mapping techniques have to be applied. These techniques are discussed in Chapter 5. At the end of this chapter the influence of the spatial resolution on edge profiles is described using the example of the VTS.

4.1 Electron Cyclotron Emission (ECE)

The electron cyclotron emission radiometry (ECE) is a passive measurement of the electron temperature a in the plasma. In the presence of a magnetic field hot electrons experience the Lorentz force. If the motion of the electrons is not exactly parallel to the field lines they will be forced into a gyro motion around the magnetic field lines. Due to this accelerated motion the electrons emit cyclotron radiation with a characteristic frequency $\omega_\mathrm{ce} = eB/m_\mathrm{e}$. In a tokamak plasma the total magnetic field B is dominated by the toroidal field which goes like $1/R$. Therefore, the cyclotron radiation can be associated with a radial location in the plasma. This is possible because the radiation is only emitted and absorbed in small band around the cyclotron frequency ω_ce. The width of this band is determined by relativistic and Doppler broadening and its extension can be several cm [58]. However, when the plasma

is optically thick radiation emitted in this band is reabsorbed several times. Therefore, the radiation measured outside the plasma originates from a layer which is only about 0.5 cm wide [59]. Another effect of the optical thickness is that the radiation leaving the plasma follows Planck's law of black body radiation. Therefore, the intensity of the cyclotron emission can be directly related to the radiation temperature of the plasma.

At AUG the intensity of the plasma radiation is measured with a multichannel heterodyne radiometer between 89 GHz and 187 GHz [60]. The radiometer is calibrated for absolute temperature measurements. With this calibration the electron temperature T_e is determined from the radiation temperature with an accuracy of $\sim 7\%$. The system has 60 channels which have a radial spacing of 0.3-0.6 GHz. In Figure 4.2 it is illustrated how these frequencies translate into radial positions for a central magnetic field of $B_{t0} \simeq 2.5$ T. The ECE is generally sampled with 32 kHz, with special settings the sampling rate can be increased up to 1 MHz. This makes the ECE one of the fastest diagnostics suited to investigate the plasma edge. The spatial resolution of ~ 0.5 cm would also allow to measure in the steep gradient region. Unfortunately, the plasma looses its optical thickness near the plasma edge due to decreasing density. Therefore, the assumption of a black body radiator is not valid anymore and the measured intensity does not correlate directly to the electron temperature. This effect is generally referred to as shine through [61]. For typical pedestal densities in AUG H-modes ($4 - 8 \cdot 10^{19}$ m^{-3}) the shine through starts a few mm inside of the separatrix which generally means about 1/3 of the steep gradient region is affected, an example is shown in Figure 4.2 where the shine through is indicated with open symbols. How the shine through is treated is described in Section 5.2.

4.2 Li-Beam Diagnostic

The Li-beam diagnostic is an active diagnostic to measure the electron density. High energy Li atoms are injected into the plasma. Due to collisions with the plasma they are excited and emit line radiation while relaxing. This line radiation is observed and its intensity can be correlated to the electron density. The Li-beam gets strongly attenuated due to ionisation and scattering which also influences the intensity of the line radiation. To reliably determine the density from the intensity measurement the processes responsible for the attenuation of the beam have to be taken into account. A detailed description of the principles of Li-beam diagnostics can be found in [62].

At AUG the Li-beam [63] is accelerated with 50 keV and has an ion current of 2 mA. The beam is observed on 35 channels, their optics are optimised to view tangential to flux surfaces. The intensity of a single line transition is measured with a filter combined with a photomultiplier. The geometry of beam and optics result in an observation volume with 5 mm radial extent and an elongation of ~ 12 mm. The position of the volumes is illustrated in Figure 4.3. The beam attenuation is taken into account with forward modeling and a probabilistic Li-beam data analysis is used [64]. For low electron densities of $\sim 4 \cdot 10^{19}$ m^{-3} the Li-beam diagnostic measures a reliable density profile up to ~ 10 cm within the separatrix or $\rho_p \sim 0.85$. For larger densities the beam is more strongly attenuated and the radial extent for reliable measurements shrinks. The limit to observe the pedestal top lies around 6-7$\cdot 10^{19}$ m^{-3}, for even larger densities only the steep gradient region can be measured. In Figure 4.3 (a) two discharges with pedestal top densities of $\sim 5 \cdot 10^{19}$ m^{-3} (blue) and $\sim$

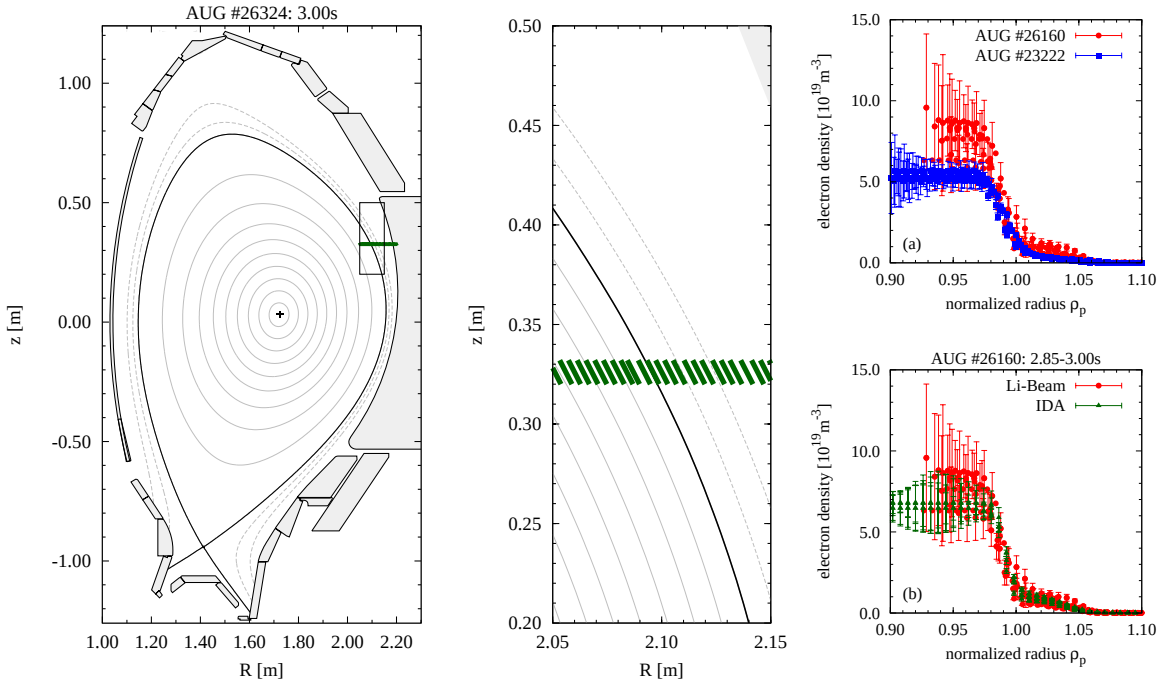

Figure 4.3: Poloidal view of the Li-beam scattering volumes in sector 9. The distance of the field lines is $\Delta\rho_\mathrm{p} = 0.1$ for the full view and $\Delta\rho_\mathrm{p} = 0.02$ for the edge zoom. The vertical elongation of the observation volumes marked in green is determined by the Li-beam width. The width of the volumes was reduced in the illustration to see a difference between the individual channels. On the right examples of Li-beam measurements are given for different densities (a) and the Li-beam is compared to the IDA fit which includes interferometer measurements (b).

$7 \cdot 10^{19}$ m^{-3} (red) are illustrated. The high density case (red) has a significant scatter at the pedestal top because of the beam attenuation. The Li-beam data is routinely combined with the Interferometry (Section 4.4) in an integrated data analysis approach (IDA) [65]. With information from the edge Interferometer channel the pedestal top density can be determined even for densities $> 7 \cdot 10^{19}$ m^{-3}. In Figure 4.3 (b) the uncertainty of the pedestal top density is reduced by a factor of 2 with the IDA approach (green). The sampling rate of the diagnostic is 20 kHz and data is written into shotfiles with 1 kHz. This allows to observe a whole ELM cycle. To obtain the background radiation from the plasma the Li-beam is chopped with 24 ms off and 56 ms on time. In a stationary plasma and when using ELM synchronization this background subtraction works reasonably well. For observations of transients during a single ELM cycle it is possible to apply faster chopping with a frequency of 2 kHz.

4.3 Thomson Scattering (TS)

The Thomson Scattering is an active measurement of electron temperature and density. Photons of a high energy laser pulse are scattered on free electrons in the plasma. The scattered light holds information about the temperature and density of the electrons. The intensity of the scattered light depends on the laser energy and the plasma density. The spectral distribution of the detected light depends on the electron temperature.

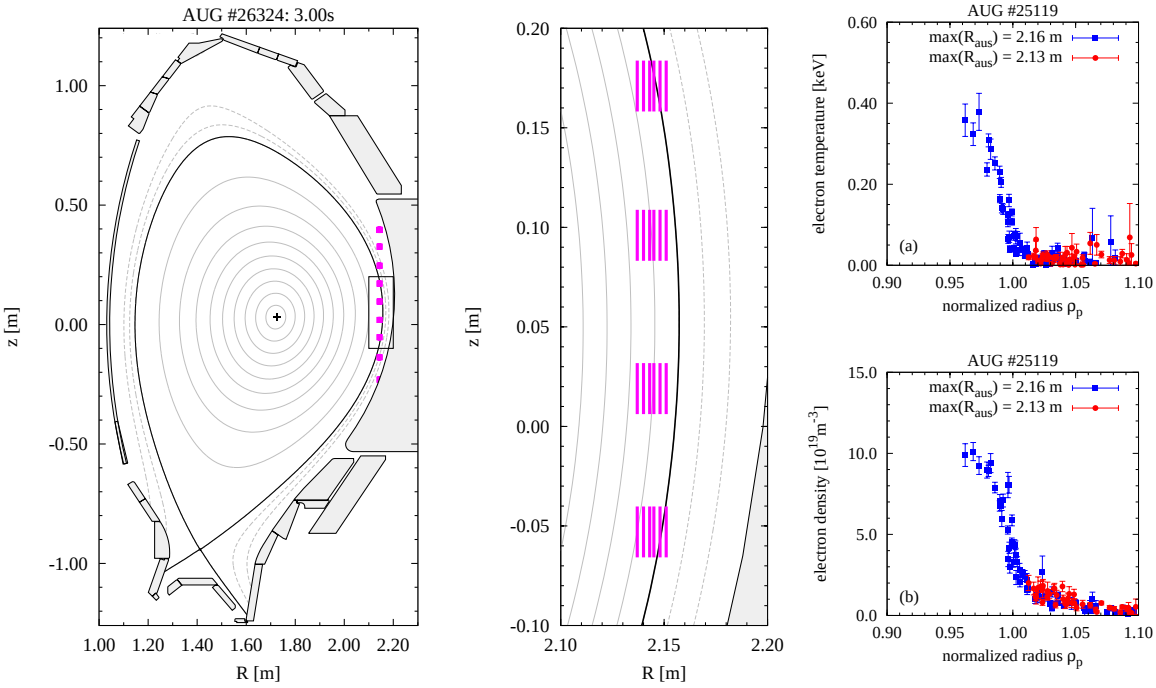

Figure 4.4: Poloidal view of the edge Thomson scattering volumes in sector 3. The pink areas mark the intersection of the vertical laser beams and the horizontal lines of side. The lasers are fired successively and do not interfere with one another. The distance of the field lines is $\Delta\rho_\mathrm{p} = 0.1$ for the full view and $\Delta\rho_\mathrm{p} = 0.02$ for the edge zoom. On the right two different separatrix locations in the plasma are illustrated for the electron temperature (a) and density (b).

4.3.1 ASDEX Upgrade

The Thomson scattering system of the ASDEX Upgrade tokamak is equipped with 6 multipulse Nd:YAG (neodymium-doped yttrium aluminium garnet) lasers at 1065 nm for edge and 3 lasers for core measurements [66, 67]. The laser energy is about 1 J and the pulse length 15 ns. This short exposure time allows to measure a real snapshot of the plasma. The scattering volumes of the edge system are illustrated in Figure 4.4. The laser path is from bottom to top through the edge region. The scattering volumes where the laser beam intersects the line of sight are indicated in pink. The scattering volumes have a vertical extent of 2.56 cm and their width is determined by the Gaussian laser beam with a FWHM of about 0.5 mm. All lasers are horizontally displaced by 3 mm to improve the radial coverage. For better profile resolution it is possible to fire the lasers in 100 μs intervals. This increases the radial resolution of the edge at expense of the temporal resolution. Each laser has a repetition rate of 20 Hz. Therefore, the AUG TS is able to measure the plasma edge with a frequency of 120 Hz in standard operation and 20 Hz in profile mode. The scattered light can propagate through a window out of the vacuum vessel and is focused by a lens onto 16 four channel polychromators for the core and 10 for the edge system. The four channels of the polychromators consist of filters in front of avalanche diodes. The filters are optimised to uniquely define the spectral distribution of the scattered electrons.

The setup of the AUG TS has the advantage of high radial resolution at the edge. Because of the tangential alignment with the flux surfaces the radial extent of the scattering volumes is relatively small. This avoids problems in the steep gradient region as will be discussed in

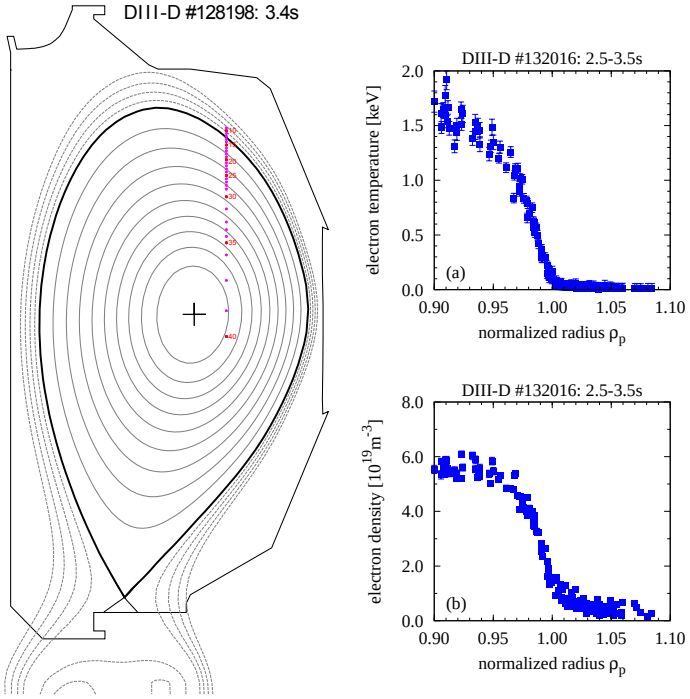

Figure 4.5: Poloidal cross section with the TS system at DIII-D (left). Examples for measured profiles of electron temperature (a) and electron density (b).

Section 4.7. However, this is also a disadvantage because it does not allow continuous profiles into the plasma center without using data from other systems. Furthermore, the visibility of the edge pedestal strongly depends on the plasma scenario, in particular the outer radius of the separatrix. Because of increased number of in-vessel components the distance of the last closed flux surface to the wall has decreased, while the ports in the vacuum vessel for the laser beams cannot be moved. For sufficient data from the TS system the outer plasma position has to be around 2.15-2.16 m and for resolving the pedestal top even larger. This setting leaves only little space between the wall and the last closed flux surface, therefore, in standard operation a separatrix position of 2.12-2.13 m is more common. In Figure 4.4 (a),(b) the different settings are illustrated, for values of 2.16 m (blue) most of the pedestal can be resolved, for a maximum separatrix position of 2.13 m (red) measurements only exist up to the separatrix. For optimal data from the edge TS system dedicated discharges are needed with a optimized plasma shape and position.

4.3.2 DIII-D

The Thomson scattering system at DIII-D [68] has a different setup than the AUG system. The laser path corresponds to the AUG core TS. The use of in-vessel optical heads and fibers which transmit the scattered light to seven channel polychromators allows a view on the pedestal at the top of the plasma. The positions of the measurements are indicated in Figure 4.5. The different setup has two main consequences for the measurements. In contrast to AUG it is possible to measure a continuous profile from the SOL into the plasma center. This is a great advantage because combining different diagnostics for T_e and n_e measurements becomes obsolete. This comes at the expense of spatial resolution. Because of the position at the top of the plasma the scattering volumes cannot be aligned with the field lines. This

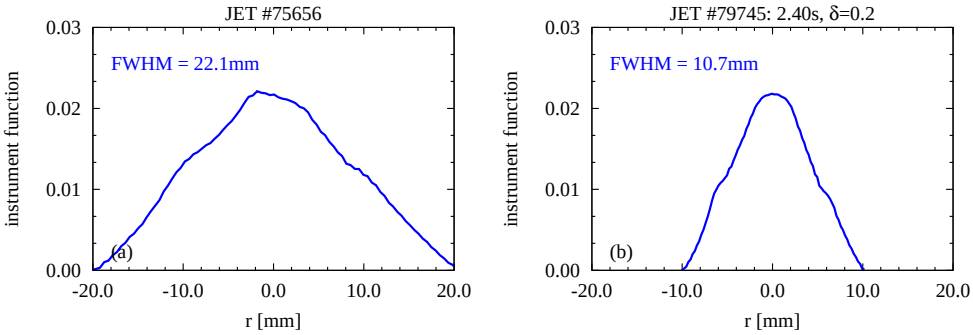

Figure 4.6: Scattering volumes of the TS mapped to R_{maj} at the midplane. The x-axis is a relative coordinate centered at the measurement positions stored in the shotfile. (a) shows a scattering volume with the old optics and (b) a case with the new optics.

means the spatial resolution with ~ 6 mm is typically 2 times lower compared to the AUG edge system. As photon source also multipulse 1 J Nd:YAG lasers are used. All lasers are guided on the same path through the plasma.

4.3.3 JET

At JET a third approach was chosen were the lasers are fired horizontally at the midplane into the plasma and the optics are located in a top port of the vessel [69]. To determine the spectrum of the scattered electrons JET uses four channel polychromators like AUG. In order to obtain a good photon rate 3 J Nd:YAG lasers are used at JET. The higher energy compared to the 1 J lasers used at AUG and DIII-D increases the intensity of the scattered light, however, it does not allow a comparable narrow beam width. For a 3 J beam the energy density would be larger and could easily damage the optics which guide the laser. A direct consequence are larger scattering volumes in the plasma. The size of the scattering volume mapped to the midplane would be 1-2 cm. For older discharges (discharge number $<$79000) the size was 2 cm and could be improved with a change of the optics to 1 cm. The detailed scattering volume is illustrated in Figure 4.6. This is still too large to obtain detailed results from measurements in the steep gradient region. The effect of the scattering volume size is discussed with examples in Section 4.7. Here it is important to note that the data cannot be directly used when the assumptions in the analysis were wrong. For this work a Richardson-Lucy-Deconvolution [70] using the approximation found in [71] was applied to the data. For discharges with a scattering volume of around 1 cm this method yielded good results. In the case of a 2 cm kernel it was not possible to recover the correct temperature profiles. Therefore, only discharges with the improved optics were analysed. A more precise technique based on forward modelling of the TS system is planned for JET, but was not available for the analysis done in the present work.

4.4 DCN Interferometer

The interferometry makes use of the different optical properties in the plasma compared to a reference medium. In particular, the light of a probe laser beam experiences a different

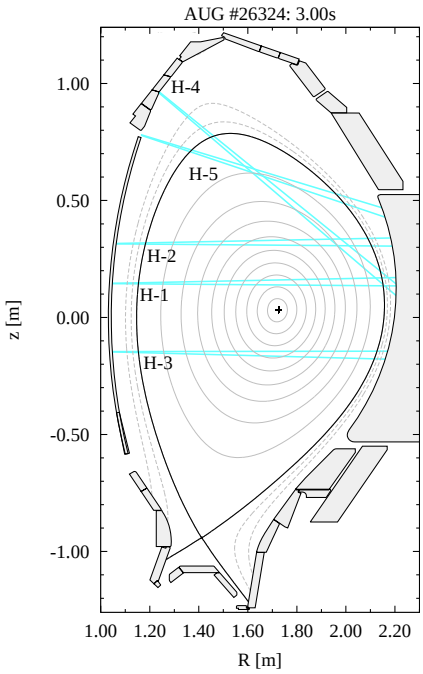

Figure 4.7: Poloidal view of the DCN laser paths in sector 11. The laser beams are reflected at the inner wall and pass the plasma column twice.

phase shift in the plasma than in air. This phase shift is proportional to the line integrated electron density of the plasma. By measuring the phase shift with an interferometer the line integrated density along the laser beam can be derived.
The interferometer system at AUG [72] consists of one DCN (deuterium cyanide) laser at 195 μm. This laser has 5 different paths through the plasma which range from central (H-1) to off-axis (H-5). The exact geometry is illustrated in Figure 4.7. The system allows a sampling rate of 10-20 kHz. This means the interferometry is suited for very fast measurements. However, it does not contain detailed radial information. Nevertheless, a radial profile can be constructed by use of Abel inversion. This gives useful information about the shape of the electron density profile in the plasma core. This shape might be biased by boundary conditions used in the tomographic reconstruction - e.g. a polynomial shape of the profile. A spline reconstruction is provided within the integrated data analysis (IDA) approach [65]. The IDA combines the DCN with the Li-Beam diagnostic - discussed in Section 4.2 - to provide full density profiles via Bayesian forward modelling.

4.5 Charge Exchange Recombination Spectroscopy

The temperature, density and rotation of impurity ions can be derived from their spectrum of emitted light. This is done with charge exchange recombination spectroscopy (CXRS). Generally, at the temperatures present in fusion devices these ions are fully stripped of their electrons. Therefore, they do not emit characteristic light. However, in the path of a neutral heating beam charge exchange collisions occur with the beam neutrals. The neutrals are ionized while the impurity ions capture electrons. For a few ns the ion remains in an excited state before relaxing to the ground state and emitting characteristic line radiation. The Doppler shift of the spectrum is directly proportional to the rotation velocity of the ions.

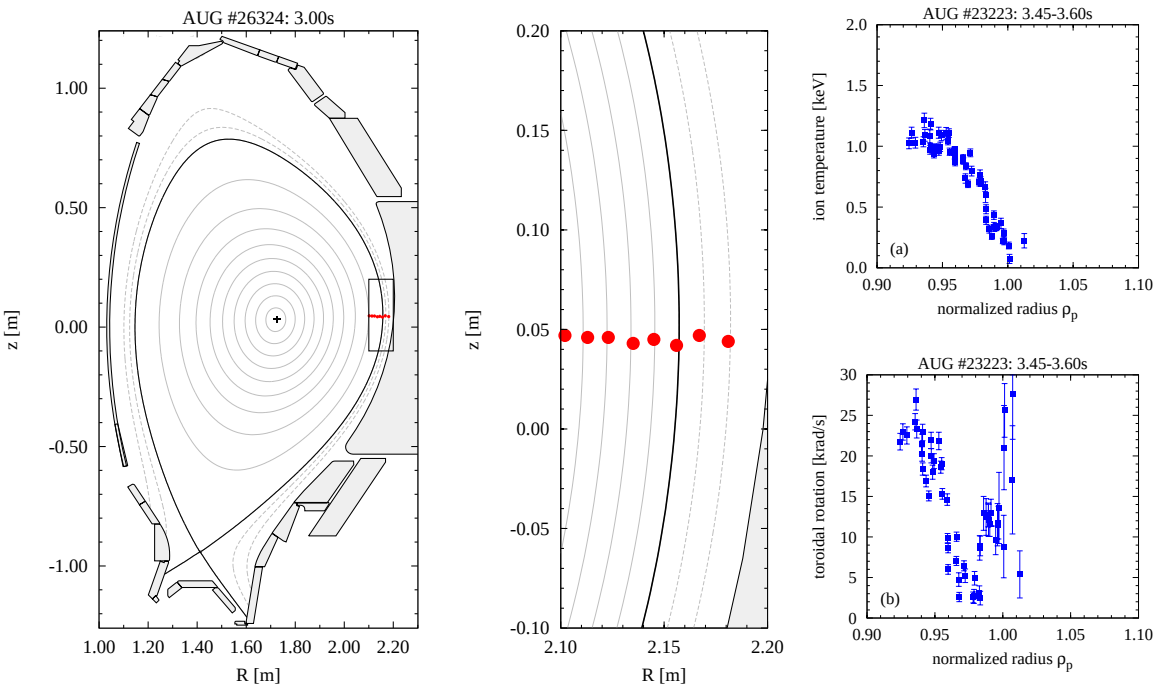

Figure 4.8: Poloidal view of the edge CXRS volumes in sector 15. The distance of the field lines is $\Delta\rho_{\mathrm{p}} = 0.1$ for the full view and $\Delta\rho_{\mathrm{p}} = 0.02$ for the edge zoom. Two profiles of ion temperature (a) and toroidal rotation (b) are shown on the right.

The Doppler broadening of the lines is related to the ion temperature and the impurity density can be derived from the intensity of the observed radiation.

4.5.1 ASDEX Upgrade

AUG is equipped with several charge exchange systems at different locations: in the plasma center, at the edge on the high- and low-field side with toroidal and poloidal lines of sight. For the present work the toroidal edge CXRS at the low-field side viewing the heating beam in sector 15 is used [10]. The position of the measurements is illustrated in Figure 4.8. The size of the red circles resembles the radial resolution of 3 mm. The lines of sight with a focal width of 4 mm cross the neutral beam with a FWHM of 20 cm. Due to the small toroidal curvature this corresponds to a mapped observation volume with a width of 5 mm. The large gradient of the impurity density in the pedestal reduces the width of an intensity profile along one line of sight. This results in a radial resolution of 3 mm in the steep gradient region. The CXRS system allows to diagnose the last 10-20% of the plasma radius with a exposure time of 1.9 ms. This exposure time is at the limit to resolve the ELM cycle but with ELM synchronisation it is possible to obtain pre ELM profiles - profiles of ion temperature (a) and toroidal rotation (b) are illustrated in Figure 4.8. It is possible to observe different impurity species, the most common are Boron, Carbon and Nitrogen. Depending on the discharge scenario and machine condition the observed impurity species is chosen appropriately.

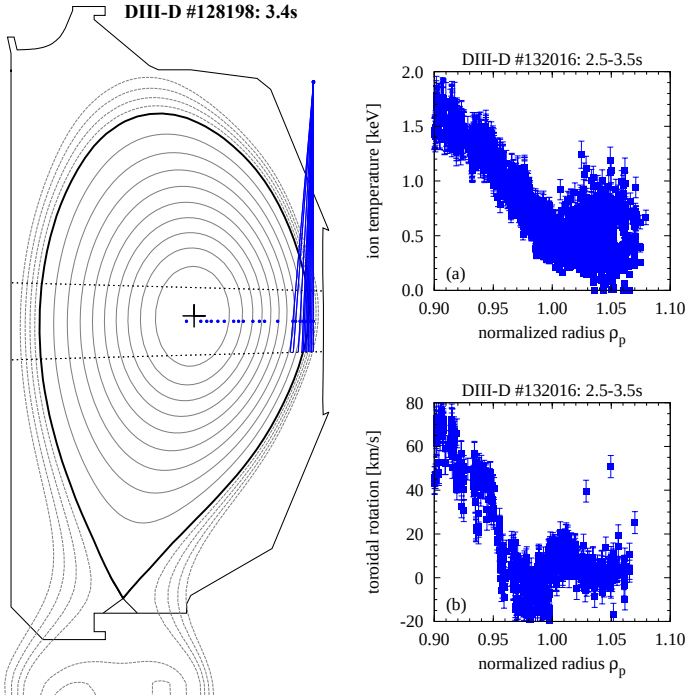

Figure 4.9: Poloidal view of the CXRS in DIII-D. The centers of the observation volumes of the core CXRS are shown by blue circles, for the edge CXRS also the lines of sight are included. The heating beam is indicated by the horizontal dotted lines. Two profiles of ion temperature (a) and toroidal rotation (b) are shown on the right.

4.5.2 DIII-D

The charge exchange system at DIII-D has a very similar setup compared to the AUG system [73]. The lines of sight and the centers of the observation volumes are illustrated in Figure 4.9. The edge CXRS uses an integration time of 0.3-0.5 ms and the spatial resolution is ±0.5-1.0 cm [74]. This means the temporal resolution is good enough to obtain inter ELM profiles. The spatial resolution is at the limit to resolve the steep gradients in the pedestal region.

4.6 Reflectometry

Reflectometry is an active measurement of the electron density in the plasma. The plasma is generally optically thin for most microwave frequencies. However, there are certain frequencies where waves can be absorbed or reflected by the plasma. The wave absorption was utilized for the ECE diagnostic described in Section 4.1. For the reflectometry the reflections are important. At the cutoff frequencies the refractive index of the plasma goes to zero and waves are reflected. The electro-magnetic waves which propagate perpendicularly to the magnetic field with their electric field component parallel to the field have their cutoff frequency at the plasma frequency $f_{\mathrm{pe}} = (n_{\mathrm{e}}e^2/(4\pi^2\epsilon_0 m_{\mathrm{e}}))^{0.5}$ which only depends on the electron density. In reflectometry the position of a certain density layer is determined by probing the plasma with a wave of known frequency. The time a wave needs to get reflected back into the detector is measured via the phase shift of the reflected wave. This gives information about the position of the reflecting layer. By sweeping over different frequencies

a density profile is obtained.
The reflectometry measurement has no error associated with the density values but only with the position in the plasma. This has the advantage that the pedestal top density is determined very precisely. Small gradients inside of the pedestal top can also be resolved more accurate than it is possible with the Li-beam which is already attenuated in this region. However, in the presence of steep gradients the reflectometry has disadvantages because these measurements demand a very high radial accuracy which is difficult to achieve with time measurements of only a few ns. The reflectometry can only measure monotonously increasing density profiles, for example a hollow profile cannot be measured because the probing wave is reflected at the first cutoff layer. This can be a problem when for example MHD modes cause local density variations. Unfortunately, data from the reflectometry was not available for most of the discharges analysed for this work. Therefore, reflectometry measurements are only used when explicitly mentioned.

4.7 Finite Radial Resolution

In regions where the profile changes on a small radial scale the spatial resolution of diagnostics becomes important. The interpretation of most measurements is based on assuming constant plasma conditions over the measurement volume. However, in regions like the pedestal with large gradients and small radial extent this prerequisite might be violated. This can lead to systematically wrong results when not taken into account. The effect of the radial resolution is illustrated in this section with the example of electron density measurements with the Thomson scattering. One method to recover data which was analysed with wrong assumptions is introduced.

As described in Section 4.3 the electron density can be derived from the observed intensity in the scattering volume. The general assumption is a constant value for the density in the measured volume. When this assumption is fulfilled the measured density will equal the ‘real‘ plasma density. If the density does vary within the scattering volume only a mean density is measured for this volume. This can result in wrong gradients in regions where the scattering volume is of similar size as the measured structure.
A forward model can determine the effect of a density gradient within the scattering volume. The scattering volume is mapped onto the same radial coordinate as the profile and one obtains a 1D kernel function. In the case of the TS a mean profile is obtained with a convolution of a ‘real‘ profile with a realistic kernel for the scattering volume. Only with a δ-function kernel the ‘real‘ profile is measured directly. The real geometry of the scattering volume is determined by convolution of the Gaussian laser beam and the line of sight. At AUG the beam has a FWHM of 0.5 mm. The line of sight is 2.56 cm in z direction and uniformly illuminates the detector. The volume is then mapped to the midplane - see Section 5.1 for details on mapping procedures and necessary assumptions. The mapped kernel becomes wider when the inclination between laser path and field lines increases. The worst case observed at AUG has a high triangularity δ. The geometry of two realistic scattering volumes is illustrated in Figure 4.10. For the case with low triangularity (a) the FWHM of the kernel in the steep gradient region is 1.2 mm at the separatrix where scattering volumes and field lines are less aligned this increases to 4.6 mm. In the case with high triangularity (b) the kernel width in the gradient region is larger by 40% and becomes 1.7 mm. At the separatrix is stays the same in both cases. Scattering volumes for the JET TS were shown in

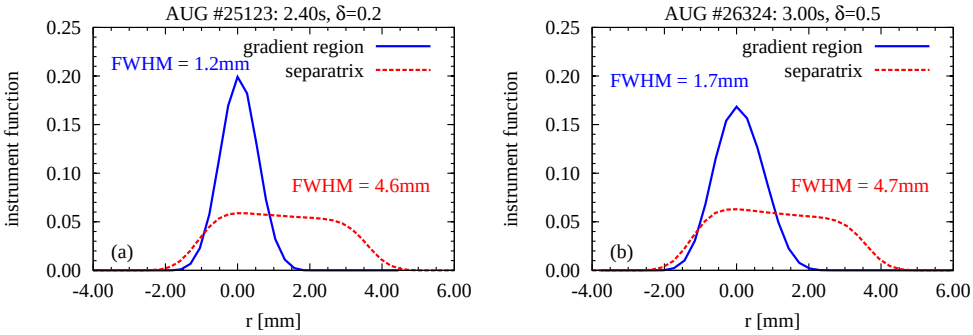

Figure 4.10: Scattering volumes of the TS mapped to R_{maj} at the midplane. The x-axis is a relative coordinate centered at the measurement positions stored in the shotfile. (a) shows a case with low triangularity and (b) a case with high triangularity. The kernel is determined at two positions the steep gradient region (blue,solid) and at the separatrix (red,dashed).

Figure 4.6 and the resolution at DIII-D is about 6 mm. These different scattering volumes are tested with a typical density profile from AUG with a pedestal width of 1.7 cm. For this example a hyperbolic tangent shape is used for the pedestal. Figure 4.11 shows the result for four different realistic kernel functions (green). When assuming a constant density in the scattering volumes the profile would appear as the red,solid one. It is plotted together with real profile (blue,solid) and the corresponding gradients (dashed). For the largest kernel from a JET discharge with the old optics (a) a reduction of the gradients of over 25% is observed. This error could be reduced to 10% with the improved optics (b). At AUG such a problem does not exist, the case with a kernel of ∼5 mm (c) shows only a deviation of about 1%. This corresponds to the worst kernel of the AUG TS system and a typical resolution of other diagnostics at AUG and DIII-D. In the normal case of the TS (d) the deviation is less than 1% which is well below any other uncertainty in the measurement. These numbers were calculated for a typical pedestal width. In general the ratio of kernel width and pedestal width is relevant for the error made in the analysis. This is shown in Figure 4.12 where the deviation of the gradient in the pedestal is shown against the ratio of kernel FWHN and pedestal width. The kernel was arbitrarily chosen to be a triangle. When the kernel width is about half the actual pedestal width the error is about 5%. In the case of equal width the error increases to 20% and becomes even larger for wider kernels.
With the example of a simple photon count measurement like the TS electron density measurement the influence of the size of one observation volume (kernel) was illustrated. In this example the influence is visible when the gradients of the observed parameter are not constant within the observation volume. In the pedestal region the deviation is about 5% as long as the kernel width is half the size of the pedestal width. For AUG and DIII-D diagnostics this is true for pedestal widths down to ∼1 cm. For pedestal width >1.5 cm the deviation drops below 2%. For pedestal widths smaller than 1 cm the deviation would consequently increase. At JET the errors are significantly larger because of the larger kernel size. This analysis is true for the particular example of the TS density measurement. Depending on the physical processes behind the measurement the results can vary. In particular, it generally becomes more complicated to track the consequences of non-constant parameters in the observation volume through the analysis procedure. An example for this is the electron temperature measurement with the TS which will be described in the next subsection. It might also be possible that one component is obscured by another, for example in the case

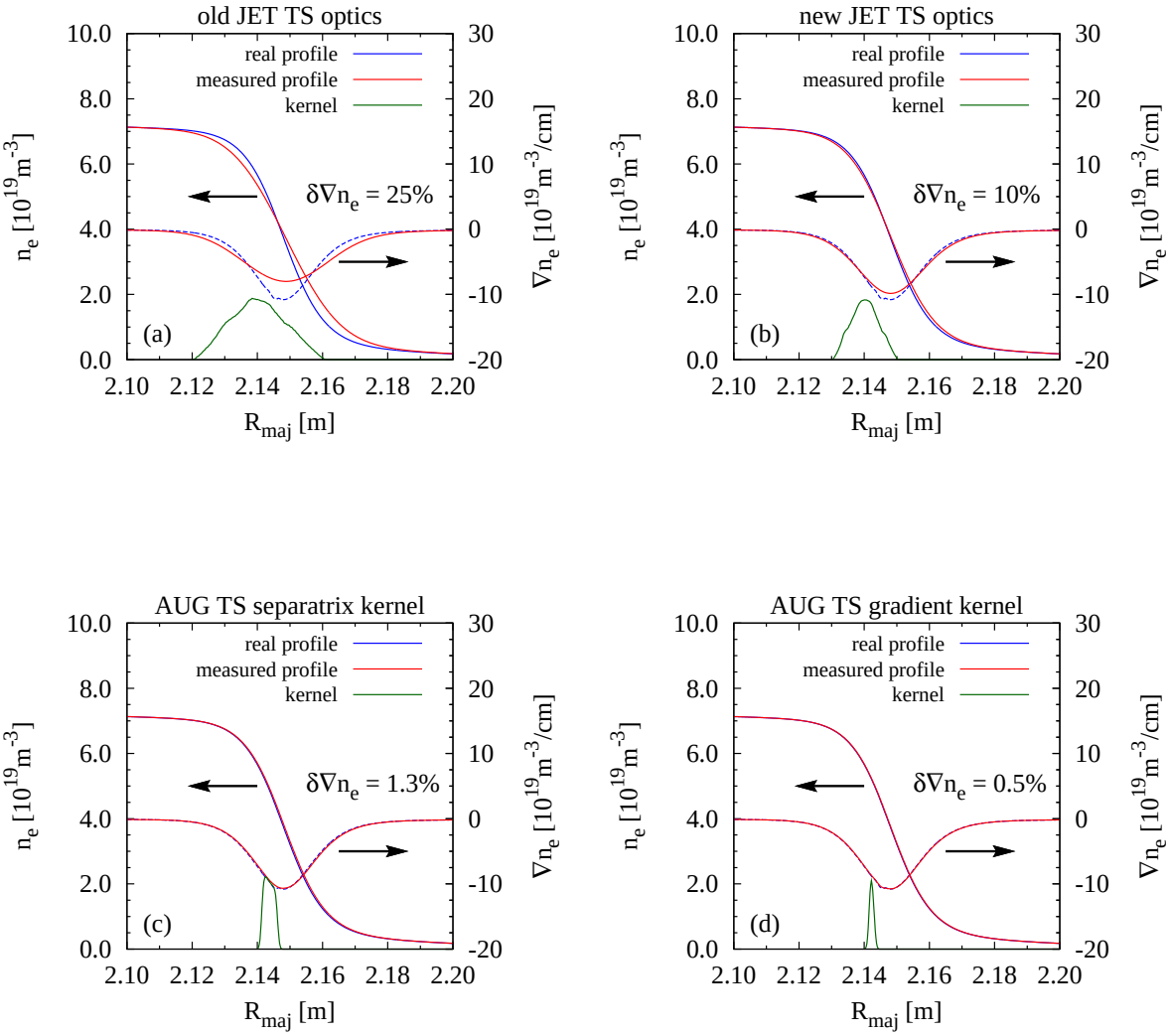

Figure 4.11: Influence of the scattering volume size for several realistic volumes. The real profile is in blue, the profile how it would appear with the wrong assumptions for the analysis in red and the scattering kernel in green. The change of the profile is also indicated by its gradients in dashed lines. The different kernels are for the old optics at JET (a), the new optics at JET (b), the kernel at the separatrix in AUG (c) and a typical kernel in the steep gradient region of AUG (d).

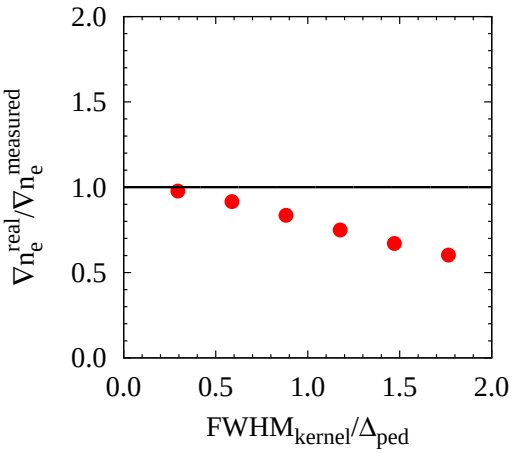

Figure 4.12: Deviation between real gradient in the pedestal and the measured one plotted against the ratio of scattering kernel FWHM and pedestal width. The kernel was approximated as triangle for all cases.

of line radiation when the broadest contribution is dominant.

To summarize, in the pedestal region with small spatial structures it is important to know the limits of the diagnostics otherwise the measurements are easily misinterpreted. Especially, additional lines of sight or virtual ones by shifting the plasma will only increase the spatial resolution if the radial distance between channels is too large - not if the observation volumes of a single channel are too large. If you have a blurred vision it will not sharpen by moving your head.

4.7.1 Richardson-Lucy Deconvolution

The problem of degraded images due to limits of the optical system is long known in optics and astrophysics. A technique to restore degraded images was developed independently by W.H. Richardson [70] and L.B. Lucy [75]. The Richardson-Lucy deconvolution RLD is an iterative method "which derives from Bayes' theorem on conditional probabilities, conserves the constraints on frequency distributions (i.e., normalization and non-negativeness) and, at each iteration, increases the likelihood of the observed sample" [75]. In general the degrading function or point spread function $\mathcal{K}$ is set by the resolution of the measurement. When the original image $\mathcal{R}$ is known the degraded image $\mathcal{S}$ is obtained by convolution

$$\mathcal{S} = \mathcal{R} * \mathcal{K}. \tag{4.1}$$

If only the degraded image is known an estimate for the original image $\mathcal{R}_i$ can be given by applying Bayes' theorem (e.g. [76]). The estimate is used as initial condition for the next iteration which improves the estimate for $\mathcal{R}_{i+1}$. For each iteration the quality of the estimate can be tested with Eq. (4.1).
The measurement of the electron density with the Thomson scattering diagnostic is a photon count measurement. Therefore, the RLD is directly applicable where $\mathcal{S}$ denotes the profile measured with the different channels and $\mathcal{K}$ the observation kernel. The convergence for the RLD with the JET kernel (Figure 4.6) and an arbitrary profile with 1.7 cm width is shown in Figure 4.13. The deviation of the maximal gradient in the pedestal is shown for the 2-4 cm

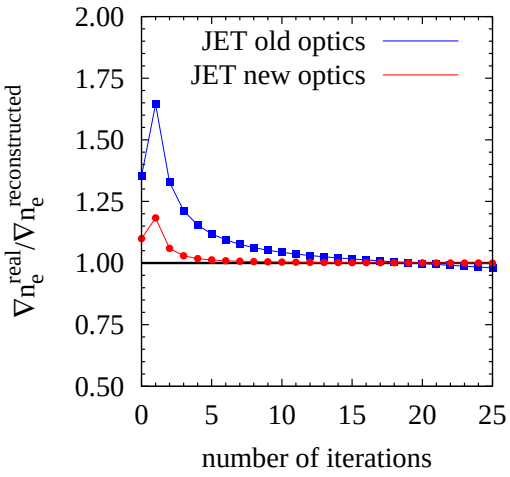

Figure 4.13: Results of the gradients of profiles reconstructed with the RLD. The real pedestal width was 1.7 cm and the observation kernels are taken from Figure 4.13.

kernel of the old optics (blue,squares) and the 1-2 cm kernel of the new optics (red,circle). In the case with the smaller kernel the reconstruction converges quite fast and reaches the original value within 1% after 10 iterations. When the kernel width is significantly larger than the real structure too much information is lost in the convolution and the RLD does not converge. After 10 iterations the deviation of the estimate and the real profile has reduced to 5%. However, the RLD will not converge for more iterations but increase the gradient further. In regions of flat profiles, where no influence of a larger kernel is expected, arbitrary profile oscillations will appear with a wavelength of ∼4 cm which do not violate Eq. (4.1) but might result in wrong pedestal top values.
The temperature measurement with the Thomson scattering is more complicated. The temperature is determined with a weighted photon count measurement. Not only the number of photons but also their spectral information is necessary to determine the temperature. This means the temperature can only be derived when the density is known. A more dense region of the plasma will contribute stronger to the spectrum than other regions. An approximation to quantify this process was given in [71]

$$\mathcal{S}_{T\mathrm{e}} = \left(\frac{\left(\sqrt{\mathcal{R}_{T\mathrm{e}}}\mathcal{R}_{n\mathrm{e}}\right) * \mathcal{K}}{\mathcal{R}_{n\mathrm{e}} * \mathcal{K}} \right)^2 . \tag{4.2}$$

The motivation for Eq. (4.2) is based on an approximation of the TS spectrum width $\Delta_{\mathrm{FWHM}} \propto \sqrt{T_\mathrm{e}}$. This approximation equals the analytical description given in [77] within 10% for 0.1-4.0 keV. The spectral width for each temperature is weighted with the density profile to account for the different intensities. The weighting by the density is removed after convolution with the observation kernel. Another approximation is that the superposition of spectra with different temperatures yield a width which is the mean of the underlying spectral widths. This approximation is only good (∼10%) when the temperature does not vary by more than a factor of 3 within the observed volume. In the pedestal the temperature can easily vary by a factor of 10 and then this approximation will be wrong by up to 100%. The deviation is reduced by the density weighting, however, it is still significant if the whole pedestal falls into the observation volume. This means the temperature pedestal cannot be

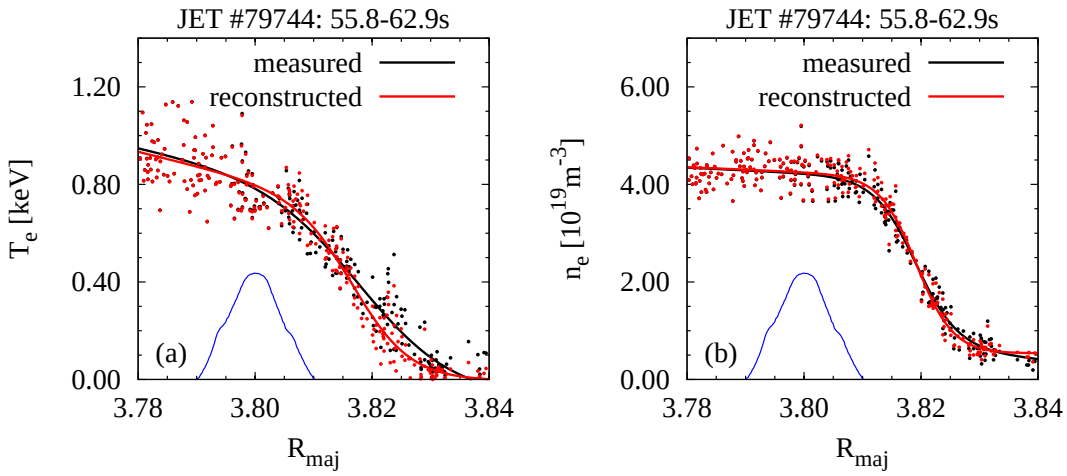

Figure 4.14: Examples for the RLD applied to data from JET. The data as obtained with the wrong assumptions for the analysis is shown in black. The reconstruction of the data with RLD and Eq. (4.2) is shown in red.

recovered with this approximation for the old diagnostic setup at JET (discharges <79000). Therefore, only measurements with the improved optics will be treated with the RLD, because the kernel is still smaller than the pedestal and the approximations in Eq. (4.2) are reasonable. Examples for the profile recovery using the RLD with real data are shown in Figure 4.14. For the electron temperature (a) the pedestal width decreased from 3.3 cm in the untreated case (black) to 2.3 cm after RLD (red). The electron density did not change that much from 1.5 cm to 1.3 cm.

In this section one technique for profile deconvolution was described. With knowledge of the observation kernel profiles can be recovered even if the resolution is too small. However, this does only work reliable for kernel widths which are the same size as the observed structure or smaller. Additionally, the applicability is restricted to cases were the physics behind the measurement are compatible with a direct convolution of signals. Application of approximations to synthetically generate such conditions can lead to undesired results. For a larger analysis with JET data it is recommended to use proper modelling of the raw signals in the individual spectral channels. For this work such an analysis was not available.

Chapter 5

Methodology

5.1 Equilibrium Reconstruction

In tokamak geometry the reconstruction of the magnetic equilibrium, i.e. the structure of the nested flux surfaces, plays an important role to combine measurements from different locations. Different boundary conditions in the equilibrium reconstruction influence the mapping of measurement locations. This can lead to deviations in the pedestal width and pedestal gradients. In this section these effects are investigated with the equilibrium reconstruction codes CLISTE [78] and EFIT [79].

The measurements themselves are conducted in machine coordinates R, z, ϕ with radial coordinate R, vertical coordinate z and toroidal angle ϕ. These coordinates are determined for each diagnostic during calibration and are assumed to be without any uncertainty in the remainder of this section. Because of toroidal symmetry ϕ is dropped. In order to compare measurements from different locations it is convenient to map R, z to 1D normalized poloidal flux coordinates

$$\Psi_{\mathrm{N}} = \frac{\Psi - \Psi_{\mathrm{ax}}}{\Psi_{\mathrm{sep}} - \Psi_{\mathrm{ax}}}, \tag{5.1}$$

with the 2D flux function Ψ, the flux at the plasma center Ψ_{ax} and at the separatrix Ψ_{sep}. This can be done for all flux surfaces. In many cases it is helpful to consider profiles again in real space. Therefore, the Ψ_{N} coordinates are mapped back to R, z. For a definite relation in the inverse mapping, z is set to the value at the magnetic axis z_{mag}. The resulting real space coordinate is then called R_{maj}. Analogous to the R_{maj} coordinate, also an un-normalized 1D flux coordinate can be defined as Ψ_{maj}. At AUG another normalized coordinate $\rho_{\mathrm{p}} = \Psi_{\mathrm{N}}^{0.5}$ is often used. Analogous to poloidal flux coordinates, toroidal flux coordinates can also be defined, however, these are not used in this work, since toroidal flux is only defined up to the separatrix.
The equilibrium reconstruction is generally done with codes like CLISTE or EFIT, which mainly consist of a Grad-Shafranov solver and several constraints defined by theory and measurement. The amount of experimental constraints applied in the equilibrium reconstruction varies for different applications. The equilibria based only on magnetic measurements will be called generic equilibria, these are always available and are normally used for profile analysis. More sophisticated equilibria can also include kinetic profiles and fast particle simulations to constrain the total pressure [80, 81] and are called kinetic equilibria. Because their preparation is normally time consuming, these equilibria are generally only used as input for further

calculations such as stability analyses. In this section the influence on profile analysis is quantified by applying generic and the more sophisticated kinetic equilibria.

5.1.1 Differences due to Experimental Constraints

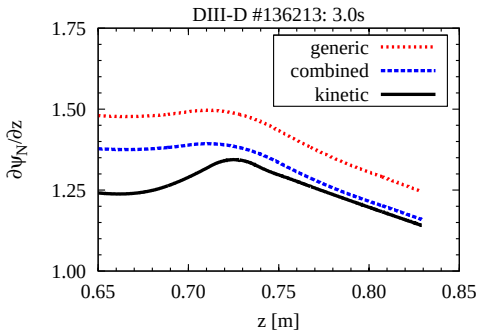

5.1.1: Absolute values

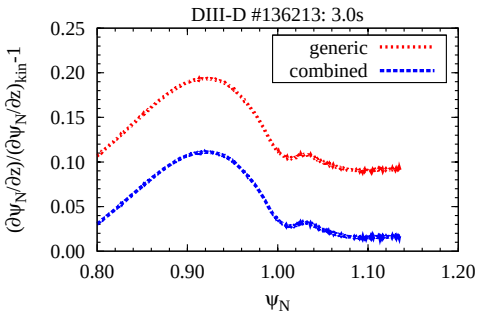

5.1.2: Relative deviation from the kinetic profile

Figure 5.1: Different results for $\partial\Psi_N/\partial z$ using a generic equilibrium (dotted,red), a kinetic equilibrium (solid,black) or a generic equilibrium combined with the normalization of the kinetic one (dashed,blue). The relative deviation is $(\partial\Psi_N/\partial z)/(\partial\Psi_N/\partial z)_{kin} - 1$.

Generic and kinetic equilibria are compared for the same discharges in order to assess the influence of the boundary conditions on the pedestal width and gradient. The flux surface compression $\partial\Psi/\partial z$ or $\partial\Psi/\partial R$ is used to quantify differences in the reconstructions. The following analysis is based on nineteen pairs (generic and kinetic) of EFIT reconstructions for DIII-D discharges involving an edge safety factor q_{95}-scan from $4-7$ at high triangularity $\delta = 0.5$ and global poloidal beta $\beta_p = 1-2$. Assuming the kinetic equilibria best resemble the reality, several uncertainties arise when using generic equilibria. The influence of normalizing the flux coordinates is illustrated in Figure 5.1 for the flux surface compression $\partial\Psi_N/\partial z$ along the Thomson Scattering chords of DIII-D. The combined $\partial\Psi_N/\partial z$ is generated with the normalisation factor derived from the kinetic equilibrium and the generic flux compression $\partial\Psi/\partial z$. The difference between generic and combined flux compression is up to 10%, mainly due to different values of Ψ_{ax}. Besides the deviation in normalization this example shows the effect of a different current profile. This difference is expected since the bootstrap current is taken into account only for the kinetic case. All EFIT reconstructions show a larger $\partial\Psi_N/\partial z$ for the generic case. In regions where the bootstrap contribution is negligible $\partial\Psi_N/\partial z$ deviates by 5-20%. In regions of significant bootstrap current the deviation increases to 10-30%. However, the difference in the reconstruction cannot be explained with deviations in normalization and current profiles alone. Also differences in Shafranov-Shift $\beta_p - li/2$, safety factor q_{95} and plasma shape (δ, κ, R_{sep}) contribute to the deviation in $\partial\Psi_N/\partial z$. Equilibrium reconstructions by CLISTE at AUG show similar behaviour as those done with EFIT at DIII-D. With CLISTE a power scan $6.5-13.5$ MW at constant q_{95} was analysed. The flux surface compression increases with heating power similarly for generic and kinetic reconstructions. However, the higher heating power results in larger edge pressure gradient and increased bootstrap contribution. This causes localised deviations in $\partial\Psi_N/\partial R$ for generic and kinetic reconstructions which scale with the heating power. In Figure 5.2 the relative deviation in flux compression is plotted over the plasma edge. At low heating power deviations below

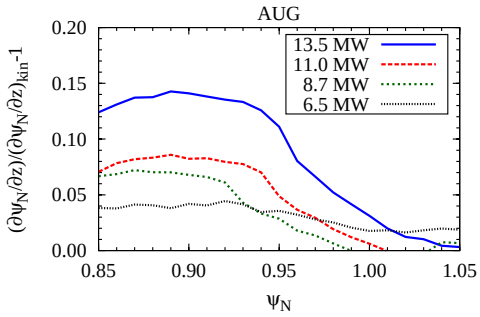

Figure 5.2: Relative deviation in flux surface compression $\partial\Psi_N/\partial R$ for generic and kinetic equilibrium reconstructions. The generic reconstruction has the larger flux compression. The difference is increasing with heating power. The absolute values are shown in Figure 5.4. (black: AUG#24167:4.225s, green: AUG#24168:4.225s, red: AUG#22898:4.625s, blue: AUG#23223:5.325s)

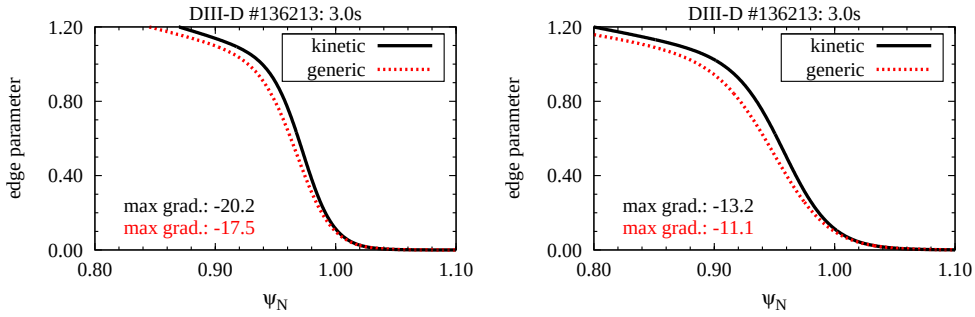

5.3.1: Initial pedestal width of 1.5 cm

5.3.2: Initial pedestal width of 2.5 cm

Figure 5.3: The same profile measured in R, z appear differently in flux coordinates depending on the underlying equilibrium reconstruction. The pedestal width becomes larger, the gradient smaller and the profile might be shifted. For comparison the profiles were aligned at the separatrix.

5% are observed while this increases to over 10% at higher heating power.
The equilibria for the analyses are all based on experimental measurements and cover a wide range of plasma parameters. However, the range was not sufficient to draw final conclusions about the mechanisms behind the observations. Therefore, a more sophisticated analysis should be conducted, with the goal to improve generic equilibrium reconstructions.

Concerning pedestal profile analysis the significance of the error introduced by the equilibrium reconstruction is assessed in the following. The error does not seem to depend systematically on global values like e.g. the Shafranov-Shift, but on the constraints in the equilibrium reconstructions. Especially, neglecting the bootstrap current leads to systematic deviations in the flux surface compression. The bootstrap current is also dependent on edge gradients [40]. The gradients themselves are determined with knowledge of the flux surface compression. This results in a systematic increase of the flux surface compression for generic equilibria which influences the mapping of measurements from R, z to Ψ_N, Ψ_{maj} or R_{maj}. With an overestimated flux surface compression a pedestal profile appears to be broader in Ψ_N coordinates and shows smaller gradients. This is illustrated in Figure 5.3 where an arbitrary edge parameter is plotted against Ψ_N. Both profiles are identical in R, z coordinates, but they deviate after mapping to Ψ_N coordinates. The profile obtained with the generic reconstruction appears to be broader. Initially broader profiles experience a larger relative

Input width [cm]	$\delta\Delta/\Delta[\Psi_N]$	$\delta\Delta/\Delta[R_{maj}]$
1.0	$+4.3 \pm 3.3\%$	$-0.9 \pm 1.9\%$
1.5	$+7.4 \pm 3.8\%$	$+0.4 \pm 1.6\%$
2.5	$+10.1 \pm 4.6\%$	$+1.5 \pm 1.9\%$

Table 5.1: Mean relative broadening for different pedestal widths in Ψ_N and R_{maj} due to use of generic instead of kinetic equilibrium reconstructions. Evaluated for 19 EFIT pairs corresponding to DIII-D discharges.

broadening. This is because the largest deviation in $\partial\Psi_N/\partial z$ or $\partial\Psi_N/\partial R$ s farther inwards than a typical pedestal (see Figures 5.1, 5.2). The results for the equilibrium reconstruction with EFIT are summarized in Table 5.1. The deviations in the flux surface compression are comparable at different plasma positions - here the position of the DIII-D Thomson Scattering system and the outer midplane. Therefore, these errors cancel each other after the transformation to R_{maj} coordinates.

In summary, uncertainties due to equilibrium reconstruction are avoided when the analysis is performed in the real space coordinate system of the measurement. This is because the mapping is applied twice and any deviations cancel each other. However, normalized flux coordinates might be important for the underlying physics, as discussed in Chapter 3 and therefore necessary for the analysis. The comparison between generic and magnetic equilibrium reconstructions showed that deviations of up to 30% in $\partial\Psi_N/\partial z$ are possible for single measurements. On average the deviation of derived quantities like pedestal width and gradient remain 10% or lower. However, this deviation is dependent on the edge bootstrap current and the initial width of the profile.

5.1.2 Influence of Experimental Conditions

A change in the plasma conditions will influence the result of equilibrium reconstructions. This section documents the influence of plasma parameters on coordinate system transformations. It is illustrated how different coordinate systems impact the multi machine comparison between ASDEX Upgrade, DIII-D and JET.
Within a single device the flux surface compression can be manipulated with different heating levels. Figure 5.4 illustrates how $\partial\Psi_N/\partial R$ increases with heating power in AUG. This is observed for kinetic (b) and generic (a) equilibrium reconstructions alike. The agreement suggests that generic reconstructions are suitable for analysing general dependencies. However, some effects might be lost when using less constraints in the equilibrium calculations. The analysis in the remainder of this section is performed with generic equilibria.
At the midplane the poloidal flux surface compression becomes $\partial\Psi_{maj}/\partial R = -RB_p$. However, the local poloidal field is not easily accessible experimentally. At the pedestal $\partial\Psi_{maj}/\partial R$ is fairly constant as shown in Figure 5.4 (a) and can be regressed from AUG, DIII-D and JET

$$\frac{\partial\Psi_{maj}}{\partial R} \simeq 12.0 R_{mag}^{1.08\pm0.14} \langle B_p \rangle^{1.01\pm0.05} \beta_{p,ped}^{0.14\pm0.04}, \tag{5.2}$$

with $\partial\Psi_{maj}/\partial R$ measured in Vs/m, the normalized pedestal top pressure $\beta_{p,ped}$ (see Eq. (6.4)), the radius of the magnetic axis R_{mag}, the flux surface averaged poloidal field $\langle B_p \rangle = \mu_0 I_p/l$ and $l \propto a$ the plasma circumference at the last closed flux surface where a is the minor radius of the plasma. In Figure 5.5.1 $\partial\Psi_{maj}/\partial R$ is averaged over the last 10% of the plasma

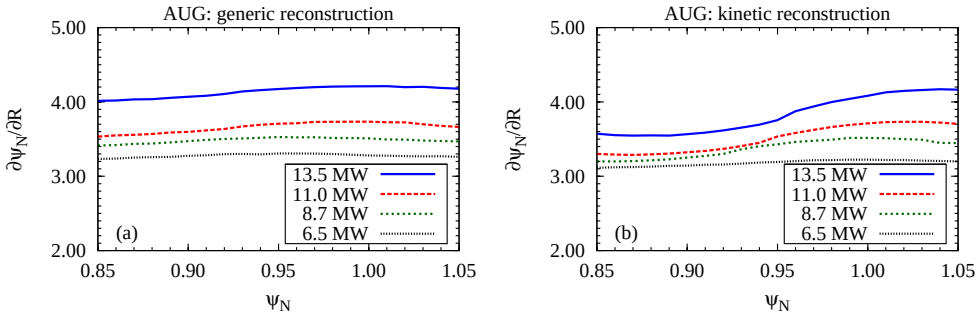

Figure 5.4: Flux surface compression at the outer midplane for different heating scenarios at ASDEX Upgrade (black: AUG#24167:4.225s, green: AUG#24168:4.225s, red: AUG#22898:4.625s, blue: AUG#23223:5.325s). The generic equilibrium reconstruction with CLISTE (a) shows increasing flux surface compression similar to the kinetic reconstruction (b). The influence of the increased current density due to edge currents becomes visible for the kinetic reconstruction at about $\Psi_N \sim 0.95$.

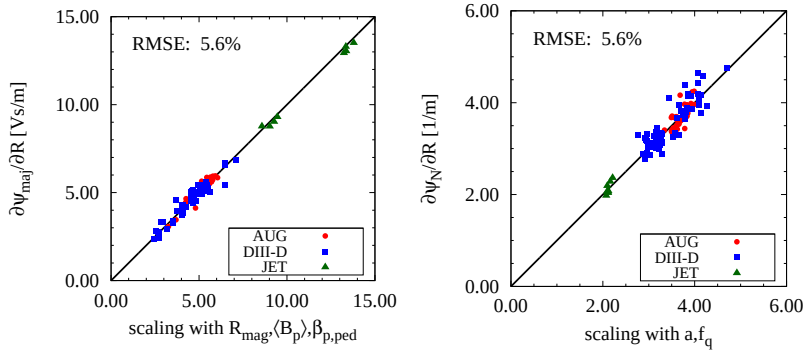

5.5.1: $12.0 R_{\mathrm{mag}}^{1.08} \langle B_{\mathrm{p}} \rangle^{1.01} \beta_{\mathrm{p,ped}}^{0.14}$ 5.5.2: $1.65 a^{-0.70} (q_{95}/q_{cyl})^{1.07}$

Figure 5.5: The flux compression averaged over the last 10% of the plasma radius at the outer midplane is plotted against a best-fit-model. Left for the poloidal flux and right for the normalized poloidal flux. The root mean squared error RMSE was calculated after [44] and is with 5% fairly low in both cases. The subcaptions show the used regression model. For an expression with uncertainties see Eq. (5.2) and (5.5).

radius (Ψ_N) and plotted against the approximation of Eq. (5.2). The regression is in quite good agreement with the data. This result is strong evidence that there are no systematic deviations between the equilibrium reconstructions for the individual machines. This also illustrates the difference between the flux surface averaged poloidal field and its local value at the outer midplane. It becomes $B_{\mathrm{p}} \propto \langle B_{\mathrm{p}} \rangle \beta_{\mathrm{p,ped}}^{0.14}$ and therefore $\beta_{\mathrm{p,ped}} = \beta_{\mathrm{p,ped,local}}^{0.72}$. This means the local poloidal field is roughly 25% larger than the flux surface averaged field.
The compression of normalized flux in real space can be divided into two components by using the definition of the normalized flux in Eq. (5.1)

$$\frac{\partial \Psi_{\mathrm{N}}}{\partial R} = \frac{1}{\Psi_{\mathrm{sep}} - \Psi_{\mathrm{ax}}} \frac{\partial \Psi}{\partial R}, \tag{5.3}$$

where $\Psi_{\mathrm{sep}} - \Psi_{ax}$ is the normalization factor. For a cylindrical plasma the normalisation factor becomes $\Psi_{\mathrm{sep}} - \Psi_{\mathrm{ax}} \propto \mu_0 I_{\mathrm{p}} a$ with the total plasma current I_{p}. If we neglect the pressure and approximate $B_{\mathrm{p}} \sim \langle B_{\mathrm{p}} \rangle$ the dependence on the plasma current drops and only

a machine size dependence remains

$$\frac{\partial \Psi_N}{\partial R} \propto \frac{1}{a}\frac{1+\epsilon}{\epsilon}, \tag{5.4}$$

where $\epsilon = a/R_0$ is the inverse aspect ratio. The estimations which led to Eq. (5.4) neglect the real shape of the plasma and the local poloidal field. However, a correction can be introduced in form of the shaping factor f_q which will be discussed in detail in Section 6.3. For the scaling to AUG, DIII-D and JET the machine size dependence is found to be inverse but slightly less than linear.

$$\frac{\partial \Psi_N}{\partial R} \simeq 1.65 a^{-0.70\pm0.05} f_q^{1.07\pm0.10}. \tag{5.5}$$

The aspect ratio dependence in Eq. (5.4) could not be reproduced since there is no variation in ϵ for the available database. The quality of the approximation Eq. (5.5) is illustrated in Figure 5.5.2 and shows reasonable agreement for all three machines. In this representation the shaping factor was introduced instead of $\beta_{p,ped}$, because it is the better quantity to describe the problem. With the regression parameters a and $\beta_{p,ped}$ the RMSE increases by 50%. When applying the regression to all three parameters a, f_q and $\beta_{p,ped}$ Eq. (5.5) does not change but the exponent of $\beta_{p,ped}^b$ is found to be $b < 0.03$.

Applying a coordinate transformation - e.g. from real space to normalized flux space ($\partial\Psi_N/\partial R$) - will influence all comparisons of widths and gradients. This coordinate transformation is dependent on machine size, aspect ratio, magnetic field, shaping and plasma pressure. All these parameters are also possible candidates in determining the pedestal width. In particular, following Eq. (5.5), the two dimensionless descriptions of the width flux space Δ_{Ψ_N} and in real space Δ_m/a are not equivalent and will result in different scalings with f_q or $\beta_{p,ped}$. For multi-machine comparisons it is important to use the correct coordinate system which is set by the underlying physics. For example normalized flux coordinates for MHD related physics and real space coordinates when atomic processes dominate the plasma edge, as described in Chapter 3.

5.2 Pedestal Building

The H-mode edge pedestal s only over few percent of the plasma radius and the diagnostics described in Chapter 4 have generally few channels in the steep gradient region. Therefore, the analysis of single profiles exhibits unsatisfactorily large uncertainties. There are two commonly used methods to reduce these uncertainties. One method is to characterise each measurement individually and then average over a large number of supposedly identical measurements. Another method is to build a composite profile out of multiple measurements, the result of which is more accurate than profiles of individual measurements. An example for the differences between single and composite profiles is given in Figure 5.6 with data from the AUG TS diagnostic. In the present work the latter method is applied because multiple diagnostics are included which complement one another. These diagnostics have different time bases and therefore rely on composite profiles.
The following sections describe the steps necessary for preparation of the data. First the procedure of synchronising the data with respect to ELMs, then the mapping procedure of multiple diagnostics to create a single composite profile and finally the advantages of shifting the plasma column to improve the resolution of the pedestal are described.

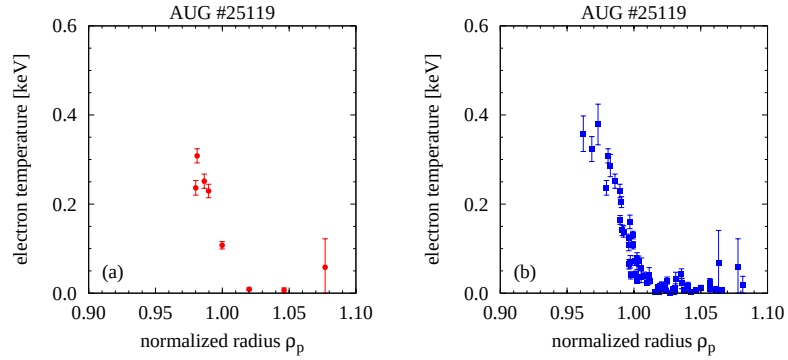

Figure 5.6: Comparison of a single measurement (a) with a composite profile of 10 measurements (b).

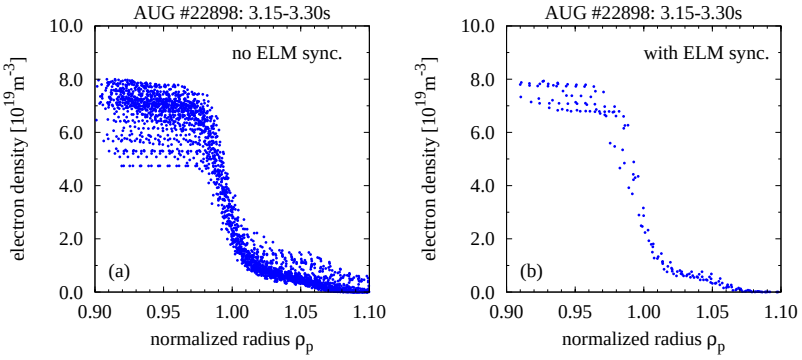

Figure 5.7: Comparison of composite profiles without (a) and with (b) ELM synchronisation.

5.2.1 ELM synchronisation

The main goal of this thesis is to characterise the H-mode edge pedestal at the stability limit of ELMs. In Section 2.1 the impact of an ELM on the plasma edge was described as a collapse of the whole pedestal region in temperature and density. Taking an average profile, including parts of this collapse, would yield extremely scattered composite profiles as shown in Figure 5.7 (a) for n_e profiles from the Li-beam diagnostic. In such a case no reasonable characterization of the pedestal is possible. Therefore, the data is synchronised in time relative to the onset of an ELM. The restriction to time points which lie immediately before an ELM gives a sharper pedestal (b). In this case the pedestal can be characterized accurately as will be described in Section 5.3. The synchronisation is only helpful with the assumption that the pedestal parameters reach the same limit values before each ELM. This can be expected because of the similar characteristics the ELMs show when the global plasma parameters are not varied.

The decision for the actual values for the ELM synchronisation is motivated with knowledge of the ELM cycle as discussed in Section 2.1. The *pre-ELM* time window for AUG is illustrated in Figure 5.8. Before the ELM onset 1.5 ms are excluded as margin for possible errors in the ELM recognition and time delays between different diagnostics. From this time mark a 2.0 ms interval is chosen and only measurements are selected as pre-ELM whose exposure time lies completely within this interval. In the case of diagnostics with longer or

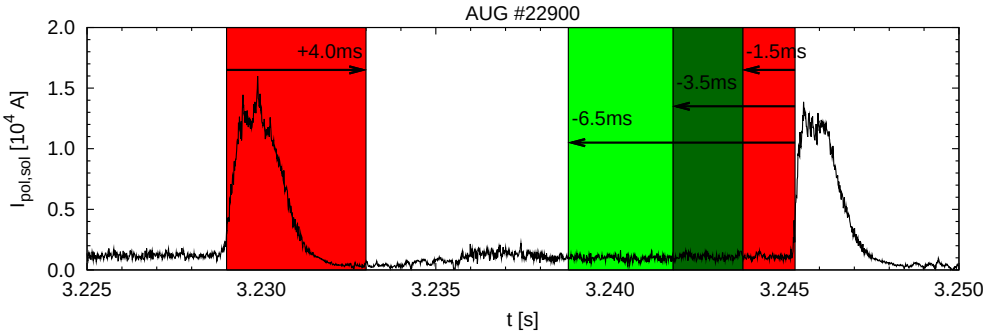

Figure 5.8: Schema of ELM synchronisation using the divertor current signal $I_{\mathrm{pol,sol}}$. The red shaded region is always excluded from the analysis. For diagnostics with high temporal resolution the dark green shaded region from 3.5 to 1.5 ms before an ELM is analysed. The light green shaded region with up to 6.5 ms before the ELM onset is only included for diagnostics with lower time resolution.

comparable exposure times, like the CXRS, this interval is broadened to 5.0 ms. In order to avoid problems at high ELM frequencies (>100 Hz) a distance of at least 4.0 ms is set to the previous ELM. At DIII-D and JET the pre-ELM time window is defined as the last 20% of the ELM cycle. At an ELM frequency of 100 Hz this corresponds fairly well to the definition used at AUG.

5.2.2 Mapping of Multiple Diagnostics

In order to use data from more than one diagnostic the measurements have to be mapped to a common coordinate system. In general diagnostics do not measure at the same position in machine coordinates R, z, ϕ which was illustrated in Figure 4.1. The common coordinate system used throughout this thesis is the normalized radius ρ_{p}, based on the poloidal flux. With equilibrium reconstructions (see Section 5.1) and the assumption of toroidal symmetry all diagnostics are mapped onto ρ_{p} coordinates.

After the mapping procedure diagnostics regularly appear to be radially displaced up to 1 cm with respect to each other. Because some of the measured quantities are constant on flux surfaces like the pressure, all diagnostics should measure the same values for these in flux coordinates. Since this radial displacement is unphysical, an error has occurred on the way to ρ_{p} coordinates. Three possible sources exist for such an error. First, uncertainties in the determination of the observation volumes in machine coordinates could cause a displacement. Second, a deviation of the toroidal symmetry could account for shifts between diagnostics, however, the deviations are not expected to be as large as the observed shifts. Still, when the toroidal symmetry is deliberately broken, for example, by the application of additional magnetic perturbations with magnetic field coils, a diagnostic shift of around 5 mm was observed at AUG [82]. The third possibility is an inaccuracy in the equilibrium reconstruction. At DIII-D shifts of the TS measurements with respect to the separatrix of up to 3 cm are regularly observed. The main reason for this are uncertainties in the plasma shape above the midplane. The DIII-D TS is affected strongly because it measures at the top of the plasma. For diagnostics at AUG, which are concentrated around the outer midplane, the plasma shape is a minor problem because the separatrix is well defined at the midplane. Identifying the source of this was not part of this thesis, therefore, only procedures for correction of the misalignment were applied. The main tool is the TS diagnostic which measures

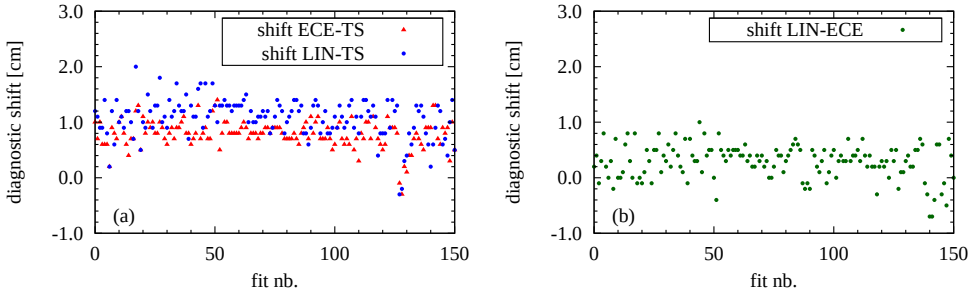

Figure 5.9: Radial displacement of diagnostics over the database. Relative shift necessary to match ECE and Li-Beam with the TS (a). The resulting shift between ECE and Li-Beam determined with TS (b).

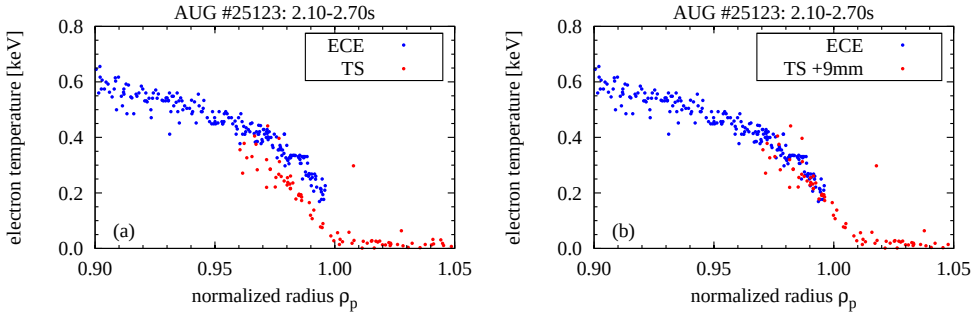

Figure 5.10: Example of diagnostic alignment with ECE and TS at AUG. The measurements of the electron temperature directly after mapping onto ρ_p (a) and with a 9 mm shift of the TS diagnostic (b).

temperature and density at the same position and is not influenced by mapping, toroidal symmetry or position in machine coordinates. This allows to align all temperature and density measurements. This is crucial to determine the pedestal pressure. In Figure 5.9 the shifts between ECE, Li-beam (LIN) and TS are plotted for the AUG database. The mean value of the shift between ECE and TS is 8 ± 2 mm, between LIN and TS it is 11 ± 3 mm and this gives a shift between LIN and ECE of 3 ± 3 mm. It has to be noted that within the AUG data set no systematic dependency between the global plasma parameters and the diagnostic shift was observed. The 1σ-error does seem to have its source only in the uncertainty of aligning the diagnostics.

The procedure to align the diagnostics was done manually. Several automated techniques were tested, however, none could guarantee a satisfactory low error rate. An example for the alignment is given in Figure 5.10, directly after the mapping onto ρ_p coordinates (a) the ECE and TS diagnostic measure the steep gradient region at different radii. The aligned profile (b) is obtained by applying a 9 mm radial shift to the TS diagnostic in R, z coordinates and then repeat the mapping to ρ_p. In the case of the electron temperature the alignment is done by matching the measurements in the upper pedestal region, because, the ECE generally does not provide measurements of the plasma temperature at the separatrix. For the density measured with the Li-beam and the TS also the profile shape at the separatrix should be included in the alignment procedure. The absolute density value of the TS has uncertainties in the calibration of around 20%, therefore, these uncertainties would be transfered to the diagnostic shift when only the steep gradient region is used for the alignment. This is

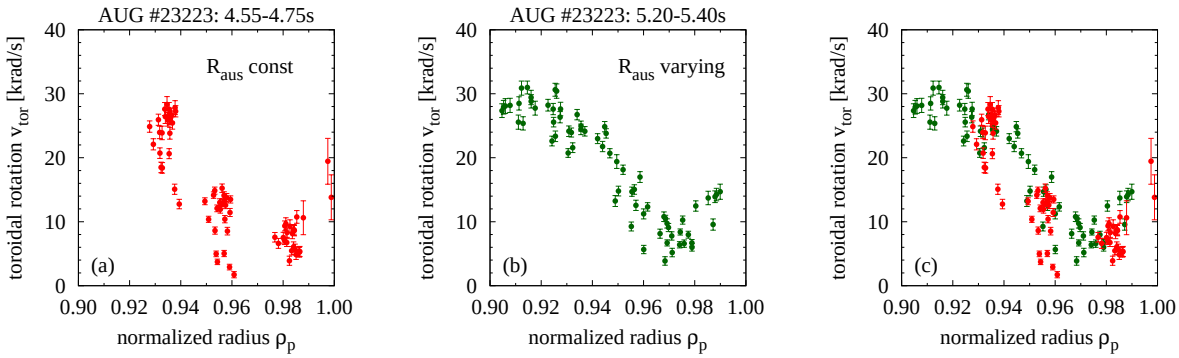

Figure 5.11: Effect of an R_{aus} scan on the toroidal rotation measurement with the CXRS system. With constant outer radius (a), varying outer radius (b) and both cases as comparison (c).

ommitted when the value and position of the pedestal bottom can be utilized for an alignment of these diagnostics. A detailed discussion on the profile shape at the separatrix is found in Section 7.1.

5.2.3 R_{aus} Scan

At AUG the so called R_{aus} scan is an important tool to improve the radial coverage of edge diagnostics. Diagnostics generally view fixed positions in the plasma with a limited number of lines of sight. With a shift of the whole plasma column new virtual lines of sight are created. The improved radial coverage can also lead to better radial resolution, however, not better than the limits of the diagnostic itself as discussed in Section 4.7. One example where the radial resolution is improved is shown in Figure 5.11 with the toroidal rotation measured with the CXRS system described in Section 4.5. When the plasma column is not moved and R_{aus} is constant (Figure 5.11 (a)) the different diagnostic channels are separated from each other. With only this measurement one could think of a monotonously decreasing rotation with smaller gradients at larger radii. However, with movement of the plasma column in (b) and the information of additional lines of sight this is proven wrong. The rotation shows a real minimum at around $\rho_{\mathrm{p}} = 0.97$ and the gradient is increasing up to this radius rather than decreasing. In (c) both cases are plotted together for better comparison. In this example R_{aus} was scanned over about 1.5 cm which corresponds roughly to the spacing between the diagnostic channels.

At AUG the R_{aus} scans are included in many discharges routinely and typically consist of an R_{aus} movement from 2.14 m to 2.16 m and back to 2.14 m in 600 ms. The pendant at DIII-D is called breathing and results in roughly 1 cm movement of the outer plasma radius. The majority of the time slices analysed for the database include scans of R_{aus}. In [26] it was suggested that the plasma edge is significantly perturbed by moving the plasma column. For the database in this work each R_{aus} scan was divided in intervals of 150 ms and then the intervals were compared to each other. No systematic deviation in the pedestal parameters derived from the different intervals could be identified. The major difference in the two approaches was the use of individual measurements in [26] and the composite profiles of the present work. The analysis, which showed no systematic impact of the R_{aus} scan in

a_0	pedestal top position
a_1	pedestal top value
a_2	inner slope
a_3	pedestal gradient

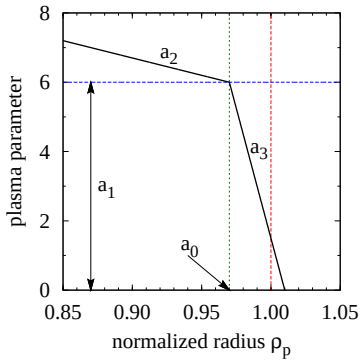

Figure 5.12: Coefficients determined with the two-line method. The vertical red line corresponds to the separatrix which is not determined with Eq. (5.6)

the database, and the improvement of the profiles, as seen in Figure 5.11, suggest that the use of R_{aus} scans is beneficial for the analysis of pre ELM H-mode plasmas.

5.3 Pedestal Characterisation

The characterization of the pedestal in several parameters is important for the comparison of a large number of experiments. In a direct comparison of measurements it is possible to describe differences of profiles by plotting them into the same figure. With a larger data set such a method reaches its limits very fast. Therefore, the pedestal is characterised by its top value, the gradient and the width of the steep gradient region. With these 3 values also large sets of data are easily compared.

In the course of long years of H-mode research several different approaches have been used to describe the pedestal. These methods have strongly evolved with the improvement of plasma edge diagnostics. Often the pedestal top value is defined as the outer most measurement position of a core plasma diagnostic. This is convenient for crude comparisons. However, in many cases plasma core diagnostics are not optimised for the small spatial scales in the pedestal and can systematically deviate from edge-optimised diagnostics. The outer most channel is not necessarily located at the pedestal top and therefore might be influenced by physics which is not affecting the pedestal directly. A definition for the pedestal top might be arbitrarily chosen to be certainly outside of the steep gradient region for example $T_{\mathrm{e,ped}} = T_{\mathrm{e}}(\rho_{\mathrm{p}} = 0.9)$ while the pedestal top measured with edge diagnostics might lie at $\rho_{\mathrm{p}} = 0.95 - 0.98$. Other approaches involve a functional form to describe the pedestal. Three of these methods are described in the next sections and are compared in detail.

5.3.1 Two-Line Method

The two-line method allows to determine the parameters which characterise the pedestal. This method utilises the shape of the pedestal. In particular, the definition that the pedestal is the steep gradient region at the plasma edge. The beginning of the steep gradient zone lies at the pedestal top. Therefore, the gradient changes significantly at the pedestal top. In

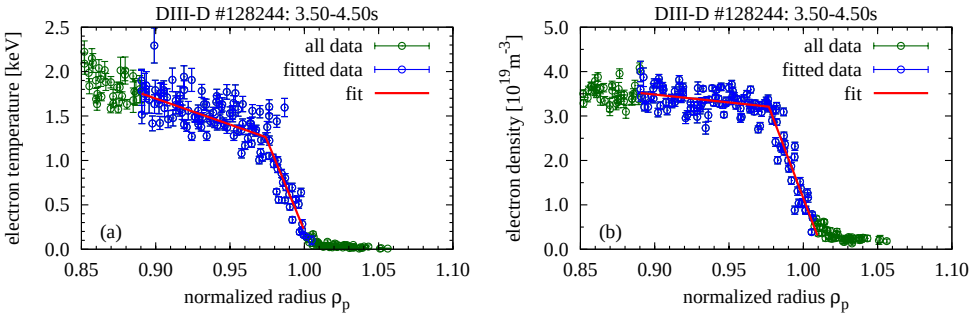

Figure 5.13: Example for two-line fits to experimental data of temperature (a) and density (b).

order to define this position it is convenient to use a bi-linear fit with two different slopes and one intersection

$$f(x) = \begin{cases} a_2(a_0 - x) + a_1 & \text{for } x \leq a_0 \\ a_3(x - a_0) + a_1 & \text{for } x > a_0 \end{cases} \tag{5.6}$$

where the pedestal top position a_0 and value a_1 are free parameters along with the inner slope a_2 and the mean pedestal gradient a_3. A sketch to illustrate this function is given in Figure 5.12. This figure also shows that the pedestal width is not determined directly by Eq. (5.6). While pedestal top and gradient are directly accessible via fit coefficients, the pedestal width can only be determined with additional information. In this work the definition of the pedestal width is from pedestal top up to the separatrix x_{sep}, the separatrix is indicated by the vertical red line in Figure 5.12. The width of the pedestal Δ is then $x_{\text{sep}} - a_0$. How the separatrix position is determined is described in Section 7.1. The definition of the pedestal width as used for the presented work is different to studies which used a similar bi-linear method. For example at JT60-U the pedestal width was defined as $\Delta = a_1/a_3$ [83]. In Figure 5.13 the two-line method was applied to temperature (a) and density (b) edge data from DIII-D. It is also shown that the data for the fit is restricted, only the blue measurements are used to determine the pedestal parameters. In practise the last 20% of the plasma radius in Ψ_{N} ($\rho_{\text{p}} > 0.89$) turned out to be a reasonable choise for the two-line method. The inner limit of the definition regime is not very crucial and can be varied depending on positions of diagnostic channels. The fit depends strongly on the outer limit of the definition regime namely the separatrix. Therefore, the separatrix position has to be determined accurately which will be discussed in more detail in Section 7.1.

5.3.2 MTanh Method

The mtanh method gives a possibility to fit a smooth function through the pedestal, plasma core and SOL. The pedestal parameters are derived from the symmetry of a modified hyperbolic tangent function which is used to fit experimental data. The modification applied to the hyperbolic tangent are polynomials which are added to fit core and SOL plasma. Several definitions are possible for the mtanh function, one for example is given in [84]. The version

a_0	SOL value or offset
a_1	pedestal top value
a_2	symmetry radius
a_3	half width
a_4-a_6	core polynomial
a_7-a_9	edge polynomial

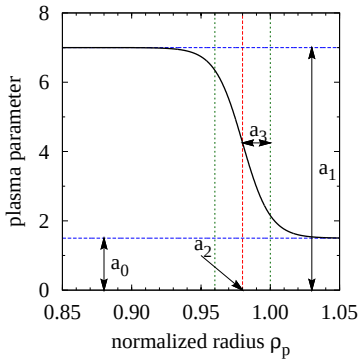

Figure 5.14: Coefficients of mtanh function. The definitions given on the left are not necessarily correct, see the text for details.

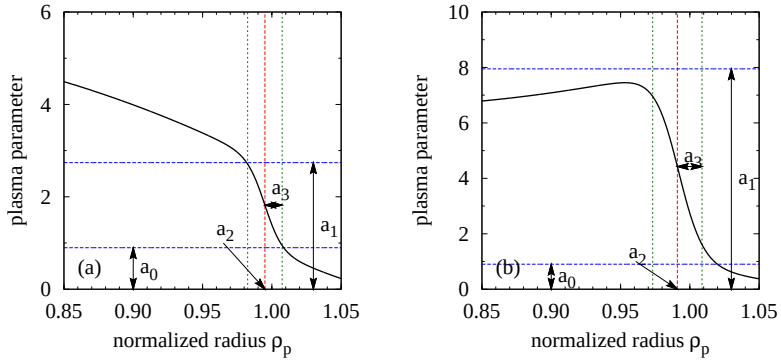

Figure 5.15: Two examples of mtanh fits to AUG density data. In the typical case (a) the coefficients a_n represent the definition as given in Figure 5.14. In a case with a hollow profile (b) the coefficients do not resemble their definition.

used for this work is implemented within the *augped*-program by L. D. Horton

$$f_{\mathrm{mtanh}}(z) = \frac{a_0 + a_1}{2} + \frac{a_1 - a_0}{2} \times \frac{\left(1 + a_4 z + a_5 z^2 + a_6 z^3\right) e^z - \left(1 + a_7 z + a_8 z^2 + a_9 z^3\right) e^{-z}}{e^z + e^{-z}}, \tag{5.7}$$

with $z = (a_2 - x)/a_3$. The meaning of the coefficients a_n is illustrated in Figure 5.14. In the representation without polynomials for the plasma core and the SOL, the pedestal width, as indicated by the dashed green lines, is not correlated to the pedestal top and bottom values which are highlighted with broken blue lines. In general the polynomials can be included up to 3rd order. However, for consistency with the analysis made at other machines (e.g. [84, 85, 54]) the polynomial for the core is included only to the 1st order, meaning $a_5 = a_6 = 0$. At DIII-D the SOL is often included only as offset, therefore, $a_{7,8,9} = 0$. For AUG this is not possible, because the density is still changing in the SOL, this requires at least $a_7 \neq 0$ but often also $a_8 \neq 0$. The standard setting is with polynomials only to the 1st order, therefore, $a_{4,7} \neq 0$ and $a_{5,6,8,9} = 0$.
The definition of the mtanh coefficients a_n as given in Figure 5.14 is not necessarily valid for all profiles. In Figure 5.15 a typical example (a) is shown, where the coefficient a_1 represents the pedestal top and the coefficient a_0 the SOL or pedestal bottom value (horizontal blue

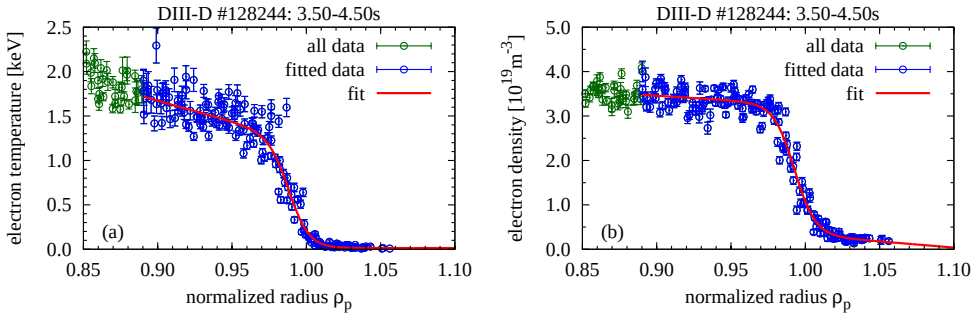

Figure 5.16: Example for mtanh fits to experimental data of temperature (a) and density (b).

lines). More importantly the pedestal width (vertical green lines) is defined by pedestal top and pedestal bottom. Other cases might also occur, like the example shown in (b), where the coefficient a_1 does not resemble the pedestal top at all. In order to avoid these mismatches, the definition for the pedestal top and bottom used in this work are: the pedestal top and bottom value are given by

$$v_{\text{pedtop}} = f_{\text{mtanh}}(+1) \tag{5.8}$$
$$v_{\text{pedbot}} = f_{\text{mtanh}}(-1), \tag{5.9}$$

this corresponds to $x = a_2 - a_3$ for the pedestal top and $x = a_2 + a_3$ for the pedestal bottom. In Figure 5.15 this is the intersection of the vertical green lines with the fit function. For typical cases this definition is equivalent with the one given in Figure 5.14. In other cases this definition helps to avoid using wrong values for pedestal top and bottom.

The radial range of the fit is important for the quality of the results. Similar to the two-line method it is not recommended to fit data over the whole radius. Although, it is possible to get a fair fit to all data when allowing 3rd order polynomials for the plasma core, the fit to the pedestal will loose quality. Due to the small spatial extent of the pedestal the contribution of the pedestal to χ^2 is negligible compared to the rest of the plasma. Therefore, it is not guaranteed that the fit resembles the pedestal at all. To avoid such problems the radial range for the fit has to be restricted to the plasma edge. A reasonable definition for the plasma edge are the last 20% of the poloidal flux - this corresponds to $\rho_{\text{p}} > 0.89$. An example where the mtanh fits the data nicely is given in Figure 5.16.

5.3.3 Filter Method

Most methods to determine the pedestal parameters use specific features in the profile shape. The change of the gradients is the most pronounced feature in the plasma edge profile related to the pedestal. The largest change of the gradients is found where the curvature becomes extremal. However, the scatter in the experimental data prevents direct determination of the profile curvature. Fitting the data with various functional forms helps to determine the profile shape. A different approach is to smooth the scattered data.

One possibility to smooth the data is to apply a low-pass filter. If the radial coordinate is interpreted as temporal coordinate the radially distributed data becomes a frequency signal. The scatter in the data corresponds to a high frequency component. The relevant low

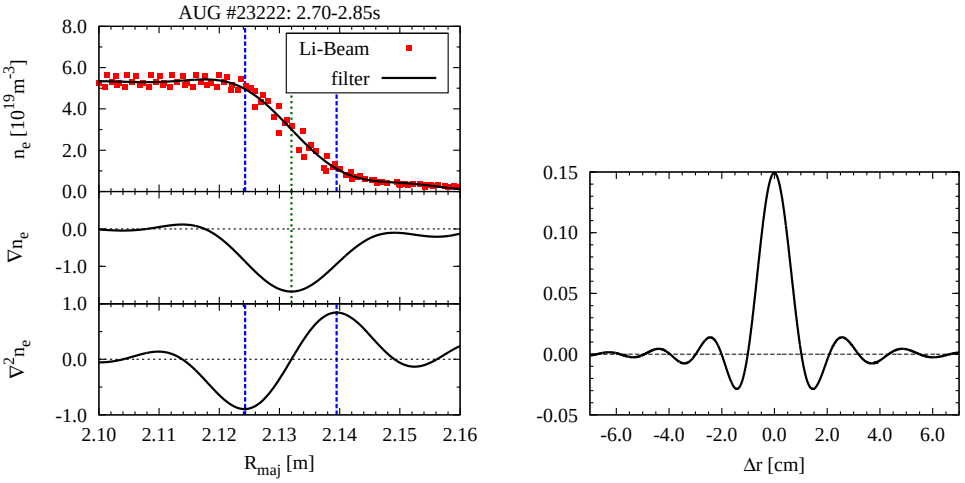

5.17.1: Example for data smoothing

5.17.2: Smoothing kernel in real space

Figure 5.17: Left: (top) electron density measurement and smoothed curve, (middle) gradient and (bottom) curvature derived from smoothed curve. The extrema in gradient and curvature are indicated with the dashed vertical lines. Right: Butterworth kernel in real space which was used to generate the smoothed curve.

frequency component can be extracted in frequency space with a low-pass filter. An example with a Butterworth frequency filter is shown in Fig. 5.17. Topmost in Fig. 5.17.1 density data from the Li-Beam diagnostic is shown with a smoothed curve for the pedestal region in AUG. Below the density profile the gradient and curvature are illustrated as derived from the smoothed profile, the vertical lines indicate pronounced features in the pedestal structure. Fig. 5.17.2 shows the smoothing kernel for this example, the FWHM of the central maximum is about 1.4 cm. The correct choice of this width is essential for useful curvature values. The curvature is declared as useful when it defines a clear pedestal top and pedestal bottom. The advantage of the frequency filtering is an optimal balance between a smooth curve and preserving the pedestal structure. In comparison, smoothing with a Gaussian kernel would not satisfy both needs. The information about gradients would be lost when optimising the kernel width for well defined curvature values. The pedestal top is defined as the point of extremal curvature which is located inside of the maximal gradient. The pedestal bottom also has extremal curvature but lies outside of the maximal gradient.

The low-pass filter method does not include uncertainties of individual data points. The scatter in the data must represent the uncertainties. Therefore, the low-pass filter method is more sensitive to outliers than least squares fitting which accounts for larger uncertainties of single data points. Without special treatment for outliers the resulting pedestal parameters will be wrong. For a Thomson Scattering measurement with individual uncertainties this means to set an upper threshold for the uncertainty which reduces the number of outliers. The filter method inherits no shape regularisation like the mtanh or two-line method. On the one hand, this will lead to large uncertainties when the data has a low spatial resolution. On the other hand, local parameters like the maximal gradient will be more accurate as separated regions in the edge do not influence each other. However, this is only true if the kernel width was chosen correctly. Therefore, the filter method is not adequate as a stand alone technique to analyse the pedestal. But in combination with knowledge of a good kernel width, obtained with the mtanh or two-line method, the filter method can provide

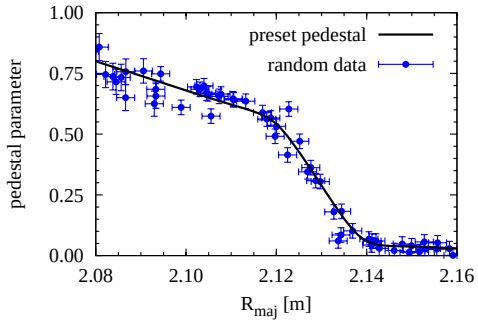

Figure 5.18: Example for an artificial pedestal profile. The preset pedestal profile is indicated with the solid black line. One set of corresponding random data is indicated with blue circles.

supplementary information about the pedestal structure. Using the advantages of more than one method improves the results of the analysis.

5.3.4 Benchmark

For the discussion of the results it is important to document the properties of the different methods to characterize the edge pedestal. Several tests were performed to assess these properties. First, the methods were applied to simulated data with known pedestal parameters and asymmetric profile shape. Second, real data was analysed for similar discharges where the pedestal parameters are expected to be unchanged. Further tests are presented which show comparison with individual discharges and the whole database.

5.3.4.1 Tests on Simulated Profiles

The simulated pedestals are setup with three regions of constant, but different, gradients and continuous transitions between the regions. The profile is than described by 7 parameters, the three gradients and position and value for the two intersections. The artificial data points are distributed normally around this curve. The standard deviation of the data points is 7% in vertical and 2 mm in radial direction. These values are chosen to resemble typical measurements at AUG. An examplary artificial pedestal profile is illustrated in Figure 5.18. One simulation consists of 500 profiles with the same properties but randomly scattered data points. Multiple simulations are selected to test and document the influences of asymetries in the pedestal. The parameters of each pedestal - top, width, gradient - are determined with the three methods: two-line, mtanh and filter. This gives one mean value with a certain standard deviation for each simulation, method and pedestal parameter.
In Figure 5.19 the results of three tests are shown. For each pedestal parameter the relative deviation from the set value is illustrated. The set value is of no real importance since it was arbitrarily chosen to match the definition of the two-line method. Therefore, a constant offset from the set value only illustrates the differences with the two-line method. Of interest are the variations in the parameters found with one method within a given test, where one or more of the set values were fixed. In the first test, shown in the first column of Figure 5.19, the pedestal itself is unchanged and only the core gradient is varied. A temperature profile is generally more peaked than the density profile. Therefore, a core gradient in arbitrary

units of $1-5$ would correspond to a density like profile and $6-12$ to a temperature or pressure like profile. The filter and two-line method are not influenced by the change of the core gradient. The mtanh method reproduces the pedestal width accurately. However, it shows a clear variation of about 20% in pedestal top and gradient, although, these parameters were the same in these simulations. This is likely a result of the point symmetry of the hyperbolic tangent function. Because of its symmetry the mtanh's ability to fit asymmetric profiles is diminished. Although, the additional polynomials in the mtanh should cope with assymetries, they do not resolve the problem completely.
A second test is shown in the middle column of Figure 5.19. Again the pedestal width is kept constant but the pedestal top value and consequently the pedestal gradient is varied. Filter and two-line method yield constant width and can follow the variation in the pedestal top. The mtanh method reproduces the pedestal parameters well unless the ratio of pedestal gra-

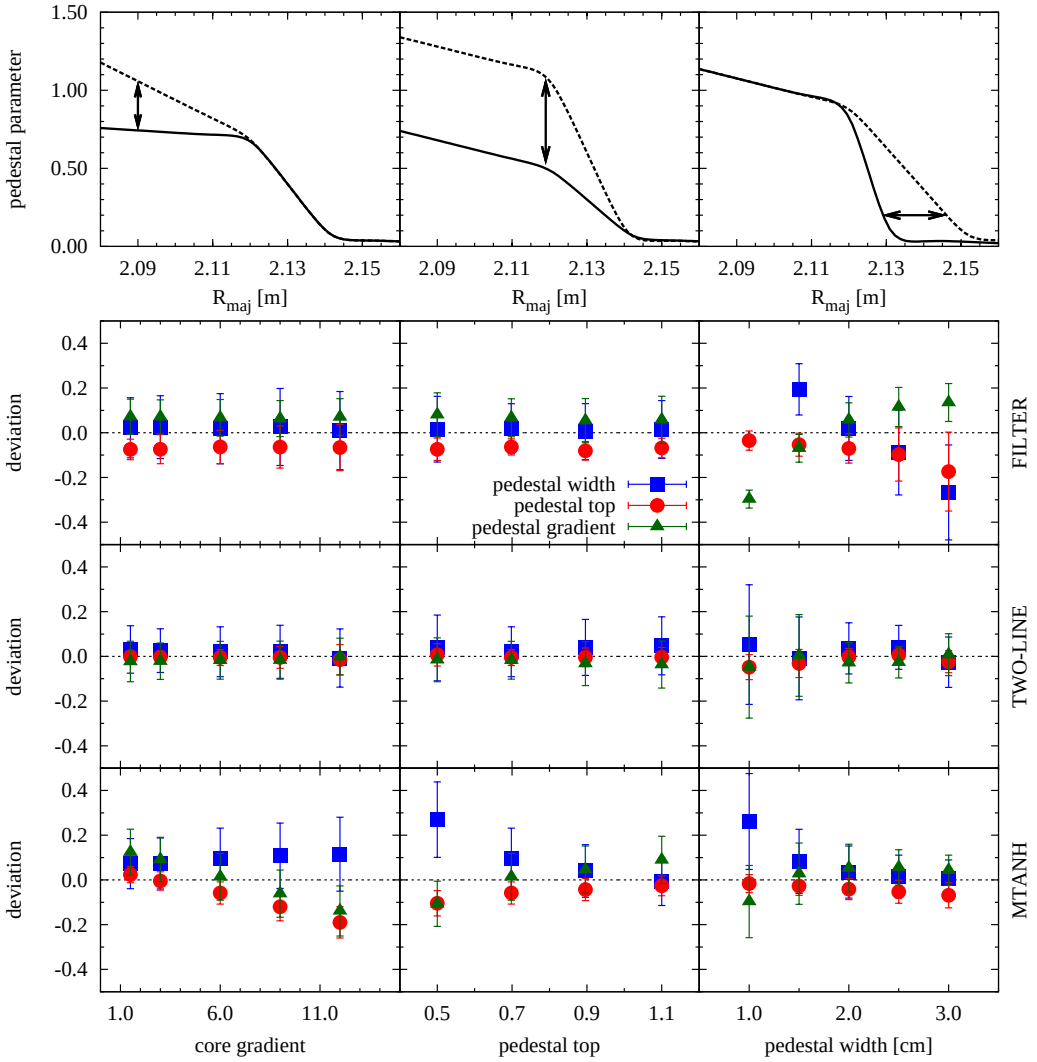

Figure 5.19: In the top row a sketch illustrates how the pedestal is varied during each simulation. In the lower three rows the results of the pedestal simulation are shown. The relative deviation of mtanh (bottom), two-line (middle) and filter method (top) from preset properties is indicated for the pedestal width (blue, square), the pedestal top (red, circle) and the pedestal gradient (green, triangle). In the left column only the gradient inside of the pedestal top is varied, while the whole pedestal is unchanged. In the middle column pedestal top and gradient are varied, while the pedestal width is unchanged. In the right column pedestal width and gradient are varied, while the pedestal top is unchanged.

dient and core gradients becomes small. This is visible when low pedestal top values (small pedestal gradients) are compared to large pedestal top values. The mtanh method finds a 25% variation of the pedestal width, although, the width was not varied in the parameter scan.
In the third column pedestal width and gradient were varied. Pedestal top and core gradient were set to values where all three methods showed good results before. The pedestal parameters determined with two-line and mtanh are in good agreement with each other for widths larger than 1.5 cm. The large relative deviation for the case with 1.0 cm pedestal width is due to the finite radial resolution in the simulation. The filter method does not give useful results as stand-alone method, as expected. Therefore, the width of the kernel has to be chosen appropriately, an appropriate width can be obtained with one of the other methods.

In summary, the simulation covered a variety of different possible pedestal shapes and the two-line and mtanh methods were found to agree within 10% in the pedestal parameters for most cases. The radial scatter of the data points in the simulation was normally distributed with a standard deviation of 2 mm. This scatter is represented by the error bars of pedestal width and gradient in Figure 5.19. In this case the pedestal width cannot be determined to better than ±3 mm.

5.3.4.2 Tests on Experimental Profiles

In real measurements the conditions are not so predefined as in a simulation. In order to get useful statistics an AUG standard scenario with plasma current 1 MA, toroidal field 2.5 T, heating power 6 MW and gas puffing $1.2 \cdot 10^{22}\mathrm{s}^{-1}$ was chosen to compare the two-line and the mtanh method. The pedestal width determined with the two-line method depends on the pedestal top and the separatrix position. The separatrix position has to be determined separately as described in Section 7.1. For this series of over 50 independent time slices in different discharges reproducible pedestal parameters are expected. The profiles were analysed with both methods. The mtanh model yielded a mean width $\Delta_{ne} = 1.8$ cm with a standard deviation of 0.8 cm, a pedestal top density $n_{\mathrm{e,ped}} = (7.6 \pm 0.9) \cdot 10^{19}$ m^{-3}, a temperature pedestal width $\Delta_{T\mathrm{e}} = (1.9 \pm 0.5)$ cm and $T_{\mathrm{e,ped}} = (0.38 \pm 0.09)$ keV. The results for the two-line method were $\Delta_{ne} = (1.7 \pm 0.2)$ cm, $n_{\mathrm{e,ped}} = (6.9 \pm 0.5) \cdot 10^{19}$ m^{-3}, $\Delta_{T\mathrm{e}} = (1.7 \pm 0.3)$ cm and $T_{\mathrm{e,ped}} = (0.43 \pm 0.03)$ keV. Within the uncertainties both methods result in the same pedestal parameters. However, the two-line method shows significantly reduced scatter. In Figure 5.20 this discharge set is illustrated with a histogram. The pedestal width determined with the two-line method shows a narrower and more peaked distribution for the electron temperature (a) than for the mtanh method. Both methods yield a very similar distribution for the density pedestal width (b), however, the mtanh method produces a number of outliers with $\Delta_{ne} > 2.0$ which increase the standard variation. The observation made with real discharges shows a similar scatter as was observed in the artificial test Section 5.3.4.1. In particular, the comparison of the scatter in the temperature and density width. When ignoring the outliers in Δ_{ne} with the mtanh method, the scatter is comparable to the 10% obtained with the two-line method. For $\Delta_{T\mathrm{e}}$ the mtanh method yields an appreciably larger scatter of about 25%. The same observation is made in the simulation when varying the core gradient from a density like profile (1 in [a.u.]) to a temperature like profile (10 in [a.u.]) as shown in Figure 5.19 in the bottom left plot. There the scatter also increases from 10% to 20% only due to a change in the symmetry of the profile.

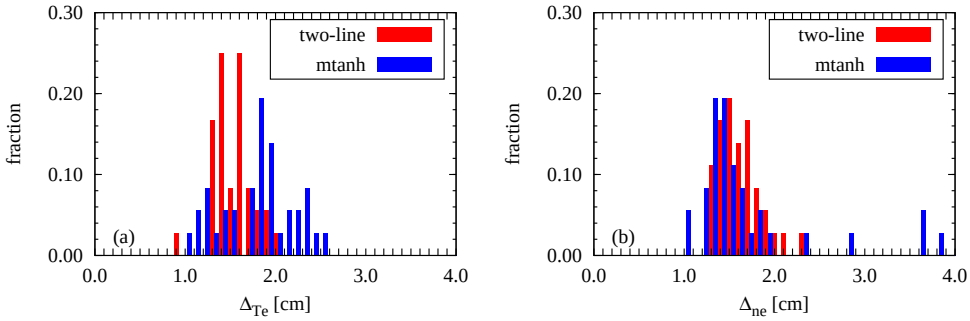

Figure 5.20: Histogram of pedestal widths of electron temperature (a) and electron density (b) for an AUG standard scenario. The width is determined with two different methods: two-line (red) and mtanh (blue).

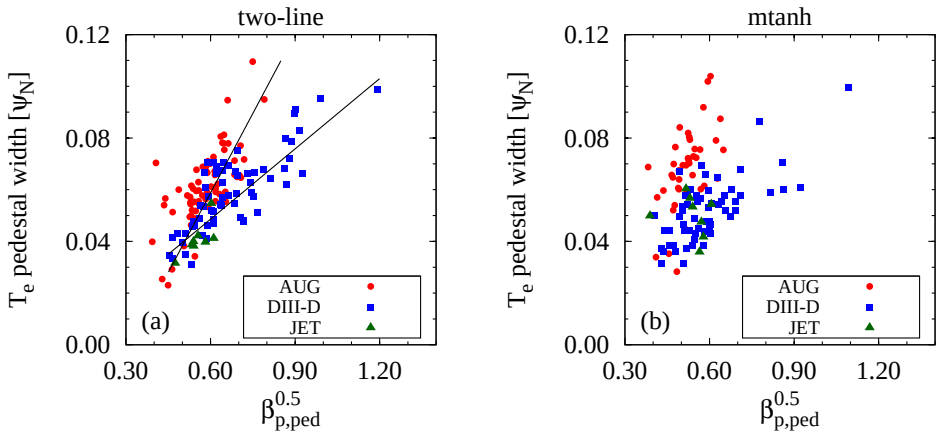

Figure 5.21: The pedestal width in normalized poloidal flux plotted against the normalized poloidal pedestal pressure $\beta_{p,ped}$. The pedestal parameters were determined with the two-line (a) and mtanh (b) method.

A different approach to compare the methods characterizing the pedestal region, is with a database of different discharges. In this approach the difficulty arises that physics related changes can occur at the same time as method related changes. Therefore, the scatter in the data could increase for two different reasons: the uncertainty due to the applied method or simply a wrong model was used to describe the data. A plot from Chapter 7 with the two-line method was remade with the mtanh method. In Figure 5.21 the comparison shows that in general the same trends are obtained with both methods. However, the data obtained with the two-line method (a) shows a separation of the DIII-D data into two branches, one branch which matches the AUG data and another which shows a different slope. The larger scatter, in the case with the mtanh method (b), does not allow to resolve these details in the data. The second comparison shows two regressions to the pedestal width data in Figure 5.22. The resulting regression coefficients are fairly similar, however, the scatter in the data described by the root mean square error RMSE (see Eq. (5.13)) is significantly larger in the case where the mtanh method was applied to the data (b).

As last example three very similar discharges from DIII-D were chosen. The measurements with the TS diagnostic show a pronounced pedestal. All methods should give optimal

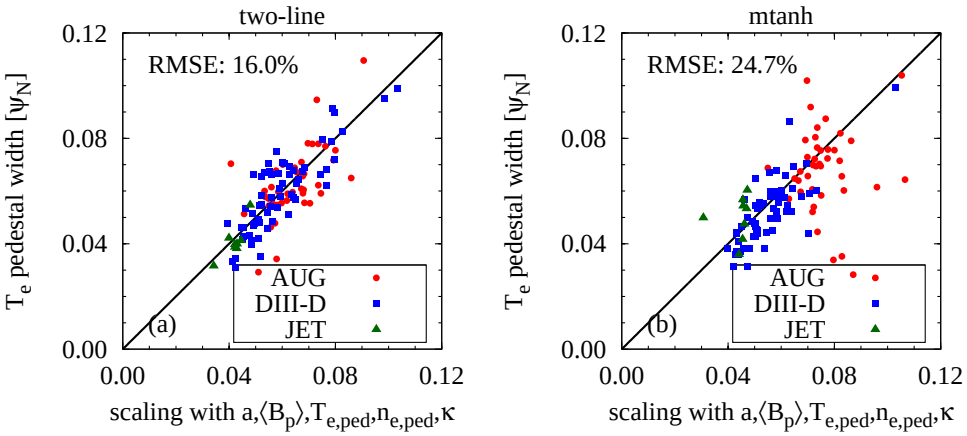

Figure 5.22: The pedestal width in normalized poloidal flux fitted with several parameters in a log-linear regression. The pedestal parameters were determined with the two-line (a) and mtanh (b) method.

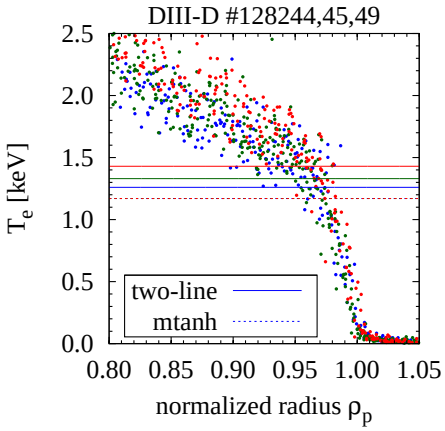

Figure 5.23: Electron temperature pedestal of three discharges with only small differences in heating power (#128244: 7.1 MW - blue, #128245: 7.6 MW - green, #128249: 8.1 MW - red). The pedestal top values obtained with the two-line method are indicated as solid line and the ones of the mtanh method as dashed line.

results. This allows to get an impression of the accuracy of the methods. Besides the heating power, the discharge settings were identical for the 3 discharges. The heating was increased in steps of 0.5 MW from 7.1 MW to 8.1 MW. In Figure 5.23 the electron temperature of these discharges is plotted at the plasma edge. The electron temperature is only increasing a little at the plasma edge, but the red case with 8.1 MW shows clearly a higher T_e than the blue case with 7.1 MW. The green case with 7.6 MW lies in between the other two. The pedestal analysis with the two-line method can follow this trend nicely, as indicated with the solid lines in Figure 5.23 which mark the pedestal top value. The mtanh method does not allow to resolve this trend, for all three different heating levels the same pedestal top temperature is obtained (dashed line).

To summarize, different tests were performed to assess the quality of the results with the different methods. The results of this comparison suggest that the characterisation of the pedestal with the two-line method, without the shape regularisation imposed by the

hyperbolic tangent function, gives the more accurate representation of the pedestal parameters. Therefore, the two-line method will be used to determine the pedestal parameters throughout this thesis.

5.4 Log-Linear Data Regression

The concept of a data regression helps to identify correlations between a quantity of interest and multiple other parameters. A quantity often depends on more than one parameter. One approach to study a certain dependence would be to vary one parameter and keep all other parameters constant. However, this is not always possible. In the case of the present study there was not enough dedicated experimental time available to conduct studies for all the parameters in question, but a large amount of data from other discharges was accessible. Therefore, a regression was applied in order to extract parameters which influence the quantity of interest.
A linear regression is based on the equation

$$\boldsymbol{q} = \text{const} + c_0\boldsymbol{p_0} + c_1\boldsymbol{p_1} + \ldots + c_\text{n}\boldsymbol{p}_\text{n} \tag{5.10}$$

with the quantity vector $\boldsymbol{q}$, parameter vectors $\boldsymbol{p}_\text{n}$ and coefficients c_n. A standard regression algorithm uses a least square method to find the optimal values for c_n to fulfill Eq. (5.10). For $n = 0$ the regression is reduced to a linear fit with offset. When the dependence between $\boldsymbol{q}$ and $\boldsymbol{p}_\text{n}$ is not additive it is often useful to use a power law

$$\boldsymbol{q} = \text{const} \cdot \boldsymbol{p_0}^{e_0}\boldsymbol{p_1}^{e_1} \ldots \boldsymbol{p}_\text{n}^{e_\text{n}}. \tag{5.11}$$

Taking the logarithm of Eq. (5.11) transforms the power law into a linear Equation

$$\ln \boldsymbol{q} = \ln \text{const} + e_0 \ln \boldsymbol{p_0} + e_1 \ln \boldsymbol{p_1} + \ldots + e_\text{n} \ln \boldsymbol{p}_\text{n} \tag{5.12}$$

which can be solved with a linear regression algorithm.
The quality of a regression is quantified with the relative root mean squared error RMSE(%)[44]

$$\text{RMSE}(\%) \equiv 100 \cdot \sqrt{\frac{1}{N-1}\sum_{j=1}^{N}\left(\ln q_{\text{exp}_j} - \ln q_{\text{mod}_j}\right)^2} \tag{5.13}$$

where N is the number of experiments used in the regression. The RMSE is a degree for how much the experimental values $\boldsymbol{q}_\text{exp}$ deviate from the model values $\boldsymbol{q}_\text{mod}$ and is used to compare the fit quality between different sets of data or different models for the same data set. Besides physics reasons there are a couple of rules applied in the search for the best model to describe a quantity with a certain number of parameters. The fit of the data should become better the more parameters are allowed in the model. However, the best model describes the data with the least parameters and still has the lowest possible RMSE(%). Therefore, parameters with exponents less than 2σ or an improvement of less than 5% of the RMSE are discarded as insignificant in this study.

When working with regression analysis, correlations between different parameters can become a problem and adulterate the results. One way to identify the impact of correlations between parameters is to alternate their use in the regression. A strong hint for correlated

parameters is when after adding a further parameter the exponents change significantly while the RMSE does not. A trivial example for a correlation in the database is the minor and the major radius which have a correlation of 0.82. Including both can result in bad scalings, as:

$$T_{\mathrm{e,ped}} = 0.3969 \cdot P_{\mathrm{heat}}^{0.64} n_{\mathrm{e,ped}}^{-0.97} I_{\mathrm{p}}^{0.79} a^{-1.25} \qquad \text{RMSE: } 13.3\% \qquad (5.14)$$

$$T_{\mathrm{e,ped}} = 0.0049 \cdot P_{\mathrm{heat}}^{0.42} n_{\mathrm{e,ped}}^{-0.77} I_{\mathrm{p}}^{1.04} a^{-4.85} R_{\mathrm{mag}}^{3.62} \qquad \text{RMSE: } 14.9\% \qquad (5.15)$$

Here the RMSE is even increased by adding a further parameter, still both scalings fit the given data set reasonably well. In particular, do the exponents of a and R_{mag} give the same result for both scalings, since with the correlation $a = \epsilon R_{\mathrm{mag}}$ follows $a^{-4.85} R_{\mathrm{mag}}^{3.62} = a^{-1.23} \epsilon^{-3.62}$ and with $\epsilon \sim 0.3$ one gets $\epsilon^{-3.62} \sim 0.3969/0.0049$. However, the scaling which includes both correlated parameters a and R_{mag} will only fit to data with a single aspect ratio ϵ and will be wrong when the aspect ratio changes. Therefore, possible correlations within the database are discussed in detail for every regression analysis. The correlation matrix for the main parameters can be found in Section 6.

Chapter 6

Database

This section introduces the principle of a database approach to study parameter dependencies. Different dimensionless *physics* parameters are introduced along with engineering parameters. The engineering parameters are in principle controlled in the discharge setup but always restricted by machine design. The database used throughout this work will be described in terms of these parameters. A special focus is put on the plasma shape in a separate section.

The present study tries to pursue the progress in understanding the pedestal physics. This is done by identifying the main parameters responsible for changes in the pedestal of AUG, DIII-D and JET. The pedestal is characterised for all devices with the two-line method as described in Section 5.3.1. This study includes discharges from other studies [86, 27, 54] which are extended with new experiments from AUG including a current and triangularity scan. The main difference between this and previous studies is the database approach. In the studies listed above dedicated experiments were performed in order to study the influence of a single parameter on the pedestal. This was generally done in carefully designed similarity experiments or parameter scans. As a result precise information of one parameter was obtained. In consequence, the information about other parameters and their correlations is not easily explored in these experiments. In particular, this is true for the plasma shaping which is generally matched in comparison experiments. It will be shown in Section 6.3 that for the present data set the shaping factor q_{95}/q_{cyl} plays an important role and cannot simply be expressed in terms of geometrical shaping parameters or the normalized pressure. The database approach for analysing experiments might come at the expense of obscuring dependencies which do not appear statistically significant in the data set. Another uncertainty is included by influences on the plasma which are difficult to quantify, like e.g. gas fuelling patterns, impurity content or radiation characteristics. Those influences can be reduced in dedicated experiments but not in a database approach. One very important advantage of the database approach is the amount of experimental time needed. Single parameter studies need a lot of experimental time. With the database approach it is possible to include measurements from various experiments which might aim at different results. The use of other experiments is also possible when no precise requirements on plasma shape and gas fuelling are required. In this thesis the database approach is chosen because of the advantages, but its disadvantages have to be addressed in the discussions.
Before the database is described in detail, it is important to highlight one crucial aspect of the database approach. If a trend is observed between two or more parameters within

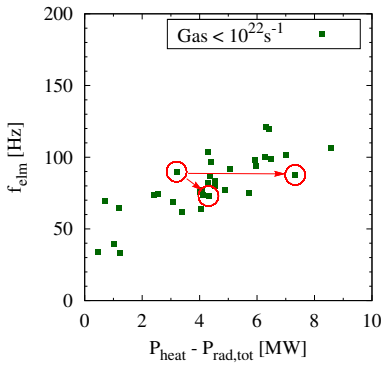

Figure 6.1: Copy of Figure 2.11 to illustrate how individual discharges can *break* a trend.

the database, this does not mean that every single discharge follows this trend. On the contrary, it will certainly be possible to find a discharge pair which seems to contradict this trend. One example can be taken from Section 2.1 and is shown again in Figure 6.1, where a trend of increasing ELM frequency with larger heating power is shown. There are also three discharges highlighted which do not follow the trend, when compared in pairs. The first example includes a doubling of the heating power but no change in the ELM frequency. The second example shows a decreasing ELM frequency for larger heating power. There might be different reasons for such an observation: first, it could be the result of measurement uncertainties and therefore, only a statistical effect. Second, the model - here $P_{\mathrm{heat}} - P_{\mathrm{rad,tot}}$ - used to describe a parameter - here f_{elm} - is not complete. Other parameters still play an important role and can explain deviations from the trend.
In the database approach two types of parameters can be distinguished: the parameters documented in the database and the parameters not documented in the database. The goal of a database approach is to document as many of the relevant parameters as possible and then identify trends between these parameters which allow to draw conclusions about the physical processes in the plasma. At the same time, the influences on the plasma, which could not be documented, have to be discussed.

The parameters documented in the database are discharge settings and plasma properties. The plasma properties are the pedestal characteristics, determined with the two-line method for electron temperature T_{e}, ion temperature T_{i}, electron density n_{e} and electron pressure p_{e}, and equilibrium information, such as flux compression $\partial\Psi/\partial R$, safety factor at q_{95}, radius of the magnetic axis R_{mag}, minor radius a, triangularity δ or elongation κ. The discharge settings are the plasma current I_{p}, toroidal magnetic field B_{t}, heating power P_{heat} and external gas puffing. To some extent the discharge settings could also include equilibrium information, like the plasma shape, however, it will be discussed in Section 6.3 why the classification into plasma properties is also valid. A third group of parameters consists of derivations of parameters from the first two groups. A list of the ranges for the main parameters, available from the three machines AUG, DIII-D and JET, is given in Table 6.1. Most of the key parameters have a range of over a factor of three within the database and the pedestal characteristics range over a factor of 5-16. The database lacks a variation of aspect ratio $\epsilon = a/R$, has only a small variation of the elongation κ and also a limited range of machine size. The correlations between these parameters is discussed in Section 6.1. The derived dimensionless parameters $\rho_\star$, β and $\nu_\star$ are described in the next paragraphs.

A typical length in the plasma is the normalized toroidal Larmor radius $\rho_\star$ which is the

		AUG	DIII-D	JET	range
Nb. data		69	64	8	Σ141
I_p	[MA]	0.60-1.15	0.5-1.5	1.7-2.7	x5.4
$\langle B_\mathrm{p}\rangle$	[T]	0.18-0.34	0.12-0.37	0.27-0.40	x3.3
B_t	[T]	1.8-2.8	0.7-2.1	1.8-2.7	x4
$p_\mathrm{e,ped}$	[kPa]	1.8-9.7	0.8-11.8	3.2-12.7	x16
P_heat	[MW]	2.6-13.7	1.3-14.6	5.2-17.3	x13
a	[m]	0.47-0.51	0.52-0.61	0.89-0.91	x1.9
R_mag	[m]	1.70-1.74	1.75-1.86	3.02-3.09	x1.8
q_{95}		3.4-7.2	2.7-13.4	3.4-3.6	x5
q_{95}/q_cyl		1.23-1.45	1.11-1.89	1.16-1.22	x1.7 (8)
$T_\mathrm{e,ped}$	[keV]	0.2-0.9	0.2-2.1	0.5-0.9	x10
$T_\mathrm{i,ped}$	[keV]	0.3-1.0	0.3-1.5	-	x5
$n_\mathrm{e,ped}$	$[10^{-19}\mathrm{m}^{-3}]$	3.7-7.2	1.2-6.1	3.9-9.3	x8
κ		1.59-1.74	1.69-1.88	1.74-1.78	x1.2 (1.5)
δ		0.21-0.42	0.20-0.64	0.40-0.43	x3
$\rho_\star$	$[10^{-3}]$	3.5-6.9	5.0-14.3	3.7-5.4	x4
$\nu_\star$		0.30-3.4	0.1-0.8	0.4-0.9	x34
$\beta_\mathrm{t,ped}$	$[10^{-3}]$	2.4-12.0	3.7-18.3	5.6-15.0	x8
$\beta_\mathrm{p,ped}$		0.15-0.54	0.21-1.4	0.23-0.37	x9
Gas		D	D	D	

Table 6.1: Range of key plasma parameters in the database of the three machines AUG, DIII-D and JET. The last column indicates the range available the parameter spans for the three machines.

fraction of minor radius occupied by one ion gyroradius. $\rho_\star$ is important for turbulence and therefore transport physics. Different theories can be distinguished by their different dependence on $\rho_\star$. Examples were given in Chapter 3. The Lamor radius $\rho_\mathrm{i,L}$ is determined from the particle energy and its cyclotron frequency. With it $\rho_\star$ becomes

$$\rho_\star = \frac{\rho_\mathrm{i,L}}{a} = \frac{m_\mathrm{i} v_\perp}{a q_\mathrm{i} B_\mathrm{t}}, \tag{6.1}$$

with the particle velocity $v_\perp^2 = 2eT_\mathrm{i}/m_\mathrm{i}$ and the ion charge q_i. Since only deuterium plasmas are considered in this thesis $\rho_\star$ can be calculated at the pedestal

$$\rho_\star = 0.00646 \frac{T_\mathrm{i,ped}^{0.5}[\mathrm{keV}]}{a[\mathrm{m}] B_\mathrm{t,ped}[\mathrm{T}]}. \tag{6.2}$$

The edge toroidal field is calculated as $B_\mathrm{t,ped} = B_\mathrm{t0}/(1+\epsilon)$. Throughout this thesis two versions of $\rho_\star$ will be used: $\rho_{\mathrm{i}\star}$, which is equivalent to Eq. (6.2), and $\rho_{\mathrm{e}\star}$, which is the ion Larmor radius calculated with $T_\mathrm{i,ped} = T_\mathrm{e,ped}$. Introducing $\rho_{\mathrm{e}\star}$ is only necessary because for some discharges no $T_\mathrm{i,ped}$ measurement is available and the approximation $T_\mathrm{i,ped} = T_\mathrm{e,ped}$ is applied.

The normalized pressure β is defined as the ratio of kinetic pressure p and magnetic pressure $B^2/2\mu_0$. It is often used as a measure for the plasma performance. One often distinguishes between poloidal and toroidal magnetic pressures which leads to a toroidal

beta β_t and a poloidal beta β_p. For pedestal physics the edge values $\beta_\mathrm{t,ped}$ and $\beta_\mathrm{p,ped}$ are used

$$\beta_\mathrm{t,ped} = \frac{p_\mathrm{ped}}{B^2_\mathrm{t,ped}/(2\mu_0)} = 0.00251\frac{p_\mathrm{ped}[\mathrm{kPa}]}{B^2_\mathrm{t,ped}[\mathrm{T}]} \tag{6.3}$$

$$\beta_\mathrm{p,ped} = \frac{p_\mathrm{ped}}{\langle B_\mathrm{p}\rangle^2/(2\mu_0)} = 0.00251\frac{p_\mathrm{ped}[\mathrm{kPa}]}{\langle B_\mathrm{p}\rangle^2[\mathrm{T}]} \tag{6.4}$$

$$\beta_\mathrm{ped} = \frac{p_\mathrm{ped}}{(\langle B_\mathrm{p}\rangle^2 + B^2_\mathrm{t,ped})/(2\mu_0)} = 0.00251\frac{p_\mathrm{ped}[\mathrm{kPa}]}{\langle B_\mathrm{p}\rangle^2[\mathrm{T}] + B^2_\mathrm{t,ped}[\mathrm{T}]} \tag{6.5}$$

where $\langle B_\mathrm{p}\rangle = \mu_0 I_\mathrm{p}/l_\mathrm{lcfs}$ is the flux surface averaged poloidal field, with l_lcfs as the length of the last closed flux surface.

The collisionality $\nu_\star$ or more precisely the ion collisionality $\nu_{\mathrm{i}\star}$ and the electron collisionality $\nu_{\mathrm{e}\star}$ are important quantities when comparing different experiments. The collisionality quantifies how important collisions are and therefore which neoclassical transport mechanism should be dominating [2]. The collisionality is the ratio of collision frequency ν and bounce frequency ω_b

$$\nu_{\mathrm{j}\star} = \frac{\nu_\mathrm{j}}{\epsilon\omega_\mathrm{bj}} \tag{6.6}$$

where $\mathrm{j} = \mathrm{e}, \mathrm{i}$ stands for electrons or ions. In other words the collisionality is the number of collisions a particle undergoes during the time it would need to complete one banana orbit. Unfortunately, plenty of different variants of Eq. (6.6) are published in literature. It should be noted that some of these definitions are wrong or at least not reproducible because the assumptions were not named. Therefore, the next paragraph focuses on a calculation of Eq. (6.6) with measured quantities and tries to name all assumptions and explain the evaluation of coefficients. The starting point are the characteristic collision times for electron-ion (e) or ion-ion (i) collisions $\tau_\mathrm{j} = \nu_\mathrm{j}^{-1}$ in a plasma with ions of charge Z as found in [2] in the Section about collision times.

$$\tau_\mathrm{j} = c_\mathrm{j}\frac{1}{Z^{\zeta_\mathrm{j}}\ln\Lambda}\frac{\epsilon_0^2 m_\mathrm{j}^{1/2} T_\mathrm{j}^{3/2}}{n_\mathrm{i} e^4} \tag{6.7}$$

where $c_\mathrm{i} = 12\pi^{3/2}$, $c_\mathrm{e} = 3(2\pi)^{3/2}$, $\zeta_\mathrm{i} = 4$, $\zeta_\mathrm{e} = 2$, the vacuum permittivity ϵ_0, the electron and ion temperatures T_i and T_e, the electron and ion mass m_i and m_e, the ion plasma density n_i and the Coulomb logarithm $\ln\lambda$. The Coulomb logarithm $\ln\lambda$ is the integral over collision impact parameters and the calculation can be found in [87], the results are also available in [2]

$$\ln\Lambda = \begin{cases} 17.3 - \frac{1}{2}\ln(n_\mathrm{e}[10^{20}\mathrm{m}^{-3}]) + \frac{3}{2}\ln(T_\mathrm{i}[\mathrm{keV}]) & \text{ion-ion collisions} \\ 15.2 - \frac{1}{2}\ln(n_\mathrm{e}[10^{20}\mathrm{m}^{-3}]) + \ln(T_\mathrm{e}[\mathrm{keV}]) & \text{electron-ion collisions} \end{cases} \tag{6.8}$$

The formula for ion-ion collisions is valid for singly charged ions and for $T_\mathrm{e} < 20$ keV in a deuterium plasma. The formula for ion-electron collisions only holds at temperatures above 10 eV. In Table 6.2 values of the Coulomb logarithm are listed for H-mode parameters. The values can deviate by more than 10% and therefore the exact value should be included in the calculation. The bounce frequency in Eq. (6.6) is evaluated for thermal particles $v_\mathrm{T} = \sqrt{2T_\mathrm{j}/m_\mathrm{j}}$ [2]

$$\omega_\mathrm{bj} = \frac{v_\perp}{qR_0}\left(\frac{r}{2R_0}\right)^{1/2} = \frac{T_\mathrm{j}^{1/2} r^{1/2}}{m_\mathrm{j}^{1/2} q R_0^{3/2}}, \tag{6.9}$$

$n_{\mathrm{e,i}}[10^{20}\ \mathrm{m}^{-3}]$	$T_{\mathrm{e,i}}[\ \mathrm{keV}]$	$\ln\Lambda_{\mathrm{e\text{-}i}}$	$\ln\Lambda_{\mathrm{i\text{-}i}}$
0.3	2.0	16.5	18.9
0.8	1.0	15.3	17.4
1.0	0.5	14.5	16.3
2.0	0.5	14.1	15.9

Table 6.2: Values of the Coulomb logarithm for different H-mode pedestal top parameters.

with Eq. (6.7) and Eq. (6.9), Eq. (6.6) becomes

$$\nu_{\mathrm{j}\star} = \frac{Z^{\zeta_{\mathrm{j}}} q \ln\Lambda}{c_{\mathrm{j}}\epsilon} \frac{R_0^{3/2} n_{\mathrm{i}} e^4}{r^{1/2} T_{\mathrm{j}}^2 \epsilon_0^2}. \tag{6.10}$$

To rewrite Eq. (6.10) for the use of common units one uses $\epsilon_0 = 5.5526 \cdot 10^7 \mathrm{V}^{-1}\mathrm{m}^{-1} e$ and $\nu_{\mathrm{j}\star}$ becomes

$$\nu_{\mathrm{j}\star} = \begin{Bmatrix} (\mathrm{j}=\mathrm{i}) & 4.900 \cdot 10^{-5} Z^4 \\ (\mathrm{j}=\mathrm{e}) & 6.930 \cdot 10^{-5} Z^2 \end{Bmatrix} \frac{q R_0^{3/2} \ln\Lambda n_{\mathrm{i}}[10^{19}\ \mathrm{m}^{-3}]}{r^{1/2}\epsilon (T_{\mathrm{j}}[\mathrm{keV}])^2}. \tag{6.11}$$

Eq. (6.11) is the exact representation for the collisionality of thermal particles. One should note that all quantities besides R_0, ϵ and Z are functions of the radius. The most common approximation uses the assumption of a pure deuterium plasma with $Z = 1$, therefore, $n_{\mathrm{i}} = n_{\mathrm{e}}$, and evaluates $\nu_\star$ at the plasma edge where $q \simeq q_{95}$ and $r \simeq a$

$$\nu_{\mathrm{j}\star} \simeq \begin{Bmatrix} (\mathrm{j}=\mathrm{i}) & 4.900 \cdot 10^{-5} \\ (\mathrm{j}=\mathrm{e}) & 6.930 \cdot 10^{-5} \end{Bmatrix} \frac{q_{95} R_0 \ln\Lambda n_{\mathrm{e}}[10^{19}\ \mathrm{m}^{-3}]}{\epsilon^{3/2} (T_{\mathrm{j}}[\mathrm{keV}])^2}, \tag{6.12}$$

this approximation is similar to the collisionality used in Eq. (18) of [40] and is primarily used in this work. The determination of the collisionality becomes more difficult if the plasma is not pure but consists of impurity ions which is generally the case. In such an environment Eq. (6.8) and Eq. (6.11) are not valid anymore. A consistent treatment of this case is beyond the scope of the present work. In [40] an approximation of $\nu_{\mathrm{e}\star}$ was obtained by a variation of the charge number Z and an estimate for the Coulomb logarithm

$$\nu_{\mathrm{e}\star} = 0.0012 \frac{q R_0 Z_{\mathrm{eff}} n_{\mathrm{e}}[10^{19}\ \mathrm{m}^{-3}]}{\epsilon^{3/2} (T_{\mathrm{e}}[\mathrm{keV}])^2}. \tag{6.13}$$

The form of Eq. (6.13) suggests it was determined at $r = a$, therefore, the radial form should become

$$\nu_{\mathrm{e}\star} = 0.0012 \frac{q R_0^{3/2} Z_{\mathrm{eff}} n_{\mathrm{e}}[10^{19}\ \mathrm{m}^{-3}]}{r^{1/2}\epsilon (T_{\mathrm{e}}[\mathrm{keV}])^2}. \tag{6.14}$$

The normalized plasma parameters are all radial profiles, but generally only one value is given of this profile. Throughout this work the one value corresponds to the pedestal top as discussed above. However, due to the difficulties in the profile alignment, as discussed in Section 5.2.2, the calculation cannot be performed at a definite position in the plasma. For parameters with large uncertainties like the profile of the safety factor q it is not convenient to rely on a position like the pedestal top. Already small uncertainties in the position can result in large deviations, because of the large gradients of q in the edge. In this case the

pedestal top value q_{ped} is approximated with the safety factor at 95% of the flux q_{95}. Another example is the poloidal magnetic field, it is approximated with its flux surface averaged value at the last closed flux surface ($\langle B_{\mathrm{p}} \rangle = \mu_0 I_{\mathrm{p}} / l_{\mathrm{lcfs}}$). Also the values of $T_{\mathrm{e,ped}}$ and $n_{\mathrm{e,ped}}$ are not necessarily taken at the same position. The pedestal width of temperature and density is often different as will be discussed in Section 7.2. However, in this case it is beneficial that the density is generally flat within the pedestal top and the temperature pedestal top lies typically at smaller radii than the density pedestal top. Therefore, derived quantities are calculated at the pedestal top of the electron temperature. This is a reasonable approach as will also be shown in Section 7.4 Figure 7.29.

6.1 Parameter Correlations

In this section an overview of the parameter dependencies in the database is given. The correlations between the different parameters are important for the discussion of certain trends found in the database. First the correlations of the different engineering parameters are discussed, then the correlations between the dimensionless *physics* parameters. The plasma shape will be discussed in a separate section Section 6.3.

The correlations of the engineering parameters with each other illustrate the different operational regimes of the machines which were discussed in Chapter 1. In Figures 6.2-6.5 all combinations of the parameters heating power P_{heat}, toroidal magnetic field B_{t}, plasma current I_{p}, pedestal top electron density $n_{\mathrm{e,ped}}$, pedestal top electron temperature $T_{\mathrm{e,ped}}$, safety factor q_{95} and minor radius a are plotted against each other. This is intended as a general overview of the database and in later chapters individual plots are referenced when necessary for a discussion. Here only the parameter combinations are discussed which show correlations. Figure 6.2 (a) shows low toroidal magnetic fields $B_{\mathrm{t}} < 1.5$ T are only found for low heating powers $P_{\mathrm{heat}} < 3$ MW. This is a result of the B_{t} dependence of the L-H transition power threshold [88], because the H-mode access requires larger heating power for higher toroidal field. For larger fields P_{heat} and B_{t} are uncorrelated (Figure 6.2 (a)). The electron temperature is strongly correlated with the heating power (Figure 6.2 (d)) for each machine. Because of the different plasma densities and plasma volume this correlation is broken in the machine comparison. Figure 6.3 (c) shows that due to the correlation of P_{heat} and B_{t} at DIII-D also B_{t} shows a correlation with $T_{\mathrm{e,ped}}$, which is again broken by the other machines. A significant correlation is observed between the toroidal field and the pedestal top density as shown in Figure 6.3 (b). For DIII-D and JET the toroidal field is correlated with the plasma current, however, this correlation is broken with discharges from AUG (Figure 6.3 (a)). Further correlations are visible for $n_{\mathrm{e,ped}}$ and I_{p} (Figure 6.4 (a)) and a and I_{p} (Figure 6.4 (d)). All other parameter combinations show little or no correlation with each other. Even in the partly correlated parameters there is enough variation in each parameter to be able to distinguish between them. The correlation matrix is given as overview in Table 6.3. The only exceptions are a and I_{p} and of course a and R. A combination of these parameters has to be handled with care in data regressions, examples with these parameters are given in Section 5.4.

The dimensionless parameters $\beta_{\mathrm{p,ped}}$, $\rho_\star$ and $\nu_{\mathrm{i}\star}$ are of course correlated with the engineering parameters according to their definition in Eq. (6.4), Eq. (6.2) and Eq. (6.12). In Figure 6.6 the correlations of the dimensionless parameters with each other are illustrated.

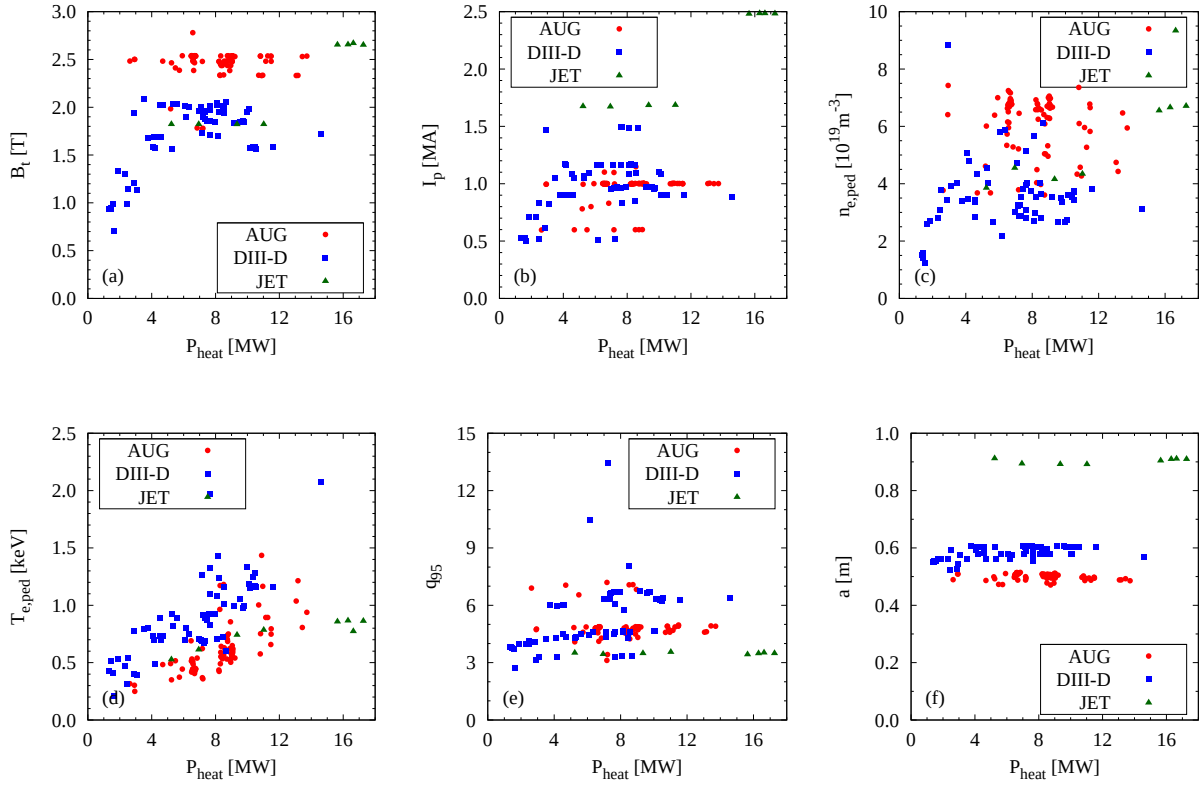

Figure 6.2: Dependence of several plasma parameters on the heating power for the whole database.

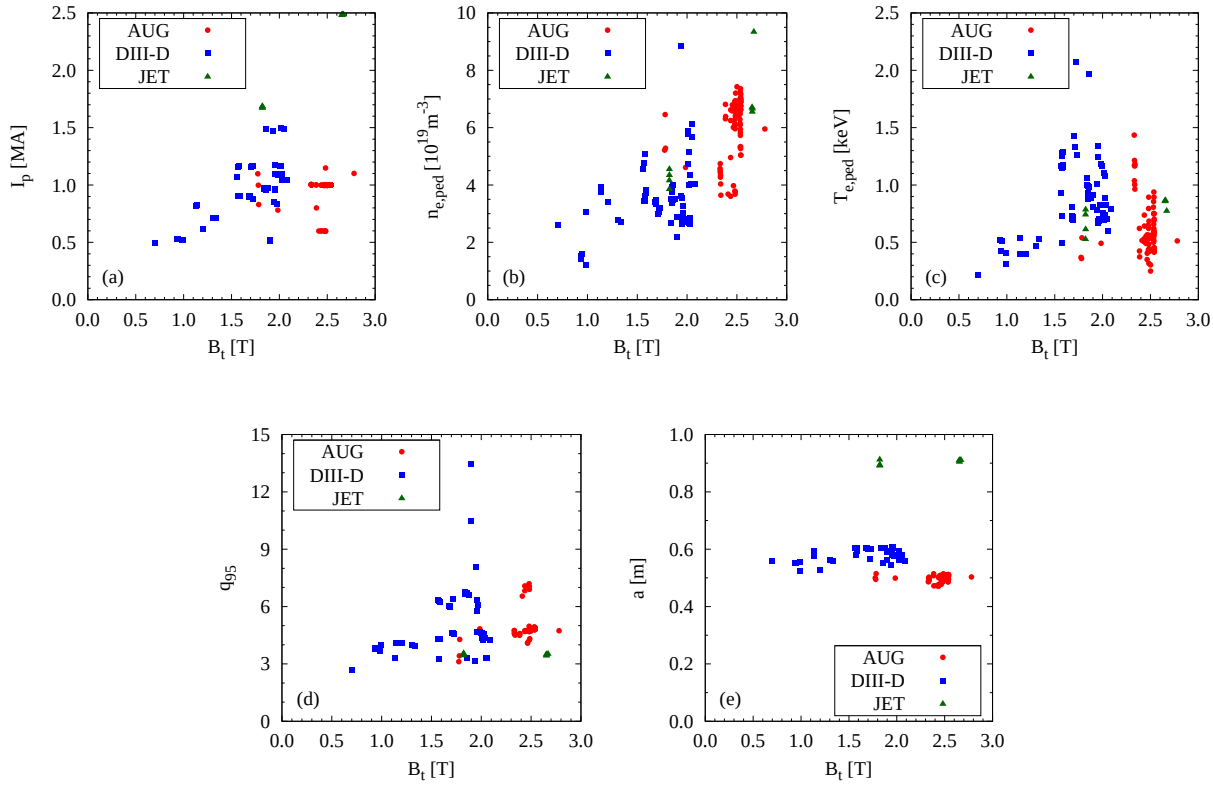

Figure 6.3: Dependence of several plasma parameters on the magnetic field for the whole database.

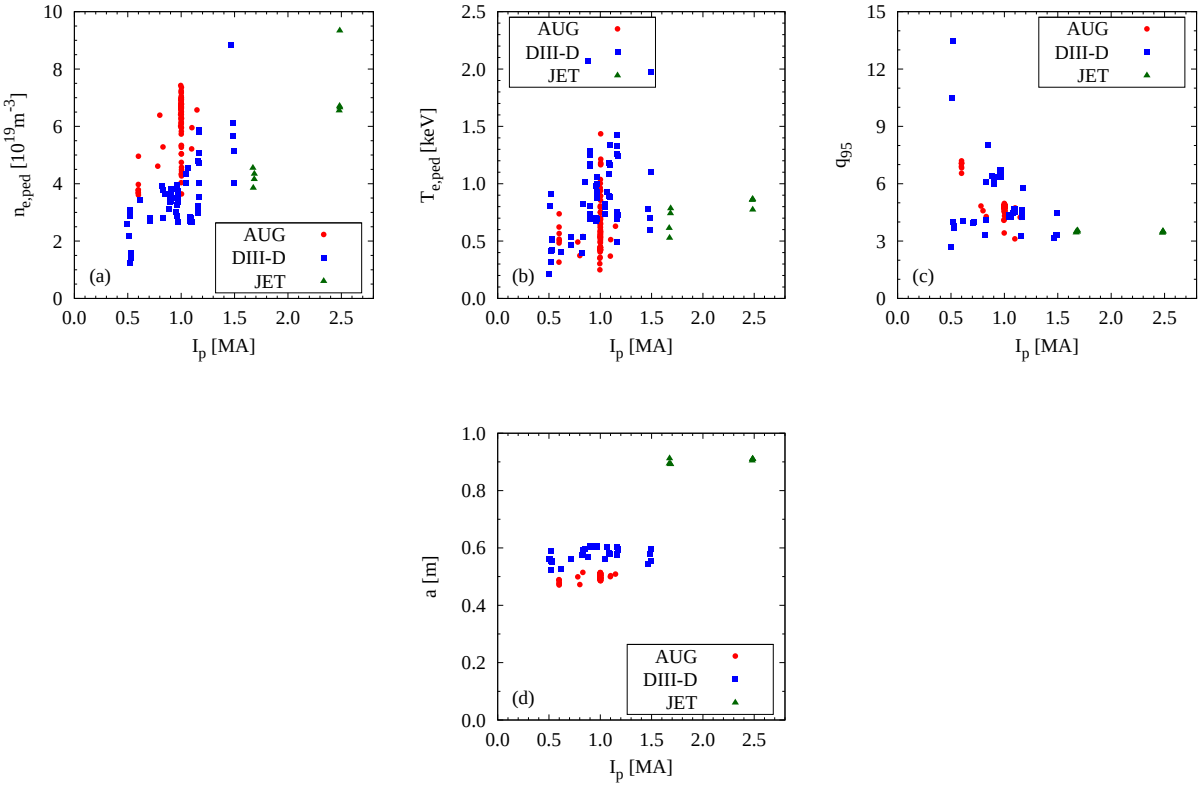

Figure 6.4: Dependence of several plasma parameters on the plasma current for the whole database.

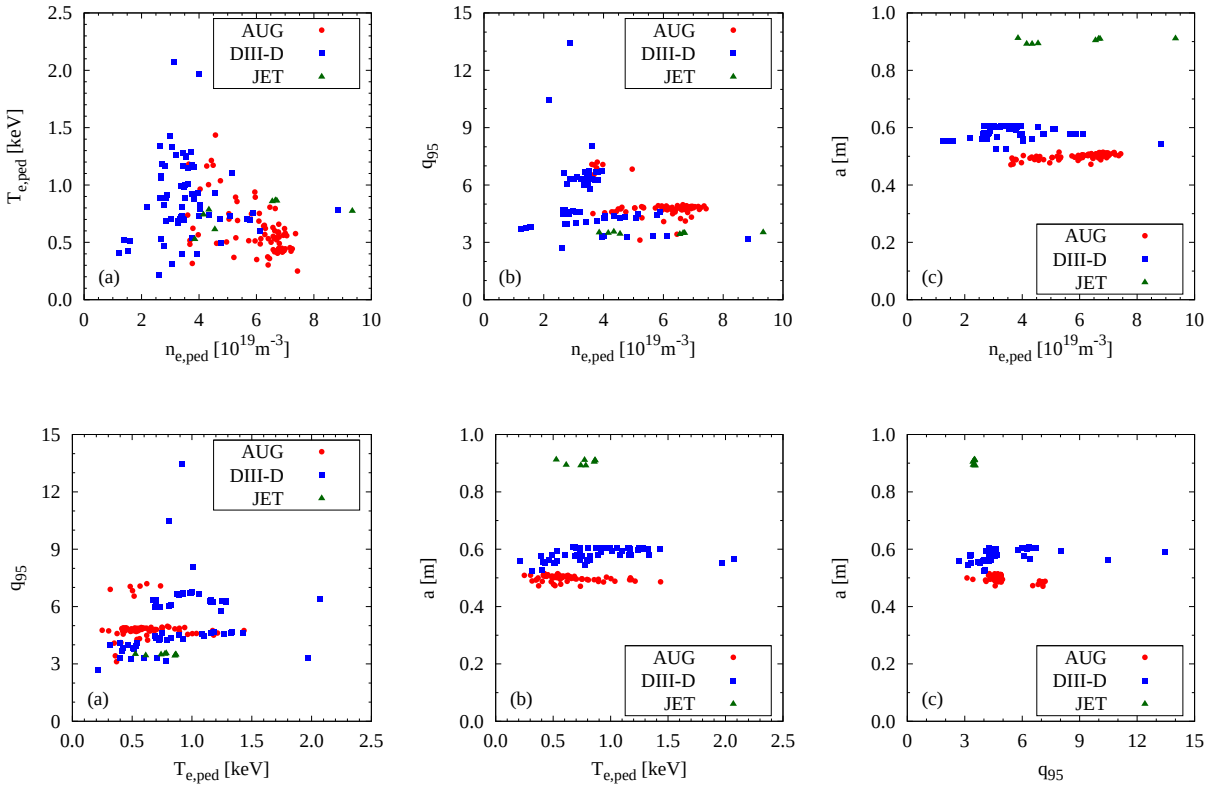

Figure 6.5: Dependence of selected plasma parameters on $n_{\mathrm{e,ped}}$, $T_{\mathrm{e,ped}}$ or q_{95}.

	$T_{\mathrm{e,ped}}$	$n_{\mathrm{e,ped}}$	I_{p}	B_{t}	P_{heat}	q_{95}	a
$T_{\mathrm{e,ped}}$	1.00	-0.34	0.22	-0.15	0.49	0.25	0.24
$n_{\mathrm{e,ped}}$	-0.34	1.00	0.42	0.78	0.44	-0.29	-0.11
I_{p}	0.22	0.42	1.00	0.35	0.61	-0.41	0.75
B_{t}	-0.15	0.78	0.35	1.00	0.50	0.03	-0.17
P_{heat}	0.49	0.44	0.61	0.50	1.00	0.07	0.34
q_{95}	0.25	-0.29	-0.41	0.03	0.07	1.00	-0.15
a	0.24	-0.11	0.75	-0.17	0.34	-0.15	1.00

Table 6.3: Correlation matrix of the main plasma engineering parameters.

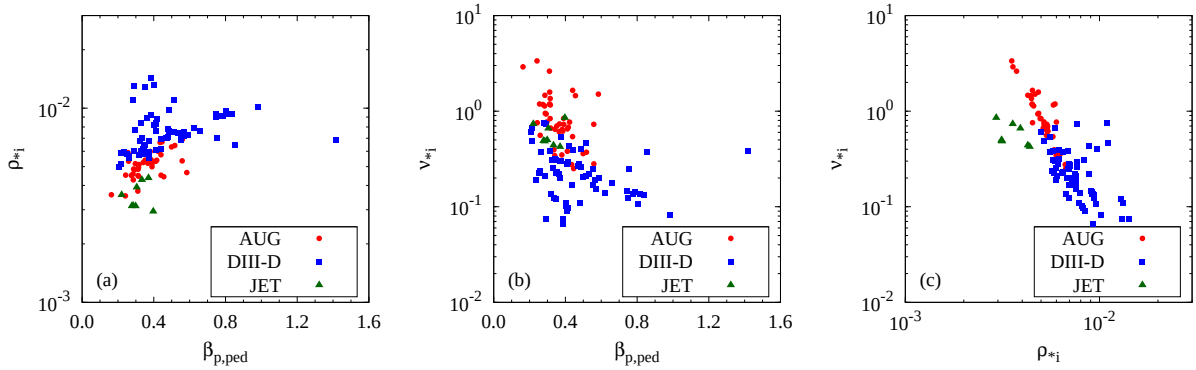

Figure 6.6: Dependence of the dimensionless parameters $\beta_{\mathrm{p,ped}}$, $\rho_{\star}$ and $\nu_{\mathrm{i}\star}$ with one another.

	$\beta_{\mathrm{p,ped}}$	$\rho_{\mathrm{i}\star}$	$\nu_{\mathrm{i}\star}$
$\beta_{\mathrm{p,ped}}$	1.00	0.42	-0.39
$\rho_{\mathrm{i}\star}$	0.42	1.00	-0.56
$\nu_{\mathrm{i}\star}$	-0.39	-0.56	1.00

Table 6.4: Correlation matrix of the main dimensionless plasma parameters.

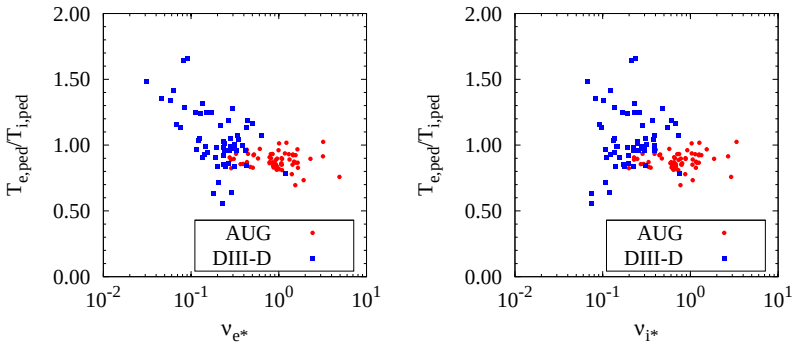

Figure 6.7: The temperature ratio $T_{\mathrm{e,ped}}/T_{\mathrm{i,ped}}$ plotted against the electron (a) and ion (b) collisionality.

The collisionality decreases strongly with larger $\beta_{\mathrm{p,ped}}$ (b) and $\rho_\star$ (c). Accordingly, $\rho_\star$ increases with larger $\beta_{\mathrm{p,ped}}$ (a). Despite these trends, the numerical correlation is below 0.6 for the three parameter combinations. In the database one finds a stronger correlation between the dimensionless parameters for AUG data only. The reason for this is that at AUG the parameter variation is achieved mainly with current and heating power scans - this results in a strong correlation of 0.82 between $\rho_\star$ and $\nu_{\mathrm{i}\star}$ for AUG. This correlation can be reduced significantly with the toroidal field variation in the DIII-D and JET data set. The correlation matrix for all three devices is given in Table 6.4. At AUG a large B_{t} variation is difficult to achieve, because the electron cyclotron heating is required in the plasma center to avoid tungsten accumulation which would cause a radiative collapse of the discharge [89].

In summary, the database covers a sufficiently wide range for most relevant parameters. Exceptions are the aspect ratio, which is not varied at all, and the plasma elongation which is limited to relatively high elongation, because no circular plasmas are included in the database. Only three pairs of engineering parameters showed a correlation of over 0.50: $n_{\mathrm{e,ped}}$-B_{t}, I_{p}-P_{heat} and I_{p}-a. However, all three pairs are decoupled for the individual machines and this will help to identify possible co-dependencies in the regressions.

6.2 Electrons vs. Ions

In the presented data set the common assumption $T_{\mathrm{i}} = T_{\mathrm{e}}$ is not always appropriate. Therefore, in this section the differences between electrons and ions are documented for the database.

Measurements of electron and ion temperature reveal a collisionality dependence of the the temperature ratio $T_{\mathrm{e,ped}}/T_{\mathrm{i,ped}}$. In Figure 6.7 this ratio is shown for data from AUG (red) and DIII-D (blue). The temperature ratio increases for small electron collisionality (a) and saturates around 0.9 for large $\nu_{\mathrm{e}\star}$. The ion collisionality (b) shows a less distinct correlation and a larger variation of $T_{\mathrm{e,ped}}/T_{\mathrm{i,ped}}$ for low $\nu_{\mathrm{i}\star}$. It has to be noted, $T_{\mathrm{i,ped}}$ is determined at the position of the electron temperature pedestal top. This is important because in the data set several T_{i} edge measurements exist which show no pedestal top defined by any of the methods described in Section 5.3. Therefore, $T_{\mathrm{e,ped}}/T_{\mathrm{i,ped}}$ could be wrong when different positions are chosen as pedestal top. Not for all AUG discharges in the database edge ion temperature measurements exist, therefore, two different subsets of data are used for AUG data: one

	Z_{eff}		
Z	1.0	2.0	3.0
5	1.00	0.75	0.50
7	1.00	0.83	0.67
9	1.00	0.88	0.75

Table 6.5: Calculation of $(Z - Z_{\text{eff}})/(Z - 1)$ for different Z_{eff} and Z.

where T_{i} measurements exist, which is used in cases T_{i} enters the discussion explicitly, and a second where the ion temperature is approximated as $T_{\text{i,ped}} = 1.1T_{\text{e,ped}}$, motivated by Figure 6.7.
To determine the ion pressure, besides T_{i} the main ion density n_{i} is important. Unfortunately, no direct measurement of the main ion density is available. In principle, the main ion density can be derived from the principle of quasi-neutrality in the plasma with knowledge of the effective ion charge number Z_{eff} and types of impurities in the plasma. For a plasma with one impurity of charge number Z the main ion density would be

$$n_{\text{D}} = \frac{Z - Z_{\text{eff}}}{Z - 1} n_{\text{e}}. \tag{6.15}$$

The uncertainties in this representation are hidden in Z_{eff} and Z. AUG measurements of the average charge number have a very large uncertainty at the plasma edge. This can be up to a factor of 2. Another source for uncertainties are the impurity ions which are not of a single species and can be a mixture Boron, Carbon, Nitrogen, Oxygen and others. This mixture is difficult to document, therefore, the calculation of n_{D} relies on various assumptions and measurements with large uncertainties. These are the reasons why for this work the assumption of a pure Deuterium plasma with $n_{\text{i}} = n_{\text{D}} = n_{\text{e}}$ is made. Both approaches to treat the ion density are not optimal, but there is no better treatment which is also feasible in a database approach. In general the ion density and therefore, the ion pressure are overestimated with the assumption of a pure Deuterium plasma. To illustrate the influence of impurities on the main ion density a few examples are given in Table 6.5. If the impurity charge number would be an average of Carbon and Oxygen $Z = 7$ and $Z_{\text{eff}} = 2$, then n_{i} is overestimated by 20% with the assumption of a pure Deuterium plasma. The uncertainty due to Z_{eff} measurements is of the same order, but less predictable. An overestimation of 20% in the ion density results in a total pressure which is too large by less than 10%.

6.3 Plasma shape

Shaping of the plasma is an important tool to modify plasma parameters. In general, the plasma shape is characterized by the geometric quantities elongation κ and triangularity δ. In this section κ and δ are introduced and their correlation with other parameters is described. A third parameter to describe the plasma shape $f_{\text{q}} = q_{95}/q_{\text{cyl}}$ is introduced.

The elongation is defined as $\kappa = b/a$ where b is the vertical and a the horizontal minor radius. The minor radius is calculated as

$$a = 2\sqrt{\langle (R_{\text{sep}}(z) - R_{\text{geo}})^2 \rangle}, \tag{6.16}$$

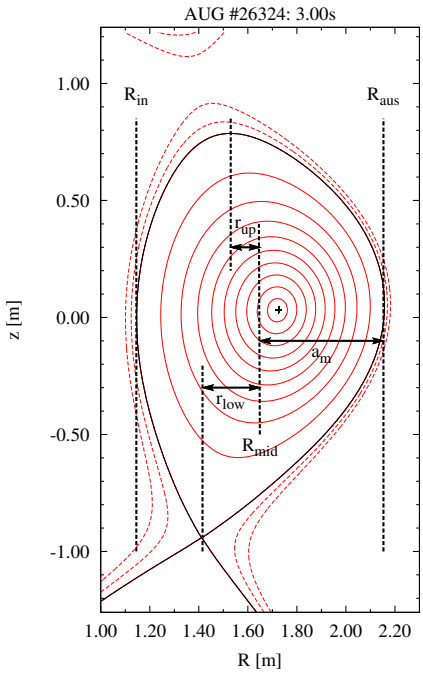

Figure 6.8: Geometrical definition of the upper and lower triangularity $\delta_{\mathrm{up,low}} = r_{\mathrm{up,low}}/a_{\mathrm{m}}$. The distances r_{up} and r_{low} are taken from the upper most and lowest point radially to the mid radius.

where $\langle\cdot\rangle$ denotes the flux surface average taken at the separatrix, R is the radial coordinate of the separatrix and R_{geo} the geometrical center of the plasma. This definition yields a value for a which is about 1 cm smaller than the intuitive definition of the geometrical minor radius, $a_{\mathrm{m}} = (R_{\mathrm{aus}} - R_{\mathrm{in}})/2$, where R_{aus} and R_{in} are the outer and inner radius of the separatrix at the midplane. The vertical minor radius, b, is defined accordingly to Eq. (6.16) using the vertical coordinates $z_{\mathrm{sep}}(R)$ and z_{geo}. The triangularity is defined $\delta = (\delta_{\mathrm{up}} + \delta_{\mathrm{low}})/2$ where δ_{up} respectively $\delta_{\mathrm{lo\,w}}$ is the relative deviation from an elliptical shape and defined as

$$\delta_{\mathrm{low,up}} = \frac{r_{\mathrm{low,up}}}{a_{\mathrm{m}}} \tag{6.17}$$

where $r_{\mathrm{low,up}}$ is the distance of the lowest, upper most radius of the separatrix to the mid radius R_{mid}. In a shape with $\delta = 0$ the lowest and upper most point of the last closed flux surface would be on the same radius as the mid radius. A $\delta = 1$ configuration would mean both points would lie on the same radius as the separatrix on the inboard midplane forming a 'D' shaped plasma cross section. An example how these parameters are calculated is given in Figure 6.8.

The shape of the plasma can be described with a magnetic shaping factor

$$f_{\mathrm{q}} = \frac{q_{95}}{q_{\mathrm{cyl}}}, \tag{6.18}$$

where q_{95} is the safety factor at 95% of the poloidal flux and is determined from equilibrium reconstruction in full geometry (see Section 5.1), q_{cyl} is the cylindrical safety factor, including the elongation as elliptical approximation, defined with global plasma parameters

$$q_{\mathrm{cyl}} = \frac{2\pi a^2 B_{\mathrm{t0}}}{R I_{\mathrm{p}} \mu_0} \frac{1+\kappa^2}{2}. \tag{6.19}$$

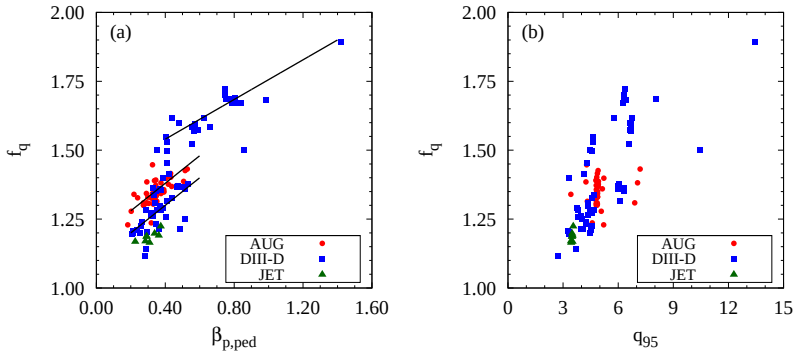

Figure 6.9: Variation of the magnetic shape with the normalized poloidal pedestal pressure (a) and the safety factor at 95% of the poloidal flux (b).

	δ	κ	f_q	P_{heat}	$\langle B_p \rangle$	B_t	q_{95}	p_{ped}	$\beta_{p,ped}$
δ	1.00	0.61	0.56	-0.00	-0.42	-0.49	0.41	0.06	0.57
κ	0.61	1.00	0.30	0.04	-0.24	-0.53	0.25	0.05	0.41
f_q	0.56	0.30	1.00	0.28	-0.30	-0.12	0.73	0.31	0.83

Table 6.6: Correlation matrix of the plasma shape with main engineering parameters.

The physical meaning of the shaping factor f_q could not be assessed within the database approach. Different approaches were investigated which gave no a satisfying match with f_q. q_{95} is taken at 95% of the flux, meaning the current density in the last 5% of the flux does not contribute to q_{95}. q_{cyl} does include the total current. Since q_{95} can be determined very accurately with standard equilibrium reconstructions [90], the shaping factor f_q might be an estimate for the integrated edge current density. Since the edge current density influences the local poloidal magnetic field which is responsible for the q-profile, f_q would also be linked to the magnetic shear s. Therefore, f_q inherits higher order effects which are associated with the pedestal width (see e.g. Section 3.1.1) or pedestal stability (see e.g. Section 2.1). Unfortunately, there are no measurements available for the magnetic shear which would help to clarify its connection to f_q.
The magnetic shape is found to be correlated with the normalized plasma pressure $\beta_{p,ped}$. The correlation factor is 0.83 and illustrated in Figure 6.9 (a). In the plot, different subsets of data show individual trends which are indicated by solid black lines. This would suggest that both parameters do not directly depend on each other. The correlation between $\beta_{p,ped}$ and f_q would be consistent with the idea of a relation between f_q and the current density, if $\beta_{p,ped}$ would be proportional with $\langle j \rangle$, as suggested by [56]. However, the individual trends in Figure 6.9 (a) do not support with this picture. The same is true for the observation in Figure 6.9 (b) which shows a strong correlation with q_{95}. This suggests that at higher q_{95} the plasma can deviate more easily from the cylindrical reference. It has to be stressed that this is a real trend with q_{95} and not a trend with the plasma current I_p which would allow to argue that at lower total current the bootstrap contribution at the edge might be relatively larger.
Because of the uncertainty in the meaning of f_q it will be still referred to with its ambiguous name magnetic shaping factor or shaping factor. The remainder of this section focuses on further influences of the plasma shape.

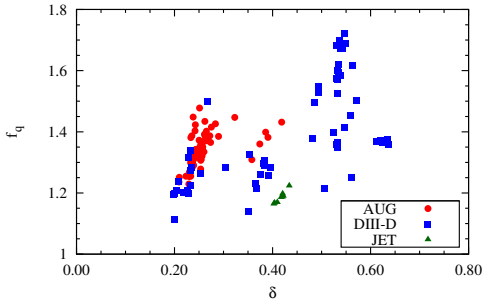

Figure 6.10: Variation of the shaping factor $f_q = q_{95}/q_{cyl}$ with the triangularity.

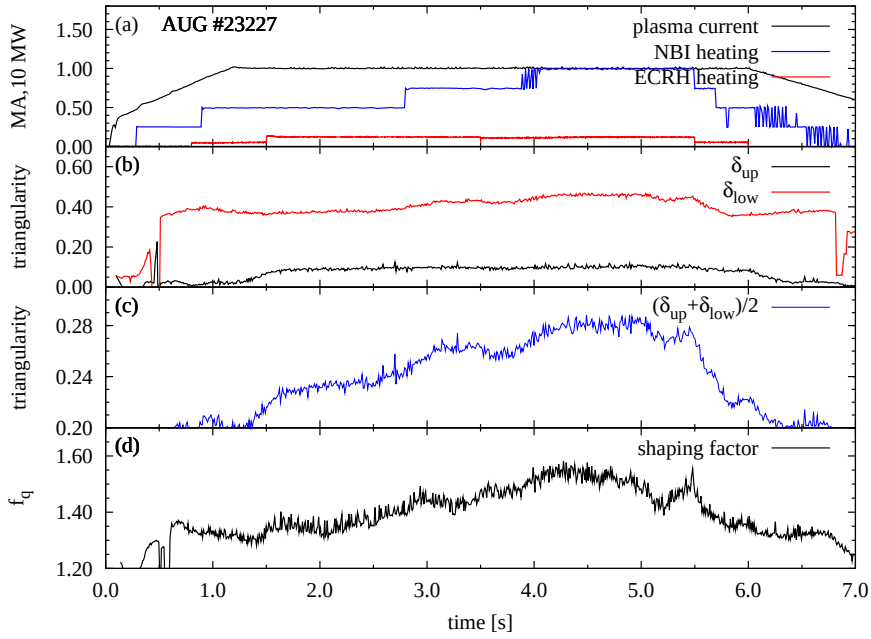

Figure 6.11: Time traces of an AUG discharge with power scan. With increasing heating power the lower triangularity (red) and therefore the mean triangularity (blue) increase. At the same time the shaping factor (black) increases.

An overview of the correlations between the plasma shape and global engineering parameters is given in Table 6.6. The geometrical shape is not correlated to global parameters. Also the magnetic shape shows only little correlation with the global parameters, besides q_{95}. For the analysis in later chapters it is important to note that f_q is not correlated to either $\langle B_p \rangle$ or B_t individually. The triangularity correlation with f_q is the result of a complex relationship. In this relationship the pedestal pressure plays an important role. In Figure 6.10 the variation of f_q with the triangularity is shown. There is no global trend with δ but several distinct trends for different regimes in triangularity. For low δ, the triangularity is correlated with the magnetic shaping. At high δ, no correlation between the triangularity and the magnetic shaping is observed. The individual regimes at low δ, where f_q seems to scale with δ, can be explained with the triangularity dependence on the pedestal pressure. When the pedestal pressure increases the plasma triangularity increases. This can be observed in a AUG power scan Figure 6.11 where the triangularity increases by 20% (c) and the shaping factor by 10% (d), when the heating power is doubled (a). The influence on the

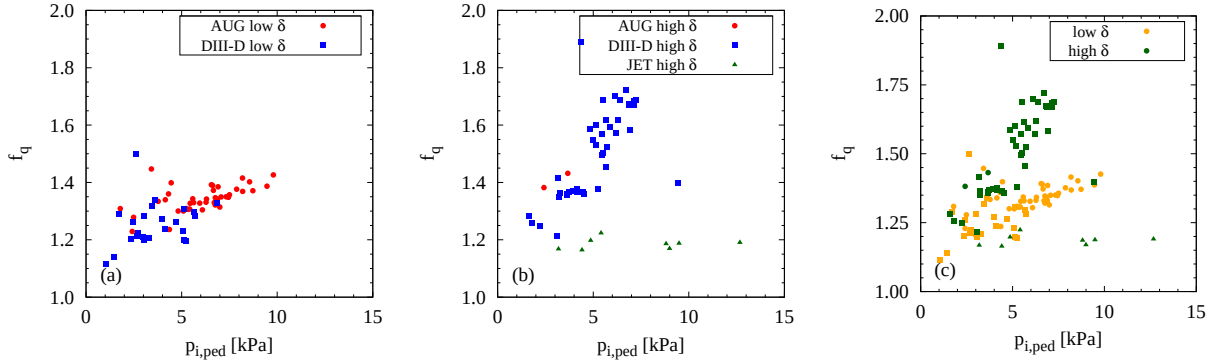

Figure 6.12: Influence of the pedestal pressure on the shaping factor at low ($\delta < 0.39$) and high ($\delta > 0.39$) triangularity.

mean triangularity is mainly an effect of the lower triangularity (b) and therefore, it is an influence of the x-point position. This could be a side effect of the control system for the plasma position which tries to keep a plasma with increased energy content in position. At high triangularity no correlation between f_q and δ is observed.

Motivated by the relation of f_q with δ and the pedestal pressure, two regimes of triangularity are defined: low triangularity $\delta < 0.39$ and high triangularity $\delta > 0.39$. The reason for this choice is illustrated in Figure 6.12. In (a) the low triangularity discharges of the database are shown and the f_q increases with the ion pressure. A similar picture is given in (b) for the high triangularity, the shaping factor increases strongly with $p_\mathrm{i,ped}$ for the AUG and DIII-D data. In (c) both triangularity regimes are included and they are illustrated with different colors. The discharges from AUG and DIII-D show two distinct branches, where f_q increases more strongly at high δ (green) than with low δ (orange). JET data shows no variation in the shaping factor and therefore, it does not fit with the AUG and DIII-D data. The reason for this is not clear. With the limited number of JET measurements in the database, in particular, because of the lack of a q_{95} variation, a profound investigation is difficult for this case.

To summarize, besides the geometrical shape of a poloidal plasma cross section, the magnetic shape f_q was introduced. The physical meaning of f_q is not quite clear. However, the observations, that will be discussed in Chapter 7, suggest an important role of f_q. Here, the pedestal pressure shows strong influence on the magnetic shape f_q or vice verse. At a given pedestal pressure two shaping factors are possible. The difference defines different triangularity regimes. With the same pedestal pressure, high triangularity generally results in the larger shaping factor than low triangularity. Below $p_\mathrm{i,ped} \sim 4$ kPa both regimes are not distinguishable any more. At low triangularity, δ increases with the pedestal pressure, for high triangularity, no such correlation is observed. For the analysis presented in the following chapters it is important that besides their influence on each other, the pedestal pressure p_ped and the magnetic shaping f_q have a small correlation factor. Therefore, their dependence should not hamper regression analyses. In general one can say that the data sets of AUG and DIII-D are not equivalent in terms of plasma shape but complement each other.

Chapter 7

Pedestal Characteristics

The importance of the pedestal for the plasma performance was discussed in detail in Chapters 2 and 3. In this chapter the results of the pedestal characterization with the two-line method, described in Section 5.3, are shown for the database introduced in Section 6. The focus is put on results which are consistent for the whole database and in particular all three machines AUG, DIII-D and JET. Where necessary also individual discharges are used for better illustration of certain results. First the position of the separatrix is analysed, then the three pedestal characteristics width, gradient and top value are described in detail, the chapter closes with study of the temperature and density gradient lengths in the pedestal and their ratio.

7.1 Separatrix

Measuring profiles of a single plasma parameter with different diagnostics may result in profiles which are misaligned with respect to each other after mapping in a 3D machine to 1D flux coordinates. In Section 5.2.2 this was discussed in detail, with the result that this cannot be physical and therefore, must be an artifact of the spatial calibration or the mapping procedure. The separatrix as a prominent feature at the pedestal edge can be used to align different diagnostics. The separatrix position is also essential to determine the pedestal width with the two-line method.

Strategies to determine the separatrix position individually for temperature and density profiles use theoretical predictions for T_e and n_e at the separatrix based on divertor measurements and transport parallel to the field lines [91, 92]. A temperature of around 100 ± 20 eV at the separatrix is predicted for devices like AUG or DIII-D and 135 ± 30eV for JET. The temperature at the separatrix is only very weakly dependent on plasma parameters like heating power. The density can also be determined with this method, however, the uncertainty is larger and the value is not independent of gas fuelling. Fuelling has three major contributions: the regularly used gas puffing, neutral beam heating and recycling from the walls. Recycling strongly depends on the machine condition and previous discharges. Therefore, the exact gas fuelling rate cannot be determined precisely. A more detailed discussion of the influences on the density pedestal is given in Section 7.4.1.
Another possibility to determine the separatrix position is a variation in the profile shape.

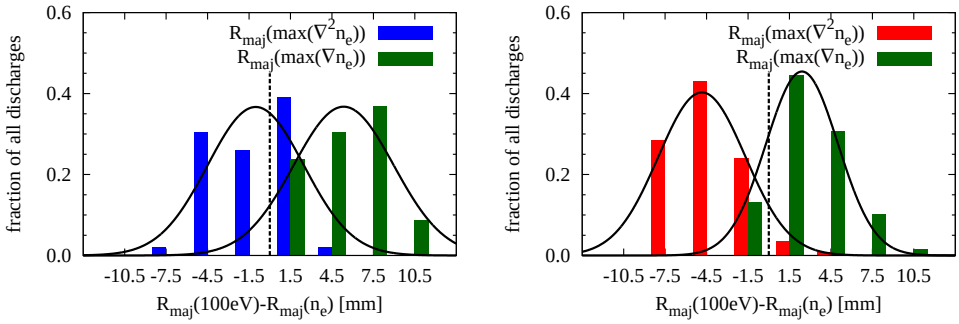

7.1.1: DIII-D: TS only - T_e and n_e intrinsically aligned

7.1.2: AUG: ECE, Li-Beam - T_e and n_e not aligned

Figure 7.1: Histograms of the difference of positions of T_e =100 eV and max($\nabla^2 n_e$) (blue/red) respectively max(∇n_e) (green). The binsize is 3mm and the tics correspond to the middle of each bin. No deviation between positions is indicated with the dashed line. The normal distribution fitted to the histogram is indicated by the solid black line. For DIII-D (left) the position of T_e =100eV matches the one of max($\nabla^2 n_e$) quite well. The AUG (right) data is influenced by a systematic shift of ECE and Li-Beam with respect to each other.

Outside of the separatrix the field lines are not closed anymore and the large parallel transport becomes important [93]. When the particle transport is dominated by diffusion the gradients should have a discontinuity at the separatrix [91]. A similar discontinuity in the density gradient is predicted by a semi-analytical neutral penetration model for the plasma edge when the transport changes at the transition from closed to open field lines and should be independent of the gas fuelling [53]. In this section, the position where the gradients change most is compared with the separatrix determined by temperature measurements. The largest change of the gradients is associated with a maximum in the curvature.

The Thomson scattering (TS) system is used to evaluate the accuracy of a definition for the separatrix using only the n_e profile shape. TS is able to measure T_e and n_e simultaneously at the same location. Therefore, a comparison of T_e and n_e profiles with TS is not influenced by mapping uncertainties. The radial location of the 100eV-line is compared to unique features of the n_e profile. The instrument kernel of the TS system is around 6 mm at DIII-D and 3 mm for AUG, as discussed in the Sections 4.3 and 4.7. Therefore, a sharp kink in the gradient as expected from theory cannot be resolved experimentally. Consequently the point of maximal curvature in the density max($\nabla^2 n_e$) is determined. This position is compared to the point of maximal gradient max(∇n_e) which should lie inside of the separatrix. These profile features are determined with the low-pass filter method described in Section 5.3.3. In the case of AUG the effective uncertainty increases a bit due to the mapping procedure which was described in Section 5.2.2. The uncertainty arising in determining the gradients is assumed to be normally distributed. The distributions $R_{maj}(100eV) - R_{maj}(max(\nabla n_e))$ and $R_{maj}(100eV) - R_{maj}(max(\nabla^2 n_e))$ then give information about the relative position of density profile features with respect to the separatrix determined via the temperature profile. In Figure 7.1 this is illustrated in a histogram. The relative frequency of discharges lying in a 3 mm bin is plotted. For DIII-D the distribution of the maximal curvature is peaked around -1 mm indicating a good match with the 100 eV position from T_e. The distribution of $R_{maj}(100eV) - R_{maj}(max(\nabla n_e))$ is peaked around 5 mm showing that the point of maximal gradient is well inside the separatrix. In the case of AUG the TS is never available for the whole pedestal. Therefore, the profiles consist largely of ECE and Li-Beam mea-

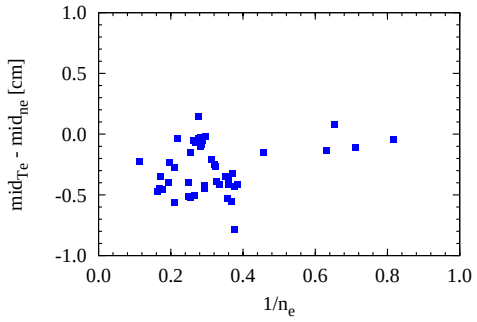

Figure 7.2: Difference of the position of the maximal gradient in T_e and n_e plotted against the inverse of the pedestal top density.

surements. Due to their different locations these diagnostics are influenced by systematic misalignment due to the mapping. This becomes visible in Figure 7.1.2 where the distribution of $R_{maj}(100eV) - R_{maj}(\max(\nabla^2 n_e))$ peaks at -4.5 mm. With additional information of the TS system the average misalignment of ECE and Li-Beam was measured to be around 3 mm (see Section 5.2.2). When including this diagnostic shift the distribution of the maximal curvature of the density profile also peaks around -1 mm relative to the separatrix.

For the present data set of AUG and DIII-D discharges the position of maximal curvature of the n_e profile lies 1 mm outside of the separatrix determined via the 100 eV position of T_e. Regarding the FWHM of the distribution the uncertainty of this positioning is ± 3 mm. The absolute position of $T_e = 100$ eV can also not be determined more accurately than 3 mm. Therefore, the positioning of the separatrix is comparably accurate for the two presented methods, namely the 100 eV (135 eV for JET) position for T_e and the $\max(\nabla^2 n_e)$. These are convenient methods to determine the pedestal width in T_e and n_e without including uncertainties in the separatrix position from equilibrium reconstruction (several mm to few cm) and uncertainties by mapping different diagnostics to the same 1D coordinates (few mm).
In the investigated data set no systematic dependencies of the positions on gas fuelling, heating power, shaping or collisionality were found within the spread of 6 mm. However, such dependencies cannot be excluded completely. Because a variety of different discharges was included in the analysis some effects might cancel each other. In a similarity experiment a dependence between the relative position $R_{maj}(\max(\nabla T_e)) - R_{maj}(\max(\nabla n_e))$ and the pedestal density was observed [54]. Especially, the plasma shape and normalized pressure $\beta_{p,ped}$ were kept fairly constant. This is different to the data set applied here, which was selected to maximise the variation in shape and $\beta_{p,ped}$. The difference between the positions of the maximal gradients in T_e and n_e is shown for the DIII-D measurements in Figure 7.2.

7.2 Pedestal Width

The radial extension of the steep gradient zone in the plasma edge is named pedestal width or often just width. Within the picture of an unstable edge due to instabilities limiting the gradients, the extension of the steep gradient region would be essential to determine the pedestal top. In this section, the properties of the pedestal width are documented for the analysed database. The analysis is ordered in three subsections with the details of one

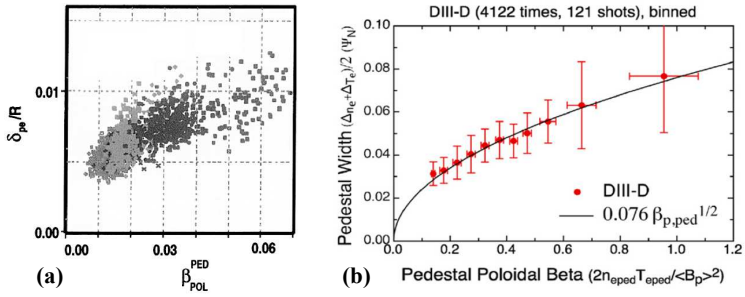

Figure 7.3: Pedestal pressure real space width (a) and mean T_e and n_e pedestal width (b) plotted against the averaged normalized poloidal pedestal pressure. (Reprinted from [94] (a) and [95] (b))

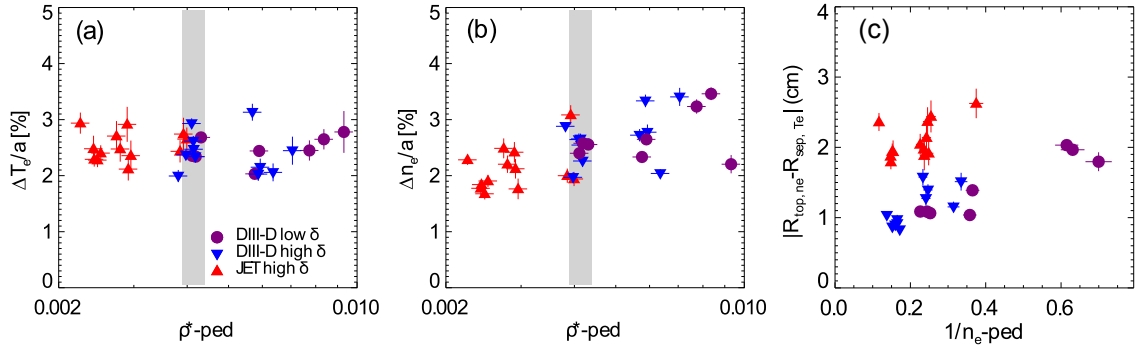

Figure 7.4: Real space pedestal width of DIII-D and JET versus $\rho_\star$ (a),(b) and $1/n_e$ (c). (Reprinted from [54])

pedestal parameter each. The subsections will be divided into different blocks with the focus on different coordinate systems. Before this a short overview of the most important results of the recent years is given.

The pedestal width in AUG and DIII-D was reported to be correlated with the square root of the poloidal pedestal beta $\beta_{\mathrm{p,ped}}^{0.5} \propto p_{\mathrm{ped}}^{0.5} \langle B_{\mathrm{p}} \rangle^{-1.0}$. This was observed in DIII-D for the electron pressure pedestal width for real space coordinates [94] and is shown in Figure 7.3 (a). The mean pedestal width $(\Delta_{ne} + \Delta_{Te})/2$ was also found to fit to $\beta_{\mathrm{p,ped}}^{0.5}$ in normalized poloidal flux coordinates Ψ_{N} [56, 86] as shown in Figure 7.3 (b). For AUG the $\beta_{\mathrm{p,ped}}^{0.5}$ correlation could be reproduced for the electron and ion temperature but no dependence in the density pedestal width was found in ρ_{p} coordinates [27]. The mean pedestal width for AUG showed again a linear correlation with $\beta_{\mathrm{p,ped}}^{0.5}$ in Ψ_{N} but no correlation in real space [54]. The theory of

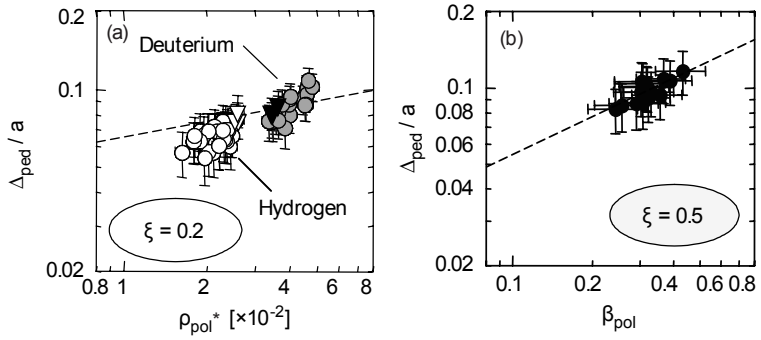

Figure 7.5: Real space ion temperature pedestal width of JT60-U against $\rho_\star$ (a) and $\beta_{\mathrm{p,ped}}$ (b). (Reprinted from [96])

kinetic ballooning modes predicts a $\beta_{\mathrm{p,ped}}^{0.5}$ dependence of the pedestal width in Ψ_{N} [95]. Besides the $\beta_{\mathrm{p,ped}}$ dependence of the pedestal width a $\rho_\star \propto T_{\mathrm{i}}^{0.5} M^{0.5} a^{-1} B_{\mathrm{t}}^{-1}$ dependence was also often discussed [94, 96, 86, 54], where M is the atomic mass number. However, both quantities, $\beta_{\mathrm{p,ped}}$ and $\rho_\star$, have a similar dependency on the temperature and are difficult to distinguish. In [94] the temperature was varied while the total pressure was kept constant. The electron pressure width was found unchanged which supports a $\beta_{\mathrm{p,ped}}$ dependence of the pressure width instead of a $\rho_\star$ dependence. In JT-60U also the mass number of the plasma's main ions was varied, the dependence of the ion temperature width on $\rho_\star^\xi$ was found to be less than $\xi = 0.2$ [96] and is shown in Figure 7.5. In DIII-D the variation of mass number was repeated to test a $\rho_\star$ dependence of the mean pedestal width in flux coordinates and no mass number dependence was found [86]. More recently a $\rho_\star$ test was performed with variation of machine size between DIII-D and JET [54]. The electron temperature and electron density pedestal width in real space r/a showed different correlations with $\rho_\star$. While Δ_{Te}/a was uncorrelated with $\rho_\star$ (Figure 7.4 (a)), Δ_{ne}/a increased with $\rho_\star$ (Figure 7.4 (b)). In theory of turbulence suppression via different mechanisms the pedestal width should scale with $\rho_\star$ to powers of 0.5-2.0 [97, 44, 98]. The density pedestal width in real space was found to scale with $1/n_{\mathrm{e}}$ for DIII-D [54] (Figure 7.4 (c)) this would be evidence for a role of neutral penetration in the pedestal [53].

7.2.1 Electron Temperature

In this section an overview of the electron temperature pedestal width is given for the database of AUG, DIII-D and JET discharges. The overview consists of the width in different coordinate systems: real space, poloidal flux space and normalized poloidal flux space. The width is analysed in terms of dependencies proposed by theory (see Chapter 3) and empirical dependencies found in the database.

In Figure 7.6 the pedestal width of electron temperature in normalized coordinates is plotted against the single parameters $\beta_{\mathrm{p,ped}}^{0.5}$ (a),(c) and $\rho_{\mathrm{i}\star}$ (b),(d). In certain regimes both parameters show correlations with the pedestal widths. However, they alone cannot explain the pedestal width. Although, the pedestal width in $[\Psi_{\mathrm{N}}]$ is best described with $\beta_{\mathrm{p,ped}}$ when using a single parameter, there is a systematic separation visible in (a) towards larger $\beta_{\mathrm{p,ped}}$. This separation is more pronounced without the influence of the flux compression in Figure 7.6 (c). More important, the separation is not an effect occurring only for different machines, but it is visible within the DIII-D data.
A linear fit through the origin, for the $\beta_{\mathrm{p,ped}}^{0.5}$ case, yields a coefficient of 0.11 ± 0.02 for the AUG data. The uncertainty in the fit to density pedestal width would be larger without the boundary condition at $\beta_{\mathrm{p,ped}} = 0$. For the temperature an offset linear fit with a slope of 0.13 would fit the data better. For DIII-D data the coefficient becomes 0.088 ± 0.014. These results agree within the uncertainties with other studies which used the mtanh analysis method [57]. A linear fit for all machines would yield $\Delta_{Te} \simeq (0.10 \pm 0.02)\beta_{\mathrm{p,ped}}^{0.5}$ with an RMSE of 21.0%.
The plots with $\rho_{\mathrm{i}\star}$ Figure 7.6 (b),(d) show correlations between $\rho_{\mathrm{i}\star}$ and the pedestal width $[\Psi_{\mathrm{N}}]$ for certain regimes. However, $\rho_{\mathrm{i}\star}$ as single parameter is clearly not sufficient to describe the pedestal width. In normalized real space coordinates $[r/a]$ no correlation of $\rho_{\mathrm{i}\star}$ with the pedestal width is found.

To identify further influences on the pedestal width a log-linear regression analysis

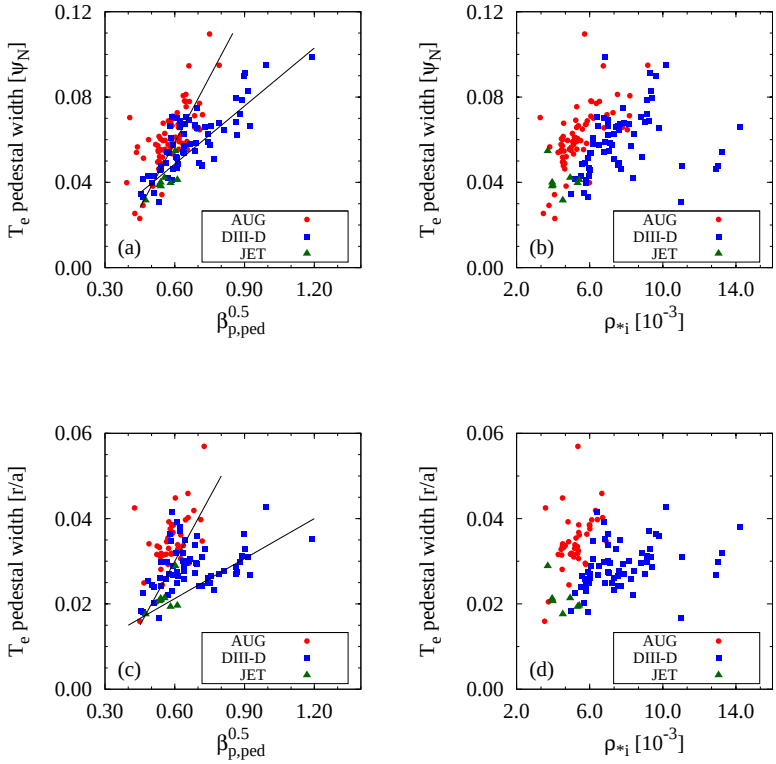

Figure 7.6: The temperature pedestal width in normalized coordinates of AUG (circle, red), DIII-D (square, blue) and JET (triangle, green) plotted against the square root of the normalized poloidal pedestal pressure (a)+(c) and the normalized toroidal gyroradius (b)+(d). Different trends are indicated by solid black lines.

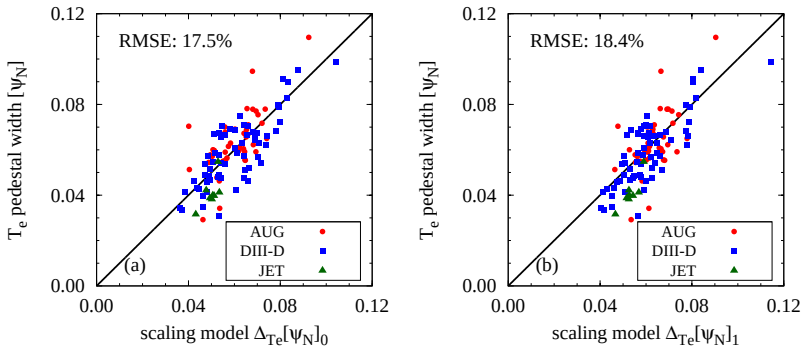

Figure 7.7: Log-linear regression applied to temperature pedestal width in Ψ_N for AUG (circle, red), DIII-D (square, blue) and JET (triangle, green). Two different regression models are used: with 6 dimensionless parameters (a) and two significant parameters (b).

is performed with the dimensionless quantities $\beta_{\mathrm{p,ped}}$, $\rho_{\mathrm{i}\star}$ and additionally $\nu_{\mathrm{i}\star}$, κ, f_{q} and $T_{\mathrm{e,ped}}/T_{\mathrm{i,ped}}$. The regression to all these parameters yields that most of them do not have a significant influence on the electron temperature pedestal width in normalized poloidal flux coordinates:

$$\Delta_{Te}[\Psi_{\mathrm{N}}]_0 = 0.77 \cdot \rho_{\mathrm{i}\star}^{-0.01\pm0.30} \nu_{\mathrm{i}\star}^{-0.12\pm0.10} \beta_{\mathrm{p,ped}}^{0.49\pm0.19} f_{\mathrm{q}}^{-0.03\pm0.59} \kappa^{-4.03\pm1.09} \left(\frac{T_{\mathrm{e,ped}}}{T_{\mathrm{i,ped}}}\right)^{0.05\pm0.19} . \quad (7.1)$$

Most of the parameters appear insignificant in the regression since their exponent is not two times larger than its uncertainty. This leaves only two relevant parameters in this selection and the scaling becomes

$$\Delta_{Te}[\Psi_{\mathrm{N}}]_1 = 0.42 \cdot \kappa^{-2.59\pm0.85} \beta_{\mathrm{p,ped}}^{0.51\pm0.09} \qquad \text{RMSE: } 18.4\% \quad (7.2)$$

In Figure 7.7 both scalings are illustrated and they show little differences which suggests the selection of parameters was reasonable. Adding the elongation improved the RMSE by 15% which is quite large considering the rather small available range $1.59 < \kappa < 1.88$. For the AUG and DIII-D data fitted individually also a similar dependence with the elongation κ^k was found with $k_{\mathrm{AUG}} = -1.43 \pm 2.62$ and $k_{\mathrm{DIII\text{-}D}} = -2.24 \pm 1.57$. Because of the reduced range in the analysis with individual machines, κ does not appear statistically relevant in this case, but the exponents match those of the multi-machine scaling within the uncertainties. In Section 6.1 the parameter correlations between $\beta_{\mathrm{p,ped}}$, $\rho_{\mathrm{i}\star}$ and $\nu_{\mathrm{i}\star}$ were described. Therefore, the parameters were exchanged for one another in the regression, with the result that in all cases the quality of the fit deteriorated compared to Eq. (7.2). This would suggest a real $\beta_{\mathrm{p,ped}}$ dependence of the temperature pedestal width in normalized poloidal flux coordinates. However, small widths width $\Delta_{Te} < 0.05$ appear systematically overestimated by the scaling. Therefore, the width is further investigated with scalings to the factors of the dimensionless parameters. The factors are the four independent parameters machine size, magnetic field, temperature and density and they are extended with the elongation κ, as this parameter was found to be significant in Eq. (7.2). The resulting regressions improve the fit to the data significantly

$$\Delta_{Te}[\Psi_{\mathrm{N}}]_2 = 0.025 \cdot a^{-0.56\pm0.28} \langle B_{\mathrm{p}} \rangle^{-0.93\pm0.20} T_{\mathrm{e,ped}}^{0.62\pm0.11} n_{\mathrm{e,ped}}^{0.54\pm0.15} \kappa^{-2.30\pm1.16} \quad (7.3)$$

RMSE: 16.0%

$$\Delta_{Te}[\Psi_{\mathrm{N}}]_3 = 0.047 \cdot a^{-0.59\pm0.28} \langle B_{\mathrm{p}} \rangle^{-0.73\pm0.23} T_{\mathrm{e,ped}}^{0.72\pm0.12} n_{\mathrm{e,ped}}^{0.41\pm0.17} \kappa^{-2.62\pm1.17} \left(\frac{T_{\mathrm{e,ped}}}{T_{\mathrm{i,ped}}}\right)^{-0.46\pm0.23}$$

RMSE: 14.2% (7.4)

The fit quality can be improved by more than 10% with inclusion of the temperature ratio $T_{\mathrm{e}}/T_{\mathrm{i}}$ which is above the improvement expected for uncorrelated parameters. In Figure 7.8 the quality of both regressions is shown, once without the ion temperature (a) and with the ion temperature (b). The extended scaling (b) shows a uniform distribution around the experimental data and an overall improvement compared to the dimensionless case. This is also observed in the reduction in the RMSE of over 20%. The reason for this difference is the broken coupling between temperature and magnetic field in Eq. (7.4) contrary to $\beta_{\mathrm{p,ped}}$ in Eq. (7.2). This can be illustrated with a an extension of the dimensionless case which then gives the same improved RMSE and alignment with the measurements as does the dimensional description

$$\Delta_{Te}[\Psi_{\mathrm{N}}] \propto \beta_{\mathrm{p,ped}}^{0.35\pm0.11} \kappa^{-2.80\pm1.04} T_{\mathrm{i,ped}}^{0.36\pm0.14} a^{-0.56\pm0.28} \qquad \text{RMSE: } 14.5\%. \quad (7.5)$$

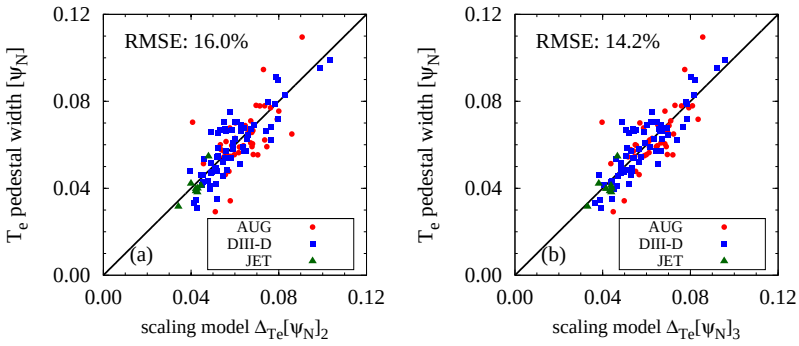

Figure 7.8: Log-linear regression applied to pedestal widths in Ψ_N for AUG (circle, red), DIII-D (square, blue) and JET (triangle, green). The temperature pedestal width is plotted against different regression functions.

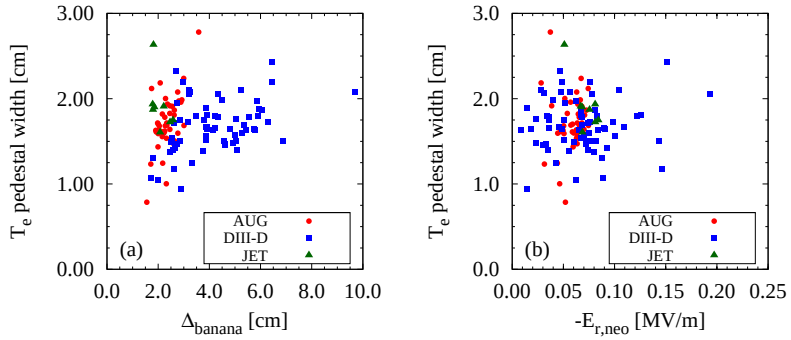

Figure 7.9: Temperature pedestal width in real space at the outer midplane plotted against the uncorrected banana width (a) and the calculated radial electric field well depth (b) for AUG (circle, red), DIII-D (square, blue) and JET (triangle, green).

This is essentially the same form as Eq. (7.4)) and illustrates a reduced dependence on poloidal field and pedestal density compared to the dimensionless description in Eq. (7.2)).

The comparison of Eq. (7.2) and Eq. (7.4) with Eq. (5.5) suggests that a significant fraction of the pedestal width variation observed in Ψ_N coordinates will vanish when going to real space coordinates. In Ψ_N coordinates the pedestal width varies more than a factor of 4. In real space coordinates this variation is reduced to roughly a factor of 2.5. A significant fraction of the difference in total variation can be explained with the influence of the magnetic shaping f_q on the coordinate transformation Eq. (5.5). This reduction in variation hampers the possibility to apply a regression analysis to this data set, because the influences of different parameters are too small to be significantly above the uncertainties. Therefore, for the real space coordinates only single parameter dependencies are explored. In the discussion about the dimensionless pedestal width it was found that $\Delta_{Te}[\Psi_N]$ and $\Delta_{Te}[r/a]$ showed little correlation with normalized toroidal Larmor radius in Figure 7.6. The investigation of the individual engineering parameters suggested that Δ_{Te} is dependent on temperature and poloidal magnetic field, but not on the toroidal magnetic field B_t. In Figure 7.9 (a) the temperature pedestal width is plotted against the poloidal gyroradius or the banana width $\Delta_{banana,m} \propto T_{i,ped}^{0.5}/\langle B_p \rangle$ as in Eq. (3.5). No correlation is visible between

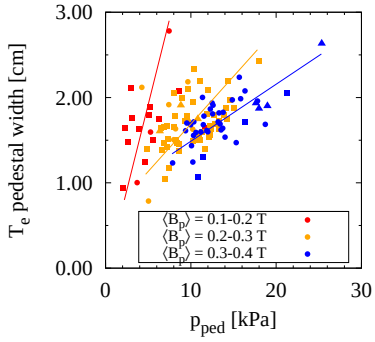

Figure 7.10: Pedestal width of T_e plotted against p_ped. The data is color coded for different ranges of $\langle B_\mathrm{p}\rangle$. The different symbols denote the three machines (AUG: circle, DIII-D: square, JET: triangle). The lines are drawn to guide the eye.

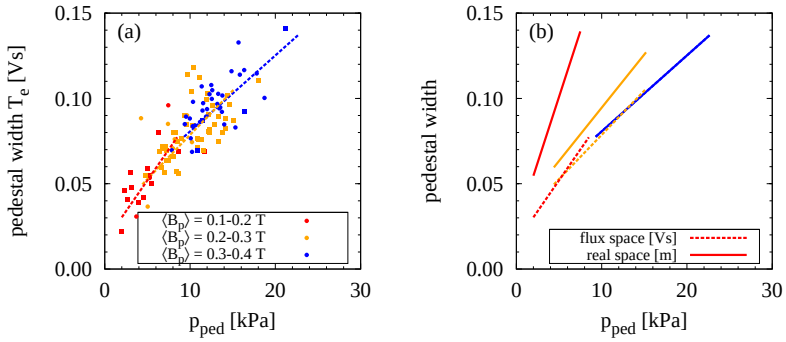

Figure 7.11: T_e pedestal width for AUG (circle) and DIII-D (square) in flux coordinates plotted against the total pedestal pressure and color coded for different ranges of $\langle B_\mathrm{p}\rangle$. On the right side it is indicated how the flux space trend (dashed) would appear in real space (solid) when simply applying a single $\partial\Psi_\mathrm{maj}/\partial R$ for each colored trend. The coordinate transformation is normalized to the high $\langle B_\mathrm{p}\rangle$ case.

$\Delta_{T\mathrm{e}}$ and $\Delta_\mathrm{banana,m}$, however, the corrections due to orbit squeezing, as described in Section 3.1, could not be applied. Without reliable measurements of the radial electric field shear the correction is not defined well enough. In Figure 7.9 (b) the radial electric field shear is crudely estimated with the radial electric field well depth. No correlation is visible between the temperature pedestal width and $E_\mathrm{r,neo} \propto \nabla p_\mathrm{i}/n_\mathrm{e} - (\beta_1, g_\mathrm{2i})\nabla T_\mathrm{i}$, where p_i is approximated according to Eq. (7.10) and (β_1, g_2i) is calculated after Eq. (2.41) in [9]. For more robust conclusions, about a correlation of the ion orbit width and the electron pedestal width, accurate measurements about the radial electric field shear are necessary. With the limited possibilities of the available database no indication for such a correlation was found.

In the single parameter representations of the pedestal width, with $\beta_\mathrm{p,ped}$ in $[\Psi_\mathrm{N}]$ (Figure 7.6 (a)) and $\Delta_\mathrm{banana,m}$ in [m] (Figure 7.9), one finds the pedestal width dependence with the pedestal pressure is changing for different poloidal magnetic fields $\langle B_\mathrm{p}\rangle$. In Figure 7.10 this is illustrated with different color coding for three poloidal field intervals and the usual symbols represent the different machines. For low $\langle B_\mathrm{p}\rangle$ the pedestal width increases more strongly with pedestal pressure than it is the case for large poloidal fields. This separating of the width-pressure correlation could be explained if the width were determined in poloidal

flux space. When considering only AUG and DIII-D the machine size dependence can be neglected. The temperature pedestal width shows a strong correlation with the pedestal top pressure and is separated in $\langle B_\mathrm{p}\rangle$. As known from Eq. (5.2), $\partial\Psi_\mathrm{maj}/\partial R$ depends linearly on the poloidal field. Therefore, when transformed to real space the pedestal appears to be wider when $\partial\Psi_\mathrm{maj}/\partial R$ is smaller. This is illustrated in Figure 7.11 in three stages: The pedestal width shows a distinct trend with p_ped (a). The measurements are again color coded according to their poloidal field and the width p_ped correlation is indicated with dashed lines. Each interval of $\langle B_\mathrm{p}\rangle$ is associated with an average $\partial\Psi_\mathrm{maj}/\partial R$ which increases by a factor of two over the three regimes. Then trends of the width with p_ped are transformed into real space with this approximation. The result is indicated with solid lines in Figure 7.11 (b) and shows the same effect as was initially observed in Figure 7.10 for real space coordinates. Therefore, the effects visible in the other coordinates might only be an artifact of the coordinate transformation or the normalisation of the flux with global parameters. The observations would suggest the un-normalized flux space is important for the spatial extent of the steep gradient region, however, no available theory explains such a correlation.

7.2.2 Electron Density

This section is an overview of the electron density pedestal width in different coordinates. The section is closely connected to the section about the electron temperature width. They were only separated for a better overview of the relevant results. The argumentation is to large parts the same as in Section 7.2.1, therefore, it will not be repeated and only the differences with the electron temperature width are highlighted.

Figure 7.12 shows an overview of the correlations between the density pedestal width Δ_{ne} in dimensionless form and the dimensionless parameters $\beta_\mathrm{p,ped}^{0.5}$ (a),(c) and $\rho_{\mathrm{i}\star}$ (b),(d). The differences to $\Delta_{T\mathrm{e}}$ are: the separation of the different regimes observed in the plots with $\beta_\mathrm{p,ped}$ becomes more pronounced for Δ_{ne} in Figure 7.12 (a),(c) compared to Figure 7.6 (a),(c). Δ_{ne} shows a strong correlation with $\rho_{\mathrm{i}\star}$ for DIII-D and JET, in particular, for normalized real space coordinates. However, AUG does not fit within this picture and shows a larger pedestal width. The comparison with $c\beta_\mathrm{p,ped}^{0.5}$ would give the following coefficients c: 0.11 ± 0.01 (AUG only), 0.080 ± 0.015 (DIII-D only) and 0.09 ± 0.02 (all machines) with an RMSE of 22.5%.

The regression analysis of the density pedestal width in $[\Psi_\mathrm{N}]$ suggests a stronger influence of $\rho_{\mathrm{i}\star}$ on Δ_{ne} which is in contrast to the electron temperature width, where $\beta_\mathrm{p,ped}$ appeared to be more important in the regression.

$$\Delta_{ne}[\Psi_\mathrm{N}]_0 = 3.54 \cdot \rho_{\mathrm{i}\star}^{0.61\pm0.15} \nu_{\mathrm{i}\star}^{0.18\pm0.06} f_\mathrm{q}^{1.14\pm0.43} \kappa^{-2.07\pm0.83} \beta_\mathrm{p,ped}^{0.14\pm0.15} \left(\frac{T_\mathrm{e,ped}}{T_\mathrm{i,ped}}\right)^{0.05\pm0.17} \tag{7.6}$$

RMSE: 13.9%

$$\Delta_{ne}[\Psi_\mathrm{N}]_1 = 2.90 \cdot \rho_{\mathrm{i}\star}^{0.65\pm0.12} \nu_{\mathrm{i}\star}^{0.18\pm0.05} f_\mathrm{q}^{1.45\pm0.29} \kappa^{-1.78\pm0.75}. \tag{7.7}$$

RMSE: 14.3%

The strong influence of the magnetic shaping f_q on the pedestal width might originate from the coordinate transformation from real space (see Eq. (5.5)). Or the f_q dependence is physical and only vanishes when observing the pedestal width in real space. The strong negative dependence of Δ_{ne} on the plasma elongation is similar to what was found for $\Delta_{T\mathrm{e}}$.

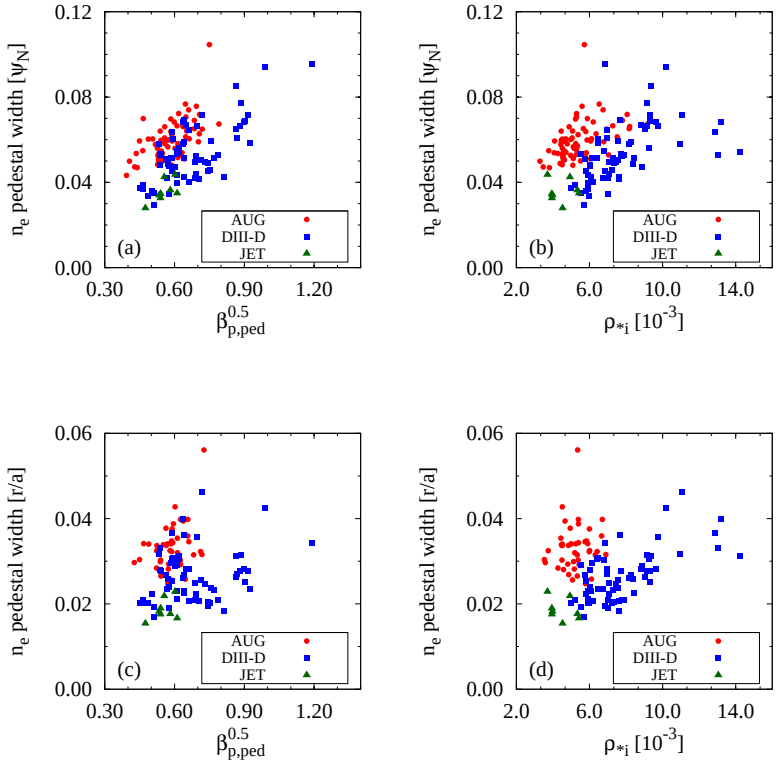

Figure 7.12: The density pedestal width in normalized coordinates of AUG (circle, red), DIII-D (square, blue) and JET (triangle, green) plotted against the square root of the normalized poloidal pedestal pressure (a),(c) and the normalized toroidal gyroradius (b),(d). Note that the abscissa is not starting at zero.

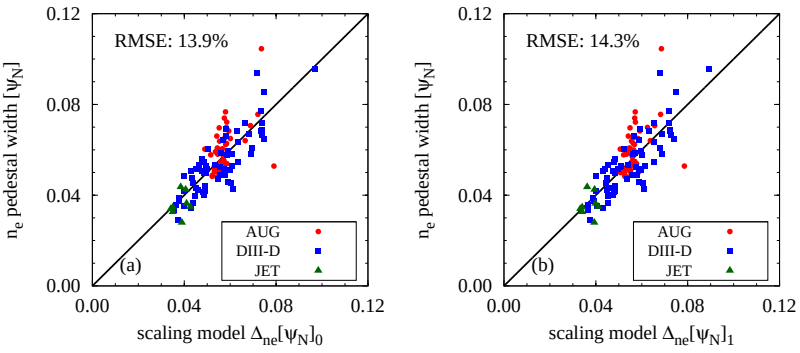

Figure 7.13: Log-linear regression applied to density pedestal width in Ψ_N for AUG (circle, red), DIII-D (square, blue) and JET (triangle, green). Two different regression models are used: with 6 dimensionless parameters (a) and 4 significant parameters (b).

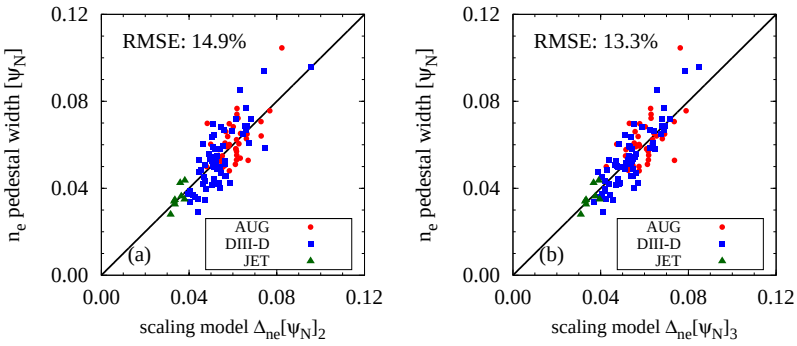

Figure 7.14: Log-linear regression applied to pedestal widths in Ψ_N for AUG (circle, red), DIII-D (square, blue) and JET (triangle, green). The density pedestal width is plotted against different regression functions.

In the regression $\kappa^{-1.78}\nu_{i\star}^{0.18}$ account for larger pedestal width of AUG for a given $\rho_{i\star}$ which can be observed in Figure 7.12 (b). In Figure 7.13 the two dimensionless regressions are illustrated and show a nice match with the experimental data and an RMSE which is over 20% smaller as for electron temperature width. This would suggest the model in Eq. (7.7) is better suited to describe the measurements of Δ_{ne} than it was the case for Δ_{Te} and Eq. (7.2). In the case of the pure $c\beta_{p,ped}^{0.5}$ model the match with the measurements was about 50% worse than the model $\Delta_{ne}[\Psi_N]_1$.

The regressions with the engineering parameters become

$$\Delta_{ne}[\Psi_N]_2 = 0.011 \cdot a^{-0.67\pm0.19}\langle B_p\rangle^{-1.01\pm0.22}T_{e,ped}^{0.37\pm0.09}n_{e,ped}^{0.51\pm0.15}\kappa^{-1.43\pm0.81} \tag{7.8}$$

RMSE: 14.9%

$$\Delta_{ne}[\Psi_N]_3 = 0.011 \cdot a^{-0.73\pm0.20}\langle B_p\rangle^{-1.30\pm0.25}T_{e,ped}^{0.45\pm0.10}n_{e,ped}^{0.65\pm0.16}\kappa^{-1.49\pm0.81}q_{cyl}^{-0.42\pm0.17}. \tag{7.9}$$

RMSE: 13.3%

Here the differences to the electron temperature are again visible. As in the dimensionless case Δ_{ne} shows a negative correlation with the toroidal magnetic field B_t which is inherited in q_{cyl} or $\rho_\star$. No dependence of Δ_{ne} on the temperature ratio T_e/T_i was observed which is different to the electron temperature pedestal width. The exponent of the elongation appears again strongly negative and also different from the one in the electron temperature regression. As discussed in Section 7.2.1 the large uncertainty in this exponent can only be reduced with a larger variation of κ in the database. The plot with the regressions, in Figure 7.14, shows a nice alignment with the measurements for the whole database.

In real space coordinates the density pedestal width is compared to the uncorrected banana width $\Delta_{banana,m}$ and the radial electric field depth $E_{r,neo}$ as indicator for the orbit squeezing. In Figure 7.15 (a) the density pedestal width shows no correlation with $\Delta_{banana,m}$. Furthermore, no machine size dependence is observed in the data set for real space coordinates. The minor radius dependence found in normalized coordinates vanishes or appears due to the coordinate transformation. The radial electric field depth in the steep gradient region shows a trend with Δ_{ne} (b) where the pedestal width decreases for larger $E_{r,neo}$. This would correspond to the effect expected from orbit squeezing. However, it might also be a result of $1/n_e$ included in $E_{r,neo}$. A $1/n_{e,ped}$ correlation of the density pedestal width would be expected when the density pedestal is governed by neutral penetration processes as described

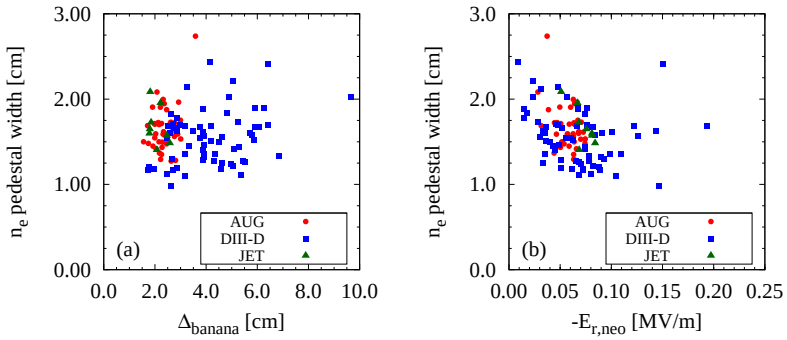

Figure 7.15: Density pedestal width in real space at the outer midplane plotted against the uncorrected banana width (a) and the calculated radial electric field well depth (b) for AUG (circle, red), DIII-D (square, blue) and JET (triangle, green).

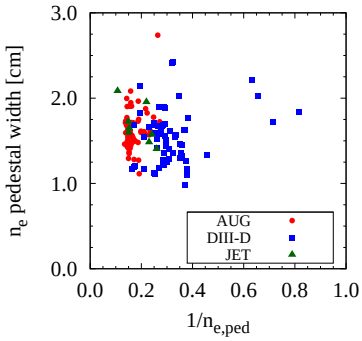

Figure 7.16: Density pedestal width in real space at the outer midplane plotted against one over the pedestal top density for AUG (circle, red), DIII-D (square, blue) and JET (triangle, green).

in Section 3.1.2. In Figure 7.16 the real space pedestal width is plotted against the inverse of the pedestal top density and no correlation is found which would support an influence of the neutral penetration in the pedestal. This is no contradiction to the example shown in Figure 7.4 from [54]. In the DIII-D, JET comparison less discharges were included and those experiments had similar conditions in the SOL. The neutral penetration is strongly dependent on the parameters in the SOL which vary significantly over the database and were not documented within the database.

7.2.3 Ion Temperature

The ion temperature pedestal width is important to asses the influence of ion orbit losses on the pedestal. In the previous sections also Δ_{Te} and Δ_{ne} were tested against the orbit losses, but only because it was assumed the pedestal width of the three quantities is coupled. A problem is that the ion temperature pedestal width cannot be determined with an accuracy comparable to the electron temperature and density. Two reasons for this are the inferior time resolution and problems of measuring outside of the separatrix. In the SOL the CXRS signal is strongly influenced by background radiation and therefore, no ion temperatures are available in this region - an example for this was given in the diagnostics chapter Figure

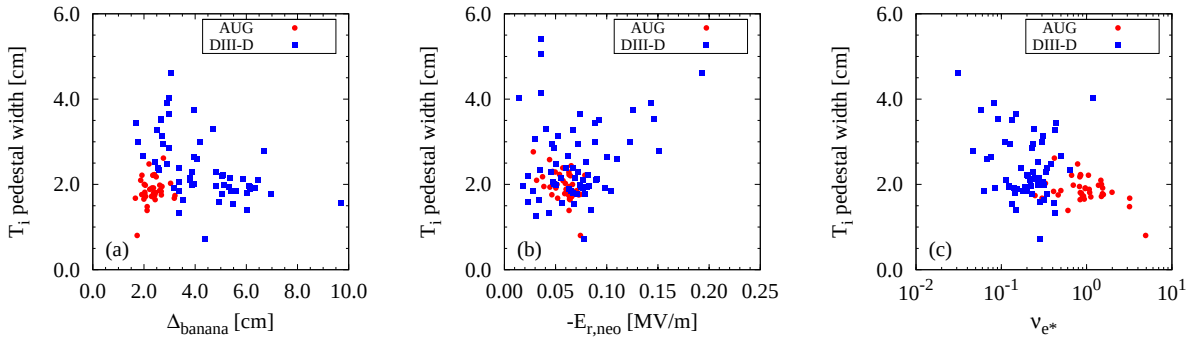

Figure 7.17: Ion temperature pedestal width in real space at the outer midplane plotted against the uncorrected banana width (a), the calculated radial electric field well depth (b) and the electron collisionality (c) for AUG (circle, red) and DIII-D (square, blue).

4.9 (a). Other measurements of the ion temperature in the SOL are not routinely available. Therefore, the definition used in this section for the ion temperature pedestal width is the distance between pedestal top and the separatrix. The separatrix is defined by the magnetic equilibrium.

In the data set of AUG and DIII-D no correlation between $\Delta_{T\mathrm{i}}$ and the banana width is found. In Figure 7.17 (a) the ion temperature pedestal width is plotted against the uncorrected banana width and the width does not change for large banana widths. Quite contrary, the pedestal width increases only for small banana widths. A similar picture is found in (b), the width does not show a trend with the radial electric field, as one would expect when orbit squeezing is involved. These observations would not suggest any effect of the ion orbit losses on the pedestal width of the ion temperature. In Figure 7.17 (c) it is shown that the trend of the pedestal width is strongly correlated with the electron collisionality of the plasma. At high collisionality $\Delta_{T\mathrm{i}}$ is of the order of $\Delta_{T\mathrm{e}}$, while they can differ by more than a factor of 2 at low collisionality. This would suggest that the ion temperature pedestal width is coupled with the electron temperature width at high collisionalities. At low collisionalities $\Delta_{T\mathrm{i}}$ can deviate from the T_e width and is not set by ion orbit losses. However, the uncertainty in determining the pedestal width for T_i are quite large and lead to a limitation of the significance of these results.

7.3 Pedestal Gradients

The gradients in the pedestal are important for different aspects in pedestal physics. The pressure gradient is often regarded in connection with the MHD stability of ELMs. But also the gradients of temperature and density are individually important independently of the pressure. For example the bootstrap current depends on the ratio of temperature and density gradients [40]. For transport mechanisms also temperature and density gradients play an essential role (see e.g. appendix of [16]). In this section the dependencies of temperature, density and pressure gradient are discussed.

In Figure 7.18, an interesting feature of the pedestal gradients is illustrated, namely, the gradients are strongly correlated with the pedestal top values. In particular, the electron

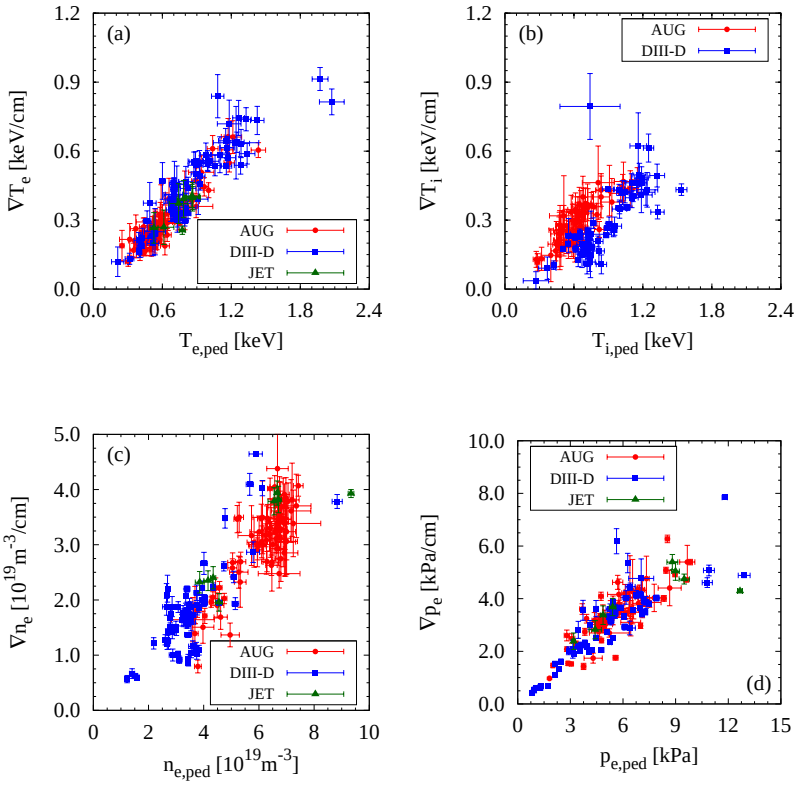

Figure 7.18: Mean real space gradient in the steep gradient zone of the pedestal plotted against the pedestal top value of electron temperature (a), ion temperature (b), electron density (c) and electron pressure (d).

pedestal top temperature (a) shows a solid trend with the temperature gradient in the pedestal for the whole data base with all three machines. The temperature gradient scales linearly with the pedestal top temperature and gives $T_{e,ped}/\nabla T_e \sim 2$ cm regardless of other plasma parameters like I_p, B_t, $\nu_\star$ or the machine size. For the electron density (c) also a strong correlation between top value and gradient is found which is consistent for all machines. The difference to the electron temperature is the broader distribution in $n_{e,ped}$. This can be explained to some extent with the external gas puff. For AUG and JET it was observed that it is possible to increase the pedestal top density with a gas puff while not changing the pedestal gradient. See for example Figure 7.18 (c) at around $\nabla n_e = 4 \cdot 10^{19}$ m^{-3}/cm: the high density discharge of JET was performed with 10 times larger gas puff than the discharges at lower density. In Section 7.4.1 it will be shown that the effect of the gas puff on the pedestal top density is limited. The electron pedestal pressure (d) shows a similar correlation with its gradient as temperature and density. This correlation between pedestal top and real space gradient would suggest a constant pedestal width in real space coordinates. A constant real space pedestal width is in agreement with the observations made in Section 7.2. An ion temperature pedestal width defined as $T_{i,ped}/\nabla T_i$ would be roughly constant for each machine, but significantly larger for DIII-D than for AUG. This is because the ion temperature gradient in DIII-D discharges is significantly lower than ∇T_i at AUG for the same $T_{i,ped}$ - this is visible in Figure 7.18 (b). The smaller ion temperature gradient at DIII-D is not only observed in the machine comparison but also in comparison to the electron temperature. At AUG electron and ion temperature have a comparable relation between pedestal top value and gradient which is illustrated in Figure 7.19 (a). For DIII-D

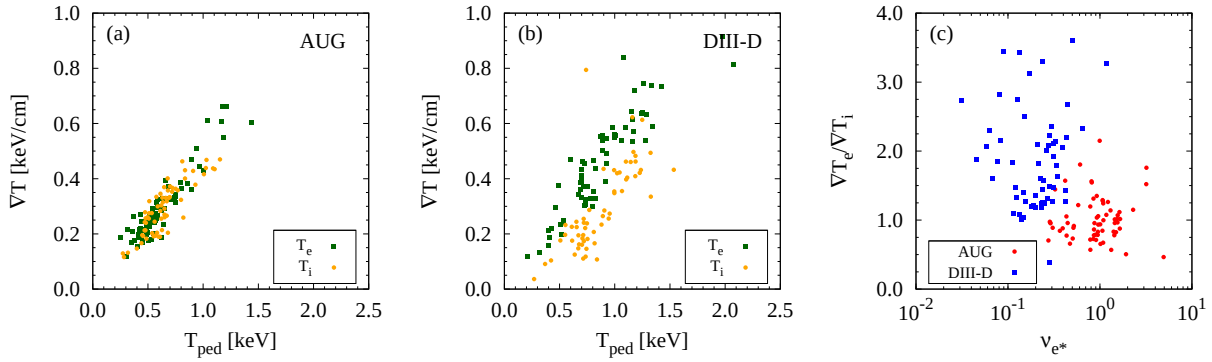

Figure 7.19: Pedestal gradient versus pedestal top temperature for electrons (green,square) and ions (orange,circle) with the discharges from AUG (a) and DIII-D (b). The ratio of electron and ion gradients as function of the electron collisionality (c).

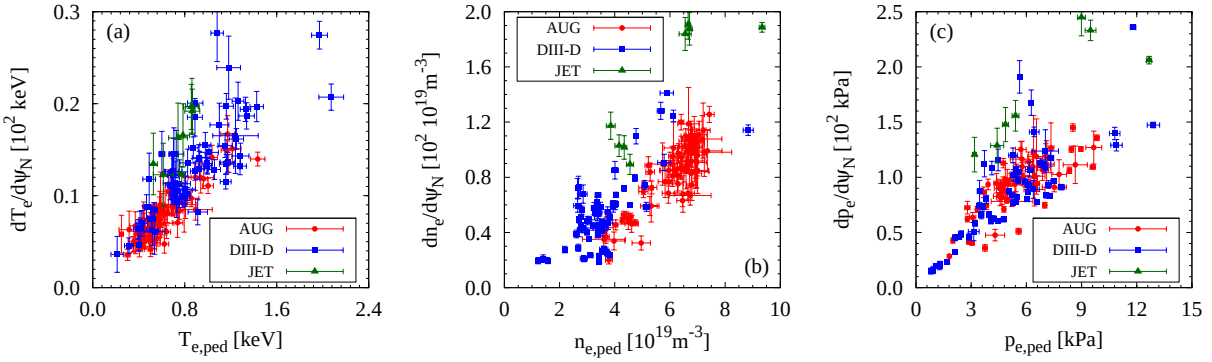

Figure 7.20: Mean gradient in normalized poloidal flux coordinates plotted against the pedestal top value of electron temperature (a), electron density (b) and electron pressure (c).

(b) the ion temperature gradient is significantly lower than ∇T_e for comparable temperatures. The reason for the different observations at AUG and DIII-D might be connected with the collisionality in the plasma. With the high collisionalities in AUG T_e and T_i appear to be closely coupled and at DIII-D with lower collisionality electrons and ions can scale separately. In Figure 7.19 (c) this is illustrated with the gradient ratio of T_e and T_i plotted against $\nu_{e\star}$. Although the scatter is quite large, a trend to larger ratios for lower collisionality is observed. While most AUG discharges with $\nu_{e\star} > 0.3$ lie between a gradient ratio of 0.5 and 1.5, the discharges with lower $\nu_{e\star}$ from DIII-D lie all above 1.0.

Some theories are not applicable in real space coordinates, but need normalized flux coordinates. In particular, the peeling-ballooning theory requires normalized quantities. In Figure 7.20 an intermediate step towards a dimensionless representation is plotted. This is not directly relevant for a MHD based theory like peeling-ballooning, however, illustrates the differences between real space and normalized poloidal flux coordinates Ψ_N. The temperature gradient $\partial T_e/\partial \Psi_N$ in (a) still shows a trend with the pedestal top temperature, but the scatter in the data is significantly larger than it was for real space coordinates in Figure 7.18 (a). The density in Figure 7.20 (b) shows a trend between pedestal top value and gradient in normalized flux coordinates for individual machines, but is not consistent for all three

machines. The shape of the pressure gradient $\partial p_e/\partial \Psi_N$, plotted against the pedestal top electron pressure in (c), is similar to an arrow head. This would suggest an upper and lower limit of $p_{e,ped}$ at constant gradient which correspond to a large variation in the pedestal width. In particular, a variation larger than inferred from Figure 7.18 (d) for the real space gradients.
The normalisation leading to a dimensionless pressure gradient α was introduced in Section 2.1 as

$$\alpha \equiv -\frac{1}{2\pi^2}\frac{\partial V}{\partial \Psi}\left(\frac{V}{2\pi^2 R_0}\right)^{1/2}\mu_0\frac{\partial p}{\partial \Psi}.$$

This equation is used to calculate the values for α throughout this section. However, different expressions can be used for the total pressure gradient $\partial p/\partial \Psi$. Often the total pressure is taken as $2p_e$, the normalized pressure gradient calculated with this approximation will be called α_e. This approximation is reasonable for AUG, but is a poor choice for DIII-D as was illustrated in Figure 7.19. The differences in electron and ion temperature are taken into account in an improved approximation:

$$\frac{\partial p}{\partial \Psi} \sim \left(1 + \frac{1}{2}\frac{\frac{\partial T_i}{\partial \Psi}}{\frac{\partial T_e}{\partial \Psi}} + \frac{1}{2}\frac{T_{i,ped}}{T_{e,ped}}\right)\frac{\partial p_e}{\partial \Psi}. \tag{7.10}$$

This approximation is using $Z_{eff} = 1$ for the reasons discussed in Section 6 and implies a constant pedestal width for T_e and n_e in real space. The normalized pressure gradient calculated with Eq. (7.10) will be called α_{ei}. A profile of p_i was not used in this thesis because no alignment procedure was applied to the ion temperature with respect to the electron density. In Figure 7.21 the normalized pressure gradient is plotted against the three dimensionless physics variables $\beta_{p,ped}$, $\rho_{i\star}$ and $\nu_{i\star}$. The differences between α_e (a)-(c) and α_{ei} (d)-(f) are not large, however, the match between AUG and DIII-D at low α is improved when using α_{ei}. All three dimensionless parameters show strong correlations with the normalized gradient. α_{ei} increases strongly with $\beta_{p,ped}$ (d). A similar trend is observed for $\rho_{i\star} < 1.0 \cdot 10^{-2}$, for larger $\rho_{i\star}$ the normalized gradient drops again. The larger the collisionality (f) becomes, the smaller α_{ei} becomes. For low collisionalities $\nu_{i\star} < 0.4$ there is no correlation with the normalized gradient. Comparing AUG and DIII-D reveals differences in the trends. The normalized pressure gradient measured at AUG shows the largest correlation with the collisionality. In the case of DIII-D the correlation is strongest between $\beta_{p,ped}$ and α_{ei}.
From simulations it is expected that larger normalized gradients are possible with stronger shaping [99]. In Figure 7.22 α_{ei} is plotted against the geometric and magnetic plasma shape. In (a) the mean triangularity δ shows no direct correlation with α_{ei}, however, for $\delta > 0.5$ significantly larger normalized pressure gradients are possible than at low triangularity. In the peeling-ballooning theory this would suggest stronger shaping can alter the stability boundary, however, the operational point does not necessarily lie at the optimal (highest α) location. In Figure 7.22 (b), the shaping factor f_q is strongly correlated with α_{ei}. The trend with the normalized gradient is similar as the one with $\beta_{p,ped}$, this could be expected from the observations made in Section 6.
In Section 3.1.3 it was described how the normalized pressure gradient should scale with the normalized pressure in the presence of kinetic ballooning modes. Therefore, in Figure 7.23 α_{ei} is divided by $\beta_{p,ped}^{0.5}$ and tested for remaining dependencies which might be lost due to approximations in the theory. In (a) it is found that a strong correlation with $\rho_{i\star}$

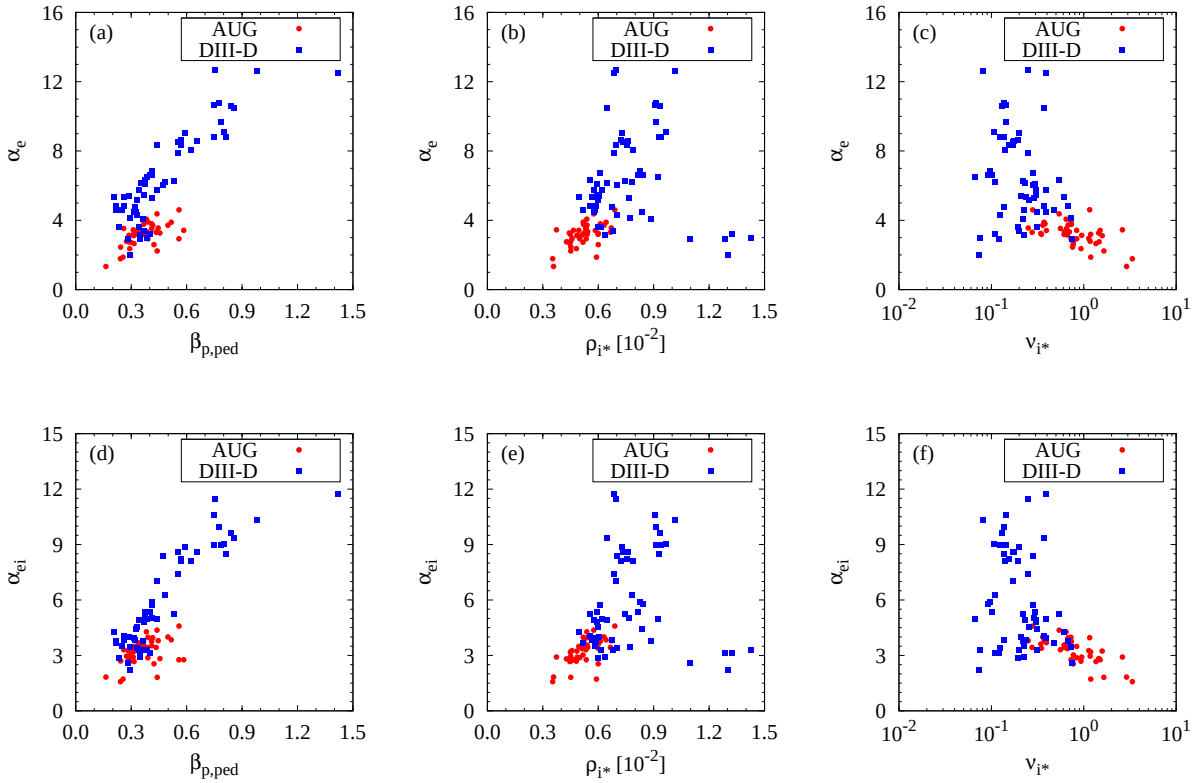

Figure 7.21: Normalized pressure gradient against (a),(d) normalized pressure, (b),(e) normalized gyro radius and (c),(f) normalized collision frequency. Two different approximations are used for the normalized pressure gradient (a)-(c) $p = 2p_e$ and (d)-(f) with Eq. (7.10).

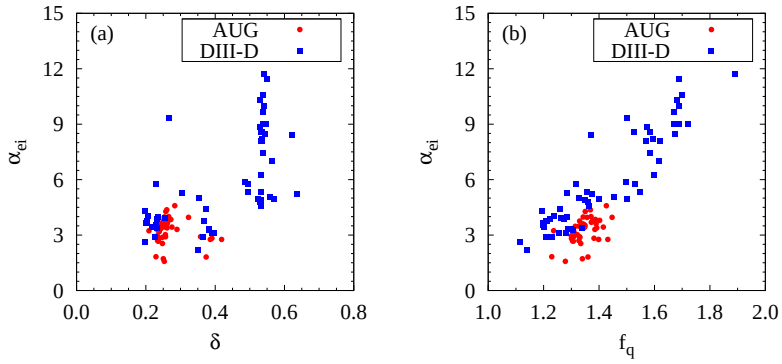

Figure 7.22: Normalized pressure gradient plotted against the mean triangularity δ (a) and the shaping factor $f_q = q_{95}/q_{cyl}$ (b).

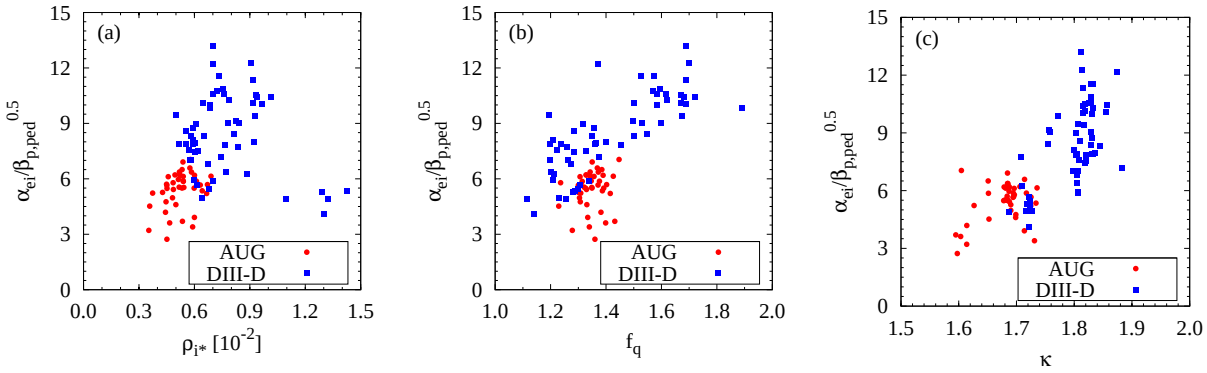

Figure 7.23: Normalized pressure gradient divided by $\beta_{\mathrm{p,ped}}^{0.5}$ and plotted against $\rho_{\mathrm{i}\star}$ (a), the shaping factor $f_{\mathrm{q}} = q_{95}/q_{\mathrm{cyl}}$ (b) and the plasma elongation (c).

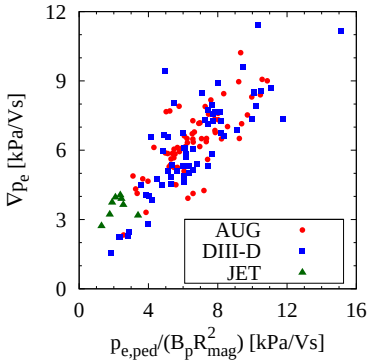

Figure 7.24: Pressure gradient in flux coordinates versus a modified pedestal pressure to match the units [kPa/Vs].

remains for $\rho_{\mathrm{i}\star} < 1.0 \cdot 10^{-2}$ and in (b) a strong correlation with f_{q} is observed for DIII-D data. The plasma elongation κ, in (c), shows a very strong correlation with the normalized pressure gradient, despite the small variation in plasma elongation. The results suggest these parameters play an important role for the physics in the pedestal besides $\beta_{\mathrm{p,ped}}$. This is similar to the observations made for the pedestal width.

The pedestal gradients can be decently described in dimensionless form (Figure 7.21), however, the real space gradients were better described by a single quantity namely the pedestal top value (Figure 7.18). Therefore, it seems reasonable to find a representation with the correct units as in the dimensionless case and the nice correlations found for the real space gradients. In Figure 7.24 the pressure gradient in flux coordinates is plotted against the pedestal top pressure divided by $B_{\mathrm{p}}R_{\mathrm{mag}}^2$, which has the units of magnetic flux [Vs]. Both quantities show a nice correlation. However, this representation would suggest a major radius dependence of the pedestal width which would contradict the observations made in Section 7.2 and in the first paragraph of this section.

To summarize: A strong correlation was found between pedestal top value and the gradients in real space. This would suggest a constant real space width without machine size dependence which is consistent with the results of direct pedestal width analysis. The proportionality between $T_{\mathrm{e,ped}}$ and ∇T_{e} is not only independent of the machine size but also independent of the collisionality, normalized pressure, magnetic field and plasma current.

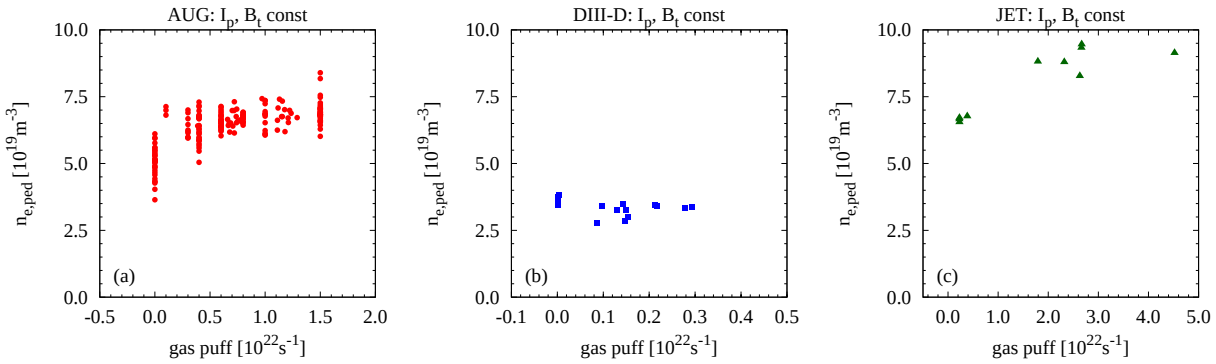

Figure 7.25: Influence of the gas puffing rate on the pedestal top density at constant plasma current and toroidal field for AUG (a), DIII-D (b) and JET (c). Note the different ranges for the gas puff.

The relation between $T_{\mathrm{i,ped}}$ and ∇T_{i} is not so robust and varies with collisionality, where lower $\nu_\star$ corresponds to smaller gradient. The relation between $n_{\mathrm{e,ped}}$ and ∇n_{e} could be varied with the gas puff level. The normalized pressure gradient α was found to be correlated with all three dimensionless physics variables $\beta_{\mathrm{p,ped}}$, $\rho_\star$ and $\nu_\star$. A correlation of $\alpha \propto \beta_{\mathrm{p,ped}}^{0.5}$ as suggested by KBM theory in Section 3.1.3 could not be reproduced, $\alpha/\beta_{\mathrm{p,ped}}^{0.5}$ varies by a factor of 4 and is strongly correlated with low $\rho_\star$ and with f_{q}.
It has to be stressed that this relation between pedestal top and pedestal gradient is no artifact of the analysis method. In Section 5.3.4 several tests were performed and no correlation between pedestal top and gradient was imposed by the applied method, as can be seen in Figure 5.19 in the middle column for the two-line method.

7.4 Pedestal Top

The efforts to understand the mechanisms of the pedestal width and gradients in the previous sections aimed towards a first principle prediction of the pedestal top. However, as was shown in Chapter 3 most theoretical predictions inherit approximations which restrict the capability of these predictions. In this section the properties of the pedestal top values are characterized empirically for temperature, density and pressure with engineering and dimensionless variables.

7.4.1 Electron Density

The density pedestal top value $n_{\mathrm{e,ped}}$ is influenced also by parameters which could not be quantified for each discharge in the database. Therefore, a consistent description of $n_{\mathrm{e,ped}}$ for all three machines is not possible. One of the main unknowns is the contribution of gas recycling from the wall. It has been shown at AUG that the gas inventory of the walls is influenced by preceding discharges [100]. The influence of different pumping is also not documented for the machines. For example, DIII-D is more flexible in terms of divertor pumping than AUG or JET. Therefore, it can reach lower neutral divertor pressures than the other machines. Whether this capability was utilized for the discharges of DIII-D or not was not documented in the database. Another unknown is the fuelling efficiency of gas puffing

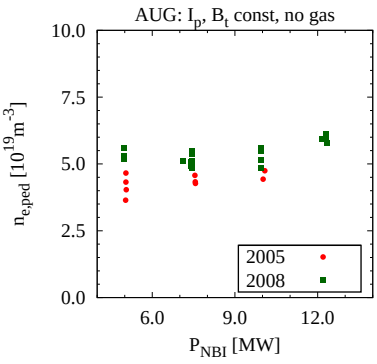

Figure 7.26: Influence of different wall materials on the pedestal top density. The discharges from the 2005 AUG campaign (red,circles) are done with mainly carbon first wall, those in 2008 (green,squares) are done with mainly tungsten as first wall material. In both cases no gas puffing was applied during the discharges.

systems. The absolute number of particles, puffed into the vacuum vessel, is easily compared for the different machines. However, the efficiency how these particles fuel the plasma is not known. In Figure 7.25 examples are shown how the gas puff can influence the pedestal top density at constant plasma current and magnetic field. For AUG (a) the gas puff is increased significantly at constant current $I_\mathrm{p} = 1.0$ MA and constant field $B_\mathrm{t} = -2.5$ T. An effect of additional gas puffing is only visible at relatively low rates ($< 0.5 \cdot 10^{22} s^{-1}$), above these rates more puffing does not affect the pedestal top density any more. This does not mean the high gas puffing rates do not influence the plasma edge. One example was shown in Figure 2.11 (a) where the ELM frequency increased for larger gas puff. The gas puffing applied at DIII-D is generally significantly lower than the one at AUG. At the rates applied at DIII-D (b) no influence on the pedestal top density is observed for $I_\mathrm{p} = 0.9$ MA and $B_\mathrm{t} = -1.7$ T. The conversion between the units used at DIII-D is 1 torr l/s $\sim 1 \cdot 10^{19}$ particles/s. The effect of the gas puff in JET (c) is similar to the observation made at AUG: an influence of the gas puff is only visible at low rates. For larger rates $n_\mathrm{e,ped}$ seems to saturate at a maximum value despite increasing gas puff rates. This example also shows that the particle puff rates have different effects on different machines. A possible explanation could be different fuelling efficiencies of the gas puffs, however, those are unknown. Additionally, the wall material does seem to influence the pedestal top density. In Figure 7.26 discharges from two campaigns are compared: in 2005 the wall was mainly carbon (red,circles), in 2008 the first wall was mainly tungsten (green,squares). Discharges with the same plasma current, same toroidal field and without any gas puffing are selected. The discharges performed with tungsten wall have a systematically larger density. A reason for this might be different deuterium recycling properties of carbon and tungsten [100], however, the details of the material properties are beyond the scope of this work. Different impurity concentrations in the plasma might also have influence on the electron density. Addition of nitrogen to the plasma caused a reduction of the electron density with increasing effective charge number Section 2.1.2. Another difference between the discharges is the heating with ICRH and ECRH. The discharges from the 2005 campaign were assisted by ICRH, while the discharges in the 2008 campaign were heated with ECRH. However, no effects of ICRH and ECRH heating on the pedestal top density could be identified within the database at DIII-D and JET. Therefore, a different wall material seems to be a likely explanation for the different pedestal electron densities.

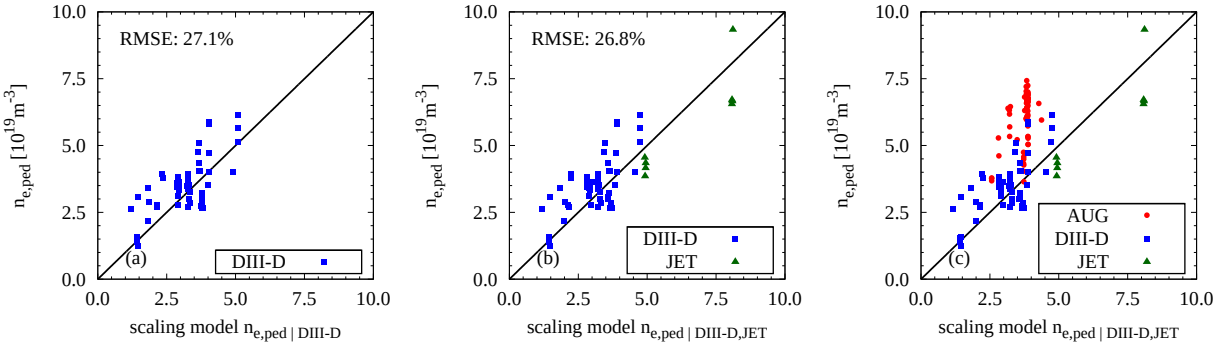

Figure 7.27: Visualisation of Eq. (7.11) in (a) and Eq. (7.12) in (b),(c).

Despite the rather unclear effect of the gas fuelling on the pedestal top density a crude estimate can be given with knowledge of the plasma current and the magnetic field. For DIII-D alone one finds with a log-linear regression analysis

$$n_{\mathrm{e,ped}}|_{\mathrm{DIII\text{-}D}} = 2.7 \cdot I_{\mathrm{p}}^{0.9\pm0.2} B_{\mathrm{t}}^{0.4\pm0.2} \qquad \text{RMSE: 27.1\%,} \tag{7.11}$$

the exponents remain similar within the uncertainties when including data from JET

$$n_{\mathrm{e,ped}}|_{\mathrm{DIII\text{-}D,JET}} = 2.4 \cdot I_{\mathrm{p}}^{0.8\pm0.1} B_{\mathrm{t}}^{0.5\pm0.1} \qquad \text{RMSE: 26.8\%.} \tag{7.12}$$

In Figure 7.27 the results of Eq. (7.11) (a) and Eq. (7.12) (b) are shown for the database. The model describes the data only with an RMSE of over 25%. However, for the regression analysis with only DIII-D data (a) a similar result is obtained as in the case with DIII-D and JET data (b). The pedestal top density of AUG does not fit within the same scheme and lies up to 50% above $n_{\mathrm{e,ped}}$ of DIII-D and JET discharges with the same plasma current and toroidal field. This is likely due to the different wall materials of the devices. The discharges performed in a Carbon AUG, the lowest red circles in Figure 7.27 (c), lie very close to what would be expected by the scaling derived from DIII-D and JET.

To summarize, several influences on the pedestal density are not easily quantified. Therefore, the trends given in this section represent mainly the available machines and give at best an estimate of the various dependencies. The scalings are most likely not capable for any extrapolation to other machines.
The observations about the pedestal top electron density were: gas puffing does increase $n_{\mathrm{e,ped}}$ up to a certain value, above this level gas puffing does not seem to affect the pedestal density further. The threshold level is different for each machine and lies around $2 \cdot 10^{21}$ s^{-1} for AUG and $2 \cdot 10^{22}$ s^{-1} for JET, at DIII-D no effect of the gas fuelling could be observed. The AUG discharges with the tungsten wall show larger $n_{\mathrm{e,ped}}$ than those with the carbon wall. The different wall materials could be the reason why the electron density of AUG (tungsten), DIII-D (carbon) and JET (carbon) cannot be described in a consistent way - with the available parameters. For the analysed data of DIII-D and JET it was found that $n_{\mathrm{e,ped}}$ scales strongly with plasma current I_{p} and toroidal magnetic field B_{t}, but no machine size dependence could be identified. This is different to previous comparisons with AUG (carbon) and JET (carbon) where a machine size dependence was suggested [101]. The density dependence on the plasma current, found in that study, was similar to the one in Eq.

(7.12) but the B_t dependence in the DIII-D, JET comparison is significantly weaker than in the AUG, JET comparison. The density pedestal top at Alcator C-Mod showed a nearly linear dependence with the plasma current [102] as was the case for Eq. (7.12), but showed a negative exponent for the toroidal magnetic field. This is different from the observations made at AUG, DIII-D and JET.

7.4.2 Electron Temperature

The pedestal top value of the electron temperature $T_{e,ped}$ is of special interest. Because of profile stiffness, any improvement at the edge strongly influences the whole plasma core as described in Chapter 2. The main mechanism to influence the plasma temperature is auxiliary heating. In general, a higher heating power results in a higher pedestal electron temperature. This is true for the data shown in Figure 6.2 (d). However, there are also limiting factors like heat transport and plasma instabilities. Above a certain heating power instabilities appear in the plasma which limit the electron temperature. One example for such an instability are ideal ballooning modes which limit the pressure gradient and therefore also the maximal temperature [20]. The discharges used in the database are generally performed within these stability boundaries, therefore, the limits on temperature at certain heating power will not appear in the data set. Another difficulty is the distribution of the heating power in the electron and ion channel. For AUG type-I ELMy H-modes the collisionality is generally large enough to guarantee equal heat distribution in both electron and ion channel. The discharges from JET in the database also fulfill this criteria. For most DIII-D discharges this is not the case as was discussed in Section 6.2. This suggests the heating power will not be sufficient to describe the electron temperature of DIII-D. Therefore, the regression analysis of the electron temperature will be restricted to AUG and JET only.

The electron temperature at the pedestal top for AUG discharges with high collisionality is reasonably well described with

$$T_{e,ped}\big|_{AUG} = 1.3 \cdot n_{e,ped}^{-1.3\pm0.1} P_{heat}^{0.7\pm0.1} I_p^{0.9\pm0.1} \qquad \text{RMSE: 12.3\%,} \tag{7.13}$$

which gives a distinct correlation between heating power, plasma current and pedestal temperature for a known electron density. Including also JET data in the regression results in a very similar scaling

$$T_{e,ped}\big|_{AUG,JET} = 0.4 \cdot n_{e,ped}^{-1.0\pm0.1} P_{heat}^{0.6\pm0.1} I_p^{0.8\pm0.1} a^{-1.3\pm0.1} \qquad \text{RMSE: 13.3\%} \tag{7.14}$$

where the density dependence is slightly less negative and the heating power dependence is fairly unchanged. The machine size had to be included to account for the different plasma volume. Intuitively one would think, heating a larger plasma volume with the same power gives only a lower temperature. The same would be valid for larger density. The exponents of heating power and minor radius can be rewritten in a way and giving $(P_{heat}/a^2)^{0.6}$ which corresponds to a power flux. This would suggest an influence of the heat transport on the pedestal temperature. The dependence on the plasma current can be connected to the stabilising effect of I_p on pressure limited MHD instabilities in the plasma core as reported for JET and INTOR (Troyon limit) [103]. In Figure 7.28 (a) and (b) the regressions of Eq. (7.13) and Eq. (7.14) show a good agreement with the experimental data. In Figure 7.28 (c) the experimental data of DIII-D is plotted against the scaling derived from AUG and

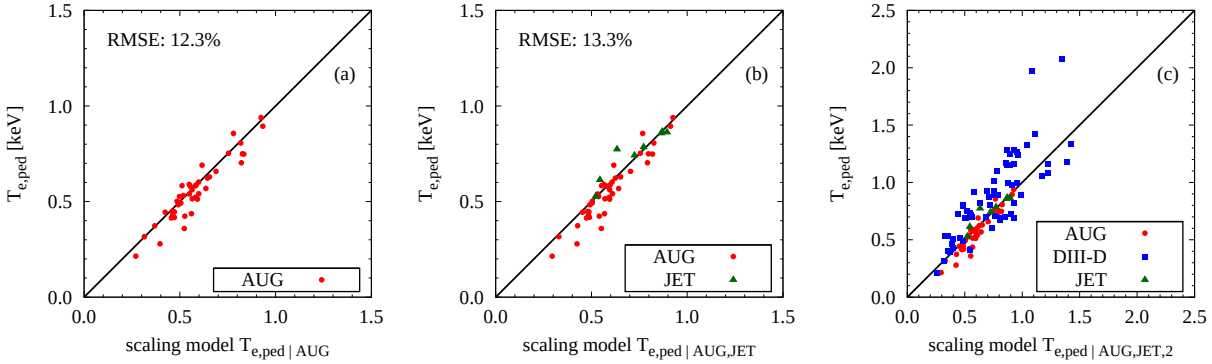

Figure 7.28: Visualisation of Eq. (7.13) in (a) and Eq. (7.14) in (b),(c) using engineering variables.

JET. The experimental $T_{\mathrm{e,ped}}$ values show a fairly good overall agreement with the scaling. However, there are also some outliers which have significantly different electron and ion temperatures what might explain their deviation from the other discharges. More energy in the electron channel gives larger electron temperatures while the ion temperatures stay on a lower level. Therefore, these measurements do not fit to the AUG and JET data where the energy was equally distributed in the ions and electrons.

In Summary, the pedestal top electron temperature can be described with heating power, electron density and plasma current. However, this simple model is only valid when the heating power is equally distributed in the electron and ion channels which is the case for AUG and JET at high collisionality. The measurements of DIII-D follow the trend derived at high collisionality fairly well, however, when electron and ion temperature deviate in the pedestal also the deviation from the scaling becomes maximal. Further influences on $T_{\mathrm{e,ped}}$, especially due to the plasma shape, could not be identified in the given data set.

7.4.3 Pedestal Pressure

The pedestal top values of electron temperature and density were discussed in the previous sections and it was found that a consistent treatment of all three machines AUG, DIII-D and JET is difficult. However, many theories do expect a trend with the plasma pressure $p = nT$ rather than with the electron temperature and density separately as described in Chapter 3. The scaling derived for the electron temperature in Eq. (7.13) appears in a form which would also allow scalings to $n_{\mathrm{e,ped}}T_{\mathrm{e,ped}}$ rather than only $T_{\mathrm{e,ped}}$. Therefore, in this section the dependencies of the electron and ion pedestal pressure as well as the total pedestal pressure $p_{\mathrm{ped}} = p_{\mathrm{e,ped}} + p_{\mathrm{i,ped}}$ are investigated. First the pressure itself is analysed in dimensional and dimensionless form and then derived quantities like W_{MHD} and τ_{E} are discussed.
In Section 7.4.2 it was found that heating power and magnetic field play an important role for the plasma pressure. The calculated value for $p_{\mathrm{e,ped}}$ from fits to T_{e} and n_{e} gives a good approximation for the value of $p_{\mathrm{e,ped}}$ determined by a fit to the pressure profile. Figure 7.29 shows $p_{\mathrm{e,ped}}$ plotted versus $n_{\mathrm{e,ped}}T_{\mathrm{e,ped}}$ which is not necessarily the same because the pedestal top positions of density and temperature do not have to be identical. Both methods to determine the pedestal pressures match very well, because the density is generally flat within the pedestal top and the temperature pedestal top lies generally at smaller radii than the

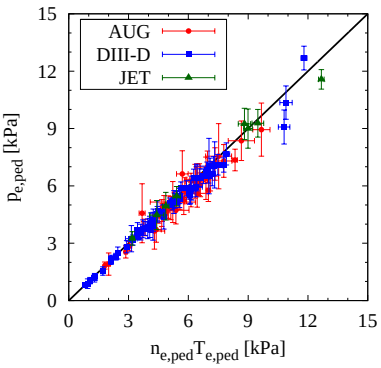

Figure 7.29: Comparison of pedestal pressure from a fit to p_e and calculated from fits to T_e and n_e.

density pedestal top. Therefore, Eq. (7.14) could already give the answer how the electron pressure should scale, however, in this section the regression is done with $p_{e,ped}$ values from fits to p_e profiles. The ion pressure is calculated with the approximation off $Z_{eff} = 1$ as $p_{i,ped} = n_{e,ped}T_{i,ped}$. In the previous sections only the relevant regressions were shown. This is changed for this section to give a better overview of the various correlations in the data set and the differences between the machines. The regressions are listed Table 7.1. The regressions with only data from AUG data show that the pedestal pressure can be fitted reasonably well already with the two parameters: heating power P_{heat} and averaged poloidal field $\langle B_p \rangle$. This is shown in Table 7.1 rows 1,15 and 29. Adding more parameters in the regression does not improve the fit quality significantly for the electron pressure and the total pressure. The dependencies become only distributed between the parameters, but do not include new information. This happens due to correlations of two or more parameters which is the case for the poloidal field and the density. This becomes visible in rows 2 and 3 or 16,17 or 30,31. In these cases the fit quality remains the same but the exponents of $\langle B_p \rangle$ and $n_{e,ped}$ do vary, but also cancel the changes as expected from Section 7.4.1. This suggests the use of $n_{e,ped}$ in the regression does not give new information. Later in this section it will be described how this correlation can be broken with data from more than one machine. The regressions, including the toroidal field B_t, suggest this is a parameter which holds additional information besides P_{heat} and $\langle B_p \rangle$. By adding B_t in the regression, the RMSE is reduced while the other exponents are unchanged (rows 1,2 and 15,16 and 29,30). The improvement of fit quality is most pronounced for the ion pressure in rows 15,16.
Rows 2,16 reveal differences between the electron and the ion pressure at AUG. While the electron pressure is more strongly dependent on the heating power the ion pressure is influenced more strongly by the magnetic field. The exponents for the total pressure $p_{ped} = p_{e,ped} + p_{i,ped}$ lie in between $p_{e,ped}$ and $p_{i,ped}$. The best fits to the AUG data with the least variables are

$$p_{e,ped}|_{AUG} = 0.66 \cdot P_{heat}^{0.95\pm0.04} \langle B_p \rangle^{0.22\pm0.13} B_t^{0.47\pm0.18} \quad \text{RMSE: } 12.0\% \quad (7.15)$$

$$p_{i,ped}|_{AUG} = 3.34 \cdot P_{heat}^{0.61\pm0.06} \langle B_p \rangle^{1.15\pm0.15} B_t^{0.77\pm0.21} \quad \text{RMSE: } 12.9\% \quad (7.16)$$

$$p_{ped}|_{AUG} = 3.94 \cdot P_{heat}^{0.78\pm0.07} \langle B_p \rangle^{0.80\pm0.21} B_t^{0.49\pm0.33} \quad \text{RMSE: } 10.5\% \quad (7.17)$$

All three scalings fit the AUG data very well and are illustrated in Figure 7.30. The magnetic shaping factor f_q was deliberately ignored in the best-fit scalings for AUG. As described in Section 6.3, the AUG discharges in the data set lie in the same regime of shaping and therefore f_q does not contain additional information. This becomes evident in Table 7.1

		AUG	DIII-D	JET	const.	P_{heat}	$\langle B_{\mathrm{p}} \rangle$	B_{t}	$n_{\mathrm{e,ped}}$	f_{q}	RMSE
1	$p_{\mathrm{e,ped}}$	x	-	-	1.05	0.94	0.24	-	-	-	12.5
2	$p_{\mathrm{e,ped}}$	x	-	-	0.66	0.95	0.22	0.47	-	-	12.0
3	$p_{\mathrm{e,ped}}$	x	-	-	1.78	0.94	0.54	0.45	-0.31	-	11.9
4	$p_{\mathrm{e,ped}}$	x	-	-	0.46	0.70	0.43	0.63	0.15	2.43	11.4
5	$p_{\mathrm{e,ped}}$	x	-	-	3.04	0.93	0.59	-	-0.34	-	12.3
6	$p_{\mathrm{e,ped}}$	x	-	-	0.73	0.74	0.52	0.59	-	1.98	11.4
7	$p_{\mathrm{e,ped}}$	x	-	-	1.25	0.78	0.48	-	-	1.52	12.1
8	$p_{\mathrm{e,ped}}$	-	x	-	48.14	0.30	2.00	-	-	-	36.6
9	$p_{\mathrm{e,ped}}$	-	x	-	11.03	0.39	1.25	0.39	-	-	29.1
10	$p_{\mathrm{e,ped}}$	-	x	-	1.28	-0.02	0.19	1.43	0.64	-	33.7
11	$p_{\mathrm{e,ped}}$	-	x	-	3.33	0.16	0.93	0.33	0.45	1.97	15.2
12	$p_{\mathrm{e,ped}}$	-	x	-	42.68	0.35	1.94	-	-0.04	-	35.3
13	$p_{\mathrm{e,ped}}$	-	x	-	16.07	0.46	1.74	-0.51	-	2.22	21.0
14	$p_{\mathrm{e,ped}}$	-	x	-	6.20	0.49	1.15	-	-	1.52	19.3
15	$p_{\mathrm{i,ped}}$	x	-	-	6.33	0.60	1.11	-	-	-	15.2
16	$p_{\mathrm{i,ped}}$	x	-	-	3.34	0.61	1.15	0.77	-	-	12.9
17	$p_{\mathrm{i,ped}}$	x	-	-	19.14	0.60	1.75	0.76	-0.53	-	12.9
18	$p_{\mathrm{i,ped}}$	x	-	-	12.64	0.50	1.78	0.85	-0.38	1.03	13.2
19	$p_{\mathrm{i,ped}}$	x	-	-	40.57	0.59	1.76	-	-0.56	-	15.0
20	$p_{\mathrm{i,ped}}$	x	-	-	3.83	0.41	1.52	0.94	-	2.01	13.2
21	$p_{\mathrm{i,ped}}$	x	-	-	6.29	0.61	1.10	-	-	-0.05	15.2
22	$p_{\mathrm{i,ped}}$	-	x	-	13.20	0.42	1.33	-	-	-	35.9
23	$p_{\mathrm{i,ped}}$	-	x	-	2.23	0.15	0.20	1.17	-	-	32.0
24	$p_{\mathrm{i,ped}}$	-	x	-	1.47	0.07	0.01	1.35	0.15	-	32.1
25	$p_{\mathrm{i,ped}}$	-	x	-	3.37	-0.17	0.65	0.69	0.22	2.47	16.6
26	$p_{\mathrm{i,ped}}$	-	x	-	19.74	0.53	1.35	-	-0.46	-	37.5
27	$p_{\mathrm{i,ped}}$	-	x	-	6.08	-0.04	0.91	0.43	-	2.41	17.9
28	$p_{\mathrm{i,ped}}$	-	x	-	11.45	-0.03	1.33	-	-	3.01	18.9
29	p_{ped}	x	-	-	6.66	0.77	0.85	-	-	-	11.3
30	p_{ped}	x	-	-	3.94	0.78	0.80	0.49	-	-	10.5
31	p_{ped}	x	-	-	13.41	0.78	1.18	0.47	-0.40	-	10.5
32	p_{ped}	x	-	-	3.35	0.51	1.10	0.68	0.05	2.74	10.8
33	p_{ped}	x	-	-	22.93	0.77	1.25	-	-0.41	-	11.3
34	p_{ped}	x	-	-	3.94	0.53	1.13	0.67	-	2.55	10.8
35	p_{ped}	x	-	-	7.81	0.57	1.14	-	-	2.10	11.8
36	p_{ped}	-	x	-	10.09	0.59	0.81	-	-	-	24.9
37	p_{ped}	-	x	-	6.87	0.46	0.56	0.47	-	-	25.3
38	p_{ped}	-	x	-	3.45	0.38	0.29	0.62	0.28	-	23.7
39	p_{ped}	-	x	-	9.99	-0.05	0.97	0.39	0.30	2.48	12.5
40	p_{ped}	-	x	-	7.36	0.57	0.70	-	0.16	-	23.4
41	p_{ped}	-	x	-	20.54	0.04	1.26	0.23	-	2.46	14.3
42	p_{ped}	-	x	-	25.48	0.08	1.40	-	-	2.54	14.7

Table 7.1: Overview over different dependencies of $p_{\mathrm{e,ped}}$, $p_{\mathrm{i,ped}}$ and p_{ped} with the parameters P_{heat}, $\langle B_{\mathrm{p}} \rangle$, B_{t}, n_{e} and f_{q}. The numbers correspond to the exponents e_{n} as in Eq. (5.12). Only those parameters are included in the regression where exponents are given. The "x" indicates which data was used in the regression.

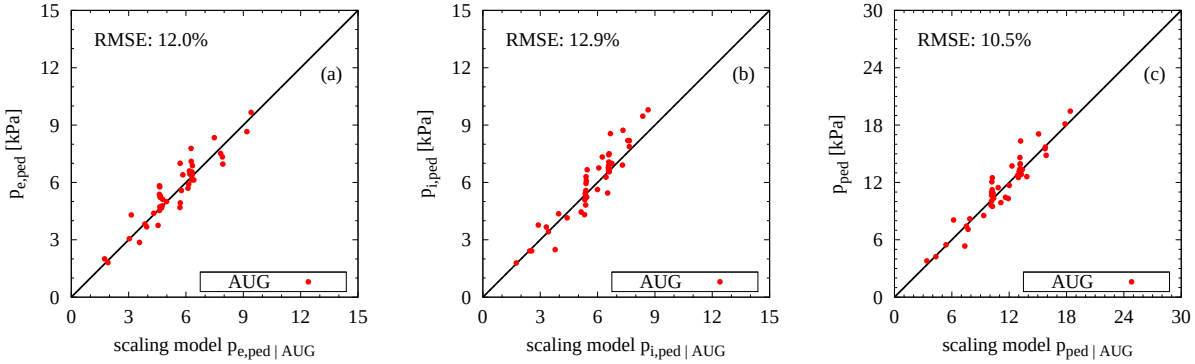

Figure 7.30: Visualisation of Eq. (7.15)-(7.17) in (a)-(c) for data from AUG.

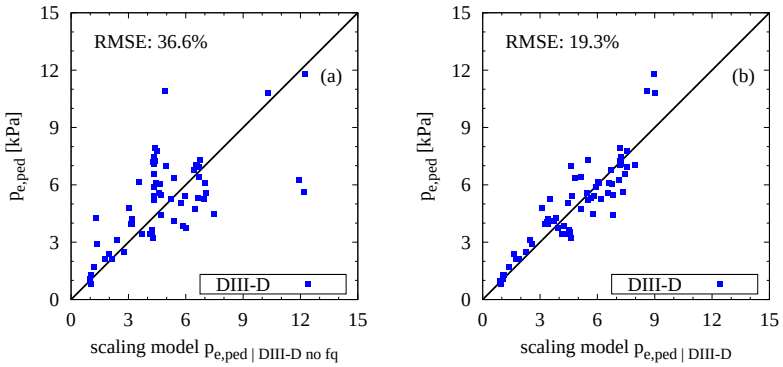

Figure 7.31: Effect of the shaping parameter f_q on the electron pressure in the DIII-D data set. In (a) the regression is done with P_{heat} and $\langle B_p \rangle$, in (b) also f_q is included in the regression.

where the regressions including f_q show only little improvement in the RMSE as for example in rows 2,6 or 3,4 in other cases the fit quality is even deteriorated with f_q as in rows 16,20 or 31,32. Another reason is the small range of f_q which results in large uncertainties of up to 100% of the exponent. This suggests, the exponent of f_q is random in the scalings with AUG data.

In the case of DIII-D data, f_q is not random and even essential for a decent fit to the pedestal pressure. This could be expected because two different regimes of triangularity exist at DIII-D where the pressure behaves differently as was was described in Section 6.3. In the regressions listed in Table 7.1, this is suggested by a comparison of the RMSEs. The regressions without f_q (e.g. rows 8,9,10,12) have all significantly larger errors than with f_q included (e.g. rows 11,13,14). In the cases without f_q the data does follow the scaling only poorly. In Figure 7.31 this is illustrated with the scalings for $p_{e,ped}$ of row 8 without f_q in (a) and of row 14 with f_q (b). While for AUG the addition of f_q did not show any effect (rows 1,7), the quality of the fit to DIII-D measurements is increased significantly from an RMSE of 36.6% to 19.3%. The shaping factor has a similar effect on $p_{i,ped}$ and p_{ped}. Since the regressions with an RMSE $\gg 20\%$ fit the measurements very poorly, exponents found for these case might not represent real trends within the dataset. This is the reason why those regressions are not discussed any further.
Besides the distinction in plasma shape also other differences can be observed in the compar-

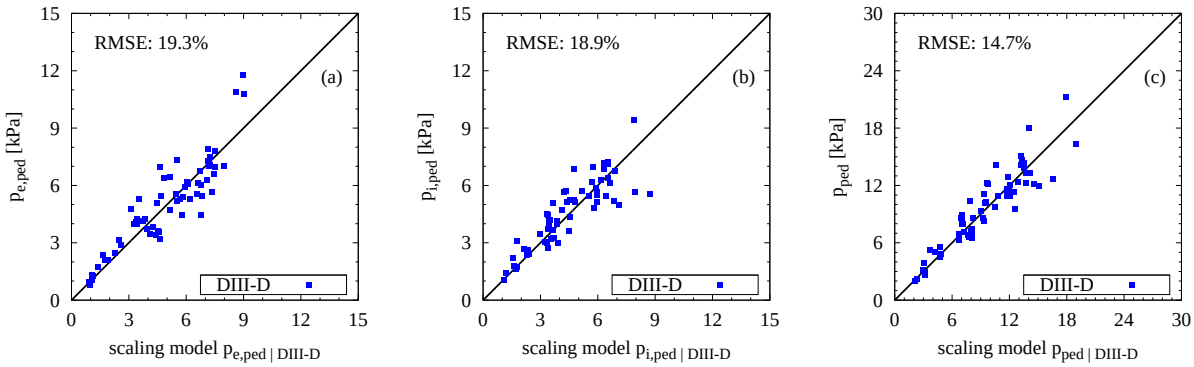

Figure 7.32: Visualisation of Eq. (7.18)-(7.20) in (a)-(c) for data from DIII-D.

ison of AUG and DIII-D. The dependence on heating power is weaker in the case of DIII-D while the dependence on the plasma current is stronger - examples are found in Table 7.1 rows 4,11, 7,14, 21,28 and 35,42. The observations made for AUG are also true for the DIII-D data set. This means the heating power shows less effect on $p_{\mathrm{i,ped}}$ compared to $p_{\mathrm{e,ped}}$ while the poloidal field is found to have a stronger impact on $p_{\mathrm{i,ped}}$. In the case of the ion and total pedestal pressure the regressions with the DIII-D data set would even suggest there is no influence of the heating power at all. A reason for this might be a different effect of the heating power in the two triangularity regimes, described in Section 6.3, which would suggest different properties of particle or heat transport. The results from the regression could suggest this to be only an indirect influence, with the shaping factor being the governing quantity. Another possible explanation originates from the different recovery of pedestal parameters in the ELM cycle [26] and will be discussed in Section 8.2.
For DIII-D the best fits with the least parameters are

$$p_{\mathrm{e,ped}}\big|_{\mathrm{DIII\text{-}D}} = 6.20 \cdot P_{\mathrm{heat}}^{0.49\pm0.02} \langle B_{\mathrm{p}} \rangle^{1.15\pm0.05} f_{\mathrm{q}}^{1.52\pm0.05} \qquad \text{RMSE: } 19.3\% \qquad (7.18)$$

$$p_{\mathrm{i,ped}}\big|_{\mathrm{DIII\text{-}D}} = 11.5 \cdot P_{\mathrm{heat}}^{-0.03\pm0.03} \langle B_{\mathrm{p}} \rangle^{1.33\pm0.05} f_{\mathrm{q}}^{3.01\pm0.09} \qquad \text{RMSE: } 18.9\% \qquad (7.19)$$

$$p_{\mathrm{ped}}\big|_{\mathrm{DIII\text{-}D}} = 25.5 \cdot P_{\mathrm{heat}}^{0.08\pm0.05} \langle B_{\mathrm{p}} \rangle^{1.40\pm0.09} f_{\mathrm{q}}^{2.54\pm0.19} \qquad \text{RMSE: } 14.7\% \qquad (7.20)$$

and are illustrated in Figure 7.32. The scaling for the total pressure (c) fits the measurements considerably better than the ones for $p_{\mathrm{e,ped}}$ and $p_{\mathrm{i,ped}}$. From the discussion in Section 7.4.2 this was to be expected, because the total pressure covers both electron and ion channel for the energy and not only a single one. For low collisionality the energy is likely not equally distributed in electron and ion channel.

Because of the different regimes covered with AUG, DIII-D and JET, multi-machine regressions are analysed. In Table 7.2 a overview is given of the regressions with different machines and the same parameters as in the one-machine analysis. The table is again for a general overview and only selected scalings are discussed. Scalings with an RSME $\gg 20\%$ fit the measurements only very poorly and the results should be handled with care. The first result catching the eye is that extending the AUG regressions with JET does not influence the outcome of the regressions. Within the uncertainties the exponents remain the same as in Table 7.1 and in particular, no machine size dependence is required to fit the pedestal pressure measurements of both machines. As suspected already from scalings with a single

		AUG	DIII-D	JET	const.	P_{heat}	$\langle B_{\mathrm{p}} \rangle$	B_{t}	$n_{\mathrm{e,ped}}$	f_{q}	RMSE
1	$p_{\mathrm{e,ped}}$	x	-	x	1.10	0.91	0.25	-	-	-	14.2
2	$p_{\mathrm{e,ped}}$	x	-	x	0.64	0.93	0.18	0.48	-	-	13.1
3	$p_{\mathrm{e,ped}}$	x	-	x	0.71	0.92	0.22	0.49	-0.04	-	13.2
4	$p_{\mathrm{e,ped}}$	x	-	x	1.16	0.83	0.50	0.38	-0.11	1.06	11.7
5	$p_{\mathrm{e,ped}}$	x	-	x	0.73	0.92	0.11	-	0.13	-	13.8
6	$p_{\mathrm{e,ped}}$	x	-	x	0.85	0.83	0.38	0.34	-	1.01	11.6
7	$p_{\mathrm{e,ped}}$	x	-	x	1.29	0.80	0.48	-	-	1.28	12.0
8	$p_{\mathrm{e,ped}}$	x	x	x	17.38	0.38	1.51	-	-	-	30.5
9	$p_{\mathrm{e,ped}}$	x	x	x	4.85	0.46	0.85	0.35	-	-	27.3
10	$p_{\mathrm{e,ped}}$	x	x	x	5.61	0.48	0.92	0.30	-0.04	-	26.9
11	$p_{\mathrm{e,ped}}$	x	x	x	5.50	0.42	1.23	-0.29	0.15	2.37	17.8
12	$p_{\mathrm{e,ped}}$	x	x	x	15.11	0.51	1.42	-	-0.15	-	27.7
13	$p_{\mathrm{e,ped}}$	x	x	x	9.20	0.51	1.46	-0.43	-	2.21	18.5
14	$p_{\mathrm{e,ped}}$	x	x	x	3.35	0.54	0.87	-	-	1.65	18.6
15	$p_{\mathrm{i,ped}}$	x	-	x	5.30	0.59	0.99	-	-	-	18.1
16	$p_{\mathrm{i,ped}}$	x	-	x	3.38	0.60	1.01	0.53	-	-	15.9
17	$p_{\mathrm{i,ped}}$	x	-	x	2.81	0.61	0.94	0.50	0.07	-	15.7
18	$p_{\mathrm{i,ped}}$	x	-	x	6.62	0.52	1.38	0.49	-0.14	0.94	14.4
19	$p_{\mathrm{i,ped}}$	x	-	x	2.14	0.60	0.69	-	0.29	-	17.1
20	$p_{\mathrm{i,ped}}$	x	-	x	4.28	0.54	1.19	0.45	-	0.76	14.3
21	$p_{\mathrm{i,ped}}$	x	-	x	6.73	0.50	1.26	-	-	1.09	15.2
22	$p_{\mathrm{i,ped}}$	x	x	x	9.95	0.44	1.20	-	-	-	28.9
23	$p_{\mathrm{i,ped}}$	x	x	x	4.61	0.37	0.74	0.39	-	-	27.8
24	$p_{\mathrm{i,ped}}$	x	x	x	10.43	0.47	1.02	0.27	-0.37	-	30.0
25	$p_{\mathrm{i,ped}}$	x	x	x	15.87	0.15	1.46	-0.13	-0.15	2.45	24.6
26	$p_{\mathrm{i,ped}}$	x	x	x	19.51	0.53	1.36	-	-0.43	-	31.7
27	$p_{\mathrm{i,ped}}$	x	x	x	12.40	0.09	1.40	-0.12	-	2.67	23.3
28	$p_{\mathrm{i,ped}}$	x	x	x	9.72	0.10	1.25	-	-	2.45	22.9
29	p_{ped}	x	-	x	6.16	0.73	0.76	-	-	-	14.2
30	p_{ped}	x	-	x	3.28	0.75	0.64	0.50	-	-	12.8
31	p_{ped}	x	-	x	3.32	0.75	0.64	0.50	-0.00	-	12.8
32	p_{ped}	x	-	x	7.31	0.63	1.06	0.21	-0.09	1.45	11.1
33	p_{ped}	x	-	x	3.32	0.74	0.56	-	0.20	-	13.5
34	p_{ped}	x	-	x	5.84	0.64	0.98	0.16	-	1.41	11.0
35	p_{ped}	x	-	x	7.31	0.62	1.05	-	-	1.58	11.4
36	p_{ped}	x	x	x	6.97	0.63	0.64	-	-	-	21.5
37	p_{ped}	x	x	x	6.83	0.63	0.63	0.01	-	-	21.5
38	p_{ped}	x	x	x	7.05	0.63	0.64	0.02	-0.01	-	21.5
39	p_{ped}	x	x	x	17.37	0.28	1.26	-0.20	0.06	2.12	15.8
40	p_{ped}	x	x	x	7.17	0.63	0.65	-	-0.01	-	21.5
41	p_{ped}	x	x	x	20.05	0.29	1.31	-0.19	-	2.10	16.1
42	p_{ped}	x	x	x	14.84	0.28	1.14	-	-	1.98	16.1

Table 7.2: Overview over different dependencies of $p_{\mathrm{e,ped}}$, $p_{\mathrm{i,ped}}$ and p_{ped} with the parameters P_{heat}, $\langle B_{\mathrm{p}} \rangle$, B_{t}, n_{e} and f_{q}. The numbers correspond to the exponents e_{n} as in Eq. (5.12). Only those parameters are included in the regression where exponents are given. The "x" indicates which data was used in the regression.

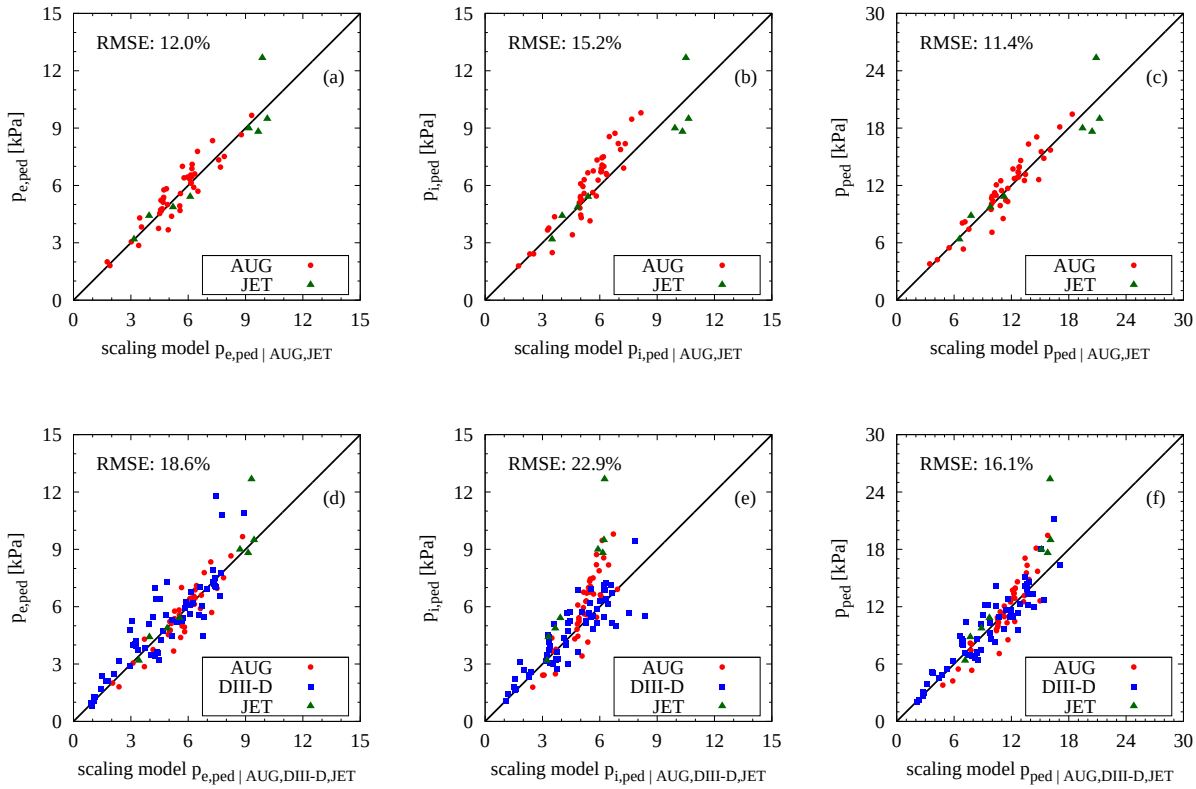

Figure 7.33: Illustration of the best fit regressions to $p_{\mathrm{e,ped}}$, $p_{\mathrm{i,ped}}$ and p_{ped} with data from different machines. In (a)-(c) only data from AUG and JET is used for the regression, in (d)-(e) DIII-D is included as third machine.

machine, the role of the pedestal top density is found to be insignificant. Evidence for this is found in Table 7.2 rows 2,3, 16,17, 30,31. In these examples the exponent of the density remains < 0.1 and also less than one $\sigma-$error and the fit to the data does not change at all by including $n_{\mathrm{e,ped}}$. In the multi-machine comparison $n_{\mathrm{e,ped}}$ cannot be expressed by the other parameters, in particular not by $\langle B_{\mathrm{p}} \rangle$ or I_{p} and B_{t}. How the density dependence with these parameters is broken in a machine comparison with AUG was discussed in detail in Section 7.4.1.

Including the pressure data of DIII-D in the regression alters the results to some extent. This is expected because with the addition of a different triangularity regime more information is available in the data set. For the $p_{\mathrm{e,ped}}$ scaling with all three machines a stronger $\langle B_{\mathrm{p}} \rangle$ dependence is found than for only AUG and JET (Table 7.2 rows 6,13 or 7,14). In the case of the total pressure the dependence with the poloidal field is fairly similar for two and three machines in rows 35,42. The dependence of the toroidal magnetic magnetic field with the pedestal pressure is not quite clear in the multi-machine comparison. The exponent ranges from -0.5 to 0.5 and in the case of the total pressure B_{t} turns out to be insignificant in the regression (rows 34,35 and 41,42). None of the ion pressure regressions to the data of all three machines fits the measurements reasonably well. Even the fit with smallest RMSE shows systematic deviations for AUG and JET data for high pressures. A possible reason for this might be the uneven energy distribution in electron and ion channels as described above. In the regressions, all three quantities $p_{\mathrm{e,ped}}$, $p_{\mathrm{i,ped}}$ and p_{ped} show less dependencies on the heating power when using data from all three machines instead of only AUG and JET.

At the same time, the magnetic shaping f_q becomes more important which was expected from the regressions with only DIII-D data. Without f_q the regressions, including DIII-D, show only a very poor match with the experimental data. Also with DIII-D data no machine size dependence in the pressure scalings is observed.
The best fits with the least parameters are illustrated in Figure 7.33 and given as formulas in the following

$$p_{e,ped}|_{AUG,JET} = 1.29 \cdot P_{heat}^{0.80\pm0.05} \langle B_p \rangle^{0.48\pm0.13} f_q^{1.28\pm0.30} \quad \text{RMSE: 12.0\%} \tag{7.21}$$

$$p_{e,ped}|_{AUG,DIII\text{-}D,JET} = 3.35 \cdot P_{heat}^{0.54\pm0.02} \langle B_p \rangle^{0.87\pm0.04} f_q^{1.65\pm0.04} \quad \text{RMSE: 18.6\%} \tag{7.22}$$

$$p_{i,ped}|_{AUG,JET} = 6.73 \cdot P_{heat}^{0.50\pm0.06} \langle B_p \rangle^{1.26\pm0.16} f_q^{1.09\pm0.37} \quad \text{RMSE: 15.2\%} \tag{7.23}$$

$$p_{i,ped}|_{AUG,DIII\text{-}D,JET} = 9.72 \cdot P_{heat}^{0.10\pm0.02} \langle B_p \rangle^{1.25\pm0.05} f_q^{2.45\pm0.08} \quad \text{RMSE: 22.9\%} \tag{7.24}$$

$$p_{ped}|_{AUG,JET} = 7.31 \cdot P_{heat}^{0.62\pm0.07} \langle B_p \rangle^{1.05\pm0.21} f_q^{1.58\pm0.40} \quad \text{RMSE: 11.4\%} \tag{7.25}$$

$$p_{ped}|_{AUG,DIII\text{-}D,JET} = 14.8 \cdot P_{heat}^{0.28\pm0.04} \langle B_p \rangle^{1.14\pm0.08} f_q^{1.98\pm0.16} \quad \text{RMSE: 16.1\%.} \tag{7.26}$$

Including geometrical shaping parameters, κ and δ, will improve the fit of the measurements by 2% and 4%. These improvements are below 5% each and therefore, they were discarded according to the rules set in Section 5.4. Both κ and δ showed positive exponents.

To summarize, the pedestal pressure was tested in log-linear regressions against the engineering parameters heating power P_{heat}, averaged poloidal magnetic field $\langle B_p \rangle$, toroidal magnetic field B_t, pedestal top density $n_{e,ped}$ and magnetic shaping f_q. An explicit machine size dependence, besides the one in $\langle B_p \rangle$, was not found for the pedestal pressure and therefore, it was not included in the detailed analysis. The density plays only a role in single machine regressions, because, within the data of one machine, it is correlated to I_p and/or B_t, in the multi-machine regressions $n_{e,ped}$ appears to be insignificant. The dependence on $\langle B_p \rangle$ or the plasma current I_p varies for the different scalings, however, for the total pressure a linear dependence is found in all cases. The correlation with the toroidal field is not so clear. While the measurements of AUG and JET show a robust trend with $\sqrt{B_t}$, the data of DIII-D shows strongly varying exponents for B_t and in the regression with all machines no dependence of p_{ped} on B_t is observed. AUG and JET show fairly similar dependence on the engineering parameters. This was found for the AUG only analysis and the combined AUG,JET analysis. DIII-D seems to have two regimes dependent on the triangularity, therefore, the magnetic shaping plays an important role in fitting DIII-D data. With DIII-D data the heating power dependence of the total pressure is strongly reduced compared to AUG and JET. The large variation of the exponents for the heating power suggests, different processes are dominating AUG and JET compared to DIII-D which will be discussed in Section 8.2. This has a significant impact on extrapolations to devices with higher heating power and will be discussed in Section 8.1.

With knowledge of the scalings with engineering parameters one can try to construct a dimensionless scaling for the pressure. The dimensionless pressure was introduced in Chapter 6 and is the total pressure divided by the square of a magnetic field. Using the poloidal field leads to $\beta_{p,ped}$, the toroidal field to $\beta_{t,ped}$ and the total magnetic field to β_{ped}. In Section 6.3 a correlation between $\beta_{p,ped}$ and the magnetic shape f_q was observed and in Section 7.2.1 the electron temperature pedestal width was found to scale more or less with $\beta_{p,ped}$. From Eq. (7.26) the most important parameters to fit the measurements are known to be the magnetic shape f_q, the poloidal field $\langle B_p \rangle$ and the heating power. The magnetic shape is already dimensionless. The poloidal field appears in the safety factor q_{cyl} or the normalized banana

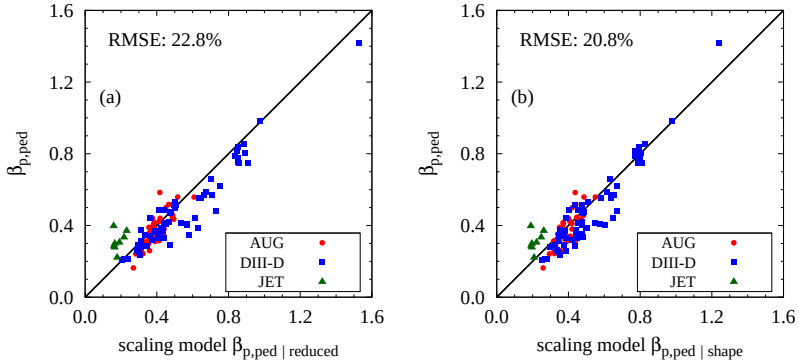

Figure 7.34: Regression of the normalized poloidal pedestal pressure with the models of Eq. (7.27) in (a) and Eq. (7.28) in (b).

width $\rho_{p\star} = \Delta_{banana}/a$. The dependence on the heating power can be expressed with the temperature as in Eq. (7.14) and therefore, incorporated in the dimensionless quantities. The normalized poloidal pedestal pressure then becomes

$$\beta_{p,ped}|_{reduced} = 2.74 \cdot \rho_{p\star}^{0.77\pm0.02} f_q^{2.04\pm0.04} \qquad \text{RMSE: 22.8\%} \qquad (7.27)$$

$$\beta_{p,ped}|_{shape} = 0.67 \cdot \rho_{p\star}^{0.63\pm0.02} f_q^{1.78\pm0.05} \left(\frac{T_{e,ped}}{T_{i,ped}}\right)^{0.29\pm0.01} \kappa^{0.66\pm0.14} \qquad \text{RMSE: 20.7\%,} \qquad (7.28)$$

the main difference compared with the engineering scalings is the machine size dependence. In Eq. (7.14) the machine size is included implicitly in $\langle B_p\rangle^{-1} \rightarrow a^1$ (remember $\beta_{p,ped} \propto p_{ped}\langle B_p\rangle^{-2}$), whereas, in the dimensionless representation no machine size dependence is found $\rho_{p\star}^{-1} \propto \langle B_p\rangle a \rightarrow a^0$. This is the reason why the JET pedestal pressure is systematically underestimated by these scalings which is indicated by the green triangles in Figure 7.34 (a). Including the elongation of the plasma improves the fit by 5%, the temperature ratio results in further 7% improvement. However, this does not solve the problem of the machine size dependence as illustrated in Figure 7.34 (b). The scaling Eq. (7.28) is fairly similar to one reported in [13]. The correlation between $\beta_{p,ped}$ and the pedestal width could not be exploited for a scaling with comparable low RMSE as in Eq. (7.28).
The normalized toroidal pedestal pressure $\beta_{t,ped}$ differs from $\beta_{p,ped}$ due to the normalization with B_t. Therefore, the banana width does not help to improve the scaling and q_{cyl} is introduced to describe the magnetic field correlation. The poloidal field originates from the total pedestal pressure and the toroidal field mainly from the applied normalization. To illustrate the behaviour of $\beta_{t,ped}$ three different scalings are compared:

$$\beta_{t,ped}|_{reduced} = 0.46 \cdot \rho_{i\star}^{0.52\pm0.11} f_q^{2.03\pm0.34} q_{cyl}^{-1.39\pm0.20} \qquad \text{RMSE: 22.5\%} \qquad (7.29)$$

$$\beta_{t,ped}|_{shape} = 0.024 \cdot \rho_{i\star}^{0.30\pm0.12} f_q^{1.57\pm0.38} q_{cyl}^{-1.55\pm0.20} \kappa^{3.41\pm1.01} (\delta+1)^{0.85\pm0.45} \qquad \text{RMSE: 14.1\%} \qquad (7.30)$$

$$\beta_{t,ped}|_{noLength} = 0.0040 \cdot f_q^{1.96\pm0.35} q_{cyl}^{-1.71\pm0.19} \kappa^{4.03\pm0.98} (\delta+1)^{0.93\pm0.45} \qquad \text{RMSE: 16.2\%.} \qquad (7.31)$$

All parameter combinations have a correlation factor of less than 0.5. In particular, there is no correlation between $f_q = q_{95}/q_{cyl}$ and q_{cyl}, because f_q is dominated by the plasma value

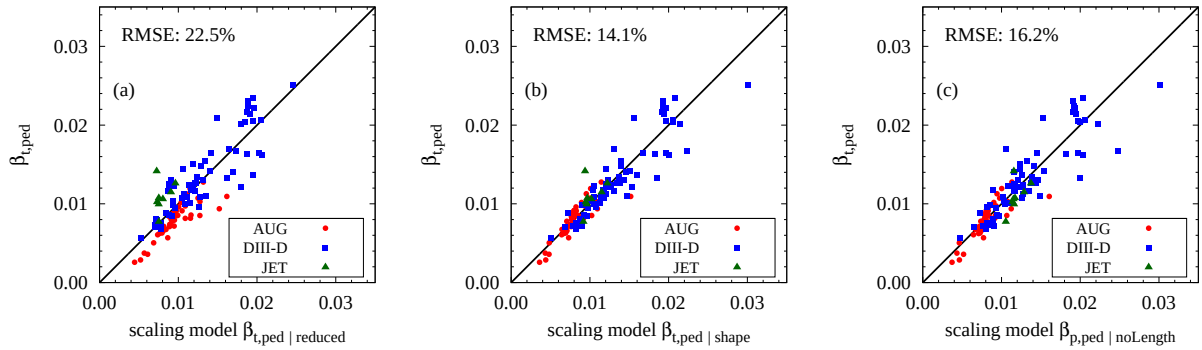

Figure 7.35: Regression of the normalized toroidal pedestal pressure with the models of Eq. (7.29) in (a), Eq. (7.30) in (b) and Eq. (7.31) in (c).

of the safety factor q_{95} and not by the cylindrical reference. Therefore, no co-dependencies are expected in the regression. The large exponent of the elongation is explained with the definition of q_{cyl} (Eq. (6.19)) where κ^2 is explicitly included. This does not impose a fixed correlation between parameters in the scaling, but explains the differences in fit quality between the reduced and the shape model. The elongation is introduced with the cylindrical safety factor. The result of the reduced regression is shown in Figure 7.35 (a), where the data of DIII-D is uniformly distributed around the scaling while AUG is systematically overestimated and JET underestimated. A solution is shown in (b), now the shape is explicitly included and removes the separation between the machines. The elongation improves the RMSE by 30% and the triangularity by another 8%. The comparison of the exponents of q_{cyl} and κ results in a similar elongation dependence as in the case with $\beta_{\mathrm{p,ped}}$.
The data is still represented very well by the scaling when removing the length parameter $\rho_{\mathrm{i}\star}$. Although, the RMSE increases by 15% without $\rho_{\mathrm{i}\star}$, the total RMSE of 16.2% is of the same level as the engineering scalings. The fit, in Figure 7.35 (c), shows no systematic deviation from the measurements. This would suggest the magnetic configuration in the edge region dominates the possible normalized pedestal pressure. Such a scaling is particularly interesting for predictions of larger machines, because no extrapolation is needed in the parameters, as will be discussed in Section 8.1. The difficulty is that f_{q} and δ are not entirely controlled externally but respond to the plasma pressure, as was discussed in Section 6.3. The total normalized pedestal pressure β_{ped} has fairly similar scalings as $\beta_{\mathrm{t,ped}}$:

$$\beta_{\mathrm{ped}}\big|_{\mathrm{shape}} = 0.023 \cdot \rho_{\mathrm{i}\star}^{0.30\pm0.12} f_{\mathrm{q}}^{1.58\pm0.38} q_{\mathrm{cyl}}^{-1.50\pm0.20} \kappa^{3.33\pm1.01} (\delta+1)^{0.85\pm0.45} \qquad \text{RMSE: } 14.2\% \tag{7.32}$$

$$\beta_{\mathrm{ped}}\big|_{\mathrm{noLength}} = 0.0038 \cdot f_{\mathrm{q}}^{1.97\pm0.35} q_{\mathrm{cyl}}^{-1.66\pm0.19} \kappa^{3.94\pm0.98} (\delta+1)^{0.93\pm0.45} \qquad \text{RMSE: } 16.2\%. \tag{7.33}$$

7.5 Confinement Time

The section about the pedestal pressure showed how the pedestal top changes with varying plasma settings and conditions. Besides the pressure, a second parameter is very important for self sustained fusion, namely the energy confinement time τ_{E} which was defined in Eq. (2.1) as the ratio of stored energy and loss power. It is particularly impor-

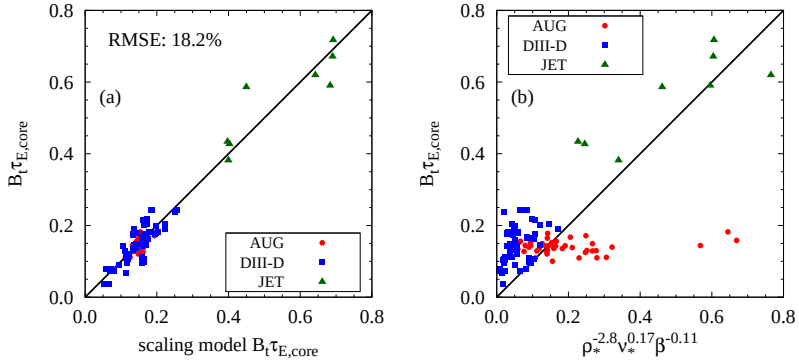

Figure 7.36: Scaling model of Eq. (7.34) plotted against measurements from AUG, DIII-D and JET (a). The gyro-Bohm like scaling from [12] plotted against the measurements (b).

tant for achieving self sustained fusion which is only possible when the "triple product" $nT\tau_\mathrm{E}$ exceeds a critical value (Lawson criterion [104]). This essentially means, the energy produced by fusion reactions balances the power loss in the plasma. The pedestal is connected to the confinement time via a two-term model, as described in Chapter 2, with the definition of $\tau_\mathrm{E,ped} = 3/2 \int p_\mathrm{ped} \mathrm{d}V / P_\mathrm{heat}$. The core confinement time is then $\tau_\mathrm{E,core} = \tau_\mathrm{E} - \tau_\mathrm{E,ped}$. The dimensionless representation of the confinement time is $B_\mathrm{t}\tau_\mathrm{E}$ because $[Be/m] = \mathrm{Vs/m^2As/kg} = \mathrm{Ns/(mkg)} = \mathrm{s}^{-1}$.

The measurements of the core confinement time at AUG, DIII-D and JET are nicely described with the following dimensionless scaling

$$B_\mathrm{t}\tau_\mathrm{E,core} = 1.97 \cdot 10^{-5} \cdot \rho_{\mathrm{i}\star}^{-1.90\pm0.04} \nu_{\mathrm{i}\star}^{-0.34\pm0.02} q_\mathrm{cyl}^{-1.16\pm0.07} (\delta+1)^{1.44\pm0.15} \quad \text{RMSE: } 18.2\% \qquad (7.34)$$

and illustrated in Figure 7.36 (a). This fit to the data favors a Bohm scaling $B_\mathrm{t}\tau_\mathrm{B} \propto \rho_\star^{-2}$ over a gyro-Bohm scaling $B_\mathrm{t}\tau_\mathrm{gB} \propto \rho_\star^{-3}$. The exponent of $\rho_\star$ is reproduced by every combination of at least two machines. This suggests all three machines operate in the same regime for the plasma core. The core confinement is independent of the pedestal pressure and the magnetic shape. Neither of both quantities would improve the RMSE when included in the regression. The observation made for the presented data set differs from a previous study [12] where the plasma core was found to be similar to the gyro-Bohm scaling. However, that result was obtained with a regression using engineering variables and a transformation to dimensionless variables. In the presented scaling Eq. (7.34) the dimensionless parameters were fitted directly. This has the advantage that the dimensionless safety factor and the plasma shape are included explicitly which will influence the quality of the fit significantly. In Figure 7.36 (b) the data used to determine Eq. (7.34) is plotted against the scaling proposed in [12]. Without an explicit dependence on the safety factor no match with the experimental data can be achieved. Both studies show similarities in the lack of a pressure dependence on the core confinement.

For the pedestal confinement time, derived from the pedestal pressure, no dimensionless representation was found which fits the experimental data uniformly. With knowledge of the pedestal pressure Eq. (7.26) it is easy to find a good scaling with engineering variables

$$B_\mathrm{t}\tau_\mathrm{E,ped}\big|_\mathrm{engineer} = 2.30 \cdot P_\mathrm{heat}^{-0.66\pm0.07} B_\mathrm{t}^{0.93\pm0.14} \langle B_\mathrm{p} \rangle^{1.24\pm0.14} f_\mathrm{q}^{1.55\pm0.27} a^{3.18\pm0.13} \qquad (7.35)$$

RMSE: 17.8%

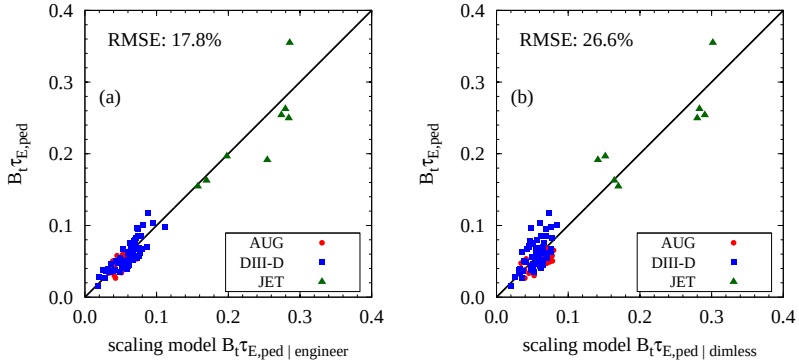

Figure 7.37: Scaling model of Eq. (7.35) (a) and Eq. (7.36) (b) plotted against measurements from AUG, DIII-D and JET.

which fits the measurements nicely as shown in Figure 7.37 (a). When replacing the engineering variables with the dimensionless variables in the regression one can remove the units step by step. In this procedure it becomes apparent that the influence of the heating power on the pedestal confinement time cannot be expressed by dimensionless quantities. The best dimensionless representation found for the pedestal confinement time has a significantly higher RMSE then the version with engineering variables

$$B_\mathrm{t}\tau_\mathrm{E,ped}\big|_\mathrm{dimless} = 3.90\cdot10^{-6}\cdot\rho_{\mathrm{i}\star}^{-2.29\pm0.08}\nu_{\mathrm{i}\star}^{-0.50\pm0.04}q_\mathrm{cyl}^{-1.50\pm0.12}\beta_\mathrm{p,ped}^{0.61\pm0.07}\left(\frac{T_\mathrm{e,ped}}{T_\mathrm{i,ped}}\right)^{-0.61\pm0.12} \tag{7.36}$$

RMSE: 26.6%.

The plot of Eq. (7.36) in Figure 7.37 (b) shows that a significant number of DIII-D discharges are underestimated by the scaling. The machine size dependence due to $\rho_{\mathrm{i}\star}$ describes the green JET measurements reasonably well. This results in a Bohm like scaling as was the case for the core confinement time. The scaling also reveals a explicit $\beta_\mathrm{p,ped}$ dependence on the pedestal which was not the case for the plasma core. The $\beta_\mathrm{p,ped}$ dependence could also be expressed with the toroidal beta which would result in a different exponent for the cylindrical safety factor, while the other exponent remain the same, in particular the one for the normalized pressure. The correlation between collisionality and temperature ratio, as described in Section 6.2, does not produce co-dependencies in the regressions which was tested by excluding individual parameters from the regression.
The IPB98 global confinement scaling was introduced in Chapter 2 as

$$\tau_\mathrm{E,IPB(y,2)} = 0.0562\cdot I_\mathrm{p}^{0.93}B_\mathrm{t}^{0.15}n_e^{0.41}P^{-0.69}R^{1.97}\kappa^{0.78}\epsilon^{0.58}M^{0.19}.$$

It is very similar to the pedestal engineering scaling, the exponents of heating power and toroidal field are identical, the dependence on the plasma current is slightly stronger in Eq. (7.35) and when taking the a dependence of $\langle B_\mathrm{p}\rangle$ into account also the exponents of the machine size are identical. Differences seem to arise in the representation of the shape, however, these are difficult to quantify without comparing the individual data sets.
The dimensionless form of $\tau_\mathrm{E,IPB(y,2)}$ was given as [3]

$$\tau_\mathrm{E,IPB(y,2)} \propto \tau_\mathrm{B}\rho_\star^{-0.83}\beta^{-0.50}\nu_\star^{-0.10}M^{0.97}q^{-2.52}\epsilon^{-0.55}\kappa^{2.72}.$$

This appears fairly different as the the dimensionless fits to the confinement time. The IPB scaling shows a gyro-Bohm dependence and a negative pressure dependence. While the core scaling Eq. (7.34) shows no pressure dependence and the pedestal scaling Eq. (7.36) a positive one. However, the fit quality of the dimensionless pedestal scaling is quite poor. The toroidal field dependence is for all scalings similar, meaning the confinement time is independent of B_t. This suggests the distinction between Bohm and gyro-Bohm type for these scalings is not conclusive.

To summarize, both contributions to the confinement time, from pedestal and core, show a Bohm like $\rho_\star$ dependence. However, the dimensionless representation of $\tau_\mathrm{E,ped}$ seems to be incomplete, because the fit quality achieved with a regression to engineering variables could not be matched. The mismatch originates from the heating power which was introduced in the definition of $\tau_\mathrm{E,ped}$. The reason for this might be that $\tau_\mathrm{E,ped}$ does not represent a physical concept, but a technical one to differentiate the contributions of core and pedestal contributions to global confinement. The global confinement time scaling $\tau_\mathrm{E,IPB(y,2)}$ was found to scale like $\tau_\mathrm{E,ped}$ in engineering parameters. The core confinement $\tau_\mathrm{E,core}$ showed no pressure dependence as is found for the global scaling. This confirms that the pressure dependence in global confinement scaling originates from the pedestal and not the plasma core [12].

7.6 Gradient Length Ratio η_e

The density and temperature gradient lengths, $L_{n\mathrm{e}}$ and $L_{T\mathrm{e}}$, and their ratio η_e are important in transport physics and determine turbulence characteristics. In this section after a short introduction of the differences between the gradient length and other pedestal parameters, previous studies are introduced and then the properties of the gradient length and η_e are described for discharges from AUG, DIII-D and JET.

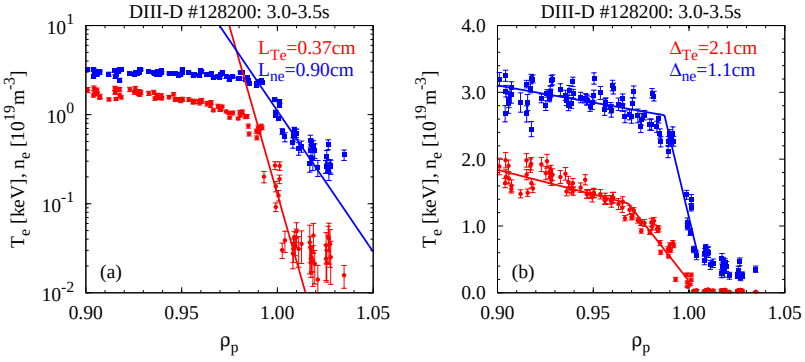

Figure 7.38: Electron temperature (red) and electron density (blue) profiles plotted on logarithmic (a) and linear scale (b). The gradient length are indicated on the logarithmic scale and the pedestal width on the linear scale.

Although connected to the pedestal characteristics described in the previous sections, the gradient lengths are a different method to describe the pedestal. In particular, it is important to understand the differences between the gradient lengths and the pedestal widths. While $\Delta_{T\mathrm{e}}$ is generally larger than $\Delta_{n\mathrm{e}}$, it is exactly the opposite for $L_{T\mathrm{e}} = (\nabla(\ln T_\mathrm{e}))^{-1}$ and

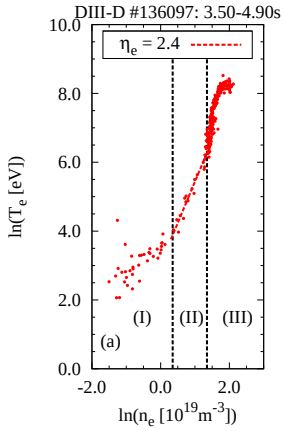

Figure 7.39: Log-log plot of T_e and n_e. The fit to data in the pedestal region (II) gives the gradient length ratio $\eta_{e(1)}$.

$L_{ne} = (\nabla(\ln n_e))^{-1}$. An Example is shown in Figure 7.38 where the gradient lengths are determined by fits on logarithmic scale (a) and the pedestal width with fits on linear scale (b). The gradients on the linear scale can be misleading when considering gradient lengths, on the logarithmic scale the differences are more clear. While the density changes only 1 order of magnitude in the pedestal, the temperature varies by nearly 2 orders of magnitude and therefore has the smaller gradient length. At this point it is also necessary to stress that the gradient length $L_{Te} = T_e/\nabla T_e$ is not the same as $T_{e,ped}/\nabla T_e$ which was discussed in Section 7.3. The gradient length is determined with a fit to only the steep gradient region and therefore technically independent of the pedestal top value.

There are two possibilities to determine the gradient length ratio $\eta_{e(1)} = \partial \ln T_e/\partial \ln n_e$ and $\eta_{e(2)} = L_{ne}/L_{Te}$. Theoretically, both methods are the same, however, in practice does the first involve two independent linear fits while the latter only needs one linear fit to determine η_e. Therefore, differences might arise in the two representations. The values given for η_e are always determined with a single fit with a log-log plot of temperature and density, as illustrated in Figure 7.39 where the slope of the indicated line corresponds to $\eta_{e(1)}$.

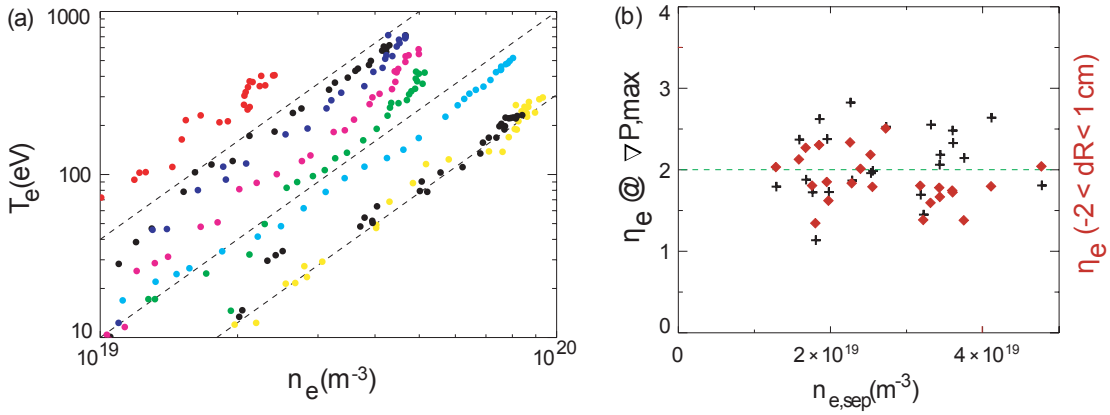

Figure 7.40: (a) electron temperature versus density in the edge region in a log-log plot. The relation $\eta_e = 2$ or $T_e \propto n_e^2$ is indicated with the dashed lines. (b) η_e versus the separatrix density. (Reprinted from [92])

In previous studies at AUG η_e was found to be close to 2 for a series of ELMy H-mode discharges with electron densities below $5 \cdot 10^{19}$ m^{-3} which would correspond to $T_e \propto n_e^2$ [92].

In Figure 7.40 these results show a good alignment with $\eta_e = 2$ (a), but in a larger data set (b) scatter from 1 to 3 in η_e is visible. At DIII-D no constant value for η_e was observed in a large data set including different plasma scenarios [105]. The H-mode data lies between η_e =1-3 as in AUG (Figure 7.41). ETG turbulence showed an η_e threshold in gyrokinetic

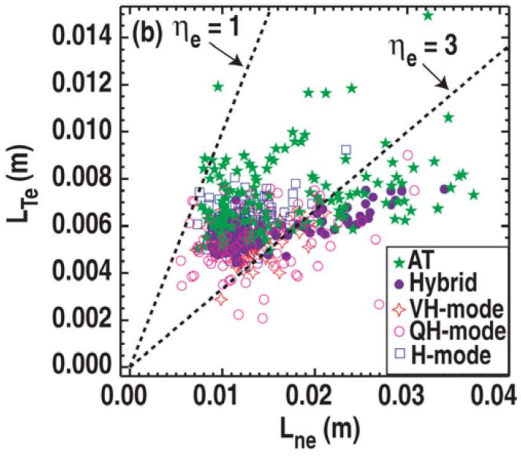

Figure 7.41: Gradient length of temperature and density in the pedestal region for different plasma scenarios. η_e varies between 1 and 3. (Reprinted from [105])

simulations [106]. Above this threshold the heat transport due to ETG turbulence was simulated to increase by one order of magnitude when η_e changes from 1 to 3. This variation of η_e was achieved by varying the L_{Te} for constant L_{ne}.

In this study the influences of heating power, magnetic field, plasma shape, collisionality and gas puffing on η_e are documented with discharge pairs and database plots for AUG, DIII-D and JET.
η_e does not vary with plasma current or gas puffing at constant heating power, constant

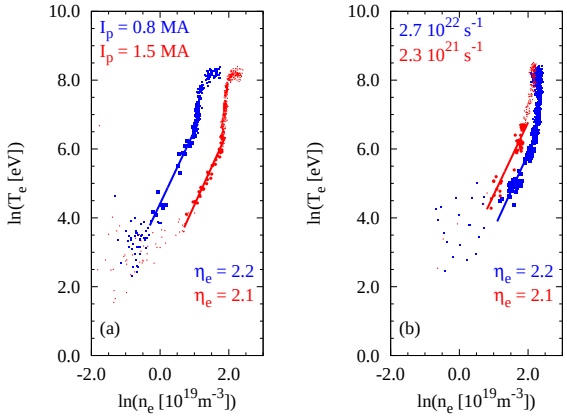

Figure 7.42: Illustration of parameters without influence on η_e. The plasma current was varied in (a) and the gas puff level in (b).

triangularity and low collisionality. In Figure 7.42 (a) the current was changed by nearly a factor of two which leads to a strong increase of the density and a slight reduction in the temperature. The normalized pressure $\beta_{p,ped}$ changed by a factor of 2 in this example. η_e

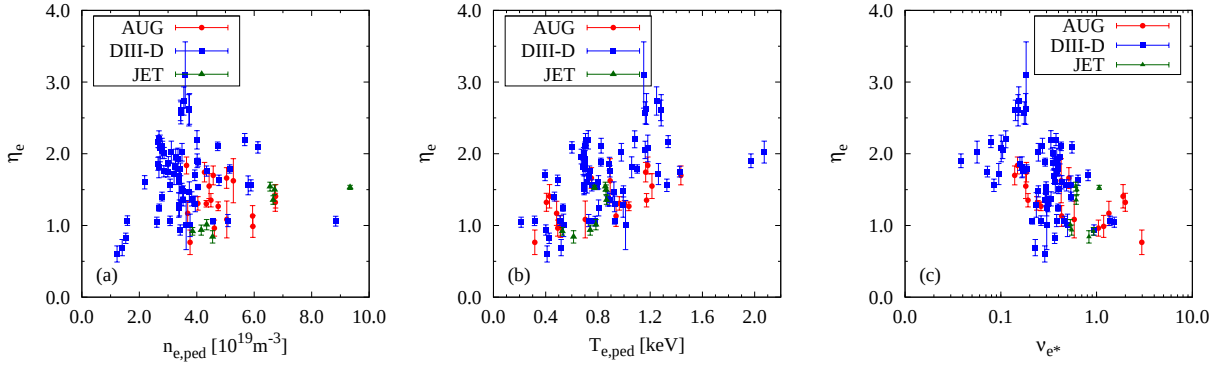

Figure 7.43: The gradient length ratio η_e plotted against the pedestal top density (a), temperature (b) and collisionality (c) for AUG (red), DIII-D (blue) and JET (green).

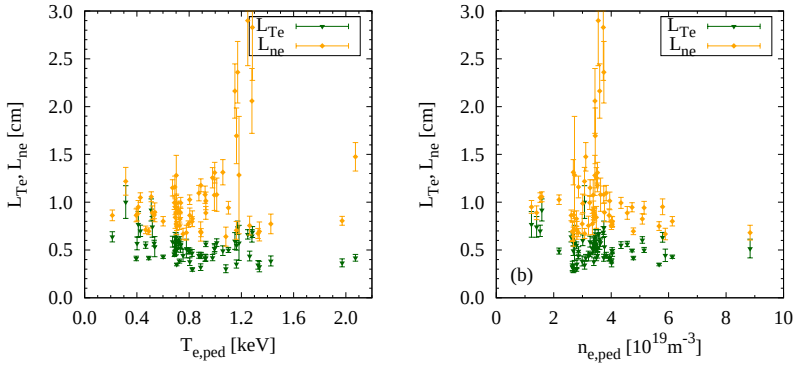

Figure 7.44: The gradient lengths in the pedestal of electron temperature (green) and density (orange) plotted against the electron pedestal temperature (a) and the pedestal top density (b).

in the pedestal is in both cases around 2.2 and the pedestal is shifted to higher densities without a significant change in the gradient lengths. The same is true for (b) where the gas puff was increased by a factor of 10 for JET. The density increases significantly, but no change in the gradient length ratio can be observed.
A strong correlation between η_e and the collisionality $\nu_{e\star}$ was identified for all machines as shown in Figure 7.43 (c). The gradient length ratio approaches a value of ~ 1 for large collisionality while it is larger ~ 2 for low collisionality. The correlation of η_e with $T_{e,ped}$ and $n_{e,ped}$ would suggest this is mainly an effect in the temperature. In Figure 7.43 (a) η_e shows no real correlation with $n_{e,ped}$ as was also the case in previous studies [92] shown in Figure 7.40. The temperature is correlated with η_e for larger pedestal temperature also the gradient length ratio increases (b). For low temperature and high collisionality the temperature gradient length L_{Te} approaches the density gradient length L_{ne} as illustrated in Figure 7.44 (a). While L_{Te} and L_{ne} seem to be coupled for large collisionalities, they show distinct behaviour for low collisionalities. This effect is dominated by the temperature, as is suggested by Figure 7.44 (b) where the gradient lengths show no correlation with the pedestal top density.

Three other parameters: heating power, toroidal magnetic field and the plasma shape are shown in Figure 7.45 and show all local trends with η_e. However, they do not match

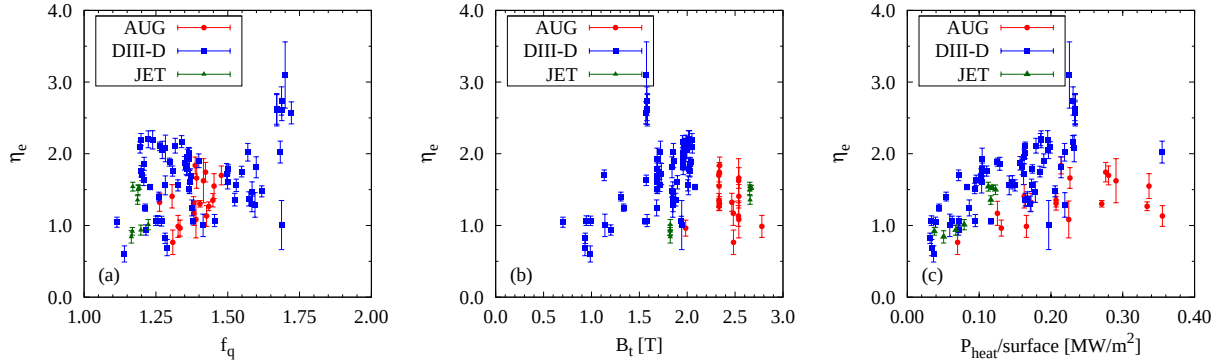

Figure 7.45: The gradient length ratio η_e plotted against the heating power per surface area (c), toroidal magnetic field (b) and shaping factor $f_q = q_{95}/q_{cyl}$ (a) for AUG (red), DIII-D (blue) and JET (green).

for the different machines as it was the case for the collisionality. For example the magnetic shaping $f_q = q_{95}/q_{cyl}$ shows a correlation with the gradient length ratio, however, between $1.2 < f_q < 1.4$ a significant number of discharges break this trend, the reason for this could not be identified. With increasing toroidal field (b), the gradient length ratio increases for the data of DIII-D and JET, but it drops again for AUG data at high B_t. A possible explanation for this is the correlation of B_t with $T_{e,ped}$ as shown in Figure 6.3 (c), which shows a similar maximum at around 2 T. This suggests the trend of η_e with B_t is a consequence of the trend of η_e with $T_{e,ped}$. A similar explanation is conceivable for the heating power per surface area in Figure 7.45 (c). All three machines show individual trends with the heating power but do not show a consistent picture. However, the gradient length ratio is strongly correlated with the heating power for DIII-D discharges with low triangularity. In Figure 7.46 η_e for low triangularity discharges with green diamonds increases with heating power. For high heating power η_e seems to saturate around a value of 2. This increase in η_e is mainly due to decreasing temperature gradient length. An example is given in Figure 7.47, the $\ln T_e$-$\ln n_e$ plot (a) illustrates the difference in η_e. The discharge with the lower heating power (blue) shows the smaller gradient, and a smaller η_e, than the high heating power case (red). In (b) the temperature profiles are compared and L_{Te}^{-1} is indicated by the gradient of $\ln T_e$ in the pedestal, the gradient length is significantly smaller in the case with the larger heating power. The density gradient length (c) is unaffected by the change in the heating power. This would suggest an impact only on the temperature and therefore, the electron heat flux. The η_e trend with the heating power is observed this pronounced only for the low triangularity regime $\delta < 0.45$. The gradient length ratio is not so well defined by the heating power in the high triangularity regime $\delta > 0.45$. The spread in η_e for the high δ discharges (orange in Figure 7.46) is significantly larger than for low δ, however, the trend to a larger gradient length ratio with higher heating power is still visible. The different triangularity regimes were introduced in Section 6.3. In Figure 7.48 an example for the influence of the plasma shape on the gradient length ratio is given. At constant heating power the triangularity was increased from $\delta = 0.38$ (red) to $\delta = 0.48$ (blue). The pedestal top values remained fairly similar in both cases, however, the gradient length ratio decreases with larger triangularity (a). The temperature gradient length stayed roughly the same in both cases (b), whereas the density gradient length was reduced (b). This example would suggest that a variation of triangularity mainly affects the density pedestal while the temperature remains unaffected. However, it has to be noted that this is but only example and no distinct effect of the

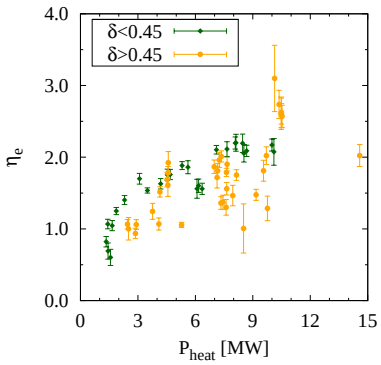

Figure 7.46: Dependence of η_e with heating power for different triangularities with the DIII-D data set. $\delta > 0.45$ is marked with orange circles and $\delta < 0.45$ with green diamonds.

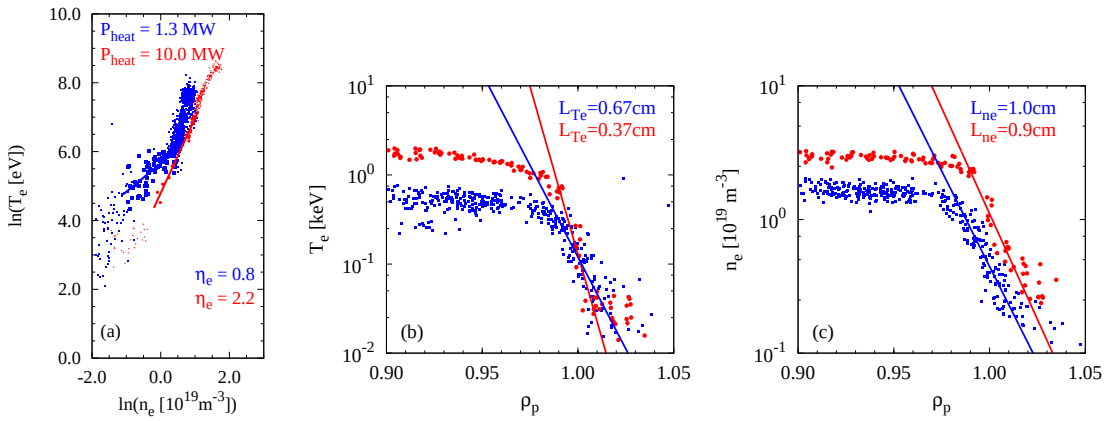

Figure 7.47: Overview of the profile changes with heating power in the low triangularity regime. (a) shows the gradient length ratio where the higher heating power (red) shows a significantly larger η_e than the low power case (blue). (b) shows the electron temperature profiles on a logarithmic scale, the gradient length is determined as the slope of the linear fit to the steep gradient region as in Eq. (2.7). (c) is shows the density profiles.

shaping could be identified within the whole data set. A reason for this might be the variety of discharges in the data set and influences on the pedestal which are not covered by the database as described in Section 6.

To summarize, the gradient length ratio η_e is not constant in the observed data set but varies with collisionality, heating power, temperature and triangularity. All except δ are coupled and show essentially the same trend: for low heating power and temperature the collisionality is generally high. In the high collisionality regime the temperature gradient length approaches the value of the density gradient length, which is larger than L_{Te} in other cases, resulting in an $\eta_e \sim 1$. For larger electron temperatures and low collisionalities L_{Te} and L_{ne} become different and η_e varies between 1-3. At very low collisionality $\nu_{e\star} < 0.2$ only values of η_e larger than 1.5 are observed. This variation in η_e is consistent with previous studies where η_e was found to be constant, because mainly plasmas with low collisionality were analysed. These observations could suggest that at high collisionality the electron density plays an important role in setting the temperature gradient length while at low collisionality the density gradient length is less important for the temperature pedestal. The

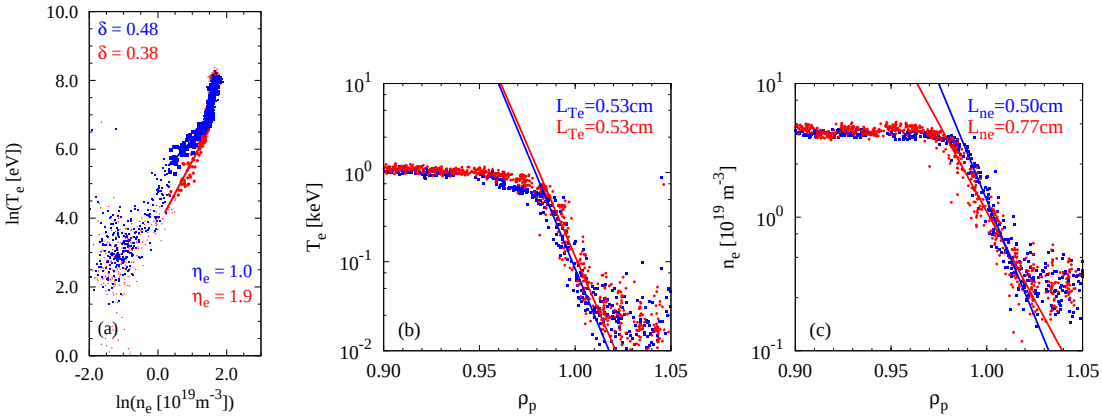

Figure 7.48: Overview of the profile changes with triangularity at constant heating power. (a) shows the gradient length ratio where the low triangularity (red) shows a significantly larger η_e than the high triangularity case (blue). (b) shows the electron temperature profiles on a logarithmic scale, the gradient length is determined as the slope of the linear fit to the steep gradient region as in Eq. (2.7). (c) is shows the density profiles.

gradient length ratio varied at with a change of the plasma shape at DIII-D. However, there was no distinct correlation observed in the data set. η_e increases with the magnetic shaping for some discharges, but not all. A larger triangularity reduces η_e at constant heating power for most discharges at DIII-D, this is different than observations made at AUG where η_e increased with larger triangularity [107].
In principle, the theory of ETG turbulence would be consistent with the observation of larger η_e at larger heating power. In steady state the energy by external heating must flow out of the plasma, therefore, larger heating results in larger heat flux. For constant temperature gradient and constant density this would require a larger heat diffusivity in the pedestal region. ETG turbulence could explain a larger heat diffusivity for higher η_e [106]. However, temperature gradient, pedestal density and energy transfer between electron and ion channels are not constant over the database. In order to draw more reliable conclusions transport simulations would be necessary from all three machines.
From AUG only a small number of measurements are included. Because only measurements with the profile mode of the Thomson scattering diagnostic, as described in Section 4.3.1, are useful to determine gradient length. Without the profile mode the uncertainty due to larger scatter makes reliable comparisons difficult. This is also the reason why only a relatively small number of AUG discharges was included in the analysis.

7.7 Summary of the Main Observations

This section is an overview of the whole chapter about experimental results. It will repeat the main observations which were already discussed in the individual sections. The consequences of this observations are discussed in Chapter 8.

The pedestal width was analysed for the three machines AUG, DIII-D and JET. The data from JET was analysed with the improved TS diagnostic which allows to measure the pedestal width more accurately. With the old system (shot numbers <79000) the pedestal width was systematically overestimated for JET (see Section 4.7). With the new diagnostics

no machine size dependence of the real space pedestal width is observed for the temperature and density. In normalized poloidal flux coordinates the pedestal width was found to scale differently for the temperature and the density. This was reproducible for scalings in dimensionless and engineering parameters. The poloidal field dependence of the real space temperature pedestal width could be explained with a coordinate transformation from flux coordinates. No indication was found that the pedestal width might scale as expected from ion orbit loss or neutral penetration theory.

A strong correlation was found between pedestal top value and the gradients in real space. This would suggest a constant real space width without machine size dependence which is consistent with the results of the pedestal width analysis. The proportionality between $T_{\mathrm{e,ped}}$ and ∇T_{e} is not only independent of the machine size but also independent of the collisionality, normalized pressure, magnetic field and plasma current. The relation between $T_{\mathrm{i,ped}}$ and ∇T_{i} is not so robust and varies with collisionality, where lower $\nu_\star$ corresponds to smaller gradient. The relation between $n_{\mathrm{e,ped}}$ and ∇n_{e} could be varied with the gas puff level. The normalized pressure gradient α was found to be correlated with all three dimensionless physics variables $\beta_{\mathrm{p,ped}}$, $\rho_\star$ and $\nu_\star$. A correlation of $\alpha \propto \beta_{\mathrm{p,ped}}^{0.5}$ as suggested by KBM theory in Section 3.1.3 could not be reproduced, $\alpha/\beta_{\mathrm{p,ped}}^{0.5}$ varies by a factor of 4 and is strongly correlated with low $\rho_\star$ and with f_{q}.

The influences on the pedestal top density are not easily quantified. Therefore, no scaling for extrapolations was derived. The observations of the pedestal top electron density were: gas puffing does increase $n_{\mathrm{e,ped}}$ up to a certain value, above this level gas puffing does not affect the pedestal density further. The threshold level is different for each machine. The wall material has an influence on the density. The AUG discharges with the tungsten wall show larger $n_{\mathrm{e,ped}}$ than those with the carbon wall. For the analysed data of DIII-D and JET it was found that $n_{\mathrm{e,ped}}$ scales strongly with plasma current I_{p} and toroidal magnetic field B_{t}, but no machine size dependence could be identified.

The pedestal top electron temperature can be described with heating power, machine size, electron density and plasma current. However, the scaling is only valid when the heating power is equally distributed in the electron and ion channels which is the case for AUG and JET at high collisionality. The measurements of DIII-D follow the trend derived at high collisionality fairly well, however, when electron and ion temperature deviate in the pedestal also the deviation from the scaling becomes maximal. Further influences on $T_{\mathrm{e,ped}}$, particularly due to the plasma shape, could not be identified in the given data set.

The pedestal pressure was tested in log-linear regressions against the engineering parameters heating power P_{heat}, averaged poloidal magnetic field $\langle B_{\mathrm{p}} \rangle$, toroidal magnetic field B_{t}, pedestal top density $n_{\mathrm{e,ped}}$ and magnetic shaping f_{q}. An explicit machine size dependence, besides the one in $\langle B_{\mathrm{p}} \rangle$, was not found for the pedestal pressure and therefore, it was not included in the detailed analysis. In the multi-machine regressions $n_{\mathrm{e,ped}}$ appears to be insignificant. The dependence on $\langle B_{\mathrm{p}} \rangle$ or the plasma current I_{p} varies for the different scalings, however, for the total pressure a linear dependence is found in all cases. The correlation with the toroidal field is not so clear. While the measurements of AUG and JET show a robust trend with $\sqrt{B_{\mathrm{t}}}$, the data of DIII-D shows strongly varying exponents for B_{t} and in the regression with all machines no dependence of p_{ped} on B_{t} is observed. AUG and JET show fairly similar dependence on the engineering parameters. This was found for the AUG only analysis and the combined AUG,JET analysis. DIII-D seems to have two regimes dependent on the triangularity, therefore, the magnetic shaping plays an important role in fitting DIII-

D data. With DIII-D data the heating power dependence of the total pressure is strongly reduced compared to AUG and JET. The large variation of the exponents for the heating power suggests, different processes are dominating AUG and JET compared to DIII-D which will be discussed in Section 8.2. This has a significant impact on extrapolations to devices with higher heating power and will be discussed in Section 8.1.

The normalized pedestal pressure could be expressed with a dimensionless scaling only when normalized to the total or toroidal magnetic field. For $\beta_{\mathrm{p,ped}}$ no dimensionless form was found. This is likely due to the machine size dependence which is implicitly included with normalization to the magnetic pressure $\propto B_p^2 \propto I_\mathrm{p}^2/a^2$. In the total pressure the poloidal field contribution is quite small because $\langle B_\mathrm{p}\rangle^2 \ll B_\mathrm{t}^2$. For β_{ped} a scaling was possible which only depends on the plasma shape.

The confinement time was separated in contributions from the pedestal and the plasma core. The most used global confinement time scaling for H-modes $\tau_{\mathrm{E,IPB(y,2)}}$ was found to scale like $\tau_{\mathrm{E,ped}}$ in engineering parameters. The core confinement $\tau_{\mathrm{E,core}}$ showed no pressure dependence as is found for the global scaling.

The gradient length ratio η_e in the pedestal is not constant in the observed data set but varies with collisionality $\nu_\star$, heating power, temperature and triangularity. For low $\nu_\star$ larger η_e are observed than for high $\nu_\star$. At high $\nu_\star$, η_e approaches unity.
The gradient length of the electron temperature could be varied separately from the density gradient length by increasing the heat flux over the pedestal. This is is only possible for low triangularity. For stronger plasma shaping the scatter in the data significantly increases which makes a direct comparison difficult.

Chapter 8

Conclusions

8.1 Future Devices

Throughout Chapter 7 regression analyses were performed on data from the three machines AUG, DIII-D and JET. All these scalings can be used to extrapolate to larger machines. In this section, design values for ITER and DEMO are given which are used to provide a prediction for these machines with selected scalings. For this exercise it is important to remember that all numbers given are based on extrapolations to values 2-5 times larger than those included in the regression analysis. The heating power of DEMO is about 30 times larger than that available for present day machines. Not only is the heating power significantly larger but the source is also different, like α-particles in the case of DEMO. Therefore, the uncertainties in the extrapolation are due not only to the quality of the fits to available data, but also whether the physical mechanisms are still the same. This is one reason why no uncertainties are given for the predicted values. Another reason is that often not only design values can used for the scalings but quantities which are only known after machine operation. For future machines those come from other scalings or are educated guesses. The variation in the results of different scalings will give indications for the confidence of the extrapolations.

For the extrapolation to ITER different discharge settings are used: standard values, half current, half current and half field, half heating power. The values for these settings are listed in Table 8.1, along with values for one DEMO design. For ITER the auxiliary heating power is used and for DEMO the α-particle heating is included. The temperature values are taken from the $T_{\mathrm{e,ped}}$ and $p_{\mathrm{e,ped}}$ scalings. The electron density is an educated guess with the boundary condition $n_{\mathrm{e,ped}} < n_{\mathrm{GW}}$. The values for f_{q} is taken from equilibrium calculations which give $q_{95} = 3$. $T_{\mathrm{e,ped}}/T_{\mathrm{i,ped}}$ and Z_{eff} are just reasonable numbers with no direct physical justification. However, there is no better estimate available.

In Table 8.2 all relevant scalings for the pedestal pressure are listed with the extrapolations towards ITER and DEMO. To compare the different representations of the pressure the corresponding temperature is indicated in every second column. The temperature varies significantly for the different scalings. The outliers are the AUG only scalings which indicate the lack of machine size variation and result in very high temperature estimates. In particular, this is visible for the $T_{\mathrm{e,ped\,|AUG}}$ scaling. Therefore, the single machine scalings have very poor predictive capability. Another extreme is found in the $\beta_{\mathrm{p,ped}}$ scalings, here the machine

		ITER	ITER $0.5P_{\text{heat}}$	ITER $0.5I_{\text{p}}$	ITER $0.5(I_{\text{p}}, B_{\text{t}})$	DEMO
P_{heat}	[MW]	74	37	74	74	477
I_{p}	[MA]	15	15	7.5	7.5	23
B_{t}	[T]	5.3	5.3	5.3	2.65	5.78
a	[m]	2.0	2.0	2.0	2.0	2.83
R	[m]	6.21	6.21	6.21	6.21	8.5
q_{95}		3.0	3.0	6.0	3.0	3.0
f_{q}		1.2	1.2	1.2	1.2	1.3
$T_{\text{e,ped}}$	[keV]	4.0	2.6	3.0	3.0	10.0
$T_{\text{e,ped}}/T_{\text{i,ped}}$		1.0	1.0	1.0	1.0	1.0
$n_{\text{e,ped}}$	$[10^{-19}\text{m}^{-3}]$	7.0	7.0	5.0	5.0	9.0
κ		1.8	1.8	1.8	1.8	1.66
δ		0.5	0.5	0.5	0.5	0.33
Z_{eff}		1.0	1.0	1.0	1.0	1.0

Table 8.1: Parameters of future fusion devices as they are used in the extrapolations.

Parameter	Eq.	ITER		ITER $0.5P_{\text{heat}}$		ITER $0.5I_{\text{p}}$		ITER $0.5(I_{\text{p}}, B_{\text{t}})$		DEMO	
			T		T		T		T		T
$T_{\text{e,ped}\,\vert\text{AUG,JET}}$	7.14	3.4	3.4	2.2	2.2	2.7	2.7	2.7	2.7	8.0	8.0
$p_{\text{e,ped}\,\vert\text{DIII-D}}$	7.18	70	6.3	50	4.5	32	4.0	32	4.0	236	16.4
$p_{\text{i,ped}\,\vert\text{DIII-D}}$	7.19	19	1.7	20	1.8	8	1.0	8	1.0	28	2.0
$p_{\text{ped}\,\vert\text{DIII-D}}$	7.20	62	2.8	58	2.6	23	1.5	23	1.5	109	3.8
$p_{\text{e,ped}\,\vert\text{AUG,JET}}$	7.21	53	4.7	31	2.7	38	4.8	38	4.8	281	19.5
$p_{\text{i,ped}\,\vert\text{AUG,JET}}$	7.23	73	6.5	51	4.6	30	3.8	30	3.8	243	16.9
$p_{\text{ped}\,\vert\text{AUG,JET}}$	7.25	147	6.6	96	4.3	71	4.4	71	4.4	623	21.6
$p_{\text{e,ped}\,\vert\text{all}}$	7.22	49	4.3	33	3.0	27	3.3	27	3.3	174	12.0
$p_{\text{i,ped}\,\vert\text{all}}$	7.24	25	2.2	24	2.1	11	1.3	11	1.3	45	3.1
$p_{\text{ped}\,\vert\text{all}}$	7.26	66	2.9	56	2.5	30	1.9	30	1.9	147	5.1
$\beta_{\text{t,ped}\,\vert\text{reduced}}$	7.29	0.007	2.1	0.007	1.9	0.003	1.1	0.009	0.9	0.010	2.6
$\beta_{\text{t,ped}\,\vert\text{shape}}$	7.30	0.013	3.7	0.012	3.5	0.004	1.7	0.015	1.5	0.012	3.0
$\beta_{\text{t,ped}\,\vert\text{nolength}}$	7.31	0.021	6.0	0.021	6.0	0.006	2.6	0.021	2.1	0.018	4.8

Table 8.2: Results for various temperature and pressure scalings. The temperature is in [keV] and the pressure in [kPa]. The first column of each parameter set gives the result of the scaling, the second column marked with T gives the temperature in [keV] corresponding to the pressure or normalized pressure.

Parameter	Eq.	ITER	ITER $0.5P_{\mathrm{heat}}$	ITER $0.5I_{\mathrm{p}}$	ITER $0.5(I_{\mathrm{p}}, B_{\mathrm{t}})$	DEMO
$B_{\mathrm{t}}\tau_{\mathrm{E,core}}$	7.34	7.8	8.8	3.4	2.9	10.5
$B_{\mathrm{t}}\tau_{\mathrm{E,ped\ |\ engineer}}$	7.35	8.0	12.6	3.4	1.8	10.4

Table 8.3: Extrapolations for the normalized confinement time towards ITER.

size is varied but not represented correctly by the scaling, as was discussed in Section 7.4.3. The remaining scalings result in a pedestal temperature for ITER of 2-7 keV and 3-20 keV for DEMO. This variation can be understood when recalling the observations of Chapter 7, the larger temperature values are observed for the scalings with stronger dependence on the heating power. The small temperature values are found when the plasma shape is the dominating term in the scaling, while the difference in the ion temperature and electron temperature pedestal at DIII-D is another reason for the large deviation between $p_{\mathrm{ped\ |all}}$ and $p_{\mathrm{ped\ |AUG,JET}}$. The ion temperature at DIII-D had significantly smaller pedestal gradients at low collisionality than observed for the high collisionality discharges at AUG. This results in $T_{\mathrm{i}} < T_{\mathrm{e}}$ at the electron temperature pedestal top and a smaller total pressure at this position. However, this is no statement about the ratio of ion and electron temperature in the plasma core. This means that the different physics in the ion pedestal of AUG and DIII-D need to be understood, before the validity of the extrapolations including DIII-D can be evaluated.
The main conclusion which can be inferred from Table 8.2 is that if the heat flux over the pedestal sets the pedestal top, higher pressure is achieved than when the plasma shape is the governing quantity. For ITER the difference is not very pronounced, but for DEMO this can result in extrapolations differing by a factor of 2-4. When reducing the heating power or plasma current for ITER the pedestal is not unaffected; the pedestal temperature drops by 1-2 keV. This is important for core transport simulations. When varying heating power or current, the boundary conditions at the pedestal top have to be adjusted as well.

The extrapolations for the confinement time are listed in Table 8.3 for the pedestal and core contributions to the total confinement time. The separation of τ_{E} was done with a so called two-term approach which was described in Section 7.5. The extrapolation to ITER and DEMO shows that the core and the pedestal contributions to the global confinement are roughly similar. For the machines used in this study the contribution of the core to the global confinement was about twice the pedestal contribution ($\tau_{\mathrm{E,ped}} \sim 0.5\tau_{\mathrm{E,core}}$). This suggests the pedestal becomes more important for the global confinement for larger machines ($\tau_{\mathrm{E,ped}} \sim \tau_{\mathrm{E,core}}$). The comparison of the global confinement time scaling IPB98 [3] with $\tau_{\mathrm{E,ped}}$ showed that both scale similar and have the same dependence on all major parameters (magnetic field, plasma current, heating power and machine size). This illustrates the link between the global confinement and the edge transport barrier. The global confinement time for ITER $\tau_{\mathrm{E,ped}} + \tau_{\mathrm{E,core}}$ is 3 s which is at the lower end of the IPB98 prediction.

The main result of the pedestal width scalings, as listed in Table 8.4, is the separation of the temperature and density pedestal width. The temperature pedestal appears to be 2-5 times wider than the density pedestal. While the temperature pedestal width in normalized flux coordinates increases toward DEMO, the density pedestal width remains the same. In real space coordinates this would correspond to a temperature pedestal width of 3-4 cm for ITER and about 8 cm for DEMO. This is significantly larger than the 1-2 cm observed

Parameter	Eq.	ITER	ITER $0.5P_{\mathrm{heat}}$	ITER $0.5I_{\mathrm{p}}$	ITER $0.5(I_{\mathrm{p}}, B_{\mathrm{t}})$	DEMO
$\Delta_{Te}[\Psi_{\mathrm{N}}]_1$	7.2	0.043	0.035	0.064	0.052	0.083
$\Delta_{Te}[\Psi_{\mathrm{N}}]_2$	7.3	0.030	0.023	0.040	0.031	0.052
$\Delta_{Te}[\Psi_{\mathrm{N}}]_3$	7.4	0.041	0.030	0.048	0.036	0.079
$\Delta_{ne}[\Psi_{\mathrm{N}}]_1$	7.7	0.012	0.012	0.013	0.018	0.013
$\Delta_{ne}[\Psi_{\mathrm{N}}]_2$	7.8	0.014	0.012	0.021	0.018	0.017
$\Delta_{ne}[\Psi_{\mathrm{N}}]_3$	7.9	0.013	0.011	0.017	0.018	0.017

Table 8.4: Extrapolations towards ITER and DEMO based on the pedestal widths scalings derived in Section 7.2.

in AUG, DIII-D and JET. The density pedestal, in the extrapolation towards ITER and DEMO, shows a real space width of 1-2 cm similar to the analysed present day machines.

8.2 Theory

A detailed summary of the experimental observations was given in Section 7.7. In this section selected observations are pointed out and a focus is put on the consequences for different theories.

The pedestal top pressure scalings, as described in Section 7.4.3 and 8.1, suggest differences between electron and ion pressure. The electron pressure shows a stronger dependence on the heating power than the ion pressure. The ion pressure is more dependent on the poloidal magnetic field and shows stronger dependence on the magnetic shaping when DIII-D data is included. A possible explanation of this difference can be provided by the interplay of transport mechanisms and MHD stability. If the pedestal is dominated by heat conduction, the heat flux, and therefore the heating power, is important for the pedestal parameters. If the pedestal is limited by MHD stability it should be possible to describe the pedestal pressure with the dimensionless quantities β and f_{q} and it should be independent of the heat flux.
The observations are consistent with a mixture of transport limit and stability limit. Consider an ELM cycle which was introduced in Section 2.1. The time traces of the soft x-ray radiation (Figure 2.9) show a continuous increase of the radiation until the ELM crash. This indicates that the edge pedestal changes until the ELM crash. However, the electron temperature and density gradients and pedestal top values can stay constant for several ms, before an ELM crash occurs [26]. This is expected when the heat flux over the pedestal is balanced by heat conduction. A particle balance must also be achieved in a similar fashion. The soft x-ray radiation from the plasma edge is still rising in this phase and indicates that the pedestal is not in equilibrium. Since the electron pedestal is constant, one possibility is that the ion pressure might still change. If this were the case, it would increase until the total pressure hits the MHD stability limit and the ELM is triggered. Unfortunately, no direct measurements of the ion pressure with sufficient time resolution are published which could confirm or negate this argument. However, the scalings of the pedestal pressure are consistent with this argument. The electron pressure shows a heating power dependence as expected from a transport limit. The ion pressure showed less dependence on the heating

power and stronger dependence on the shaping factor. In Section 7.3 a strong correlation between the shaping factor and the normalized pressure gradient, and therefore the peeling-ballooning stability limit, was found. The scalings of the total pressure seem to be a mixture of the electron and ion pressure scalings. For DIII-D data, the scalings of the ion pressure match the extreme case of a pure MHD limit without heating power dependence very well. At AUG and JET an intermediate case is observed.

The absolute value of the neoclassical heat diffusivity for electrons is of the order of 0.01 m^2/s which is one order of magnitude smaller than the heat diffusivity observed in the pedestal region [93, 108]. Most anomalous turbulent transport processes, which are candidates for core transport, cannot explain the observed heat transport or are suppressed by the strong radial electric field shear in the edge region. Electron temperature gradient modes (ETG) could account for an electron heat transport of the same order as the observed values, which was suggested by simulations [106]. In Section 7.6 observations of the gradient length were discussed. The experiments show a reduction of the temperature gradient length with increasing heat flux in the edge. This is consistent with ETG turbulence, which shows increased electron heat diffusivity for smaller temperature gradient lengths [106].
A distinct trend in the temperature gradient length was only observed for low triangularity, although at large triangularity ($\delta > 0.4$) the correlation was still visible with a significantly increased scatter. The sharp transition between low and high triangularity is indication for a change in the physics in the pedestal. This is also observed in the correlation of the pedestal pressure and the shaping factor f_q. For high triangularity, f_q increases more strongly with the pressure than is the case for low triangularity. However, no known theory explains such a distinction between high and low triangularity. In particular, a variation of the triangularity within one of the two regimes does not seem to have an influence on the plasma parameters.

The normalized pressure gradient α was investigated with the database and found to be correlated to several parameters. In particular, strong correlations are observed between α and $\beta_{p,ped}$ and also between α and the plasma shape. Both correlations are theoretically expected. The main dependencies arising from kinetic ballooning mode theory were described in Section 3.1.3 and resulted in $\alpha \propto \beta_{p,ped}^{1/2}$. This dependency could not be confirmed with the measurements, where $\alpha/\beta_{p,ped}^{1/2}$ varied by factor of 4. The plasma shaping could account for this variation. Here, the plasma shape is expressed by either the shaping factor f_q or the plasma elongation κ. A variation of the triangularity δ cannot be responsible for the variation in $\alpha/\beta_{p,ped}^{1/2}$.
The peeling-ballooning mode is predicted to be stabilized by stronger shaping [99], this is confirmed by the measurements. However, the observations suggest that this effect scales with f_q or with κ rather than with δ. A linear dependence between α and $\beta_{p,ped}$ would fit the data better than a square root dependence. This would suggest a normalized real space pedestal width which is independent of the pressure at the pedestal.

The direct analysis of the pedestal width reveals no indications for a mechanism based on ion orbit losses or neutral penetration. However, the analysis performed was not the optimal to test these mechanisms and they therefore cannot be excluded as reason for the pedestal width. To determine the width expected by ion orbit losses, detailed measurements of the radial electric field profile would be necessary which were not available for all discharges in the database. Tests of the neutral penetration model are very sensitive to conditions in the SOL. The SOL parameters were either not documented in enough detail for the database or they showed significant differences between the machines, like the impact of gas puffing on

the plasma.
In normalized flux coordinates the pedestal width model provided by KBM theory performs best in describing the pedestal with a single parameter, namely $\Delta \propto \beta_{\mathrm{p,ped}}^{1/2}$ [56]. However, the pedestal can be described significantly better (50% difference in the RMSE) when including more parameters in the pedestal width model. Particularly important for the improvement of the model is the plasma elongation, whose influence was already observed in the analysis of the gradient. Larger elongation allows larger normalized gradients and consequently results in smaller normalized pedestal widths. This is observed for several regressions and is similar for electron density and electron temperature. When tested against more than a single parameter, electron temperature and density pedestal widths, $\Delta_{T\mathrm{e}}$ and $\Delta_{n\mathrm{e}}$, show different dependencies. Aside from the strong shape dependence, the density pedestal width in Ψ_{N} scales with $\rho_{\mathrm{i}\star}^{0.6}$, the temperature pedestal width with $\beta_{\mathrm{p,ped}}^{0.5}$. In engineering parameters this translates to a toroidal magnetic field dependence of $\Delta_{n\mathrm{e}}$, while $\Delta_{T\mathrm{e}}$ is independent of B_{t}. The temperature pedestal width decreases with increasing temperature ratio at the pedestal top, $T_{\mathrm{e,ped}}/T_{\mathrm{i,ped}}$.
A separation of the pedestal widths in temperature and density is not compatible with pure MHD theories. In MHD the pressure profile is the dominating quantity and one pedestal width for the pressure would also result in similar widths in temperature and density. The pedestal width might be set differently for temperature and density by transport mechanisms, where heat and particle transport do not behave similar. This is consistent with the observations of the gradient lengths, where it was possible to vary the temperature gradient length independently of the density gradient length by increasing the heating power.
The observations showed consistently a strong influence of the plasma shape, however, not always with the geometric quantities elongation and triangularity. The shaping factor f_{q} could often provide a better fit to the measurements. However, as discussed in Section 6.3, no answer could be provided on how the plasma shaping influences the physical processes in the pedestal. The shaping factor is likely connected to higher order effects, possible candidates are the magnetic shear or the magnetic field curvature.

In summary, the pedestal does not seems to be described by one unifying theory. The different observations favour various mechanisms. The pedestal top values of electron and ion temperature and density can be individually transport limited, but together they can still hit the peeling-ballooning stability limit. At the same time the pedestal widths of temperature and density scale individually.

8.3 Future Research

During the discussion of the observations presented in this thesis, limits of the multi-machine database were described. The database could be improved by extending the parameter ranges. In particular, the aspect ratio and the plasma elongation should be varied more. Adding data from a smaller machine would improve the information about the machine size. Data with higher heating power (> 20 MW) and plasma current should be included from JET. This would reduce the distance of extrapolations towards ITER. A variation of q_{95} at JET might help to clarify the toroidal magnetic field dependence of plasma pressure.
The investigation of the database brought several questions to light which could not be answered with a database approach. In particular, the detailed interplay between plasma shape - κ, δ, f_{q} - and the pedestal pressure should be investigated. Understanding of f_{q} is

necessary to clarify its impact on the plasma edge. The database gives indications of shared influence of transport and MHD stability on the pedestal. A key to disentangle these effects could be the ion pressure. To do so, an improved time resolution of the ion temperature diagnostics would be necessary to follow the evolution of the ion pedestal until the ELM crash. Theoretical models may need to include transport processes and MHD stability at the same time and not treat them separately. A necessary feature of these models would be to treat ions and electrons as well as temperature and density differently. The drive for differences in ions and electrons seems to be the collisionality and the differences therefore are expected to become more pronounced towards larger machines with smaller collisionalities.
The theoretical implications for a strong separation of density and temperature pedestal, as suggested by extrapolations towards ITER and DEMO, should be documented, in particular, gradient driven effects like the radial electric field or the bootstrap current would be strongly impacted. Direct measurements of the radial electric field are crucial to quantify the important effect of orbit squeezing in the theory of ion orbit losses. The bootstrap current is dominating the edge current density which influences the peeling-ballooning mode and it is therefore relevant for the stability of the edge transport barrier.

Bibliography

[1] *World Energy Outlook 2009*, International Energy Agency (IEA), Paris, 2009.

[2] WESSON, J. A., *Tokamaks*, Clarendon Press, Oxford, second edition, 1997.

[3] ITER Physics Expert Group, Nuclear Fusion **39** (1999) 2137.

[4] ITER Physics Expert Group, Nuclear Fusion **47** (2007) S1.

[5] BARTELS, H.-W. et al., in *IPP Summer University for Plasma Physics*, edited by KLEIBER, R. et al., Garching, Germany, 2008, Max-Planck-Institut für Plasmaphysik.

[6] WAGNER, F. et al., Physical Review Letters **49** (1982) 1408.

[7] SCHIRMER, J. et al., Plasma Physics and Controlled Fusion **49** (2007) 1019.

[8] SCHIRMER, J. et al., Nuclear Fusion **46** (2006) S780.

[9] WIELAND, B., *Investigations on radial electric fields in the edge transport barrier of H-mode discharges*, PhD thesis, Technische Universität München, München, 2011.

[10] VIEZZER, E. et al., Submitted to Review of Scientific Instruments .

[11] SUTTROP, W. et al., Plasma Physics and Controlled Fusion **39** (1997) 2051.

[12] THOMSEN, K. et al., Plasma Physics and Controlled Fusion **44** (2002) A429.

[13] CORDEY, J., Nuclear Fusion **43** (2003) 670.

[14] RYTER, F. et al., Physical Review Letters **86** (2001) 2325.

[15] JENKO, F. et al., Physics of Plasmas **7** (2000) 1904.

[16] STACEY, W. M. et al., Physics of Plasmas **13** (2006) 72510.

[17] TOLD, D. et al., Physics of Plasmas **15** (2008) 102306.

[18] KALLENBACH, A. et al., Nuclear Fusion **48** (2008) 085008.

[19] EICH, T. et al., Phys. Rev. Lett. **107** (2011) 215001.

[20] CONNOR, J. W. et al., Physical Review Letters **40** (1978) 396.

[21] MILLER, R. L. et al., Physics of Plasmas **5** (1998) 973.

[22] GOHIL, P. et al., Physical Review Letters **61** (1988) 1603.

[23] KASS, T. et al., Nuclear Fusion **38** (1998) 111.

[24] CONNOR, J. W. et al., Physics of Plasmas **5** (1998) 2687.

[25] PEETERS, A. G., Plasma Physics and Controlled Fusion **42** (2000) B231.

[26] BURCKHART, A. et al., Plasma Physics and Controlled Fusion **52** (2010) 105010.

[27] MAGGI, C. et al., Nuclear Fusion **50** (2010) 025023.

[28] MAINGI, R. et al., Physical Review Letters **103** (2009) 18.

[29] SNYDER, P. et al., Nuclear Fusion **44** (2004) 320.

[30] SAARELMA, S. et al., Plasma Physics and Controlled Fusion **51** (2009) 035001.

[31] FENSTERMACHER, M. et al., Nuclear Fusion **45** (2005) 1493.

[32] DOYLE, E. J. et al., Physics of Fluids B: Plasma Physics **3** (1991) 2300.

[33] LOARTE, A. et al., Plasma Physics and Controlled Fusion **44** (2002) 1815.

[34] SUTTROP, W. et al., Plasma Physics and Controlled Fusion **42** (2000) A97.

[35] GRUBER, O. et al., Nuclear Fusion **49** (2009) 115014.

[36] RATHGEBER, S. K. et al., Plasma Physics and Controlled Fusion **52** (2010) 095008.

[37] SCHWEINZER, J. et al., Nuclear Fusion **51** (2011) 113003.

[38] MüLLER, H. et al., Nuclear Fusion **51** (2011) 073023.

[39] PEREVERZEV, G. V. et al., IPP Report **5/98** (2002).

[40] SAUTER, O. et al., Physics of Plasmas **6** (1999) 2834.

[41] HUYSMANS, G. et al., Nuclear Fusion **47** (2007) 659.

[42] TERRY, P., Review of Modern Physics **72** (2000) 109.

[43] HUBBARD, A., Plasma Physics and Controlled Fusion **42** (2000) A15.

[44] ONJUN, T. et al., Physics of Plasmas **9** (2002) 5018.

[45] STROTH, U., Transport in toroidal plasmas, in *Plasma Physics*, edited by DINKLAGE, A. et al., volume 670 of *Lecture Notes in Physics*, pages 213–267, Springer Berlin, Heidelberg, 2005.

[46] SHAING, K. C., Physics of Fluids B: Plasma Physics **4** (1992) 290.

[47] BERGMANN, A. et al., Monte Carlo delta-f simulations of neoclassical flows and currents in the pedestal of an H-mode tokamak plasma, in *37th EPS Conference on Plasma Phys. Dublin*, page P2.118, 2010.

[48] HINTON, F. L. et al., Physics of Fluids B: Plasma Physics **5** (1993) 1281.

[49] HORTON, W., Review of Modern Physics **71** (1999) 735.

[50] SCOTT, B. D., A pictorial introduction to drift waves, unpublished.

[51] SUGIHARA, M. et al., Nuclear Fusion **40** (2000) 1743.

[52] WAGNER, F. et al., in *Physics of Plasma-Wall Interactions in Controlled Fusion*, edited by POST, D. E. et al., NATO ASI series: Physics, page 931, 1986.

[53] MAHDAVI, M. A. et al., Physics of Plasmas **10** (2003) 3984.

[54] BEURSKENS, M. N. A. et al., Physics of Plasmas **18** (2011) 056120.

[55] HUGHES, J. W., *Edge Transport Barrier Studies On the Alcator C-Mod Tokamak*, PhD thesis, Massachusetts Institute of Technology, Cambridge, 2005.

[56] SNYDER, P. B., Physics of Plasmas **16** (2009) 056118.

[57] SNYDER, P. B. et al., Nuclear Fusion **51** (2011) 103016.

[58] BORNATICI, M. et al., Nuclear Fusion **23** (1983) 1153.

[59] CLASSEN, I. G. J., *Imaging and Control of Magnetic Islands in Tokamaks*, PhD thesis, Technische Universiteit Eindhoven, Eindhoven, 2007.

[60] SALMON, A. N., International Journal of Infrared and Millimeter Waves **15** (1994) 53.

[61] SUTTROP, W. et al., IPP Report **I/306** (1997) 1.

[62] WOLFRUM, E. et al., Review of Scientific Instruments **64** (1993) 2285.

[63] FIEDLER, S. et al., Journal of Nuclear Materials **269** (1999) 1279.

[64] FISCHER, R. et al., Plasma Physics and Controlled Fusion **50** (2008) 085009.

[65] FISCHER, R. et al., Fusion Science and Technology **58** (2010) 675.

[66] MURMANN, H. et al., Review of Scientific Instruments **63** (1992) 4941.

[67] KURZAN, B. et al., Review of Scientific Instruments **82** (2011) 103501.

[68] CARLSTROM, T. N. et al., Review of Scientific Instruments **63** (1992) 4901.

[69] PASQUALOTTO, R. et al., Review of Scientific Instruments **75** (2004) 3891.

[70] RICHARDSON, W. H., Journal of the Optical Society of America **62** (1972) 55.

[71] SCANNELL, R. et al., The Review of scientific instruments **82** (2011) 053501.

[72] MLYNEK, A. et al., Review of Scientific Instruments **81** (2010) 033507.

[73] SERAYDARIAN, R. P. et al., Review of Scientific Instruments **57** (1986) 155.

[74] GOHIL, P. et al., Review of Scientific Instruments **61** (1990) 2949.

[75] LUCY, L. B., The Astronomical Journal **79** (1974) 745.

[76] SIVIA, D. S., *Data Analysis, A Bayesian Tutorial*, Oxford University Press Inc., New York, 1996.

[77] NAITO, O. et al., Physics of Fluids B: Plasma Physics **5** (1993) 4256.

[78] MCCARTHY, P. J., Physics of Plasmas **6** (1999) 3554.

[79] LAO, L. L. et al., Nuclear Fusion **25** (1985) 1611.

[80] LAO, L. L. et al., Nuclear Fusion **30** (1990) 1035.

[81] DUNNE, M. G. et al., Inter-ELM pedestal current density evolution in ASDEX Upgrade, in *38th EPS Conference on Plasma Physics, Strasbourg, France*, page P1.070, 2011.

[82] FISCHER, R. et al., 38th EPS Conference on Plasma Physics, Strasbourg, France (2011) P1.072.

[83] HATAE, T. et al., Plasma Physics and Controlled Fusion **40** (1998) 1073.

[84] GROEBNER, R. J. et al., Physics of Plasmas **5** (1998) 1800.

[85] OSBORNE, T. H. et al., Plasma Physics and Controlled Fusion **40** (1998) 845.

[86] GROEBNER, R. J. et al., Nuclear Fusion **49** (2009) 085037.

[87] LEONTOVICH, M. A., *Reviews of plasma physics, Vol. 4*, Consultants Bureau, New York, 1966.

[88] MARTIN, Y. R. et al., Journal of Physics: Conference Series **123** (2008) 12033.

[89] KALLENBACH, A. et al., Nuclear Fusion **49** (2009) 45007.

[90] MCCARTHY, P. J., Plasma Physics and Controlled Fusion **54** (2012) 015010.

[91] NEUHAUSER, J. et al., Plasma Physics and Controlled Fusion **44** (2002) 869.

[92] KALLENBACH, A. et al., Nuclear Fusion **43** (2003) 573.

[93] CHANKIN, A. V. et al., Plasma Physics and Controlled Fusion **48** (2006) 839.

[94] OSBORNE, T. et al., Journal of Nuclear Materials **266-269** (1999) 131.

[95] SNYDER, P. B., Nuclear Fusion **49** (2009) 085035.

[96] URANO, H. et al., Nuclear Fusion **48** (2008) 045008.

[97] LEONARD, A. W. et al., Physics of Plasmas **15** (2008) 056114.

[98] ROGERS, B. N. et al., Physics of Plasmas **6** (1999) 2797.

[99] SNYDER, P. B. et al., Physics of Plasmas **9** (2002) 2037.

[100] ROHDE, V. et al., Nuclear Fusion **49** (2009) 85031.

[101] KALLENBACH, A. et al., Nuclear Fusion **42** (2002) 1184.

[102] HUGHES, J. W. et al., Physics of Plasmas **9** (2002) 3019.

[103] TROYON, F. et al., Plasma Physics and Controlled Fusion **26** (1984) 209.

[104] LAWSON, J. D., Proceedings of the Physical Society. Section B **70** (1957) 6.

[105] GROEBNER, R. J. et al., Plasma Physics and Controlled Fusion **48** (2006) A109.

[106] JENKO, F. et al., Physics of Plasmas **16** (2009) 055901.

[107] KURZAN, B. et al., Analysis of large and small scale fluctuations in the plasma edge of ASDEX Upgrade, in *34th EPS Conference on Plasma Physics*, volume 31, page P1_031, Warsaw, 2007.

[108] KALUPIN, D. et al., Nuclear Fusion **45** (2005) 468.